Czech Technical University in Prague

Faculty of Electrical Engineering

Doctoral Thesis

March 2022

Ondřej Lipčák

Czech Technical University in Prague

Faculty of Electrical Engineering
Department of Electric Drives and Traction

FIELD-ORIENTED CONTROL OF INDUCTION MOTOR WITH INCLUDED NONLINEARITIES AND PARAMETER VARIATION

Doctoral Thesis

Ondřej Lipčák

Prague, *March 2022*

Ph.D. Program: Electrical Engineering and Information Technology (P2612)
Branch of study: Electric Machines, Apparatus and Drives (2642V004)

Supervisor: *doc. Ing. Miroslav Chomát, CSc.*

Supervisor-Specialist: *doc. Ing. Jan Bauer, Ph.D.*

ACKNOWLEDGEMENT

I want to thank mainly my supervisor-specialist, colleague, and friend, Jan Bauer, who always found the time to help me with my thesis and research-related activities at the department. I would also like to thank my colleagues and friends Pavel Karlovský, Pavel Kobrle, and Jakub Zedník for creating a present and friendly atmosphere at the department, which helped me in the hard times of my studies. I also appreciate the cooperation and help of my friend and master's student at the faculty, Filip Baum, who collaborated on one of my articles. In the end, my thanks go to all those who supported me in their spirit and believed that I would successfully submit my dissertation. :-)

DECLARATION

I hereby declare that I have written my doctoral thesis on my own and used only the literature listed at the end of the doctoral thesis in the references.

Prague, 3. March 2022

.....

Ondřej Lipčák

ABSTRACT

Although there are more efficient machines than Induction Machines (IM) available on the market, such as the permanent magnet synchronous machines, IM still remains the most widely used machine type in variable speed drives worldwide due to its robustness, reliability, and low initial costs. The principle of IM and Rotor Flux Field-Oriented Control (RFOC), which is the most common IM control strategy in demanding applications, may be old and well-known, and many papers were published in both fields, but still, there is room for improvement. In electric drives, even a tiny contribution to the overall drive efficiency and dynamics counts since electric machines are an integral part of our society, making them significant consumers of the world's electrical energy.

The following doctoral thesis deals with the analysis of selected nonlinearities and the problem of parameter variation and estimation of an IM drive fed from a two-level voltage-source inverter (VSI) and controlled by the so-called Direct RFOC. Inaccurate knowledge of IM model parameters leads to the RFOC detuning, which deteriorates the drive static and dynamic behavior and causes incorrect estimation of non or hardly measurable quantities such as the machine flux and torque. This thesis strives to account for some not too well-known or often neglected phenomena such as the load-dependent saturation and the parameter estimation in the presence of the saturation and iron losses. The utilized and proposed estimation algorithms are based mainly on the Model Reference Adaptive System principle. Improved reduced-order flux estimators with the included effect of iron losses are also presented and incorporated into the FOC control schemes. The most significant VSI voltage distortion sources are identified and compensated as a prerequisite for the improved control and estimation algorithms. Furthermore, an enhanced integrator for the voltage model (which serves mainly as a reference model throughout the thesis) evaluation is also proposed. Finally, since the control algorithms are implemented on Digital Signal Processors, the influence of discretization is also discussed.

The thesis is submitted as a set of selected articles completed with an accompanying text. In the beginning, a brief theoretical background that supports and supplements the problematics in the followed-up papers is presented. Next, separate subsections are dedicated to the presented papers, completed with the papers' motivation, contribution, discussion about the achieved results, and suggestions for improvement and future work. All the algorithms were programmed in C language on a DSP from Texas Instruments and verified on a 12 kW or 3.6 kW IM drive. In addition, extensive models have been developed in MATLAB/Simulink environment to further validate the proposed approaches via computer simulations.

Keywords: Field-Oriented Control, Induction Machine Drive Nonlinearities, Induction Machine, Iron Losses, Magnetic Saturation, Mathematical Modelling, Model Reference Adaptive System, Parameter Estimation.

ABSTRAKT

Přestože jsou na trhu k dispozici účinnější stroje než asynchronní motor (AM), jako např. synchronní stroje s permanentními magnety, AM stále zůstává celosvětově nejpoužívanějším typem stroje v pohonech s proměnnými otáčkami díky své robustnosti, spolehlivosti a pořizovací ceně. Princip AM a řízení orientovaného na vektor rotorového toku, což je nejběžnější řídicí strategie AM v náročných aplikacích, je sice starý a dobře známý a v obou oblastech bylo publikováno mnoho prací, ale rozhodně nelze říci, že není dále co zlepšovat. V elektrických pohonech se totiž počítá i nepatrný příspěvek k celkové účinnosti a dynamice pohonu, a to hlavně z toho důvodu, že elektrické stroje jsou nedílnou součástí naší společnosti a jsou tak významnými spotřebiteli světové elektrické energie.

Předkládaná disertační práce se zabývá analýzou vybraných nelinearit a problematikou změny a odhadu parametrů pohonu s asynchronním motorem napájeného z dvouúrovňového napěťového střídače a regulovaného tzv. přímým vektorovým řízením. Nepřesná znalost parametrů modelu asynchronního motoru vede k tzv. rozladění vektorového řízení, což zhoršuje statické a dynamické chování pohonu a způsobuje nesprávný odhad neměřitelných nebo obtížně měřitelných veličin, jako je magnetický tok a moment stroje. Proto se tato práce snaží zohlednit některé nepříliš známé jevy, jako je saturace závislá na zatížení a odhad parametrů v přítomnosti této saturace a ztrát v železe. Využité a navržené algoritmy odhadu jsou založeny především na principu tzv. „Model Reference Adaptive System.“ V práci jsou také prezentovány vylepšené modely redukovaného řádu pro odhad rotorového toku asynchronního motoru se zahrnutým vlivem ztrát v železe, které jsou začleněny do schémat vektorového řízení. Jsou identifikovány a kompenzovány nejvýznamnější zdroje zkreslení napětí střídače jako prerekvizita pro představené vylepšené algoritmy řízení a odhadu parametrů. Dále je také navržen vylepšený integrátor pro vyhodnocování napěťového modelu, který v rámci disertace slouží především jako referenční model. A konečně, vzhledem k tomu, že řídicí algoritmy jsou implementovány na digitálních signálových procesorech, je diskutována také diskrétní povaha algoritmů vektorového řízení.

Práce je předkládána jako soubor vybraných publikací s doprovodným textem. Na začátku je představen stručný teoretický základ, který podporuje a doplňuje problematiku v navazujících článcích. Každé předkládané publikaci jsou věnovány samostatné podkapitoly doplněné o motivaci, přínos, diskusi o dosažených výsledcích a možnostech budoucího zlepšení. Všechny prezentované algoritmy byly naprogramovány na signálovém procesoru od Texas Instruments v jazyce C a ověřeny na pohonech o výkonu 12 kW nebo 3,6 kW. Kromě toho byly vytvořeny rozsáhlé modely v prostředí MATLAB/Simulink, aby bylo možné navržené přístupy dále ověřit pomocí počítačových simulací.

Klíčová slova: Vektorové řízení, nelinearity pohonu s asynchronním motorem, asynchronní motor, ztráty v železe, magnetická saturace, matematické modelování, model reference adaptive system, odhad parametrů.

LIST OF CONTENT

1 INTRODUCTION 1

1.1 MOTIVATION 2

2 THEORETICAL BACKGROUND 4

2.1 INVERTER NONLINEARITY 4
2.1.1 Dead Time 4
2.1.2 IGBT Switching 4
2.1.3 Measuring Nonlinear Inverter Characteristic 8
2.1.4 Distorting Voltage Vector and Voltage Compensation 9
2.2 MAGNETIC SATURATION 9
2.2.1 Considerations about Higher Space and Time Harmonics 9
2.2.2 Saturation of Main Flux Paths 10
2.2.3 Modeling of Saturated Machine (Conventional Saturation) 10
2.2.4 Influence of Skewing on Magnetizing Inductance 11
2.2.4.1 Variation of Rotor Current Space Vector 11
2.2.4.2 Variation of Magnetizing Current 12
2.2.4.3 Cross-Coupling of d and q-Axis Currents 13
2.2.5 Influence of Rotor Leakage Flux 13
2.2.6 Saturation of Stator Tooth Tips and Rotor Surface, Field Displacement 14
2.2.7 Pseudo Load-Dependent Saturation 14
2.3 INDUCTION MACHINE LOSS COMPONENTS 15
2.3.1 Loss Segregation of Sinusoidally-Supplied Machines 15
2.3.1.1 Stator Copper Losses 16
2.3.1.2 Rotor Copper Losses 16
2.3.1.3 Iron Losses and Mechanical Losses 17
2.3.1.4 Additional Losses 17
2.3.2 Inverter-Fed Motors 18
2.4 IRON LOSSES IN CONTEXT OF INDUCTION MACHINE MODELING 18
2.4.1 Iron Losses of Inverter-Fed Induction Machine 19
2.4.2 Equivalent Circuits with Included Iron Losses, State-Space Equations 19
2.4.3 Iron Losses Measurement Description 21
2.5 INDUCTION MACHINE PARAMETER ESTIMATION 22
2.5.1 Parameter Estimation Based on Model Reference Adaptive System 23
2.5.1.1 Survey of Existing Algorithms 23
2.5.1.2 Unified Approach to Rotor Time Constant Identification 26
2.5.1.3 Concluding Remarks 27
2.6 MODIFIED INTEGRATORS FOR VOLTAGE MODEL CALCULATION 27
2.6.1 Proposed Integrator Utilized in Thesis 28

3 SET OF ARTICLES SUBMITTED AS DOCTORAL THESIS 29

3.1 PAPER 1: ANALYSIS OF VOLTAGE DISTORTION AND COMPARISON OF TWO SIMPLE COMPENSATION METHODS FOR SENSORLESS CONTROL OF INDUCTION MOTOR 30
3.1.1 Motivation 30
3.1.2 Main Contribution and Results 30
3.1.3 Discussion and Suggestions for Future Work 31
3.1.4 Errata 31

3.2 PAPER 2: OFFLINE METHOD FOR EXPERIMENTAL IDENTIFICATION OF LOAD-DEPENDENT SATURATION OF INDUCTION MOTOR TAKING INTO ACCOUNT VARIATION OF INVERSE ROTOR TIME CONSTANT 38
3.2.1 Motivation 38
3.2.2 Main Contribution and Results 39
3.2.3 Discussion and Suggestions for Future Work 39
3.3 PAPER 3: MRAS-BASED INDUCTION MACHINE MAGNETIZING INDUCTANCE ESTIMATOR WITH INCLUDED EFFECT OF IRON LOSSES AND LOAD 50
3.3.1 Motivation 50
3.3.2 Main Contribution and Results 50
3.3.3 Discussion and Suggestions for Future Work 50
3.4 PAPER 4: INFLUENCE OF SELECTED NON-IDEAL ASPECTS ON ACTIVE AND REACTIVE POWER MRAS FOR STATOR AND ROTOR RESISTANCE ESTIMATION 67
3.4.1 Motivation 67
3.4.2 Main Contribution and Results 67
3.4.3 Discussion and Suggestions for Future Work 67

CONCLUSION 88

REFERENCES 90

APPENDIX A LIST OF AUTHOR'S PUBLICATIONS 97

A.1 PUBLICATIONS RELATED TO THESIS 97
A.1.1 Publications in Journals with Impact Factor 97
A.1.2 Publications Excerpted in Web of Science 97
A.1.3 Other publications 97
A.2 PUBLICATIONS RELATED TO TOPICS DIFFERENT FROM THESIS 97
A.2.1 Publications in Journals with Impact Factor 97
A.2.2 Publications Excerpted in Web of Science 98
A.2.3 Other publications 98

APPENDIX B NOMENCLATURE 99

APPENDIX C INDUCTION MACHINE EQUIVALENT CIRCUITS 101

C.1 TRADITIONAL T-EQUIVALENT CIRCUIT 101
C.2 T-EQUIVALENT CIRCUIT WITH INCLUDED EFFECT OF IRON LOSSES, MAIN FLUX SATURATION AND ROTOR RESISTANCE VARIATION 103

APPENDIX D CONSIDERATIONS ABOUT MODELING OF SATURATED MACHINE (IRON LOSSES EXCLUDED) 105

APPENDIX E POSSIBLE PROOFS OF MODEL REFERENCE ADAPTIVE SYSTEM STABILITY 107

E.1 STABILITY PROOF AND ADAPTATION MECHANISM DERIVATION USING POPOV HYPERSTABILITY CONCEPT 107
E.2 STABILITY PROOF AND ADAPTATION MECHANISM DERIVATION USING LYAPUNOV FUNCTION 108

APPENDIX F OVERVIEW OF MODIFIED INTEGRATORS FOR VOLTAGE MODEL CALCULATION 110

F.1 INTEGRATOR APPROXIMATION BY LOW-PASS FILTER 110
F.2 COMPENSATED FILTERS 111

F.2.1 Fixed Cutoff Frequency Filters 111
F.2.2 Variable Cutoff Frequency Filters 112
F.3 AMPLITUDE SATURATION INTEGRATORS 113
F.4 ADAPTIVE STATOR FLUX OBSERVERS 114

LIST OF FIGURES

Fig. 1.1-1 Basic indirect field-oriented control with a speed sensor. 3

Fig. 1.1-2 Basic current model-based direct field-oriented control with a speed sensor. 3

Fig. 2.1-1 Inverter line-to-neutral voltage distortion due to the dead time and IGBT switching. 5

Fig. 2.1-2 One leg of the two-level voltage-source inverter (inverter phase "a"). 6

Fig. 2.1-3 IGBT parasitic capacitances. 7

Fig. 2.1-4 Switching on IGBT module. 7

Fig. 2.1-5 Switching off IGBT module. 7

Fig. 2.1-6 IGBT module testing circuit for measuring the turn-on and turn-off times. 8

Fig. 2.1-7 Measuring the delayed switching of IGBT module CM100DY-24NF. 9

Fig. 2.2-1 Dependence of the skew coefficient on the skew angle. 12

Fig. 2.2-2 Effect of the skewed rotor when the motor consists of three slices with different rotor positions. 13

Fig. 2.2-3 (a) Space vector diagram and (b) magnetic paths. 14

Fig. 2.2-4 Flux plots in the air-gap region of the motor at three different load conditions. 14

Fig. 2.2-5 Difference between the magnetizing and rotor flux linkage vectors. 15

Fig. 2.3-1 Determining the segregated loss components of an IM according to IEC 60034-2-1 Method 2-1-1B. 16

Fig. 2.4-1 Flux paths of different leakage fluxes in IM. 19

Fig. 2.4-2 Induction motor T-equivalent circuits with possibilities of iron loss inclusion. 20

Fig. 2.4-3 Illustration of the IEC-based iron loss measurement procedure. 22

Fig. 2.5-1 Classification of parameter identification and estimation techniques for induction motor drives. 23

Fig. 2.5-2 General MRAS block diagram for inverse rotor time constant estimation. 26

Fig. 2.6-1 Adaptive integrator scheme used in the thesis. 28

LIST OF TABLES

Tab. 2.4-1 Various sources of stray-load losses... 19

Tab. 2.4-2 Different IM state-space models and their state and input matrices. 20

Tab. 2.5-1 Overview of individual MRAS schemes for rotor time constant estimation. 27

Tab. C-1 Different combinations of the torque expression. 103

Fig. C-1 Induction machine linear T-equivalent circuit..... 102

Fig. C-2 T-equivalent circuit of a saturated induction machine with included fictitious iron loss resistance..... 104

Fig. D-1 An example of induction machine no-load magnetizing characteristic..... 105

Fig. D-2 A magnetizing current vector in the stationary and general reference frame..... 106

Fig. E-1 Multivariable nonlinear time-varying feedback system..... 107

Fig. F-1 General modified integrator structure. 110

Fig. F-2 Simple low-pass filter-approximated integrator..... 111

Fig. F-3 Compensated low-pass filter with output compensation..... 111

Fig. F-4 Compensated low-pass filter with input compensation..... 111

Fig. F-5 Compensated low-pass filter with output compensation..... 112

Fig. F-6 Compensated low-pass filter with input compensation..... 113

Fig. F-7 Saturable feedback integrator..... 114

Fig. F-8 Amplitude limiter. 114

Fig. F-9 Adaptive compensation using quadrature detector..... 114

Fig. F-10 General scheme of an adaptive flux observer. 115

1 INTRODUCTION

Electric drives are and will remain an integral part of human life. The increasing deployment of electric drives in the industry, electric traction, and everyday life will continue to make demands on their dynamics, cost, and efficiency. In the past, DC commutator motors practically exclusively dominated the applications with variable speed control. DC machines have the advantage that controlling their speed, which is realized mainly by variation of the armature voltage, is simple and straightforward. Resistors or rotary converters (such as the Ward-Leonard set) were initially used for this purpose, but this was a lossy control. The situation improved with the advent and development of power electronics since it was possible to replace large and uneconomical resistors with, for example, thyristor rectifiers or DC voltage converters, thus achieving significant energy savings.

Rapid development in AC motor control technology during the 1980s and 1990s enabled the utilization of various AC machine types as variable speed drives (VSD). Advancements in semiconductor technology, control hardware, and control theory made AC VSDs more reliable and affordable to compete with the more traditional controlled DC motor drives.

It is no exaggeration to say that electric drives, especially the Induction Motor (IM), enabled the technical progress of our civilization over the past century. Although many years have passed since Nikola Tesla patented the concept of IM in the 1880s, the IM still remains the most widely used type of electrical machine in VSD worldwide. This is mainly because the IM has not yet been surpassed in terms of reliability, maintenance, and purchase price by other types of machines. However, it is true that, for example, permanent magnet synchronous machines (PMSM) offer higher efficiency and a better power density than IMs. It is also true that PMSM equipped with a frequency converter based on the voltage-source inverter (VSI) can offer lower operating costs than IM, even in constant-speed applications. Therefore, we can expect that in the future, some portion of the IM-based VSDs will be replaced by PMSM drives since the lower operating costs will compensate for their higher initial cost. However, it is the opinion of the thesis author that the reliability and maintenance aspects, along with problems regarding strategic raw materials for the production of permanent magnets, will keep the IMs as a part of VSD in many applications, including the highest power drives and railway traction vehicles.

Despite the age of the IM principle and advances in its control methods, it is still worthwhile to deal with this type of electric machine. One way to improve the effectiveness of an IM drive which is also the scope of this thesis, is to improve the actual control algorithm. The IM control in high-performance applications can be based on Direct Torque Control (DTC), Model Predictive Control (MPC), or Field-Oriented Control (FOC), with the latter being the most common strategy that is also a subject of the articles presented in the thesis.

FOC of IM drive utilizes a mathematical model of the machine. The assumptions made before deriving the IM model equations do not fully apply in real life. Several simplifications are usually accepted before the derivation of the IM space-vector equations – that the stator and rotor windings are symmetric and sinusoidally distributed, that the magnetic circuit is linear, lossless, and with infinite permeability, that all the parameters (i.e., resistances and inductances) are frequency-independent and that the slotting is neglected. Some phenomena (e.g., AC vs. DC resistance) can be quite safely omitted without affecting the performance of the controlled IM drive much. However, neglecting the iron nonlinearity and iron losses and the thermal change of the stator and rotor resistance can lead to more or less severe deviations in the IM model equations from reality and can affect the controlled IM drive performance. Furthermore, due to the strong nonlinear and operating point-dependent behavior of the power electronics devices, the voltage-source inverter (VSI) used in most cases as the supply converter cannot be simply considered a linear amplifier of the voltage command.

1.1 Motivation

Many types of FOC structures can be found in the literature. In the most basic classification, we can divide the FOC schemes into the so-called Indirect FOC (IFOC) depicted in Fig. 1.1-1 and Direct FOC (DFOC) depicted in Fig. 1.1-2, which serves as the basis for all the improved FOC control structures presented in the thesis. Both the schemes belong to the most common rotor-flux oriented FOC (RFOC), meaning the regulation of the decomposed stator current vector components occurs in the rotor flux linkage vector-attached reference frame. In IFOC, the angle is obtained by integrating the summed estimated slip speed and rotor speed. In DFOC, the transformation angle θ between the stationary and the synchronous reference frame is calculated based on the estimated components of the rotor flux linkage vector. Under ideal conditions, such a choice of the reference frame enables the decoupled control of machine flux and torque.

However, many nonideal aspects exist in a real drive that impair the RFOC ability to regulate the machine flux and torque efficiently and separately:

- Both the stator and rotor resistance change with the temperature, i.e., with the mechanical loading.
- The nonlinearity of the stator and rotor cores causes the change of the machine inductances.
- The space-vector theory (SVT) used in most cases for the machine modeling considerers only the fundamental component of Magneto-Motive Force (MMF) in the airgap. However, the resulting flux density distribution contains higher spatial harmonics due to the finite number of conductors per phase, saturation, and slotting.
- The complicated distribution of the magnetic field, rotor skewing, and rotor slotting can be the source of the magnetizing and leakage inductances saturation with increased load.
- The machine stator and rotor cores are the sources of losses that increase with the machine loading and harmonic content in the supply voltage.
- The voltage provided by the inverter is distorted by the dead time and the semiconductor's finite switching and finite conductivity.
- The control algorithm accuracy will also be influenced by the sampling time, solver, and discretization method selection in practical implementation.

The mentioned IM nonlinearities and parameter variation cause the so-called FOC detuning meaning that the flux and torque are no longer regulated independently and that the quantities estimated in the control algorithm, such as the torque or flux, are different from reality. Consequently, the FOC detuning impairs the machine's static and dynamic behavior, reduces its torque capabilities, and leads to a higher current drawn from the source. Furthermore, the IM nonlinearities and parameter variation can influence sensorless speed control, condition monitoring, fault diagnosis, field-weakening strategies, and maximum torque per ampere strategies.

Out of the many possible sources of imperfections in the IM drive mentioned above, the presented thesis focuses mainly on:

1. Analysis and compensation of inverter nonlinearity.
2. Analysis of the influence of magnetic saturation of main flux paths caused by the iron properties and load.
3. Modeling, measuring, and inclusion of iron losses into the equivalent circuit.
4. Improved estimators for magnetizing inductance and rotor resistance based on IM's conventional and iron loss model.
5. Analysis of the influence of discrete implementation of FOC algorithms on the FOC and parameter estimation process.

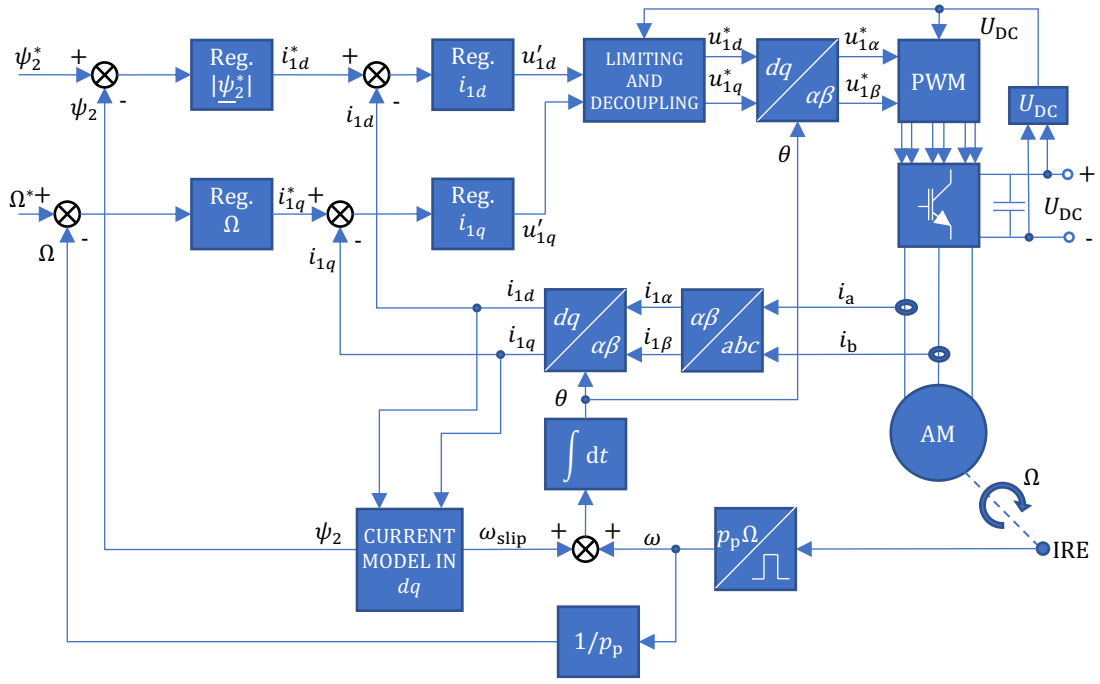

Fig. 1.1-1 Basic indirect field-oriented control with a speed sensor.

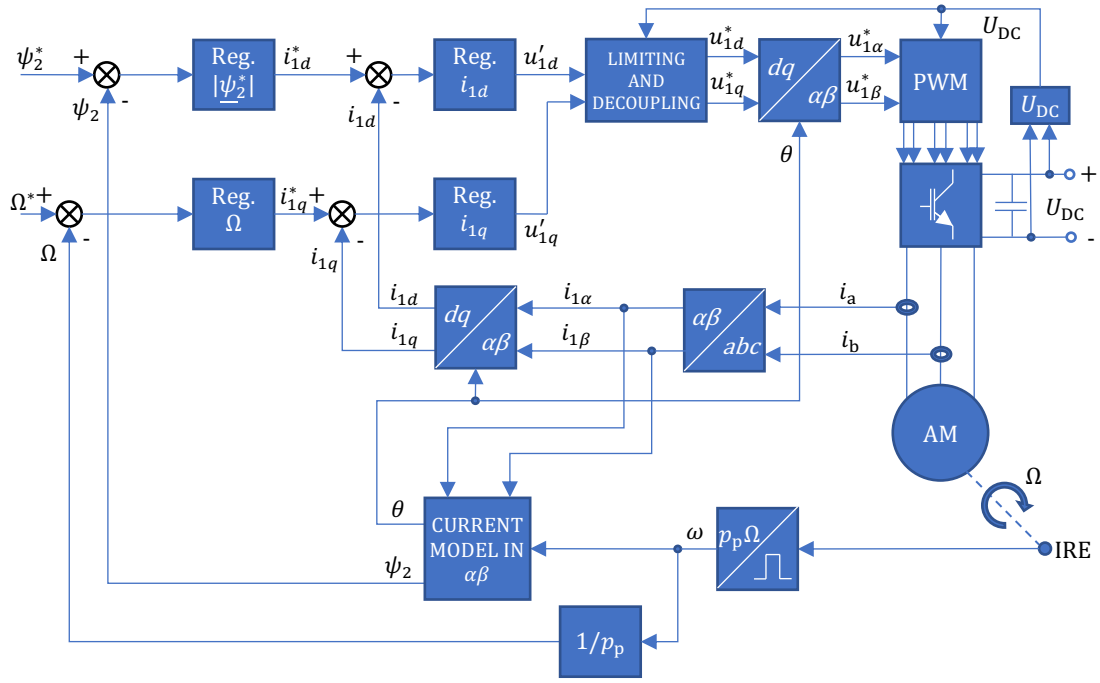

Fig. 1.1-2 Basic current model-based direct field-oriented control with a speed sensor.

2 THEORETICAL BACKGROUND

This chapter is dedicated to the theoretical background that should support or supplement the articles presented in chapter 3. In section 2.1, a thorough analysis and a physical insight into the phenomena of inverter voltage distortion are presented, along with a description of the nonlinear model measurement procedure. Section 2.2 focuses on the IM saturation phenomena, including load-dependent saturation. In section 2.3, the IM loss segregation is discussed. In 2.4, the IM iron losses are analyzed in more detail. The explanation of the phenomena is completed with considerations about IM modeling in the presence of iron losses and iron losses practical measurement. Section 2.5 briefly tackles the problematics of IM parameter estimation. Since this thesis focuses mainly on algorithms based on model reference adaptive systems (MRAS), a more detailed overview of this class of estimators is presented. Finally, since the so-called IM voltage model is a crucial component used within the presented papers, section 2.6 briefly mentions the problematics of modified integrators for the stator flux linkage vector estimation.

The aim is to keep this chapter as concise as possible while giving the reader valuable and substantive information about the theory behind the presented papers. Therefore, some additional mathematical and theoretical analysis has been moved to appendices.

2.1 Inverter Nonlinearity

For the supply of AC VSDs, a two-level three-phase VSI is utilized in most cases. The primary source of the inverter voltage distortion of the medium and high-power drives is the inserted dead time and delayed transistor switching [1]-[8]. The following analysis will be focused on IGBT inverters. However, the analysis for MOSFETs is very similar [1].

The most common 7-segment center-aligned Space-Vector Modulation (SVM) with the constant switching frequency will be considered from the possible modulation strategies. Inside the modern Digital Signal Processors (DSP) used to control the electric machines, synchronized up-down counters are usually used for this purpose. The control signal for the high-side switch is then symmetrical around the top of the counter, and the signal for the low-side switch is complementary. Furthermore, if a software dead time is implemented, then the control signal for turning on the respective IGBT is delayed by the dead time, the control signal for turning off is sent without delay. Fig. 2.1-1 shows the influence of the dead time and delayed transistor switching on the resulting SVM switching patterns and inverter line-to-neutral voltage for both current polarities.

2.1.1 Dead Time

The dead time inserted by the microcontroller or the transistor driver distorts the inverter line-to-neutral voltage u_{a0} which becomes significant in the area of small voltage vectors applied to the motor (i.e., during low-speed, low-torque operation) [2]-[3]. It is apparent that during the dead time, both switches are off, and the polarity of the voltage u_{a0}, when considering an inductive load, depends on the direction of the current i_a. If i_a is positive, then D_2 must conduct and u_{a0} is equal to $-U_{DC}/2$. If i_a is negative, then D_1 conducts and u_{a0} is equal to $+U_{DC}/2$ (see Fig. 2.1-2).

2.1.2 IGBT Switching

On an IGBT-equipped VSI, the significant contributor to the voltage distortion is the delayed IGBT switching, primarily influenced by the IGBT parasitic capacitances (Fig. 2.1-3) [9]. First, let us see what happens during switching on of Q_2 (see Fig. 2.1-2, Fig. 2.1-3, and Fig. 2.1-4). Let us assume that the inductance of the load can be treated as a current source during this analysis. In the beginning when Q_2 is off, the load current must flow through D_1. After the gate-emitter voltage U_{GE} crosses the threshold voltage, the collector current I_C starts to rise. The dI_C/dt causes a voltage drop across the parasitic inductance L_σ of the conductors that connect the DC-link with the IGBT module snubber capacitor C_{snub} (shown later in Fig. 2.1-6). When the forward current of D_1 reaches zero, an opposite reverse recovery current starts to flow through D_1 adding to the

collector current I_C. Around the peak of the recovery current, the U_{CE} starts to sharply fall to zero since D_1 is turning off, meaning that it can now pick up the reverse recovery voltage. The turn-on process is over, and Q_2 conducts the full load current.

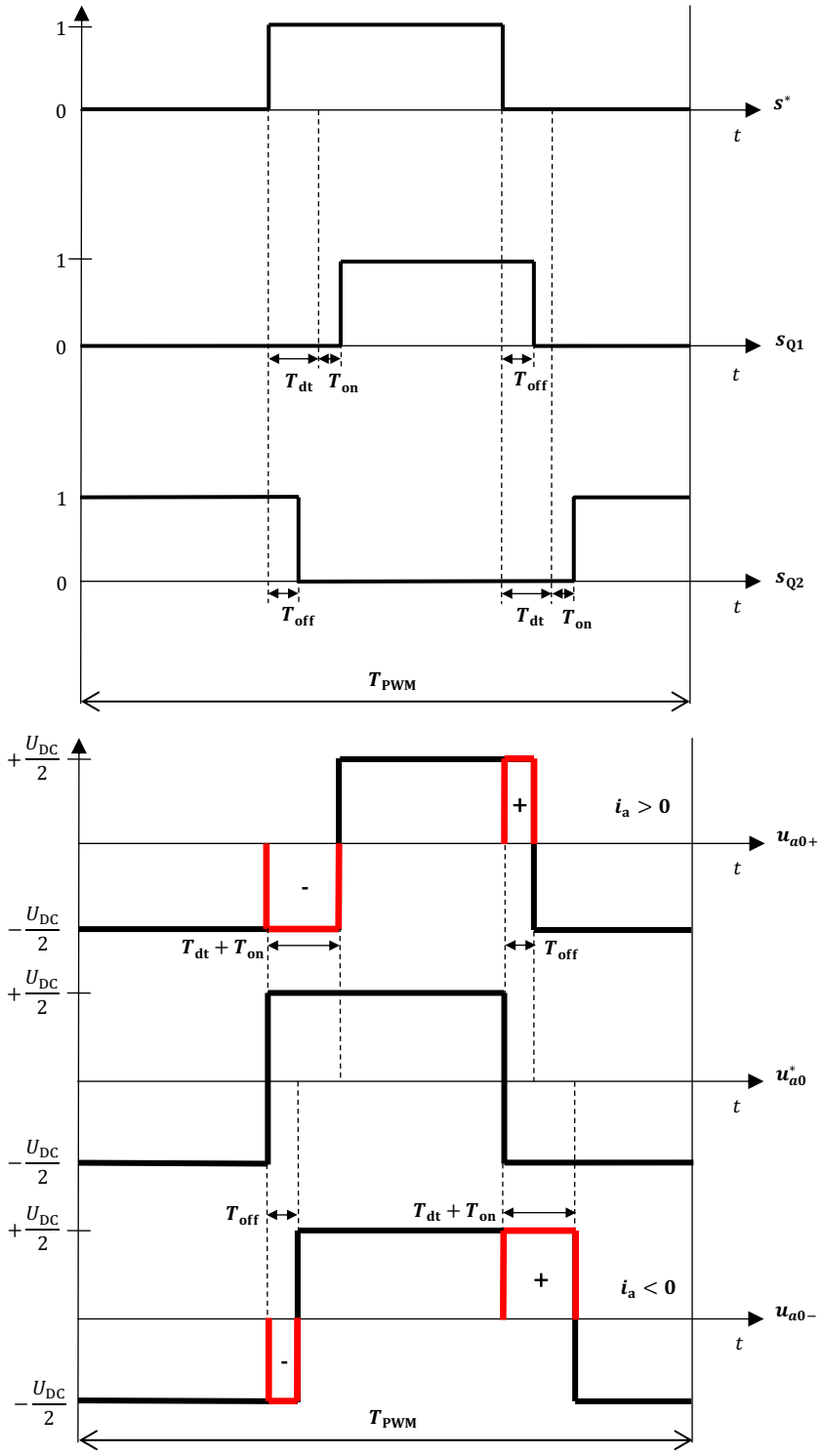

Fig. 2.1-1 Inverter line-to-neutral voltage distortion due to the dead time and IGBT switching; T_{on}: equivalent transistor turn-on delay; T_{off}: equivalent transistor turn-off delay; T_{PWM}: modulation period; T_{dt}: dead time; s^*: ideal switching signal (1 – high-side switch on, 0 – low-side switch on); s_{Q1} (s_{Q2}): equivalent state signal (1 – transistor is on, 0 – transistor is off) for high-side (low-side) switch; u^*_{a0}: ideal inverter line-to-neutral voltage (defined in Fig. 2.1-2), u_{a0+} (u_{a0-}): actual inverter line-to-neutral voltage for a positive (negative) current polarity; U_{DC}: DC-link voltage.

Now, let us move on to the analysis of the switching off (see Fig. 2.1-2, Fig. 2.1-3, and Fig. 2.1-5). After the gate-emitter capacity C_{GE} is discharged and the U_{GE} crosses the threshold voltage, the equivalent MOSFET turns off, and the collector-emitter voltage U_{CE} starts to build up to the full DC-link value with a drop in the collector current I_C. That means, the parasitic capacitances C_{CG} and C_{CE} (see Fig. 2.1-3 for definition) are being charged, and the voltage rise time is dependent on the load or collector current, respectively [5]. This explains the strong dependence of the turn-off times on the collector current, since the lower the current, the slower the charging process (the process of switching on is faster and not too much collector current-dependent since it includes only the more rapid process of the discharge of the parasitic capacitances). After the collector-emitter voltage reaches the DC-link voltage, D_1 starts to take over the current. The switching off is now over, and D_1 conducts the full load current. The tail of the collector current is one of the IGBTs' parasitic properties. After turning off the MOSFET structure, we no longer have control over the equivalent bipolar transistor. The collector current then decreases relatively slowly by recombination at the PN junction of the bipolar transistor (difference from POWER MOSFETs). Furthermore, the parasitic collector-gate capacitance can cause the unwanted transition to the "on" state during the turning off and is the reason why the gate-emitter voltage is clamped to the negative value during the off state [10].

The values that the manufacturers of the IGBT modules usually provide in the datasheet are: turn-on delay time $t_{d(on)}$, turn-on rise time t_r, turn-off delay time $t_{d(off)}$ and turn-off fall time t_f. These parameters are generally dependent on the collector current I_C, junction temperature T_j, collector-emitter voltage U_{CE}, gate-emitter voltage U_{GE}, the value of the used gate resistor R_G and the load type. The dependence of the switching times on the collector current is for other parameters as constants (usually for the nominal operating conditions) given in the product datasheet [10]-[12]. It is important to note that the stated IGBT parameters are connected with the U_{GE} and I_C waveforms, therefore we cannot simply calculate the turn-on time for the voltage compensation purposes as the sum of $t_{d(on)}$ and t_r, and the turn-off time as the sum of $t_{d(off)}$ and t_f because this does not correspond to the voltage waveforms during the switching. Furthermore, the actual operating conditions of the IGBT may be different from the ones given in the datasheet.

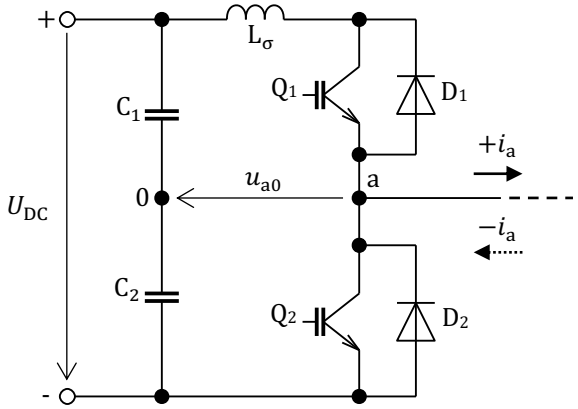

Fig. 2.1-2 One leg of the two-level voltage-source inverter (inverter phase "a"); L_σ: parasitic inductance of the interconnecting conductors.

The so-called Miller's plateau, which impairs the process of IGBT switching, is caused by the strong dependence of C_{CG} on U_{CE} (C_{CG} increases with decreasing U_{CE}) [13]. Therefore, after U_{GS} reaches the threshold voltage, i.e., when I_C starts to flow and U_{CE} starts to drop, C_{CG} begins to increase, meaning that most of the gate driver current is being used to accommodate the change in voltage across C_{CG} since the product $C_{CG} \cdot U_{CG}$ continues to increase. Since most of (or all) the driver charge flow into C_{CG}, U_{GE} stays approximately constant. The same process happens in reverse when the device is turning off.

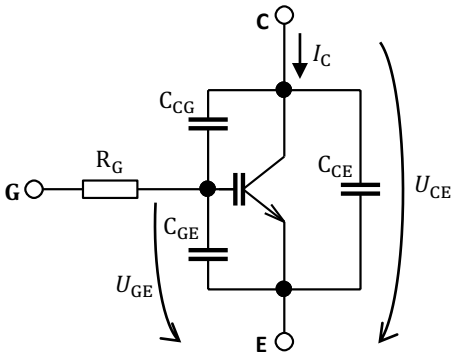

Input capacitance: $C_{ies} = C_{CG} + C_{GE}$
Output capacitance: $C_{oes} = C_{CG} + C_{CE}$
Reverse transfer capacitance: $C_{ies} = C_{CG}$

Fig. 2.1-3 IGBT parasitic capacitances.

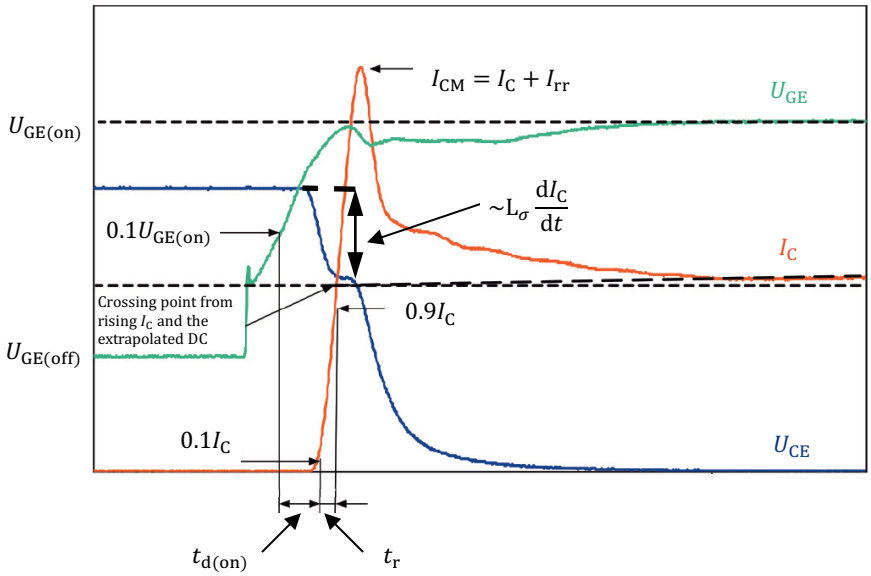

Fig. 2.1-4 Switching on IGBT module [11] (edited).

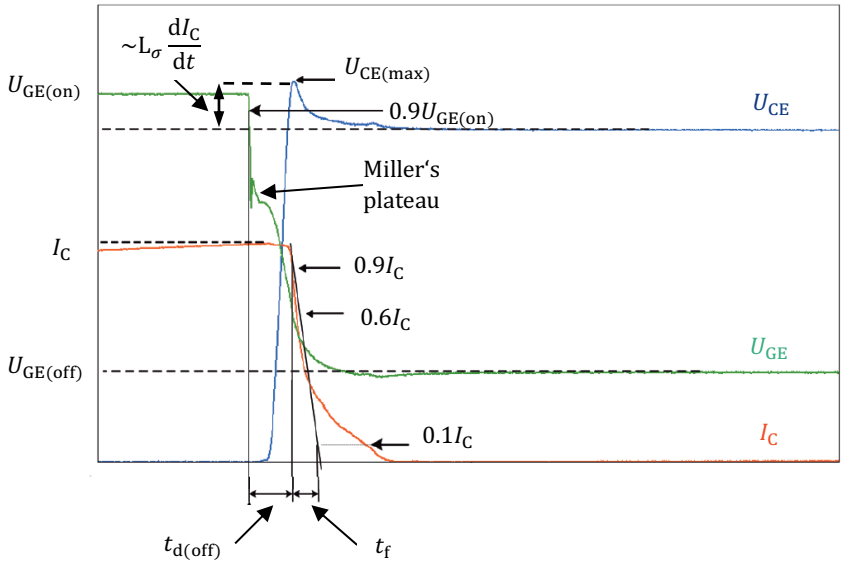

Fig. 2.1-5 Switching off IGBT module [11] (edited).

2.1.3 Measuring Nonlinear Inverter Characteristic

The above analysis shows that the most significant nonlinearities of an IGBT VSI supplied from 400 V mains are the dead time and delayed switching. In the simplest case, the dependence of the equivalent turn-on T_{on} and turn-off T_{off} times on the collector current I_C can be determined by direct measurement on the VSI. The turn-on time T_{on} is measured as the time interval between the rising edge of the microcontroller's control signal $U_{\mu P}$ and the transition of the collector-emitter voltage of the device under test (DUT). The turn-off time is measured similarly as the time interval between the microcontroller's control signal $U_{\mu P}$ and the actual transition of the collector-emitter voltage. In both cases, the actual transition of the collector-emitter voltage is best to determine when $U_{CE} = 0.5U_{DC}$. The reason is that if the transition is approximately linear, this models the average value per modulation period [5] (if an asynchronous modulation technique is used). Fig. 2.1-6 shows the testing circuit that can be used for the delayed switching measurement [11].

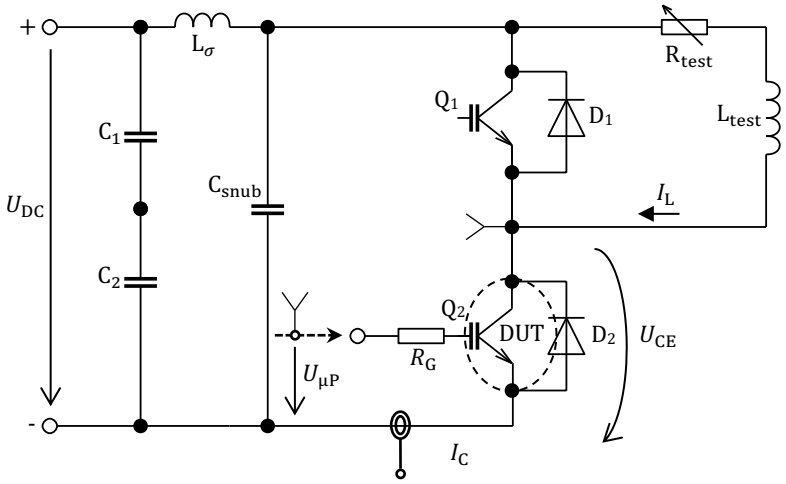

Fig. 2.1-6 IGBT module testing circuit for measuring the turn-on and turn-off times (based on [11]).

The testing procedure can be summarized in individual steps as:

1. For performing the measurement, one leg of the inverter is sufficient.
2. The testing circuit is connected, as shown in Fig. 2.1-6. The inductance value L_{test} should be selected to smoothen the DC load current as much as possible.
3. The modulator in the microcontroller is modified to generate a variable duty cycle for the respective inverter leg (the switching is in a complementary mode). The switching frequency should be the same as the one used later for the electric drive control
4. Variable current is generated by adjusting the duty cycle or the value of the auxiliary resistor R_{test}. The current should be varied from zero to a value above the peak of the nominal motor current.
5. Using an oscilloscope and voltage probes, for each value of the current, the delay between the microcontroller signal and the actual transition of the collector-emitter voltage is measured during transistor switching on and off.

The described test procedure was carried out on IGBT modules CM100DY-24NF from Mitsubishi Electric. The testing conditions were: collector-emitter voltage $U_{CE} = 560$ V, gate-emitter voltage $U_{GE} = \pm 15$ V, gate resistance $R_G = 6.8\ \Omega$, junction temperature $T_j = 25$ °C and an inductive load. Fig. 2.1-7 shows four oscillograms of the IGBT switching process during the measurement. The screenshots were made for the different values of the collector current. It can be seen that the turn-off times significantly depend on the collector current magnitude.

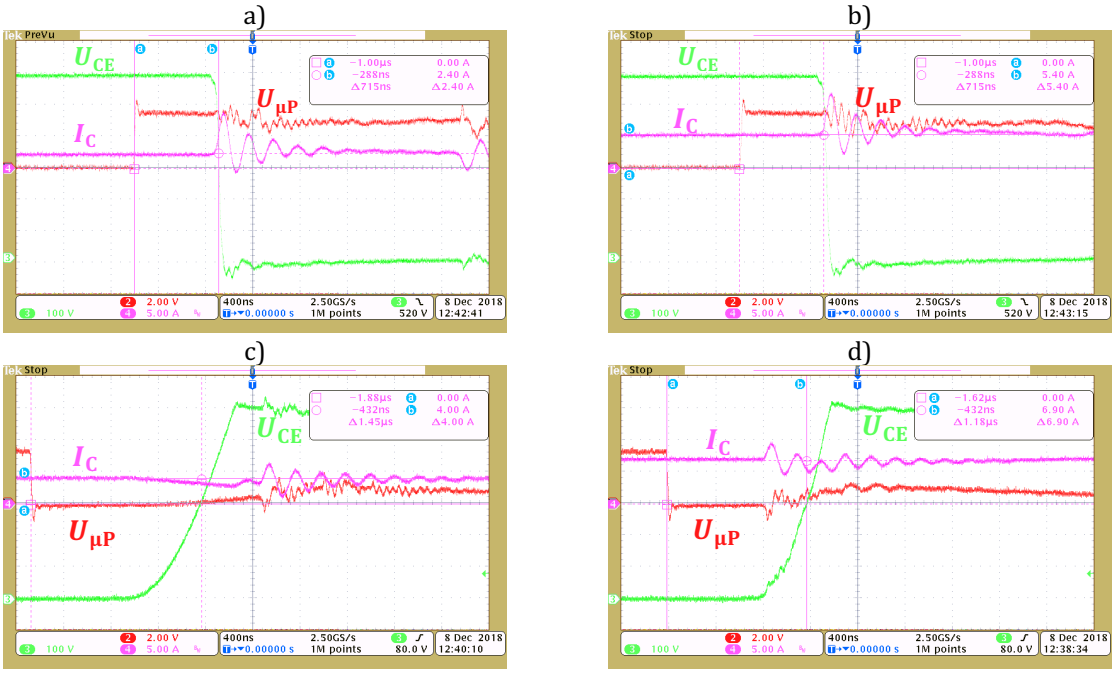

Fig. 2.1-7 Measuring the delayed switching of IGBT module CM100DY-24NF (U_{CE} – collector-emitter voltage, I_C – collector current, $U_{\mu P}$ – DSP control signal); a) turning on, $I_C = 2.4$ A; b) turning on, $I_C = 5.4$ A; c) turning off, $I_C = 4$ A; d) turning off, $I_C = 6.9$ A.

2.1.4 Distorting Voltage Vector and Voltage Compensation

Multiple methodologies for voltage distortion analysis and compensation have been presented in the literature so far. One of the possible approaches to the mathematical analysis of the variable distorting voltage vector along with the implementation of the voltage compensation is the subject of the paper presented in section 3.1

2.2 Magnetic Saturation

This section describes the main flux path saturation and its influence on the FOC performance, including the phenomenon of load-dependent saturation. The emphasis is put on the saturation analysis within the context of the most common space-vector theory used for AC electrical machines modeling. The saturation in a broader context is a very complex phenomenon, which almost all of the available theories of electrical machines are not able to respect rigorously. Therefore, the typical approach is that the equivalent linear circuit valid only for the fundamental space and time harmonics is derived, and then it is modified to include nonlinearities and parameter variation such as the magnetic saturation.

2.2.1 Considerations about Higher Space and Time Harmonics

The thesis author also considers it appropriate to acknowledge a more severe discrepancy between the model and reality. SVT inherently considers only the fundamental space wave of the MMF [13]; therefore, the fundamental flux and voltage equations along with the equivalent circuit presented in C.1 should be valid only for this space wave. However, higher space harmonics caused by a finite number of slots per phase are present in a real machine. The resulting magnetic flux density is further distorted by slotting and saturation. Rigorously, every space harmonic should be represented by a different equivalent circuit [14]-[16]. Inductances for each space harmonics caused by the winding distribution can be roughly theoretically calculated, for instance, by theory alternative to SVT elaborated by prof. Štěpina [16]-[17]. However, it is impossible to distinguish between the individual space harmonics by experimental tests since, by experiments, only the net influence can be determined. Furthermore, even the theory proposed

by prof. Štěpina fails when the finite and variable iron permeability is considered; since then, the MMF and flux density waveforms are distorted, and the principle of superposition can no longer be used.

The same holds for the higher time harmonics caused by the inverter-generated supply voltage, for which different IM parametrization should be used [18]-[21]. Higher current harmonics are introduced if the switching frequency or machine leakage inductance is low. The current harmonics are undesirable for multiple reasons. First, the FOC strategies inherently consider and control only the fundamental wave [22]. Therefore, higher time harmonics impair the FOC performance. Secondly, the harmonics cause the increase of the machine copper, and mainly iron losses, which will be discussed in sections 2.3.2 and 2.4.1. Moreover, the third important aspect is that high-frequency machine parameters are generally different from the values measured at the fundamental frequency due to the skin effect. So we are in the situation that FOC requires the fundamental wave parameters, but when the inverter is used for the parameter identification, only the net influence of all the time harmonics is obtained.

The discrepancies mentioned above are neglected in nearly all the papers dealing with IM modeling for FOC purposes, parameter measurement, and estimation and will also be neglected in this thesis. However, the study of the influence of the individual space and time harmonics on the performance of FOC strategies represents an intriguing subject for future research.

2.2.2 Saturation of Main Flux Paths

A common cause of the FOC detuning is the inexact knowledge of the magnetizing inductance. Due to the material savings, electrical machines are usually designed so that the rated point lies within the knee of the magnetization curve. Because of the conventional iron saturation, the magnetizing inductance of IM then may vary in a wide range [23]-[24]. If the machine is allowed to spin without a connected load, the saturation characteristics can be easily obtained indirectly from the measured power, voltages, and currents during a no-load test [25]-[28].

The dependence of the magnetizing inductance on the magnetizing current can be explained by the nonlinear behavior of the ferromagnetic circuit. There are mathematical models considering this type of saturation in the literature [29]-[32]. However, as pointed out in [33]-[43], the IM magnetizing inductance may also saturate as a function of the torque or rotor current, respectively, especially if the rotor slots are skewed and closed. By the nature of this phenomenon, this dependency is not possible to experimentally determine by the standard no-load test. Most papers model the magnetizing inductance only as a function of the magnetizing current. Only a few works strive to include the influence of the load or torque, respectively [33], [40]. Those papers use mainly finite element analysis (FEA). However, FEA models require knowledge of the IM geometry and used materials; therefore, they are suitable for prototyping or new machine design.

2.2.3 Modeling of Saturated Machine (Conventional Saturation)

Conventionally, the IM magnetic flux is held constant by the control algorithm. However, within maximum torque-per-ampere strategies [44]-[45] or in the field weakening region [46]-[47], the flux is varied according to the predetermined command.

The considerations in this chapter are made under the assumption that the iron losses are neglected. Generally, the induction machine saturation is considered after the derivation of the T-equivalent circuit [13]. The IM basic flux and voltage equations presented in section C.1 are valid both for saturated and linear magnetic conditions. Only if the saturation of the main flux paths is considered, then the magnetizing inductance becomes a variable parameter (i.e., $L_\mathrm{m} \neq$ const.).

However, a different situation arises during the derivation of the state-space form of IM equations due to the necessity of differentiation of the product of the inductance and current. If the flux linkage vectors are used as state-space variables, then the saturation does not explicitly appear in the equations, and it is sufficient to complete the model with equation $L_\mathrm{m} = f(i_\mathrm{m})$ or $L_\mathrm{m} = f(\psi_\mathrm{m})$, respectively. Therefore, when the state-space form of a saturated IM model is

required, selecting the flux linkages as state variables is a preferred choice [13]. A mathematical insight into the modeling of IM saturation (without iron losses) is presented in Appendix D.

The magnetizing inductance identification is then the content of papers presented in sections 3.2 and 3.3, respectively. The first of the mentioned papers strives to identify the load-dependent saturation, while the second paper also enables the identification of the conventional saturation in the presence of iron losses.

2.2.4 Influence of Skewing on Magnetizing Inductance

Many small and medium power IMs are manufactured with skewed rotor slots [35]. The main reason behind this measure is the suppression of parasitic synchronous, asynchronous, and cogging torques [35]-[36], [48]-[49]. These negative phenomena are known to deteriorate the torque-slip characteristic of the machine[15].

However, rotor skewing does not bring only positive effects. It is well known that the skewing decreases magnetizing inductance, increases rotor leakage inductance and resistance, and contributes to interbar currents [36]. In the case of the magnetizing inductance, the decrease is caused by a reduced magnetic coupling due to the skew angle.

A more interesting phenomenon is the dependence of the magnetizing inductance of a skewed machine on the rotor current. Since a skewed rotor can be modeled as an infinite amount of elementary machines connected in series with mutually phase-shifted rotor windings [48]-[49], then according to SVT, there will be a different rotor current space vector in each machine slice. The coordinate system of each rotor slice is then fixed to an axis of the reference phase. However, the individual rotor phases are mutually shifted due to the skew angle.

Within SVT, the magnetizing inductance is defined as the ratio of the magnetizing flux and magnetizing current magnitudes. If iron losses are neglected, the magnetizing current space vector is defined as the sum of the stator and rotor current space vectors. However, in a skewed machine, due to the rotor current space vector variation along the rotor axis, the magnetizing current's vector phase and, more importantly, its magnitude will also vary along the rotor axis. Consequently, a similar phenomenon as an armature reaction known from DC machines' theory can occur due to the machine core's magnetic nonlinearity. Because of the magnetizing current magnitude variation, the magnetic flux will decrease in one half of the rotor while increasing in the other half. However, due to the saturation, the decrease is higher than the increase, which reduces the net magnetizing flux.

2.2.4.1 Variation of Rotor Current Space Vector

Let us consider the rotor current space vector of an unskewed machine that is already recalculated onto the stator side:

$$\underline{i}_2 = I_2 \mathrm{e}^{\mathrm{j}\gamma_0}, \tag{2.2-1}$$

where γ_0 is the phase shift in a given coordinate system and I_2 is the vector amplitude.

As mentioned above, a machine with skewed rotor slots can be modeled as an infinite number of elementary machines on the same shaft, whose rotor windings are shifted by an angle corresponding to the skewing. Suppose that the origin of coordinates is chosen in the center of the rotor axial length L. The phase shift of the space vector at a distance x in the axial length direction can be expressed as

$$\gamma(x) = \frac{\Delta}{L} x + \gamma_0, \tag{2.2-2}$$

where $x \in \langle -L/2, L/2 \rangle$, and Δ is the skew angle expressed in electrical degrees. The rotor current vector in each slice of the machine can be then expressed as

$$\underline{i}_2(x) = I_2 \mathrm{e}^{\mathrm{j}\left(\frac{\Delta}{L}x + \gamma_0\right)}, \tag{2.2-3}$$

The resulting influence of skewing can be evaluated by integrating (2.2-3) across the rotor length, i.e.,

$$\underline{i}_{2(\mathrm{skew})} = \frac{1}{L}\int_{-L/2}^{L/2} \underline{i}_2(x)\mathrm{d}x, \tag{2.2-4}$$

which yields

$$\underline{i}_{2(\mathrm{skew})} = \frac{\sin\frac{\Delta}{2}}{\frac{\Delta}{2}} I_2 \mathrm{e}^{j\gamma_0} = k_{\mathrm{skew}}\underline{i}_2, \tag{2.2-5}$$

where $k_{\mathrm{skew}} = \sin(\Delta/2\,)/(\Delta/2)$ is the skew coefficient known from the theory of electrical machines [16]. The dependence of $k_{\mathrm{skew}} = f(\Delta)$ for a two-, four- and six-pole machine is shown in Fig. 2.2-1.

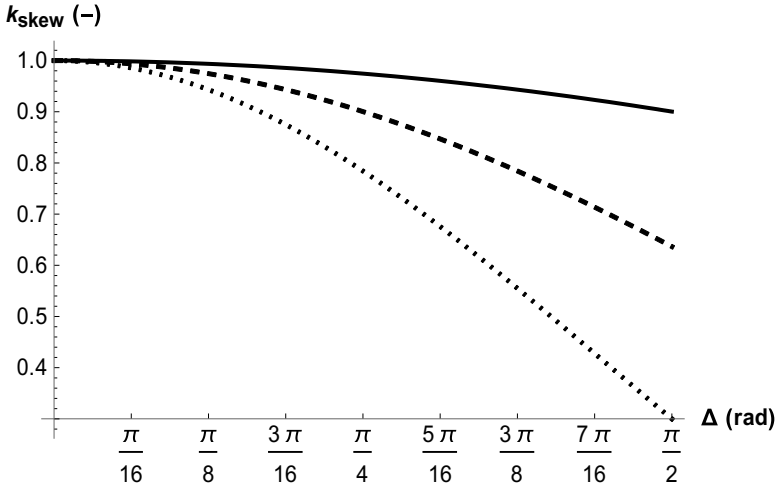

Fig. 2.2-1 Dependence of the skew coefficient on the skew angle; machine with: solid – two poles, dashed – four poles, dotted – six poles.

2.2.4.2 Variation of Magnetizing Current

Let us first consider an unskewed machine. Within SVT, the magnetizing current vector is defined (when the iron losses are neglected) as

$$\underline{i}_{\mathrm{m}} = \underline{i}_1 + \underline{i}_2. \tag{2.2-6}$$

The absolute value of $\underline{i}_{\mathrm{m}}$ can be expressed as

$$i_{\mathrm{m}} = \left|\underline{i}_{\mathrm{m}}\right| = \sqrt{I_1^2 + I_2^2 + 2I_1 I_2 \cos\delta}, \tag{2.2-7}$$

where δ is the angle between the stator and rotor current space vectors and I_1 is the magnitude of the stator vector. In a skewed machine, the magnetizing current vector will vary across the rotor length as

$$\underline{i}_{\mathrm{m}}(x) = \underline{i}_1 + \underline{i}_2 \mathrm{e}^{\mathrm{j}\frac{\Delta}{L}x}. \tag{2.2-8}$$

An absolute value of (2.2-8) yields

$$i_{\mathrm{m}}(x) = \sqrt{I_1^2 + I_2^2 + 2I_1 I_2 \cos\left(\frac{\Delta}{L}x + \delta\right)}. \tag{2.2-9}$$

Equation (2.2-9) essentially states that there will be a different magnitude of the magnetizing current in each elementary machine slice. If the machine core is magnetically linear, then $L_{\mathrm{m}} =$

const. $\Rightarrow L_\mathrm{m} \neq f(i_\mathrm{m})$, and rotor current in a skewed machine does not influence the net magnetizing flux.

Fig. 2.2-2 shows the vector diagram for the case when the rotor is modeled as three mutually shifted slices. In all cases, the stator is geometrically identical. A different equivalent rotor current vector is present in each slice due to the mutual rotor winding phase shift. It follows that the resulting magnetizing inductance can be written as

$$L_\mathrm{m} = \frac{\psi_{\mathrm{m}(1)} + \psi_{\mathrm{m}(2)} + \psi_{\mathrm{m}(3)}}{i_{\mathrm{m}(1)} + i_{\mathrm{m}(2)} + i_{\mathrm{m}(3)}}. \tag{2.2-10}$$

If nonlinear magnetic properties are considered, the saturation varies in the axial direction, and the inductance (2.2-10) is lower than for an unskewed machine.

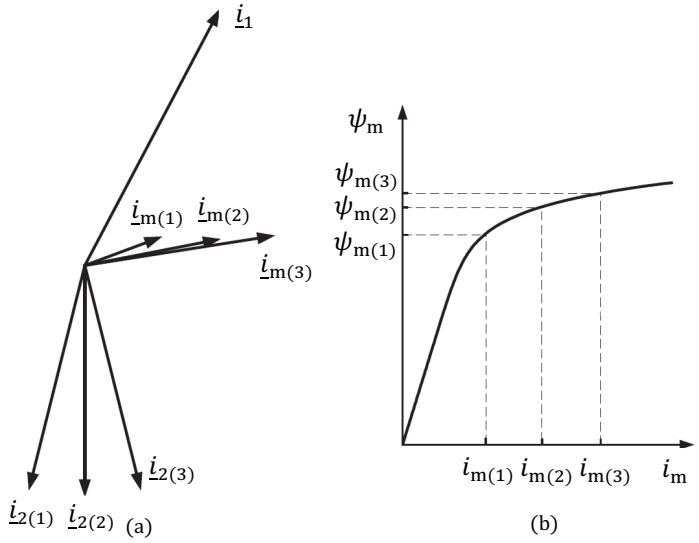

Fig. 2.2-2 Effect of the skewed rotor when the motor consists of three slices with different rotor positions: (a) current space vectors and (b) saturation characteristics. Currents at the end slices are marked by subscripts (1) and (3) and current in the middle slice by the subscript (2) [38] (edited).

2.2.4.3 Cross-Coupling of d and q-Axis Currents

Another consequence of the rotor skewing that affects RFOC is the cross-coupling of the d and q-axis currents. Let us consider that i_{1d} and i_{1q} are the space vector components in the rotor center (i.e., at $x = 0$). The "effective" current components in each slice can be expressed as [35]

$$i_{1d(\mathrm{eff})}(x) = i_{1d} \cos\left(\frac{\Delta}{L}x\right) - i_{1q} \sin\left(\frac{\Delta}{L}x\right), \tag{2.2-11}$$

$$i_{1q(\mathrm{eff})}(x) = i_{1q} \cos\left(\frac{\Delta}{L}x\right) + i_{1d} \sin\left(\frac{\Delta}{L}x\right), \tag{2.2-12}$$

where the net value $i_{1d(\mathrm{eff})}$ is aligned to the actual rotor flux linkage vector.

It can be seen that the positively misaligned elements on one side of the rotor experience a reduction in the actual flux-producing component when the torque-producing component increases. The opposite is valid for the negatively misaligned side. Therefore, the resulting magnetizing inductance or rotor flux linkage vector magnitude, respectively, can be obtained by integration similarly as in (2.2-4). Again, the decrease is more significant than the increase due to the iron nonlinearity, leading to the magnetizing inductance reduction.

2.2.5 Influence of Rotor Leakage Flux

Another cause of the dependence of the magnetizing inductance on the rotor current can be seen in Fig. 2.2-3. The figure depicts the T-equivalent circuit vector diagram along with the magnetic

flux paths. The main flux passes through the stator and rotor yoke and teeth. If the rotor slots are closed, the bridge provides a path for the leakage flux. However, because the slot bridges are relatively narrow, the rotor leakage flux saturates strongly as the function of the rotor current [50]-[51]. In Fig. 2.2-3, it can be seen that the saturation at the rotor surface and in the slot bridges caused by the rotor current appear in the main flux path, which causes the dependence of the main flux on the rotor current.

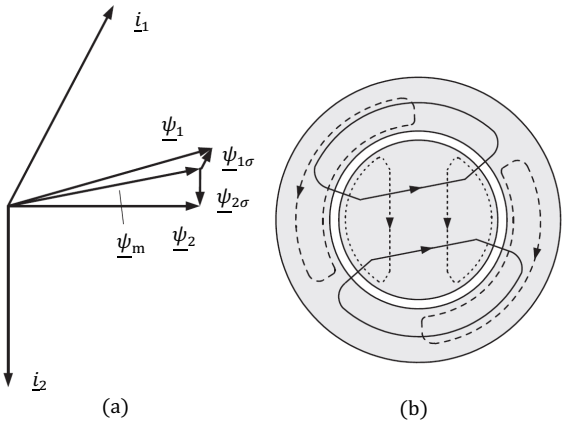

Fig. 2.2-3 (a) Space vector diagram and (b) magnetic paths: main flux (solid), stator leakage flux (dashed), and rotor leakage flux (dotted) [38] (edited).

2.2.6 Saturation of Stator Tooth Tips and Rotor Surface, Field Displacement

The last consequence of the dependence of the magnetizing inductance on the load is the saturation of the stator tooth tips and rotor surface. The increased torque of the motor increases the magnitude of the currents in the stator windings and the rotor bars. This will result in the stator tooth tips and the rotor surface starting to saturate. Due to the saturation, the effective air-gap length increases, thus resulting in a lower magnetizing inductance value. The increased angle between the stator and rotor flux linkage vector also forces the flux lines to cross slots which inevitably increases the total MMF needed [40]-[41]. The situation is depicted in Fig. 2.2-4, which shows the lines of the flux plot in the air-gap region.

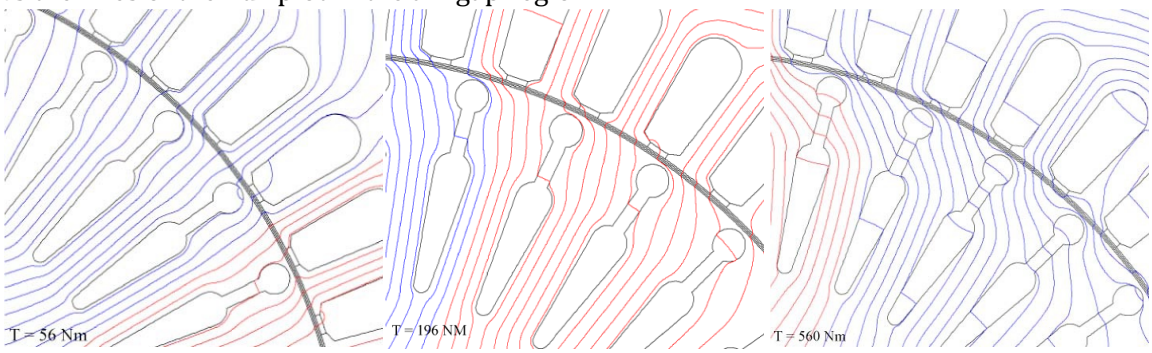

Fig. 2.2-4 Flux plots in the air-gap region of the motor at three different load conditions; left: 30 % of the nominal torque; middle: 100 % of the nominal torque; right: 290 % of the nominal torque) [41].

2.2.7 Pseudo Load-Dependent Saturation

Even though only the conventional saturation is considered, keeping the rotor flux linkage constant does not necessarily mean that the magnetizing inductance is constant. The rotor flux linkage vector is defined (if a lossless magnetic circuit is considered) as

$$\underline{\psi}_2 = \underline{\psi}_m + \underline{\psi}_{2\sigma} = \underline{\psi}_m + L_{2\sigma}\underline{i}_2. \tag{2.2-13}$$

Therefore, since the rotor current is proportional to the load, then it follows that under no-load conditions when $\underline{i}_2 \approx 0$

$$\underline{\psi}_2 \approx \underline{\psi}_\mathrm{m}. \tag{2.2-14}$$

However, keeping the rotor flux constant with increasing load means that the magnetizing flux magnitude has to be increased in a loaded machine. The situation is depicted in Fig. 2.2-5. Since in a steady state, the rotor current vector is perpendicular to the rotor flux linkage vector, it follows that the rotor flux, rotor flux leakage, and magnetizing flux linkage vectors form a right triangle with the hypotenuse equal to the magnetizing flux linkage magnitude meaning that $\left|\underline{\psi}_\mathrm{m}\right| > \left|\underline{\psi}_2\right|$.

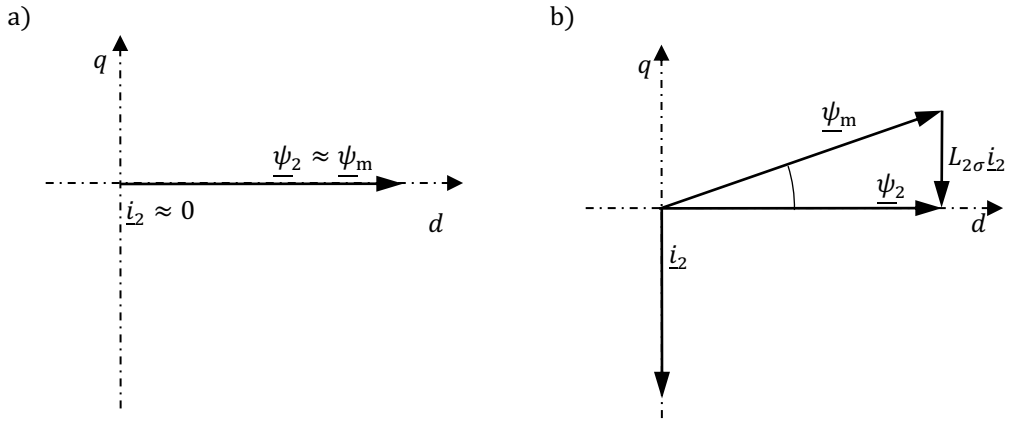

Fig. 2.2-5 Difference between the magnetizing and rotor flux linkage vectors at a) no-load and b) under load conditions.

2.3 Induction Machine Loss Components

Since electric machines consume a large portion of the world's electrical energy and since IM still remains by far the most common industrial motor type, regulations and standards exist for the determination and classification of IMs efficiency [52]. Concerning direct-online (DOL) single-speed three-phase cage machines, IEC 60034-30-1 [53] specifics four international efficiencies (IE) classes: IE4 – super premium efficiency, IE3 – premium efficiency, IE2 – high efficiency, IE1 – standard efficiency. For instance, according to [54], DOL IMs in the European Union with the rated power between 0.75 kW and 200 kW must reach the IE3 level by July 2021, and IMs between 75 kW and 200 kW must meet the IE4 level by July 2023. Furthermore, it is planned that an IE5 – ultra premium efficiency having 20% loss reduction compared to IE4 will be incorporated into the next version of the IEC standard. The efficiency categorization of inverter-fed machines is a subject of IEC TS 60034-30-2 [55], which defines five classes – IE1 to IE5.

There are two ways of determining IM efficiency. The standard input-to-output methods based on measuring the input and output power and the calorimetric method [52]. However, the calorimetric method is slow and difficult to perform [52]. Therefore, for the efficiency measurement and loss segregation, respectively, input-to-output methods are mainly used.

2.3.1 Loss Segregation of Sinusoidally-Supplied Machines

IEC [56] defines several methods for IM efficiency measurement. One of the methods is based on the efficiency determination (Method 2-1-1B) by summing of the individual components, which are classified into:

- stator copper losses,
- rotor copper losses,
- iron losses and mechanical losses,
- additional load losses.

The categories mentioned above represent the standardized, accepted, and well-understood loss components, which do not precisely capture the physical reality. The merit of the loss segregation based on the common IEC standard is that it can be used for obtaining the iron losses, additional losses, and mechanical losses for IM modeling based on the advanced equivalent circuits for the simulation or FOC implementation purposes. The test procedure for the loss segregation under a sinusoidal supply is depicted in Fig. 2.3-1. The individual loss component calculation is analyzed in the following few sections.

For completeness, it should also be noted that it is possible to use analytical equations or FEA for the loss components analysis and separation [57]. However, both approaches have the disadvantage of not capturing all the phenomena occurring inside the machine. Furthermore, FEA can be computationally demanding and requires precise machine geometry and material specification.

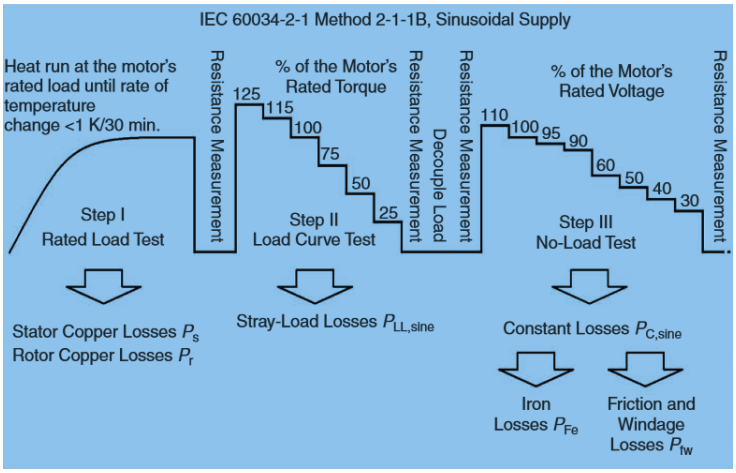

Fig. 2.3-1 Determining the segregated loss components of an IM according to IEC 60034-2-1 Method 2-1-1B [57] (edited).

2.3.1.1 Stator Copper Losses

The uncorrected stator copper losses are calculated according to IEC by using the test resistance value R_{pH} (of one phase) and phase RMS current value I_{H} as

$$P_{\mathrm{s}} = 3R_{\mathrm{pH}}I_{\mathrm{s}}^2. \tag{2.3-1}$$

According to IEC, the test resistance is defined as the resistance at the end of the heat run test, which can be further corrected to the normalized 25°C value. The calculated losses are then corrected to the ambient temperature using

$$P_{\mathrm{s},\vartheta} = k_\vartheta P_{\mathrm{s}}, \tag{2.3-2}$$

where

$$k_\vartheta = \frac{235 + \vartheta_{\mathrm{w}} + 25 - \vartheta_{\mathrm{amb}}}{235 + \vartheta_{\mathrm{w}}}, \tag{2.3-3}$$

and where ϑ_{w} is the winding temperature and ϑ_{amb} is the ambient temperature.

Since the resistance is determined by the DC test (DC resistance), the skin and proximity effect influence is hidden in the additional loss components.

2.3.1.2 Rotor Copper Losses

The slip-dependent uncorrected rotor copper losses are calculated as

$$P_{\mathrm{r}} = (P_1 - P_{\mathrm{s}} - P_{\mathrm{Fe}})s. \tag{2.3-4}$$

where P_1 is the motor input power during the heat run test, P_{Fe} are the iron losses from the no-load test, and s is the slip at the end of the heat run test. The temperature-corrected losses can then be calculated as

$$P_{\mathrm{r}} = \left(P_1 - P_{\mathrm{s},\vartheta} - P_{\mathrm{Fe}}\right) k_\vartheta s. \tag{2.3-5}$$

An error impairs both (2.3-4) and (2.3-5) since the input power contains additional losses. However, since the expression is multiplied by a slip that has a relatively low value, the error significance is also low.

2.3.1.3 Iron Losses and Mechanical Losses

The iron losses are determined from the so-called constant losses P_{c} defined as

$$P_{\mathrm{c}} = P_0 - P_{\mathrm{s},0} = P_{\mathrm{fw}} + P_{\mathrm{Fe}}, \tag{2.3-6}$$

where P_0 is the no-load input power, P_{fw} are the mechanical friction and windage losses and P_{Fe} are the iron losses, and

$$P_{\mathrm{s},0} = 3R_{\mathrm{s},0}I_{\mathrm{s},0}, \tag{2.3-7}$$

where $R_{\mathrm{s},0}$ is the resistance calculated by linear interpolation from the values before and after the no-load test.

Mechanical losses are usually calculated from four or more constant loss points between 30 % and 60 % of the rated motor voltage by developing a curve of constant losses against no-load voltage squared and then performing linear extrapolation to zero voltage. The intersection of the extrapolation curve with the vertical axis then corresponds to the mechanical losses. However, the losses generally depend on the machine's speed and temperature [57].

With the known mechanical losses, the iron loss can be determined in each point (typically 110 %, 100 %, 95 %, and 90 % of the rated voltage) as

$$P_{\mathrm{Fe}} = P_{\mathrm{c}} - P_{\mathrm{fw}}. \tag{2.3-8}$$

For the determination of the iron losses at full load, the inner voltage U_{i} that takes into account the voltage drop across the stator resistance should be used. The voltage is calculated as

$$U_{\mathrm{i}} = \sqrt{(U - I_{\mathrm{s}}R_{\mathrm{s}}\cos\varphi)^2 + (I_{\mathrm{s}}R_{\mathrm{s}}\sin\varphi)^2}, \tag{2.3-9}$$

where

$$\cos\varphi = \frac{P_1}{\sqrt{3}UI}, \qquad \sin\varphi = \sqrt{1 - \cos^2\varphi}\ . \tag{2.3-10}$$

The values of voltage, power, current, and resistance in (2.3-9) and (2.3-10) correspond to those obtained during the heat run test.

2.3.1.4 Additional Losses

The additional, i.e., stray load losses are calculated in each point of the load characteristics as

$$P_{\mathrm{Lr}} = P_1 - P_2 - P_{\mathrm{s}} - P_{\mathrm{r}} - P_{\mathrm{Fe}} - P_{\mathrm{fw}}, \tag{2.3-11}$$

where P_2 is the mechanical power on the shaft calculated from the measured speed and torque.

The additional losses calculated using (2.3-11) also contain the extra losses caused by the difference between the DC and AC resistance. Apart from this, there is still ongoing discussion about the origin of the stray-load losses [58]. However, the general agreement about the physical nature of the additional losses is that they are caused by [58]:

- the geometrical structure (stator and rotor slotting and airgap),
- limitations of the magnetic iron material that lead to the saturation on load,
- time harmonics (inverter-fed IMs).

More information about the stray-load losses is given in section 2.4.

2.3.2 Inverter-Fed Motors

If an IM is supplied from an inverter, additional losses appear due to higher time harmonics in the supply voltage [57]. The efficiency measurement of inverter-fed motors is described in IEC 60034-2-3[59]. The situation in inverted-fed motors is more difficult because the additional harmonic losses depend on the modulation strategy, switching frequency, and DC-link voltage [55]-[59]. Therefore, [55] defines the so-called "comparable converter" for the applications below 1 kV. The efficiency can then be measured by four methods. The measuring takes place at seven clearly defined operating points that can be further used for the efficiency determination in an arbitrary operating point. The additional harmonic losses compared to the sinusoidal supply can be obtained using Method 2-3-B, which is based on the IEC 60034-2-1 [56].

2.4 Iron Losses in Context of Induction Machine Modeling

Section 2.3 was focused on a general loss classification and their separation according to the widely accepted IEC standards. The following sections aim to briefly analyze the iron losses in the context of IM modeling for simulation and control purposes.

The fact that the iron losses influence the IM state, torque, and speed estimation, along with parameter identification, is undisputable [60]-[65]. One of the most widely used analytical iron losses models for a sinusoidal magnetic flux is the one that divides the iron losses into three categories: hysteresis losses, eddy-current losses, and excess losses [66]-[69], i.e.,

$$\Delta P_{\mathrm{Fe}} = k_{\mathrm{h}} f_{\mathrm{s}} B^{\delta} + k_{\mathrm{e}} f_{\mathrm{s}}^{2} B^{2} + k_{\mathrm{a}} f_{\mathrm{s}}^{1.5} B^{1.5}, \tag{2.4-1}$$

where k_{h}, k_{e} and k_{a} are the hysteresis, eddy-current, and excess losses coefficients, respectively, and B denotes the peak value of the magnetic flux density. The Steinmetz coefficient δ usually varies within $\langle 2; 3 \rangle$ [70]. It is worth noticing that the eddy-current and excess losses are sometimes merged into one loss component [69], [71]. Traditionally all the coefficients are considered to be constant. However, to achieve better accuracy, some authors consider these coefficients variable [72]-[76].

It is important to note that (2.4-1) considers only the load-independent iron losses and sinusoidal variation of the flux density [77]. However, the iron losses increase with the increasing load [77]-[79]. The slotting, saturation, rotor motion, and inverter supply harmonics cause significant distortion of the flux waveform during the load conditions leading to the decrease of the fundamental flux component and increase of the additional harmonic components [78]. The higher harmonic components then increase the losses due to additional eddy currents and minor hysteresis loops [78], [80]. The iron loss increase due to the load can be modeled using a modified Steinmetz equation or generalized Steinmetz equation [77], [81]-[82]. Furthermore, [79] summarizes that the additional or stray-load losses are caused mainly by the air-gap leakage fluxes, space harmonic, and time harmonics (see Fig. 2.4-1 and Tab. 2.4-1).

One could also conclude that the additional losses may also be caused by the rotor current. However, according to [77], [78], and [83], the losses in the rotor yoke caused by the rotor current, which alternates with the relatively low slip frequency, are negligible. The main rotor core losses occur in the rotor teeth and the rotor tooth-tips [78].

Nowadays, FEA is widely adopted within the IM iron loss modeling [84]-[86]. However, due to the extensive computational requirements, it is impossible to utilize FEA for real-time compensation, and it is also necessary to have a detailed machine geometry and material properties at disposal. Therefore, experimental methods for the iron losses determination, including the stray-load losses, are still needed.

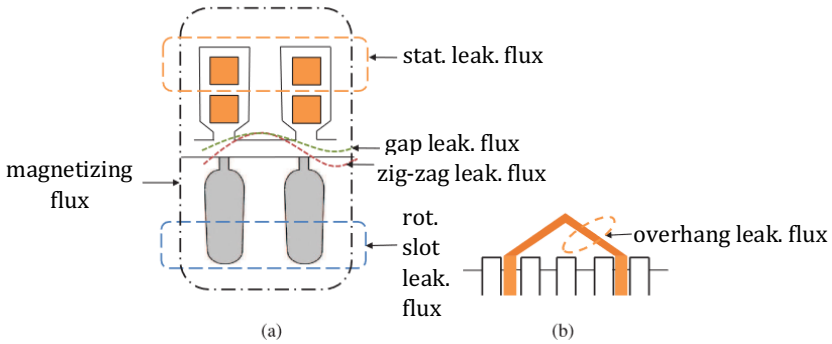

Fig. 2.4-1 Flux paths of different leakage fluxes in IM; a) slot and gap leakage fluxes; b) end leakage flux [79] (edited).

Tab. 2.4-1 Various sources of stray-load losses [79].

Number	Source	Lead to
1	Stator slot leakage flux	Leakage fluxes
2	Rotor slot leakage flux	
3	Zig-zag leakage flux	
4	Skew leakage flux	
5	Belt leakage flux	
6	Overhang leakage flux	
7	Incremental leakage flux	
8	Peripheral leakage flux	
9	Harmonics in the airgap MMF	Space Harmonics
10	Variation in slot permanence	
11	Magnetic saturation in tooth tips	Time harmonics

2.4.1 Iron Losses of Inverter-Fed Induction Machine

Using a VSI as a power supply for the IM drive introduces additional losses compared to sinusoidal supply [52], [57] since the total harmonic distortion (THD) of the motor supply voltage directly contributes to the loss increase [87].

The electric machine represents an inductive load; therefore, the switching frequency directly affects the current waveform. The influence of the switching frequency on the iron losses is particularly significant for frequencies below 5 kHz [88]-[90], where the current distortion becomes relatively high, leading to the distortion of the flux density inside the machine [91]-[92]. The iron losses increment under non-sinusoidal supply are caused mainly by increased eddy currents [93] and minor hysteresis loops [91].

Keeping the switching frequency arbitrarily high is not always possible in many applications. A good example can be high-power drives where the switching frequency must be restricted according to the used semiconductors and their cooling. On the other hand, if the control algorithms are synchronized with the switching frequency, then the restrictions provide sufficient computing time that can be utilized in the case of complicated modern control algorithms.

2.4.2 Equivalent Circuits with Included Iron Losses, State-Space Equations

In this section, two IM T-equivalent circuits considering iron losses along with their state-space representation are presented – the dominant parallel model [22], [60], [94]-[96], and the series model [98]-[100]. Also, for the sake of comparison, the traditional model with the iron losses

neglected is presented. Fig. 2.4-2 shows the topology of the IM T-equivalent circuits and Tab. 2.4-2 then presents the corresponding state-space model matrices [101]. The symbols in Tab. 2.4 2 are defined in (2.4-2). The parallel model represents physical reality better. On the other hand, it introduces additional state variables. The series model then adopts further simplifications and weakens the applicability. Furthermore, there are other IM equivalent circuits considering iron losses – Γ-equivalent circuit [102]-[103], inverse Γ-inverse equivalent circuit [104], and a π-equivalent circuit which places the iron loss resistance after the stator resistance [22], [105]. However, these models need further investigation regarding their accuracy and applicability. For modeling the stray-load losses using an equivalent circuit, one of the possible approaches is to add a resistance parallelly to the rotor leakage inductance [106].

This thesis utilizes the T-equivalent circuit with the equivalent iron loss resistance placed in parallel with the magnetizing branch. A detailed mathematical description of the equivalent circuit is given in section C.2. Such an equivalent circuit does not consider the effect of stray-load losses. However, its physical accuracy and mathematical description's complexness are still acceptable for deriving improved rotor flux, magnetizing inductance, and stator and rotor resistance estimators presented in papers from sections 3.2 and 3.3.

However, it is essential to note again that since the FOC strategies try to regulate only the fundamental wave of the machine voltage or current, respectively, only the fundamental component of the measured iron losses should be considered if the losses are compensated in a FOC algorithm [22], [107]-[108].

Tab. 2.4-2 Different IM state-space models and their state and input matrices [101].

Matrix	Levi Parallel Model	Hasegawa Series Model	Traditional Model
State Matrix A	$\begin{bmatrix} a_{11} & a_{12} & a_{13} \\ 0 & a_{22} & a_{23} \\ a_{31} & a_{32} & a_{33} \end{bmatrix}$	$\begin{bmatrix} \overline{a}_{11} & \overline{a}_{12}+d_1 & 0 \\ \overline{a}_{21} & \overline{a}_{22}+d_2 & 0 \\ 0 & 0 & 0 \end{bmatrix}$	$\begin{bmatrix} \overline{a}_{11} & \overline{a}_{12} & 0 \\ \overline{a}_{21} & \overline{a}_{22} & 0 \\ 0 & 0 & 0 \end{bmatrix}$
Input matrix B	$[b_1 \quad 0 \quad 0]^{\mathrm{T}}$	$\left[\overline{b}_1 \quad 0 \quad 0\right]^{\mathrm{T}}$	$\left[\overline{b}_1 \quad 0 \quad 0\right]^{\mathrm{T}}$

$$
\begin{aligned}
&a_{11}=-\frac{R_1+R_{\mathrm{Fe}}}{L_{1\sigma}}, \quad a_{12}=-\frac{R_{\mathrm{Fe}}}{L_{1\sigma}L_{2\sigma}}, \quad a_{13}=\frac{L_2R_{\mathrm{Fe}}}{L_{1\sigma}L_{2\sigma}}, \quad a_{22}=\mathrm{j}\omega-\frac{R_2}{L_{2\sigma}},\\
&a_{23}=\frac{L_{\mathrm{m}}R_2}{L_{2\sigma}}, \quad a_{31}=\frac{R_{\mathrm{Fe}}}{L_{\mathrm{m}}}, \quad a_{32}=\frac{R_{\mathrm{Fe}}}{L_{\mathrm{m}}L_{2\sigma}}, \quad a_{33}=-\frac{L_2R_{\mathrm{Fe}}}{L_{\mathrm{m}}L_{2\sigma}},\\
&\overline{a}_{11}=-\frac{1}{\sigma\tau_{\mathrm{s}}}-\frac{1-\sigma}{\sigma\tau_{\mathrm{r}}}, \quad \overline{a}_{12}=\left(\frac{1}{\tau_{\mathrm{r}}}-\mathrm{j}\omega\right)\frac{1-\sigma}{\sigma L_{\mathrm{m}}}, \quad \overline{a}_{21}=\frac{L_{\mathrm{m}}}{\tau_{\mathrm{r}}}, \quad \overline{a}_{22}=\mathrm{j}\omega-\frac{1}{\tau_{\mathrm{r}}},\\
&d_1=\frac{\mathrm{j}R_{\mathrm{M}}(1-\sigma)}{\sigma L_{\mathrm{m}}L_2\tau_{\mathrm{r}}}, \quad d_2=-\frac{\mathrm{j}R_{\mathrm{M}}}{L_2\tau_{\mathrm{r}}}, \quad b_1=\frac{1}{L_{1\sigma}}, \quad \overline{b}_1=\frac{1}{\sigma L_1}, \quad R_{\mathrm{m}}=\omega_{\mathrm{s}}R_{\mathrm{M}}.
\end{aligned}
\tag{2.4-2}
$$

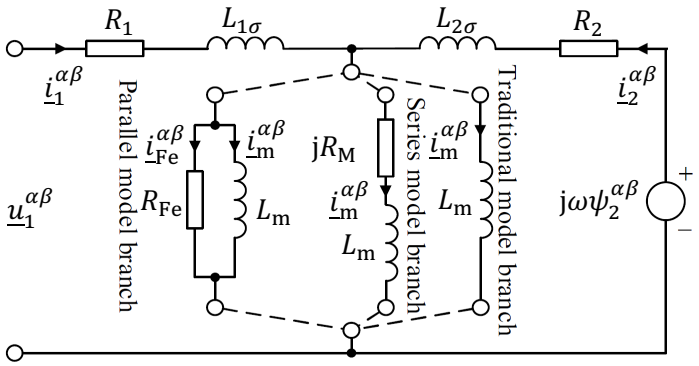

Fig. 2.4-2 Induction motor T-equivalent circuits with possibilities of iron loss inclusion [101] (edited).

2.4.3 Iron Losses Measurement Description

The iron and mechanical losses measurement utilized in the thesis is based on the IEC standard described in section 2.3.1. For the iron losses determination of the VSI supplied IM drive, it is necessary to utilize a power analyzer with sufficient bandwidth. As mentioned above, only the fundamental component of the measured iron losses should be considered.

In this thesis, the losses were measured and modeled as a function of the stator flux linkage vector amplitude ψ_1 and synchronous frequency f_s, i.e.,

$$P_{\mathrm{Fe}} = f(\psi_1, f_s). \tag{2.4-3}$$

The measured dependence in the form (2.4-3) can be implemented in the DSP as a look-up table, or the data can be fitted to one of the many analytical models proposed in the literature. In this thesis, the model proposed in [106] is utilized. The model equation can be written as

$$P_{\mathrm{Fe}} = \frac{f_s^2 \psi_1^2 + \kappa f_s \psi_1^n}{R_{\mathrm{Fe0}}}, \tag{2.4-4}$$

where f_s is the fundamental supply frequency and κ, n and R_{Fe0} are the model parameters.

If the measuring takes place on the inverter-supplied IM, then the drive should be running unloaded in an open-loop with adjustable reference voltage amplitude and frequency. The commanded voltage is varied to reach a desired stator flux linkage vector amplitude at each frequency. For this purpose, the stator voltage equation in a stationary reference frame is utilized, i.e.,

$$\underline{\psi}_1 = \int_0^t (u_{1\alpha} - R_1 i_{1\alpha}) \mathrm{d}\tau. \tag{2.4-5}$$

Then, for frequencies ranging from 5-10 % to 105-110 % of the nominal value, the fundamental component of IM input power P_{in} is measured by a power analyzer for multiple values of the stator flux amplitude. The modulation strategy and its frequency should be the same or very similar, as in the case of FOC used later for the drive control. Also, all the significant inverter nonlinearities must be identified and their compensation implemented.

From the input power P_{in}, the constant losses P_{c} are calculated as

$$P_{\mathrm{c}} = P_{\mathrm{in}} - 3R_1 I_{1(\mathrm{RMS})}^2, \tag{2.4-6}$$

where $I_{1(\mathrm{RMS})}$ is the average RMS value of the motor phase currents. Then, the mechanical losses P_{mech} are calculated from four or more constant loss points between 30 % and 60 % of the nominal stator flux linkage vector amplitude by developing a curve against no-load voltage squared (line-to-line RMS value) corresponding to the respective flux value and then performing linear extrapolation to zero voltage. The intersection of the extrapolation curve with the vertical axis then corresponds to the mechanical losses. Finally, the iron losses can be calculated from the constant losses P_{c} and the mechanical losses as P_{mech} as

$$P_{\mathrm{Fe}} = P_{\mathrm{c}} - P_{\mathrm{mech}}. \tag{2.4-7}$$

The described procedure of the iron loss measurement is illustrated in Fig. 2.4-3. The measured dependence of the iron losses fitted to (2.4-4) is then shown later in papers from sections 3.3 and 3.4.

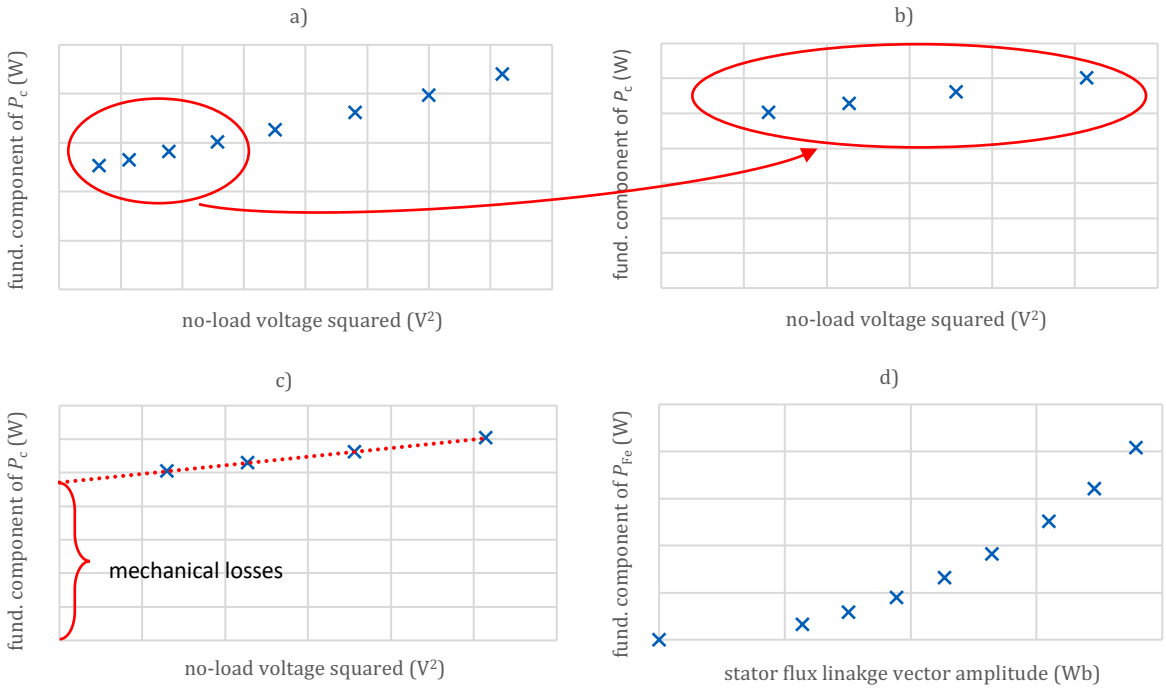

Fig. 2.4-3 Illustration of the IEC-based iron loss measurement procedure; a) curve of constant losses against no-load voltage squared at a given supply frequency; b) selection of points corresponding to the 30 %, 40 %, 50, %, and 60 % of the rated flux; c) linear extrapolation to the vertical axis for the determination of mechanical losses; d) the resulting curve of iron losses plotted against the stator flux linkage vector amplitude.

2.5 Induction Machine Parameter Estimation

The parameters of the IM mathematical models are needed for two purposes – the modeling of the machine itself and for real-time control strategies, among which we can include field-oriented control (FOC), direct torque control (DTC), and model predictive control (MPC).

The IM parameters are predominantly affected by

- temperature rise,
- skin effect,
- magnetic flux saturation,
- load.

If the parameters in the control algorithm differ from the actual ones, detuning occurs, which has the following consequences:

- the transformation angle is wrongly calculated,
- the current controllers issue inappropriate references values,
- the machine operates either in an overexcited or underexcited state,
- the control of flux and torque is not decoupled,
- performance of parameter-dependent algorithms (maximum torque per ampere, field-weakening) deteriorates.

The parameter mismatch also influences the sensorless speed control, condition monitoring, and fault diagnosis [109].

Today's trend moves towards drive auto-commissioning, which means that an arbitrary motor can be connected to an arbitrary inverter that performs the machine parameter identification. The user provides only the basic nameplate values of the motor. Therefore, an ideal state is an identification of the machine parameters at a standstill because

- generally, the blocked rotor test may not be possible to perform,
- the machine can be already coupled to load, meaning the no-load test is not possible,
- it is not generally possible to vary the load according to the predefined conditions.

Methods enabling parameter identification at a standstill are mainly based on the DC or AC signal injection. Methods that compensate for the change of the parameters based on operating conditions or methods that are intended for identification during the machine run are usually based on: model reference adaptive system, signal injection, observers, artificial neural networks, or recursive least-square algorithms (RLS). A basic classification of the possible parameter identification methods is depicted in Fig. 2.5-1. A good review of parameter estimation techniques is given in [109] and [110].

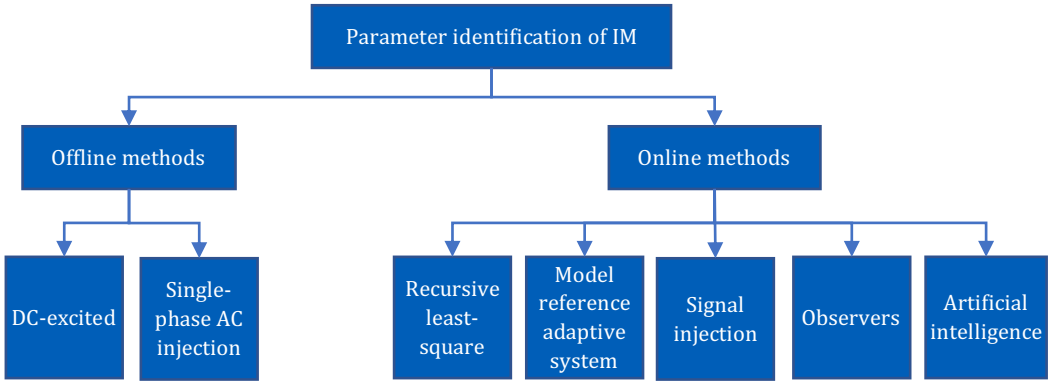

Fig. 2.5-1 Classification of parameter identification and estimation techniques for induction motor drives [109] (edited).

2.5.1 Parameter Estimation Based on Model Reference Adaptive System

Since this thesis deals mainly with MRAS-based parameter estimation methods, this category will be described in this section in more detail. In the field of electric drives, MRAS was first introduced by Tamai et al. in [111] and later elaborated by other researchers, including Schauder [112], who utilized the synthesis of MRAS based on the work of Landau [113]. The basic MRAS principle is that two mathematical models are evaluated in parallel – the so-called reference and adaptive. The reference model does not depend on the estimated quantity. On the contrary, the adaptive model utilizes directly or indirectly the estimated quantity. An adaptation mechanism (usually a simple PI controller) is used to estimate the desired variable by driving the difference between the reference and adaptive model to zero. For the MRAS design, the Lyapunov theory or hyperstability theory can be utilized [114]. More detailed information about the adaptation mechanism derivation is provided in Appendix E.

The advantage of MRAS techniques is a simple implementation and low requirements for computational power. Their major drawback is that they inherently suppose that the error between the reference and adaptive model is caused by the estimated parameter only. Control strategies with multiple MRAS algorithms were proposed in the literature [117]-[118] to overcome this problem. However, the stability analysis of such a system is complicated and is mostly omitted or greatly simplified [116].

2.5.1.1 Survey of Existing Algorithms

Various MRAS algorithms for the IM parameter estimation have been proposed in the literature. Usually, the aim is to design an algorithm that

- is affected by other parameters as little as possible,
- does not require coordinate transformations,

- is stable regardless of an operating mode (motoring, braking),
- uses measurable quantity as a reference model.

Rotor flux MRAS (F-MRAS)

Originally proposed in [112] for speed estimation. It uses the two-well known IM reduced-order models in the stationary system for the rotor flux linkage vector calculation, namely the so-called voltage model

$$\underline{\psi}_2^{\alpha\beta} = \frac{L_2}{L_\mathrm{m}}\left[\int_0^t \left(\underline{u}_1^{\alpha\beta} - R_1\underline{i}_1^{\alpha\beta}\right)\mathrm{d}\tau - L_1\sigma\underline{i}_1^{\alpha\beta}\right] + L_{2\sigma}\underline{i}_\mathrm{Fe}^{\alpha\beta} \tag{2.5-1}$$

and the current model

$$\frac{\mathrm{d}\,\underline{\psi}_2^{\alpha\beta}}{\mathrm{d}t} = \frac{L_\mathrm{m}R_2}{L_2}\underline{i}_1^{\alpha\beta} - \frac{R_2}{L_2}\underline{\psi}_2^{\alpha\beta} + \mathrm{j}\omega\,\underline{\psi}_2^{\alpha\beta}. \tag{2.5-2}$$

The reference and adaptive model selection depends on the required estimated parameter. The current model is selected as a reference if the estimated parameter is the stator resistance [119]. If the estimated parameter is the rotor resistance, the voltage model serves as a reference [120]. In [121], a similar estimator augmented with the RLS algorithm for a simultaneous rotor resistance and magnetizing inductance was proposed.

The major drawback of this estimator is that both the reference and adaptive models are non-measurable quantities. Also, pure integration cannot be used for the voltage model because of the DC offset accumulation problem [122]. Furthermore, inverter nonlinearity will affect the voltage model accuracy, especially at low speeds.

Reactive power MRAS (Q-MRAS)

Proposed in [123] for rotor time constant estimation and further elaborated by many other researchers [124]-[129]. The reference model in the dq reference frame is given by

$$Q = \Im\left\{\underline{u}_1^{dq}\overline{\underline{i}}_1^{dq}\right\} = u_{1q}i_{1d} - u_{1d}i_{1q}, \tag{2.5-3}$$

and the adaptive model by

$$\hat{Q} = \omega_\mathrm{s}\left[L_1\sigma\left(i_{1d}^2 + i_{1q}^2\right) + \frac{L_\mathrm{m}^2}{L_2}i_{1d}^2\right]. \tag{2.5-4}$$

The adaptive model does not utilize the rotor time constant directly – the time constant and the adaptive model are interconnected through slip speed (and alternatively flux) estimation. It is usually implemented in the synchronous reference frame. However, in [129] and [130], it was implemented in the stationary reference frame. The most significant advantage of Q-MRAS is that it does not depend on the stator resistance, no pure integration is required, and the reference model is parameter-free and comprises measurable quantities. One of the major drawbacks is its sensitivity to magnetizing inductance and leakage inductance variations [125]. Furthermore, it is expected that the inverter nonlinearity will affect the estimation process if not adequately compensated for.

Active power MRAS (P-MRAS)

Proposed in [131] for the stator resistance estimation and later utilized in [127] for the rotor resistance estimation using a power balance. The estimator shows common advantages and disadvantages as the Q-MRAS type. In [129], it was combined with the Q-MRAS for a simultaneous stator and rotor resistance estimation in the stationary reference frame.

The reference model in the dq reference frame is given by

$$P = \Re\left\{\underline{u}_1^{dq}\overline{i}_1^{dq}\right\} = u_{1d}i_{1d} + i_{1q}u_{1q}. \tag{2.5-5}$$

The adaptive model is obtained by substituting for the stator d and q-axis voltage components from the IM model:

$$\hat{P} = R_1 i_1^2 + \omega_s(1-\sigma)L_1 i_{1d} i_{1q}. \tag{2.5-6}$$

X-MRAS

Proposed in [132] for the stator resistance estimation. The estimator is based on a fictitious quantity that has no actual physical meaning, which is defined as

$$X = \Im\{\underline{u}_1^{dq}\underline{i}_1^{dq}\}. \tag{2.5-7}$$

The adaptive model is obtained by substituting for the stator d and q-axis voltage components from the IM model:

$$\hat{X} = 2R_1 i_{1d} i_{1q} + \omega_s\left(L_1 i_{1d}^2 - \sigma L_1 i_{1q}^2\right). \tag{2.5-8}$$

It was shown that such a controller is stable in all four quadrants of operation. It can be stated that the estimator shares common advantages and disadvantages as the P and Q-types.

PY-MRAS

Proposed in [133] for the stator resistance estimation. The functional candidate is based on the combination of the active power P and a fictitious quantity Y defined as

$$Y = -\Re\{\underline{u}_1^{dq}\underline{i}_1^{dq}\}. \tag{2.5-9}$$

The most significant advantage of the PY-MRAS is that it does not require information about the synchronous speed. The authors also claim that the estimator is stable in all four quadrants, but only simulation results are presented.

q-Axis Rotor Flux

The stability analysis and adaptation gain design of the q-axis rotor flux MRAS were thoroughly carried out in [134]. The estimated q-axis rotor flux is compared with zero and the difference is fed into the adaptation mechanism. In the estimation scheme, the sign function of the q-axis current is employed. The estimator was proven stable in the whole speed range

d-Axis Air-gap Flux

Proposed in [135] for the rotor time constant estimation. The method is based on measuring the air-gap flux from the third harmonic component of stator voltage. The third harmonic in the air-gap flux occurs predominantly due to the saturation. The adaptive model depends on the magnetizing inductance. The disadvantage is the requirement for stator phase voltage sensors.

d-Axis Stator Voltage

Proposed in [136] for the rotor time constant adaptation. The reference model is the d-axis stator voltage demanded by the d-axis stator current controller and the adaptive model is the calculated d-axis voltage component. The scheme is sensitive to voltage distortion, stator inductance, and stator resistance variation.

The scheme proposed in [137] utilizes a decoupled synchronous voltage control for the rotor time constant estimation. The advantages include a good performance under varying load/speed conditions, the absence of additional transducers, and the low sensitivity to the magnetizing inductance variations.

q-Axis Stator Voltage

Proposed in [136] for the rotor time constant adaptation. Similarly, as in the case of the d-axis voltage MRAS, the reference model is the q-axis stator voltage demanded by the q-axis stator

current controller and the adaptive model is the calculated q-axis voltage component. Again, the scheme is sensitive to the voltage distortion, stator inductance, and stator resistance variation.

Electromagnetic Torque (T-MRAS)

Proposed in [127] for the rotor time constant estimation. Both the reference and adaptive models are non-measurable quantities. Furthermore, the reference model employs the stator flux equation in the stationary $\alpha\beta$ system, which implies the integration problems and the stator resistance dependency. Also, non-monotonic dependence of the error for slip speeds lower than a threshold value was reported.

Dot Product of Stator Current and Rotor Flux

Proposed in [138] for the rotor time constant estimation. The stator current and rotor flux dot product serves as the reference model. The adaptive model is the product of the magnetizing inductance and d-axis stator current. The stability and gain design were then thoroughly performed in [139], where it was also shown that the mismatch in the stator resistance and inappropriate selection of adaptation gain would lead to low-speed instability issues. This is also due to the integration problems because the rotor flux is recalculated from the stator flux obtained from the voltage model. Another disadvantage is the magnetizing inductance sensitivity. The advantage is that the models are free of the stator frequency.

Rotor Back EMF (EMF-MRAS)

The scheme was proposed in [140] for speed identification. In [141], it was used for a simultaneous speed and stator resistance estimation. The reference model for the speed estimation is based on the expression in the dq system for the rotor flux linkage calculation derived from the stator flux linkage and voltage equation. The adaptive model is then based on the expression in the dq system for the rotor flux linkage vector calculation derived from the rotor flux linkage and rotor voltage equation. The reference and adaptive model switch their roles to identify the stator resistance. The advantage of the scheme is that no pure integration is required.

Other Schemes

Many other schemes based on different quantities used for the rotor time constant identification can be found in the earlier literature. For instance, [142] proposes MRAS based on the stored magnetic energy, while [143] utilizes the magnitude of the rotor flux linkage vector.

2.5.1.2 Unified Approach to Rotor Time Constant Identification

A unified approach to nearly all the possible rotor time constant MRAS estimators has been carried out in [114], where, based on the Lyapunov theory, the following formula was derived

$$\frac{\mathrm{d}}{\mathrm{d}t}\tau_{\mathrm{r}}^{-1} = \lambda\left[(L_{\mathrm{m}} + f_2)i_{1q}\psi_{2q} - f_1(\psi_{2d}^{*} - \psi_{2d})\right], \tag{2.5-10}$$

where λ is a positive number. By a special selection of f_1 and f_2 we can obtain the individual MRAS schemes. This is summarized in Tab. 2.5-1. Fig. 2.5-2 shows the general block diagram of MRAS for the inverse rotor time constant estimation.

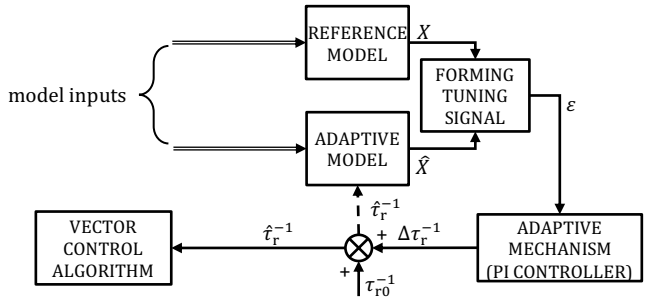

Fig. 2.5-2 General MRAS block diagram for inverse rotor time constant estimation (based on [114]).

Tab. 2.5-1 Overview of individual MRAS schemes for rotor time constant estimation (based on [114]).

Configuration parameter	Functional candidate in MRAS	Reference model	Adjustable model	Information needed in tuning signal
$\boldsymbol{f_1 = f_2 = 0}$	q-axis rotor flux	0	ψ_{2q}	i_{1q}
	d-axis stator voltage	u_{1d}	$R_1 i_{1d} - \omega_s \sigma L_1 i_{1q}$	i_{1q}, ω_s
$\boldsymbol{f_2 = -L_m}$	d-axis rotor flux	$L_m i_{1d}$	ψ_{2d}	–
	q-axis stator voltage	u_{1q}	$R_1 i_{1q} + \omega_s \sigma L_1 i_{1d}$	ω_s
$\boldsymbol{f_1 = i_{1q}^2, f_2 = L_m - i_{1d}}$	electromagnetic torque	$L_m i_{1q} i_{1d}$	$i_{1q}\psi_{2d} - i_{1d}\psi_{2q}$	i_{1q}
	active power	$i_{1q}u_{1q} + i_{1d}u_{1d}$	$R_1\left(i_{1d}^2 + i_{1q}^2\right) + \omega_s L_m^2 i_{1d} i_{1q}/L_2$	i_{1q}, ω_s
$\boldsymbol{f_1 = L_m i_{1d}, f_2 = 0}$	inner product of $\underline{i}_1$ and $\underline{\psi}_2$	$L_m i_{1d}^2$	$i_{1d}\psi_{2d} + i_{1q}\psi_{2q}$	–
	inner product of $\underline{i}_1$ and $\underline{\psi}_1$	$L_1 i_{1d}^2 + \sigma L_1 + i_{1q}^2$	$i_{1d}\psi_{1d} + i_{1q}\psi_{1q}$	–
	reactive power	$i_{1d}u_{1q} - i_{1q}u_{1d}$	$\omega_s\left(L_1 i_{1d}^2 + \sigma L_1 i_{1q}^2\right)$	ω_s

2.5.1.3 Concluding Remarks

Many of the presented schemes, including the F-MRAS, EMF-MRAS, P-MRAS, Q-MRAS, or X-MRAS, are also used for speed estimation. An excellent overview of the various MRAS estimators for the rotor speed estimation is presented in [144].

Furthermore, most of the MRAS algorithms presented in the literature do not consider the influence of iron or stray-load losses. For instance, reference [145] demonstrates that the rotor time constant depends on the additional losses and proposes its new definition. Therefore, there is still much room for improvement in MRAS-based identifiers to account for different nonlinear phenomena mathematically formally defined by augmented equivalent circuits.

Furthermore, most MRAS schemes were tested for an indirect (feedforward) field-oriented control only. Also, another hot topic is a stable and accurate simultaneous estimation of the rotor speed and rotor time constant.

2.6 Modified Integrators for Voltage Model Calculation

One of the key models utilized throughout the papers presented in this thesis is the so-called IM voltage model. It can be viewed as a reduced-order model for evaluating the rotor flux linkage vector components in the stationary $\alpha\beta$ system based on the information about the motor phase voltages and currents. If the machine iron and additional losses are neglected, the model can be written as

$$\frac{\mathrm{d}\,\underline{\psi}_1^{\alpha\beta}}{\mathrm{d}t} = \underline{u}_1^{\alpha\beta} - R_1 \underline{i}_1^{\alpha\beta}, \tag{2.6-1}$$

$$\underline{\psi}_2^{\alpha\beta} = \frac{L_2}{L_m}\left(\underline{\psi}_1^{\alpha\beta} - \sigma L_1 \underline{i}_1^{\alpha\beta}\right). \tag{2.6-2}$$

The problem is that (2.6-1) cannot be evaluated by a pure integrator (which has an infinite gain for the DC component) [122]. The reason is the uncontrolled accumulation of the DC offset on the stator flux linkage vector components caused by unknown initial conditions and imperfection of the current sensing circuitry (influence of offset and noise). Therefore, multiple algorithms for the mitigation of the problem of offset accumulation are reviewed in Appendix F.

2.6.1 Proposed Integrator Utilized in Thesis

If a symmetrical sinusoidal quantity is transformed to the $\alpha\beta$ complex plane, then in a steady state, the endpoint of the space vector follows a circular trajectory. Superposition of the DC offset on the stator flux linkage vector components causes the circular trajectory to drift from the origin. This is basically the philosophy behind the schemes proposed in [146] and [147].

The integrator scheme used in the papers in this thesis is based on the work in [147]. However, since this thesis deals mainly with the rotor flux-oriented control, the reference stator flux linkage vector used as the correction term is replaced by the stator flux linkage vector obtained from the current model. The proposed scheme is depicted in Fig. 2.6-1. Mathematically, it can be described as

$$\hat{\underline{\psi}}_1^{\alpha\beta} = \int \left(\underline{u}_1^{\alpha\beta} - R_1 \underline{i}_1^{\alpha\beta} - \hat{\underline{u}}_{\text{off}}^{\alpha\beta} \right) \mathrm{d}t, \tag{2.6-3}$$

$$\varepsilon_{\text{int}} = \hat{\underline{\psi}}_1^{\alpha\beta} \left(1 - \frac{\left| \underline{\psi}_{1(\text{cor})}^{\alpha\beta} \right|}{\left| \hat{\underline{\psi}}_1^{\alpha\beta} \right|} \right), \tag{2.6-4}$$

$$\hat{\underline{\psi}}_1^{\alpha\beta} = K_{\text{p(int)}} \varepsilon_{\text{int}} + K_{\text{i(int)}} \int \varepsilon_{\text{int}} \, \mathrm{d}t. \tag{2.6-5}$$

Since the offset usually changes slowly, the selection of the adaptive controller is not too crucial. The author has experimentally found out that high values distort the resulting estimated stator flux linkage vector. On the contrary, too low values cause imperfect offset elimination and the stator flux linkage vector amplitude fluctuation. Therefore, the aim is to find a compromise, i.e., such gains values that will reliably remove the DC offset without impairing the integrator's performance. The values can be determined in the simulations or on a real drive by observing the behavior of the evaluated stator flux linkage vector components and amplitude.

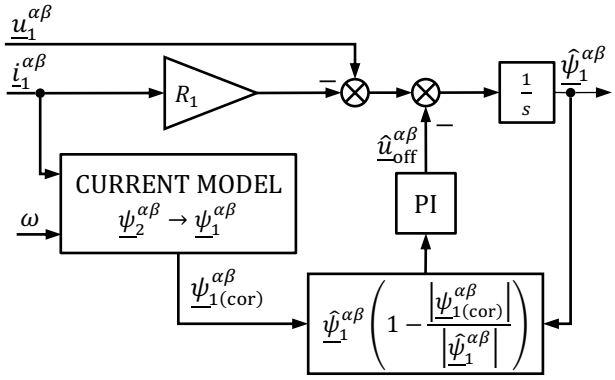

Fig. 2.6-1 Adaptive integrator scheme used in the thesis.

3 SET OF ARTICLES SUBMITTED AS DOCTORAL THESIS

In this chapter, the articles presented as the set of publications within the doctoral thesis will be presented. The articles are only a selected subset of all the author's publication activities done during the doctoral study. Each paper will be introduced by a short text that will describe the main contribution, features, and motivation behind the paper. The author of the dissertation retains the first authorship of all the articles.

The following papers will be presented in the next sections:

1. **Analysis of Voltage Distortion and Comparison of Two Simple Compensation Methods for Sensorless Control of Induction Motor**

   Published in the proceedings of the ***2019 IEEE 10th International Symposium on Sensorless Control for Electrical Drives (SLED)***. The conference was held in Turin, Italy.

   Indexed in Scopus and WoS.

2. **Offline method for experimental identification of load-dependent saturation of induction motor taking into account variation of inverse rotor time constant**

   Published in ***IET Power Electronics*** on 1st July 2020.

   Journal Impact Factor at the time of publication: ***2.641*** *(2.484 median impact factor in the category ENGINEERING, ELECTRICAL & ELECTRONIC)*

   Rank by Journal Impact Factor at the time of publication in the category ENGINEERING, ELECTRICAL & ELECTRONIC: ***126/273 (Q2)***

3. **MRAS-Based Induction Machine Magnetizing Inductance Estimator with Included Effect of Iron Losses and Load**

   Published in ***IEEE Access*** on 14th December 2021.

   Journal Impact Factor at the time of publication: ***3.367*** *(2.484 median impact factor in the category ENGINEERING, ELECTRICAL & ELECTRONIC)*

   Rank by Journal Impact Factor at the time of publication in the category ENGINEERING, ELECTRICAL & ELECTRONIC: ***94/273 (Q2)***

4. **Influence of Selected Non-Ideal Aspects on Active and Reactive Power MRAS for Stator and Rotor Resistance Estimation**

   Published in ***Energies*** on 19th October 2021.

   Journal Impact Factor at the time of publication: ***3.004*** *(3.934 median impact factor in the category ENERGY & FUELS)*

   Rank by Journal Impact Factor at the time of publication in the category ENERGY & FUELS: ***70/114 (Q3)***

3.1 Paper 1: Analysis of Voltage Distortion and Comparison of Two Simple Compensation Methods for Sensorless Control of Induction Motor

3.1.1 Motivation

The first FOC implemented earlier in the author's master's thesis was the basic DFOC based on the so-called IM current model. This type of control does not necessarily need the knowledge of the inverter-distorted voltage vector applied to the motor terminals. Generally, the VSI used for the FOC applications is considered a voltage-controlled current source. The current controllers adjust their voltage commands to compensate for the voltage distortion. Furthermore, if the current controllers' bandwidth is sufficiently high, this compensation happens very fast.

However, the situation is different when deployed IM mathematical models or additional algorithms requiring voltage vector knowledge. Since, in most cases, the voltage is obtained indirectly by reconstruction from switching signals or simply by using the reference voltage vector entering the modulator, a proper voltage compensation is needed mainly if the drive operates at low-speed low-torque conditions where the reference voltage vector's magnitude becomes relatively low.

The compensation algorithm that is considered in the following article works only for the classical SVPWM with a constant switching frequency. However, the constant switching frequency SVPWM is the most used modulation strategy in electric drives. Nevertheless, for instance, in the electric railway traction vehicles, modified modulation strategies are common:

- **SVPWM strategies modified to work close to or inside the overmodulation region**. To fully utilize the available DC-link voltage (especially in the field-weakening region), SVPWM may be extended to a non-linear mode. However, the voltage compensation cannot arbitrarily adjust the resulting duty cycles due to the minimum gate pulse length constraints for the VSI semiconductor switches. Furthermore, it is a question whether the voltage compensation at higher speeds is necessary since the relative influence of voltage distortion decreases with an increasing voltage.
- **SVPWM strategies with variable frequency.** These algorithms aim to mitigate the negative effect of a constant-frequency audible noise. Generally, a variable frequency acoustic noise may be less irritating for the human ear. Another advantage is a more uniform frequency distribution of electromagnetic interference.
- **Synchronous modulation strategies.** Due to the switching frequency limitation, a synchronous modulation strategy may be deployed in high-power electric drives for railway traction. Here, a deeper voltage distortion analysis and compensation is lacking in the literature. Probably because at higher values of applied motor voltage (i.e., at higher speed), the negative contribution of the voltage vector decreases.

Another aspect to consider is the rated voltage of the used electric machine. Since the compensation strategy in the following paper compensates only the distortion caused by the dead time and delayed switching of the IGBT transistors, it is suitable mainly for machines designed to operate with medium-to-high voltage. It may also be necessary to compensate for the voltage drop across the semiconductor switches in low-voltage drives. However, this also depends on the type of utilized transistors.

3.1.2 Main Contribution and Results

To sum up the contribution and main results of the paper:

- A formula for a distorting voltage space vector considering a variable voltage distortion in each inverter leg is derived.

- A simple procedure for obtaining the IGBT inverter nonlinear distorting characteristics is explained.
- Two simple volt-seconds-based compensation methods are compared.
- Two inverter non-linear characteristics representations are compared regarding the compensation accuracy and computational burden.
- The influence of voltage distortion on the accuracy of the speed estimation by the rotor flux MRAS is assessed.

3.1.3 Discussion and Suggestions for Future Work

The presented compensation strategy is suitable mainly for drives operated with DC-link voltage of several hundred volts and higher since it neglects the voltage drop across the semiconductor devices. Therefore, the compensation strategy could be improved for low or extra-low voltage drives by considering a voltage distortion caused by the voltage drop across the conducting diodes and transistors. The distorting voltage vector corresponding to the voltage drop could be merged with the distorting voltage vector corresponding to the dead time and delayed switching, and a summary compensation strategy could be proposed. Of course, the magnitude of the voltage drop and whether it bears any significance in the process of voltage distortion is mainly dependent on the used transistors and diodes.

The direct method of measuring the nonlinear inverter model described in section 2.1.3 is accurate and straightforward but time-consuming. Although the HW and SW modification is only moderate, additional passive components (inductance and resistance) are required. In addition, these components must be able to withstand the peak value of the nominal machine current, which can be relatively high for medium-power drives.

Another topic suitable for future research would be analyzing the voltage distortion influence in the overmodulation region, considering the constraints imposed by the switching devices. Also, a thorough analysis of the voltage distortion influence and its compensation for the different modulation strategies (e.g., synchronous modulations) is still missing in the literature. Furthermore, since the voltage compensation in volt-seconds utilizes the PWM switching frequency, the compensation algorithms must be adjusted for variable-frequency modulation strategies.

The last thing worth mentioning is that the author came up with an analytical model for the effective dead time characteristic approximation later after the paper publication. The model is given as

$$T_{\mathrm{eff}}(i_x) = \frac{m}{k_1|i_x| + k_2} + n, \qquad x = \mathrm{a, b, c,} \tag{3.1-1}$$

where k_1, k_2, m, and n are the model parameters that should be found by fitting the model to the measured data. Papers presented in sections 3.3 and 3.4 are already based on the proposed analytical approximation.

3.1.4 Errata

- Equation (16) should be in the form

$$\Delta u_{x0} = \frac{T_{\mathrm{eff}(x)}}{T_{\mathrm{PWM}}} U_{\mathrm{DC}}, \qquad x = \mathrm{a, b, c.}$$

Analysis of Voltage Distortion and Comparison of Two Simple Voltage Compensation Methods for Sensorless Control of Induction Motor

Ondrej Lipcak
Department of Electric Drives and Traction
Czech Technical University in Prague
Prague, Czech Republic
lipcaond@fel.cvut.cz

Jan Bauer
Department of Electric Drives and Traction
Czech Technical University in Prague
Prague, Czech Republic
bauerja2@fel.cvut.cz

***Abstract*—Many algorithms of induction motor sensorless control need accurate knowledge of the stator voltage vector. However, the machine is in most cases supplied by a two-level voltage-source inverter; therefore, the voltage is distorted by the inserted dead-time and also by nonlinearities of the semiconductor switches. This paper analyzes a distortion caused by the dead-time and delayed IGBT switching in terms of distorting voltage vector. An offline measurement is performed to obtain the inverter model. Then, an analysis of two simple volt-seconds-based compensation methods (compensation of the reference voltage vector and duty cycle, respectively) on the accuracy of the speed estimation of a sensorless field-oriented control based on the rotor flux model reference adaptive system is performed. The analyzed methods use either the full inverter model implemented as a look-up table or its trapezoidal approximation. Outline on computational complexity and discussion on finding optimal coefficients for the trapezoidal model are given, too.**

Keywords—induction motor, field-oriented sensorless control, model reference adaptive system, voltage-source inverter nonlinearities identification, IGBT

I. INTRODUCTION

Induction motors (IM) belong to the most popular electromechanical converters [1]. Their domination in the industrial sphere is caused mainly due to their distinct advantages such as simple construction, robustness, low maintenance, low cost, and high reliability [1]. Their disadvantage, i.e., the dependence of the rotor speed on the supply frequency that had restricted their use in variable speed drives in the past has been successfully surpassed by the development of control strategies such as field-oriented control (FOC) [1]-[4]. High computation power of today's digital signal processors (DSP) permits practical implementation of even complicated control algorithms such as speed sensorless control that becomes more and more popular [3]-[5]. In some algorithms of the sensored and many algorithms of the sensorless FOC, it is necessary to know the actual stator voltage vector applied to the motor terminals [1]-[5]. However, if a PWM controlled voltage-source inverter (VSI) is used to supply the machine, it becomes complicated and hardware demanding to measure the stator voltage directly. Because of that, the voltage is mostly determined indirectly [6].

The commonly used approach is based on using the reference voltage vector (i.e., input to the modulator) as the input to the control model [6]-[11]. This method is simple and can be quite efficient, but one must deal with a key problem, and that is a nonlinear behavior of the VSI caused by the semiconductor switches, i.e., the finite turn-on and turn-off times and the voltage drop. The voltage is further distorted by the necessary protective time, i.e., dead-time [7]-[11]. Proper compensation of the inverter most significant nonlinearities is essential in order to achieve good accuracy of the IM models and thus sensorless motor control [9]-[10],[12].

The compensation techniques can be either hardware or software-based [7]-[8]. The more preferred software compensation strategies can be generally divided into three categories [7]: current analysis-based method, estimator-based methods, and instantaneous average voltage methods (also called volt-seconds compensation methods). The average voltage methods require information about the motor currents [7]-[12] and can be further divided into square-wave models, trapezoidal models and more precise models based on a look-up table (LUT) or analytical functions that try to model the zero current clamping effect accurately [10]. The parameters for the more sophisticated models are usually obtained by the DC test or direct VSI measurement [9]-[12].

This paper analyses the influence of two simple volt-seconds based methods on the accuracy of speed estimation using sensorless FOC based on the rotor flux model reference adaptive system (RFMRAS). These methods include compensation of the reference voltage entering modulator and compensation of the duty cycle for the VSI. The compensation characteristic is evaluated using either the measured inverter model implemented as a LUT or its trapezoidal approximation. Comparison of the computational burden of the individual cases is presented, too.

This paper is organized as follows: after a brief overview of the used IM mathematical models and structure of the RFMRAS, an expression for the distorting voltage space vector taking into account current dependent distortion in each VSI leg caused by the dead-time and IGBT switching is derived. Then, the model of laboratory inverter obtained by direct measurement of the switching times for different values of the collector current is presented. After that, mathematical expressions for the two different compensation methods are presented. The paper is concluded by experimental results measured for 12 kW IM controlled by TMS320F28335. The experimental results include a comparison of the computational burden of the two different compensation methods and two different VSI models and also their influence on the accuracy of the speed estimation of the RFMRAS-based sensorless FOC. Also, the process of finding optimal coefficients for the trapezoidal model is discussed, too.

978-1-7281-0766-0/19/$31.00

II. Induction Motor Models

The IM models for the rotor flux oriented FOC are deducible from the IM basic equations and in this paper are expressed in the stationary ($\alpha\beta$) reference frame. The first possible model that uses the measured values of the stator currents and rotor angular speed is called the current model (subscript CM) [2]

$$\frac{\mathrm{d}\underline{\psi}_{2\mathrm{CM}}}{\mathrm{d}t} = \frac{L_\mathrm{m}R_2}{L_2}\underline{i}_1 - \frac{R_2}{L_2}\underline{\psi}_{2\mathrm{CM}} + \mathrm{j}\omega\underline{\psi}_{2\mathrm{CM}}, \tag{1}$$

where $\underline{\psi}_2$ is the rotor flux linkage space vector, $\underline{i}_1$ is the stator current space vector, R_2 is the rotor resistance, ω is the electrical angular speed of the rotor, L_m is the magnetizing inductance, L_2 is the rotor inductance and symbol j marks imaginary unit ($\mathrm{j}^2 = -1$).

The second, voltage model (subscript VM), is based on the knowledge of the current and voltage vector applied to the IM terminals [2]

$$\frac{\mathrm{d}\underline{\psi}_{2\mathrm{VM}}}{\mathrm{d}t} = \frac{L_2}{L_\mathrm{m}}\left(\underline{u}_1 - R_1\underline{i}_1 - \sigma L_1\frac{\mathrm{d}\underline{i}_1}{\mathrm{d}t}\right), \tag{2}$$

where $\underline{u}_1$ is the stator voltage space vector, R_1 is the stator resistance, L_1 is the stator inductance and σ is the leakage factor defined as $\sigma = 1 - L_\mathrm{m}^2/L_1L_2$. This model is, apart from the fact that it requires the proper knowledge of the stator voltage as input, also prone to accumulation of DC offset error. A possible solution to this negative phenomenon can be found, for example, in [13].

For the inner motor torque T_i, the following equation expressed in the stator-fixed coordinate system can be derived (p_p denotes the number of motor pole-pairs)

$$T_\mathrm{i} = \frac{3}{2}p_\mathrm{p}\frac{L_m}{L_2}\left(\psi_{2\alpha}i_{1\beta} - \psi_{2\beta}i_{1\alpha}\right). \tag{3}$$

III. Rotor Flux Model Reference Adaptive System

For sensorless control of IM, there are numerous MRAS schemes based on different motor quantities [5]. In the case of RFMRAS that is used within this paper, the following error to be minimized can be derived [14]

$$\varepsilon = \hat{\psi}_{2\alpha\mathrm{CM}}\psi_{2\beta\mathrm{VM}} - \hat{\psi}_{2\beta\mathrm{CM}}\,\psi_{2\alpha\mathrm{VM}}, \tag{4}$$

where the circumflex denotes the output values of the adaptive current model. The estimated speed is the output of the adaptation mechanism, which is a conventional PI controller. The block diagram of the RFMRAS is depicted in Fig. 1.

IV. Analysis of the Selected Inverter Nonlinearities

In the case of FOC of IM, the stator voltage vector applied to the motor terminals is mostly formed by space vector modulation (SVM) calculated by the microcontroller [2]. The microcontroller generates switching signals for the VSI drivers in such manner that the dead-time T_dt delays the control signal for switching on the respective IGBT; the control signal for turning off is sent without delay [2].

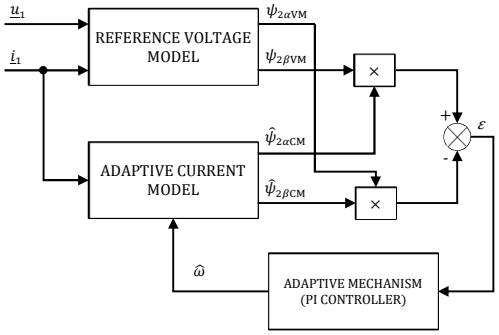

Fig. 1. Block diagram of RFMRAS

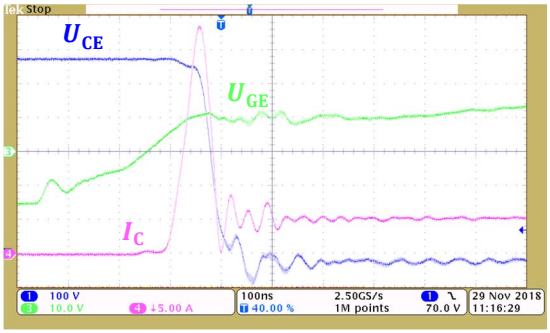

Fig. 2. Switching on IGBT module CM100DY-24NF

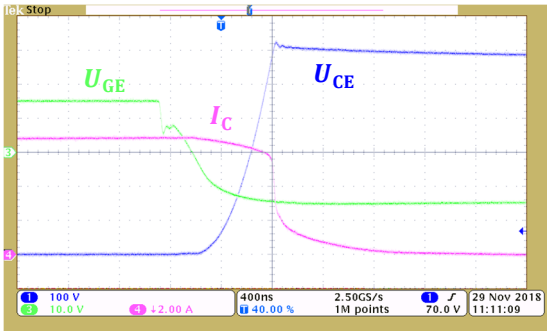

Fig. 3. Switching off IGBT module CM100DY-24NF

Fig. 2 shows the process of switching on IGBT and Fig. 3 then the process of switching off. The IGBT switching characteristics are generally dependent on the collector current I_C, junction temperature T_j, collector-emitter voltage U_CE, gate-emitter voltage U_GE, the value of the used gate resistor R_G and the load type [15]. The impact of the magnitude of the collector current on the turn-off times is usually much more significant than in the case of the turn-on times [15].

A. Distortion of the VSI Output Voltage

By a simple graphical analysis [6], it can be concluded that T_on increases and T_off decreases the resulting distortion caused by the dead-time T_dt. Therefore, we can define the so-called effective dead-time for each VSI leg as [9]

$$T_{\mathrm{eff}(x)} = T_\mathrm{dt} + T_\mathrm{on}(i_x) - T_\mathrm{off}(i_x) \quad x = \mathrm{a,b,c}. \tag{5}$$

The average distortion of the inverter line-to-neutral voltage (defined according to Fig. 4) per modulation period T_PWM can then be expressed as [9]

$$\Delta u_{x0} = \frac{T_{\mathrm{eff}(x)}}{T_\mathrm{PWM}}U_\mathrm{DC}\mathrm{sgn}(i_x) \quad x = \mathrm{a,b,c}. \tag{6}$$

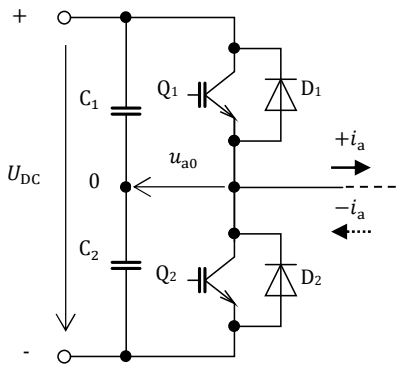

Fig. 4. One leg of two-level VSI

The switching characteristics of the IGBTs are, among others, strongly dependent on the collector current [9]. The effective dead-time for each VSI leg is, therefore, a function of the respective phase current

$$T_{\mathrm{eff}(x)} = f(i_x) \quad x = \mathrm{a,b,c}. \tag{7}$$

The distortion of the motor line-to-neutral voltages per modulation period can be expressed as a function of the distorting inverter line-to-neutral voltages as

$$\begin{bmatrix}\Delta u_\mathrm{a}\\ \Delta u_\mathrm{b}\\ \Delta u_\mathrm{c}\end{bmatrix} = \frac{1}{3}\begin{bmatrix}2\,\mathrm{sgn}\,i_\mathrm{a} & -\mathrm{sgn}\,i_\mathrm{b} & -\mathrm{sgn}\,i_\mathrm{c}\\ -\mathrm{sgn}\,i_\mathrm{a} & 2\,\mathrm{sgn}\,i_\mathrm{b} & -\mathrm{sgn}\,i_\mathrm{c}\\ -\mathrm{sgn}\,i_\mathrm{a} & -\mathrm{sgn}\,i_\mathrm{b} & 2\,\mathrm{sgn}\,i_\mathrm{c}\end{bmatrix}\cdot\begin{bmatrix}\Delta u_{\mathrm{a0}}\\ \Delta u_{\mathrm{b0}}\\ \Delta u_{\mathrm{c0}}\end{bmatrix}. \tag{8}$$

Using the definition of space vector, we can define a distorting voltage space vector as

$$\Delta\underline{u}_1 = K[1 \quad \mathbf{a} \quad \mathbf{a}^2]\cdot\begin{bmatrix}\Delta u_\mathrm{a}\\ \Delta u_\mathrm{b}\\ \Delta u_\mathrm{c}\end{bmatrix}, \tag{9}$$

where K is the transformation coefficient, and $\mathbf{a}$ is the rotational unity operator defined as $\mathbf{a} = \exp(\mathrm{j}2/3\pi)$.

Substitution of (8) to (9) yields after a few mathematical arrangements

$$\Delta\underline{u}_1 = K\begin{bmatrix}\mathrm{sgn}\,i_\mathrm{a}\\ \mathrm{sgn}\,i_\mathrm{b}\\ \mathrm{sgn}\,i_\mathrm{c}\end{bmatrix}^\mathrm{T}\cdot\begin{bmatrix}a_1 & 0 & 0\\ 0 & a_2 & 0\\ 0 & 0 & a_3\end{bmatrix}\cdot\begin{bmatrix}\Delta u_{\mathrm{a0}}\\ \Delta u_{\mathrm{b0}}\\ \Delta u_{\mathrm{c0}}\end{bmatrix}, \tag{10}$$

where

$$\begin{aligned} a_1 &= \left(\frac{2}{3} - \frac{1}{3}\mathbf{a} - \frac{1}{3}\mathbf{a}^2\right) = 1\\ a_2 &= \left(-\frac{1}{3} + \frac{2}{3}\mathbf{a} - \frac{1}{3}\mathbf{a}^2\right) = \mathbf{a}\\ a_3 &= \left(-\frac{1}{3} - \frac{1}{3}\mathbf{a} + \frac{2}{3}\mathbf{a}^2\right) = \mathbf{a}^2. \end{aligned} \tag{11}$$

Therefore, (10) can be rewritten as

$$\Delta\underline{u}_1 = K\begin{bmatrix}\mathrm{sgn}\,i_\mathrm{a}\\ \mathrm{sgn}\,i_\mathrm{b}\\ \mathrm{sgn}\,i_\mathrm{c}\end{bmatrix}^\mathrm{T}\cdot\begin{bmatrix}1 & 0 & 0\\ 0 & \mathbf{a} & 0\\ 0 & 0 & \mathbf{a}^2\end{bmatrix}\cdot\begin{bmatrix}\Delta u_{\mathrm{a0}}\\ \Delta u_{\mathrm{b0}}\\ \Delta u_{\mathrm{c0}}\end{bmatrix}, \tag{12}$$

which after separation to real and imaginary part gives

$$\begin{aligned} \Delta u_\alpha &= K\left[\mathrm{sgn}\,i_\mathrm{a}\,\Delta u_{\mathrm{a0}} - \frac{1}{2}\mathrm{sgn}\,i_\mathrm{b}\,\Delta u_{\mathrm{b0}} - \frac{1}{2}\mathrm{sgn}\,i_\mathrm{c}\,\Delta u_{\mathrm{c0}}\right]\\ \Delta u_\beta &= K\frac{\sqrt{3}}{2}[\mathrm{sgn}\,i_\mathrm{b}\,\Delta u_{\mathrm{b0}} - \mathrm{sgn}\,i_\mathrm{c}\,\Delta u_{\mathrm{c0}}]. \end{aligned} \tag{13}$$

V. Determination of the Compensation Characteristics

A practical approach is used to determine the dependence of the T_{on} and T_{off} times on the collector current I_C. The testing conditions are $U_{\mathrm{CE}} = 560$ V, $U_{\mathrm{GE}} = \pm 15$ V, $R_\mathrm{G} = 6.8\ \Omega$, $T_\mathrm{j} = 25$ °C and an inductive load. The laboratory VSI contains IGBT modules CM100DY-24NF from Mitsubishi Electric. Concept 2SD106AI-17 circuits are used as gate drivers. The maximum continuous collector current of the IGBT modules is $I_\mathrm{C} = 100$ A and the maximum collector-emitter voltage is $U_{\mathrm{CE}} = 1{,}2$ kV. A snubber capacitor 1000 V; 1.5 μF is connected to each of the modules. The T_{on} time is measured as the delay between the rising edge of the microcontroller's output control signal and the actual transition of the collector-emitter voltage U_{CE}. The transition of the U_{CE} is measured in the instant when $U_{\mathrm{CE}} = 0.5U_{\mathrm{DC}}$, which in the case of a linear transition approximates the average voltage value per modulation period [9]. The T_{off} time is measured as the interval between the falling edge of the microcontroller's output control signal and the actual transition of the collector-emitter voltage U_{CE}. The transition of the U_{CE} is also measured in the instant when $U_{\mathrm{CE}} = 0.5U_{\mathrm{DC}}$.

Fig. 5 shows the measured dependence of the effective dead-time T_{eff} calculated according to (5) on the collector current I_C. In accordance with [10], the point (0,0) is added to the measured values. The actual dead-time inserted by the microcontroller was chosen to be $T_{\mathrm{dt}} = 2$ μs. For the purpose of simplification, the measured characteristic is sometimes approximated by a trapezoidal model given by a following piecewise function

$$T_{\mathrm{eff}}(I_\mathrm{C}) = \begin{cases} kI_\mathrm{C} & \text{for } I_\mathrm{C} \le I_{\mathrm{th}}\\ kI_{\mathrm{th}} & \text{for } I_\mathrm{C} > I_{\mathrm{th}}. \end{cases} \tag{14}$$

For the collector current smaller than some threshold value I_{th}, the compensation characteristic is linear with tangent k, and for a higher value than the threshold current, the compensation characteristic is constant.

Fig. 6 shows the visualization of the voltage distortion caused by the dead-time and switching delay of the IGBTs for $T_{\mathrm{PWM}} = 100$ μs, $U_{\mathrm{DC}} = 540$ V and $\cos\varphi = 0.7$. The current vector amplitude is equal to 0.3 p.u., the voltage vector amplitude is equal to 0.1 p.u. and the synchronous frequency is equal to 0.1 p.u. which corresponds to the low-speed operation of IM. The distorting voltage vector is calculated using (13) based on the measured data in Fig. 5.

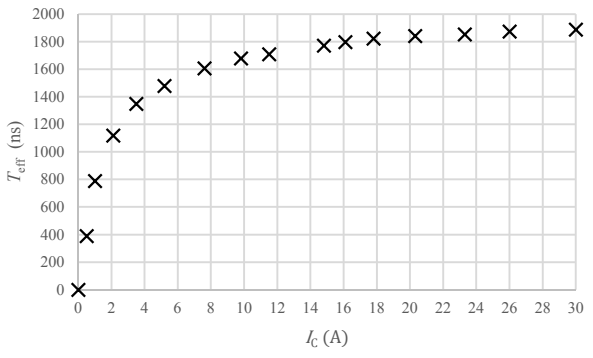

Fig. 5. Measured dependence of the effective dead-time on the collector current

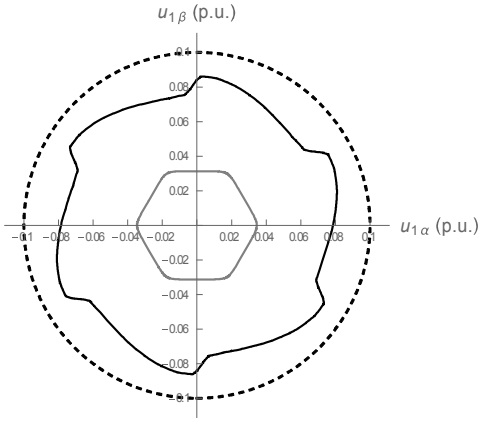

Fig. 6. Reference voltage (dashed black), distorting voltage (grey) and the resulting voltage (black solid); $U_{\mathrm{DC}} = 540$ V, $T_{\mathrm{PWM}} = 100$ µs, $\cos\varphi = 0.7$, current amplitude 0.3 p.u., voltage amplitude 0.1 p.u. and synchronous frequency 0.1 p.u.

Fig. 7 shows the phase error between the distorted and the reference voltage vector for the same operating conditions as in the case of Fig. 6. The solid line represents the instantaneous phase error and the dashed line the average phase error per one electrical revolution.

VI. Basic Voltage Compensation Methods

Among the simplest algorithms for the voltage compensation, we can include methods that either adjust the reference voltage vector entering the modulator or that adjust the duty cycle for the respective VSI leg. In the first case, the distorting voltage components (13) are added to the components of the reference voltage vector

$$\begin{aligned} u'_{1\alpha} &= u^*_{1\alpha} + \Delta u_{1\alpha} \\ u'_{1\beta} &= u^*_{1\beta} + \Delta u_{1\beta}. \end{aligned} \tag{15}$$

For SVM, it is convenient to define the duty-cycle d_x for each VSI leg such that the average value of the corresponding inverter line-to-neutral voltage u_{x0} per modulation period equals to $-U_{\mathrm{DC}}/2$ if $d_x = 0$ and $+U_{\mathrm{DC}}/2$ if $d_x = 1$. This can be mathematically expressed as

$$u_{x0} = (2d_x - 1)\frac{U_{\mathrm{DC}}}{2} \quad x = \mathrm{a, b, c.} \tag{16}$$

Using (6), the relationship between the reference u^*_{x0} and the compensated inverter line-to-neutral voltage u'_{x0} can be written as

$$u'_{x0} = u^*_{x0} + \frac{T_{\mathrm{eff}(x)}}{T_{\mathrm{PWM}}} U_{\mathrm{DC}} \mathrm{sgn}(i_x) \quad x = \mathrm{a, b, c.} \tag{17}$$

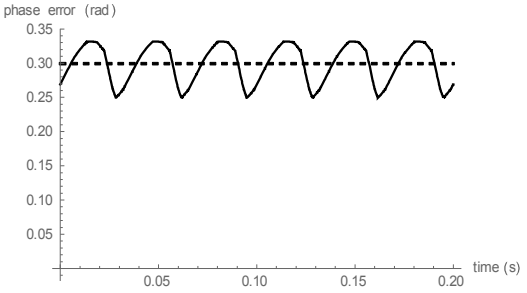

Fig. 7. Phase error between the distorted and reference voltage vector per one electrical revolution – instantaneous error (solid), average error (dashed); $U_{\mathrm{DC}} = 540$ V, $T_{\mathrm{PWM}} = 100$ µs, $\cos\varphi = 0.7$, current amplitude 0.3 p.u., voltage amplitude 0.1 p.u. and synchronous frequency 0.1 p.u.

Dividing (17) by $U_{\mathrm{DC}}/2$ and substituting for u'_{x0} and u^*_{x0} from (16) yields the following relation between the reference d^*_x and the compensated duty cycle d'_x

$$d'_x = d^*_x + \frac{T_{\mathrm{eff}(x)}}{T_{\mathrm{PWM}}} \mathrm{sgn}(i_x) \quad x = \mathrm{a, b, c.} \tag{18}$$

The compensation characteristic $T_{\mathrm{eff}(x)}$ can then be either based on the measured values of the effective dead-time (Fig. 5) or the equation (14) of the simplified trapezoidal model.

VII. Experimental Results

The different compensation techniques presented in Chap. VI are tested in terms of accuracy of the sensorless FOC based on the RFMRAS. The voltage model makes the sensorless RFMRAS FOC vulnerable to low-speed, low-torque operation when the reference stator voltage becomes low, and, therefore, the distortion of the reference voltage by the VSI nonlinearities becomes significant.

A. Experimental Setup

The sensorless RFMRAS FOC was implemented in the C language into TMS320F28335 Delphino DSP. The clock frequency was set to 150 MHz, and the calculation loop of the FOC algorithm was selected to be 100 µs, which corresponds to 10 kHz PWM. As a drive, machine set with 12 kW IM coupled with 8.8 kW separately excited DC motor has been used. The nameplate values of the IM along with the IM parameters measured by the conventional no-load and locked-rotor tests are given in Tab. 1.

B. Determination of the Optimal Parameters for the Trapezoidal Model

The parameters for the piecewise function (14) were obtained by minimization of the following error by the simulated annealing algorithm

$$e(k, I_{\mathrm{th}}) = \left| \left|\Delta\underline{\tilde{u}}_1\right| - \left|\Delta\underline{\hat{u}}_1(k, I_{\mathrm{th}})\right| \right|, \tag{19}$$

where $\left|\Delta\underline{\tilde{u}}_1\right|$ is the amplitude of the distorting voltage vector calculated using the measured compensation characteristic in Fig. 5 and $\left|\Delta\underline{\hat{u}}_1\right|$ is the amplitude of the distorting voltage vector calculated using the approximation of the measured characteristic by (14). The conditions were the same as in the case of Fig. 6. The resulting values are $I_{\mathrm{th}} = 2.35$ A and $k \cdot I_{\mathrm{th}} = 1.710$ µs. Fig. 8 shows the difference between the reference and actual voltage when the compensation characteristic is approximated by the piecewise function, and the parameters are obtained by minimization of (19). The price paid for the simplification is that the resulting voltage (solid line) contains higher harmonics that, in principle, cannot be eliminated by the trapezoidal model.

Nominal power	12 kW	R_1	0.377 Ω
Nominal current	22 A	R_2	0.25 Ω
Nominal voltage	380 V	$L_{1\sigma}$	0.00227 H
Nominal frequency	50 Hz	$L_{2\sigma}$	0.00227 H
Nominal power factor	0.8	R_{Fe}	202.1 Ω
Nominal speed	1460 min^{-1}	L_{m}	0.078 H

Tab. 1. IM nameplate parameters and measured values used by the mathematical models

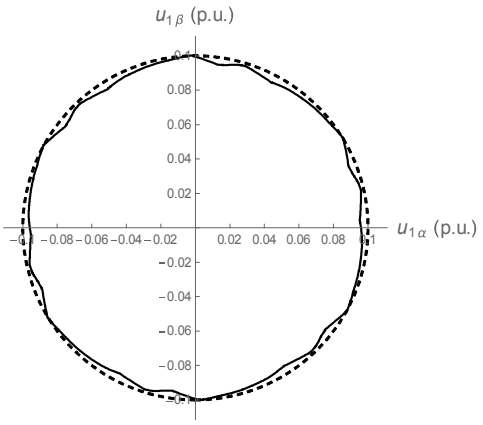

Fig. 8. Reference voltage (dashed) and compensated voltage (solid) with piecewise function; $I_{\mathrm{th}} = 2.35\ \mathrm{A}$, $k \cdot I_{\mathrm{th}} = 1.709\ \mu\mathrm{s}$, $U_{\mathrm{DC}} = 540\ \mathrm{V}$, $T_{\mathrm{PWM}} = 100\ \mu\mathrm{s}$, $\cos\varphi = 0.7$; current amplitude 0.3 p.u., voltage amplitude 0.1 p.u. and synchronous frequency 0.1 p.u.

C. *Comparison of the Computational Burden of the Different Compensation Methods*

For the implementation of algorithms for real-time control, it is also necessary to take into account the computational burden imposed on the DSP. For this reason, a comparison has been made for the two different compensation techniques based on (15) and (18), respectively, that were either based on the linear interpolation between the measured data $T_{\mathrm{eff}} = f(I_{\mathrm{C}})$ or the simplified approximation by the piecewise function (14).

Tab. 2 shows the measured computational times for the individual cases. It can be seen that adjusting the duty-cycle is about 1 µs less computationally demanding for both the interpolation and the piecewise function. The interpolation is then approximately 2.5 more time demanding than the evaluation of the piecewise function. It is worth noticing that in order to save the computational time in the case of the interpolation, the array was not always being searched from the beginning but because the current in IM is a continuous quantity, the searching started from the array index remembered in the previous step.

D. *Accuracy of the RFMRAS-Based Speed Estimation*

The individual compensation methods and compensation characteristics were tested in terms of accuracy of the estimated speed by RFMRAS during the drive reversal from $50\ \mathrm{rad}\cdot\mathrm{s}^{-1}$ to $-50\ \mathrm{rad}\cdot\mathrm{s}^{-1}$. The reference rotor flux was set to 0.8 Wb. The results are shown in Fig. 9. to Fig. 13. In the figures, the dashed line corresponds to the reference speed, the grey line then denotes measured, and the black line estimated rotor speed.

First of all, it can be seen that the voltage compensation (Fig. 9 to Fig. 12) in all the cases significantly improves the drive behavior compared to the case without compensation (Fig. 13) where the estimated speed exhibits quite heavy oscillations. Otherwise, based on the observations of Fig. 9 to Fig. 12 it can be concluded that both the compensation of the reference voltage vector and the duty cycle seem equivalent, which is an expected result. Concerning the difference between the compensation characteristics based on LUT (Fig. 9 and Fig. 11) and trapezoidal model (Fig. 10 and Fig. 12), it can be stated, that in both cases the estimated speed exhibits a drop when approaching the value $10\ \mathrm{rad}\cdot\mathrm{s}^{-1}$ that is more significant for the trapezoidal model. The absolute value of the maximum difference between the measured and estimated speed for Fig. 9 to Fig. 13 is captured in Tab. 3.

Interpolation using (15)	9.9 µs
Piecewise function using (15)	4.5 µs
Interpolation using (18)	8.8 µs
Piecewise function using (18)	3.4 µs

Tab. 2. The average computational time of the voltage compensation methods

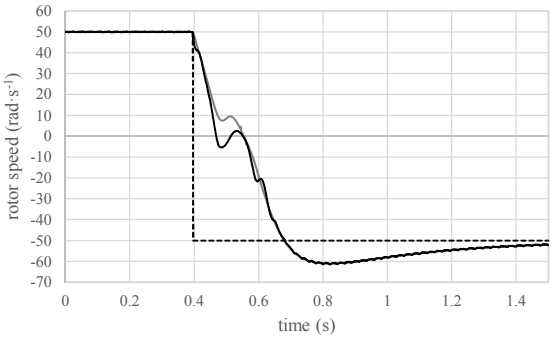

Fig. 9. Drive reversal from $50\ \mathrm{rad}\cdot\mathrm{s}^{-1}$ to $-50\ \mathrm{rad}\cdot\mathrm{s}^{-1}$; compensation of the reference voltage vector based on LUT; black dashed – reference speed, grey – measured speed, black – estimated speed; reference rotor flux 0.8 Wb

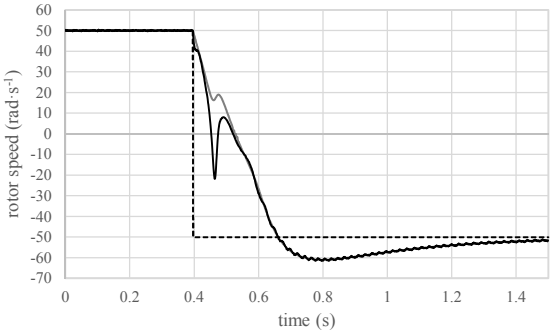

Fig. 10. Drive reversal from $50\ \mathrm{rad}\cdot\mathrm{s}^{-1}$ to $-50\ \mathrm{rad}\cdot\mathrm{s}^{-1}$; compensation of the reference voltage vector based on the trapezoidal model; black dashed – reference speed, grey – measured speed, black – estimated speed; reference rotor flux 0.8 Wb

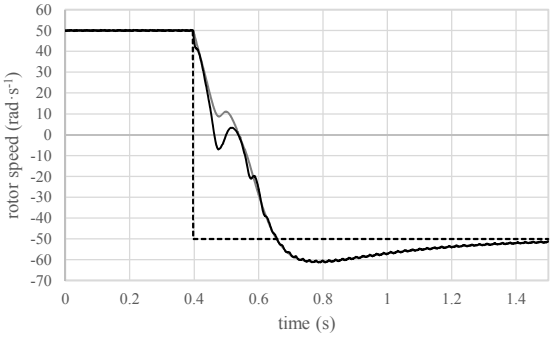

Fig. 11. Drive reversal from $50\ \mathrm{rad}\cdot\mathrm{s}^{-1}$ to $-50\ \mathrm{rad}\cdot\mathrm{s}^{-1}$; compensation of the duty-cycle based on LUT; black dashed – reference speed, grey – measured speed, black – estimated speed; reference rotor flux 0.8 Wb

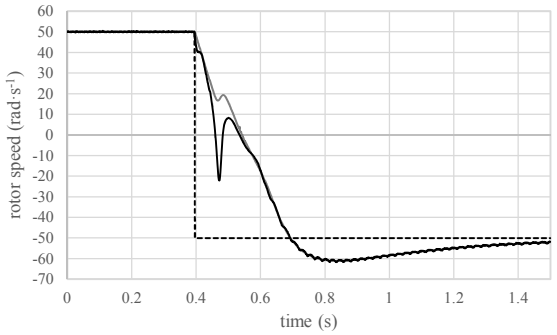

Fig. 12. Drive reversal from $50\ \mathrm{rad}\cdot\mathrm{s}^{-1}$ to $-50\ \mathrm{rad}\cdot\mathrm{s}^{-1}$; compensation of the duty-cycle based on the trapezoidal model; black dashed – reference speed, grey – measured speed, black – estimated speed; reference rotor flux 0.8 Wb

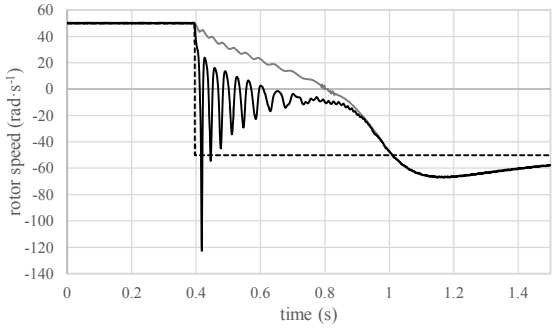

Fig. 13. Drive reversal from $50\ \mathrm{rad}\cdot\mathrm{s}^{-1}$ to $-50\ \mathrm{rad}\cdot\mathrm{s}^{-1}$; without compensation; black dashed – reference speed, grey – measured speed, black – estimated speed; reference rotor flux 0.8 Wb

Interpolation using (15)	13.6 rad ·s^{-1}
Piecewise function using (15)	38.5 rad ·s^{-1}
Interpolation using (18)	15.9 rad ·s^{-1}
Piecewise function using (18)	40 rad ·s^{-1}
Without compensation	167 rad ·s^{-1}

Tab. 3. The absolute value of the difference between the estimated and measured speed for Fig. 9. to Fig. 13.

VIII. Conclusion

In this paper, two simple compensation techniques of the voltage distortion caused by the dead-time and delayed IGBT switching (compensation of the reference voltage vector and duty-cycle, respectively) were tested in terms of the accuracy of the estimated IM speed by RFMRAS and computational complexity. As for the compensation characteristics, full inverter model measured by the direct measurement on the laboratory VSI implemented as LUT and its trapezoidal approximation implemented as piecewise function were considered. It has been shown that the compensation of the duty-cycle gives the same results as the compensation of the reference voltage but is, at the same time, less computationally demanding. By mathematical analysis of the distorting voltage vector, it was also shown that the trapezoidal model could not eliminate the higher harmonics even if its parameters were determined by mathematical optimization method. The trapezoidal model exhibits slightly worse performance compared to the LUT but its implementation can be considered if it is desirable to further reduce the necessary computational time. The speed estimation and the overall drive performance was significantly deteriorated when the voltage distortion was not compensated, which shows the significance of proper voltage compensation for sensorless control.

Acknowledgment

Research presented in this paper was supported by the Technology Agency of the Czech Republic under project No. TE02000103 and by the Student Grant Competition of the Czech Technical University in Prague under grant No. SGS19/065/OHK3/1T/13.

References

[1] F. Giri, *AC Electric Motors Control: Advanced Design Techniques and Applications*. 2. Aufl. ed. New York: Wiley; 2013.

[2] N.P. Quang and J. Dittrich, *Vector Control of Three-Phase AC Machines: System Development in the Practice*. 1. Aufl. ed. Berlin, Heidelberg: Springer-Verlag; 2008.

[3] P. Vas, *Sensorless vector and direct torque control*. New York: Oxford University Press; 1998.

[4] M. Popescu, *Induction Motor Modelling for Vector Control Purposes*, Helsinki University of Technology, Laboratory of Electromechanics, Report, Espoo 2000, 144 p.

[5] R. Kumar, S. Das, P. Syam and A. K. Chattopadhyay, "Review on model reference adaptive system for sensorless vector control of induction motor drives," in *IET Electric Power Applications*, vol. 9, no. 7, pp. 496-511, 8 2015.

[6] S. Bolognani and M. Zigliotto, "Self-commissioning compensation of inverter non-idealities for sensorless AC drives applications," *2002 International Conference on Power Electronics, Machines and Drives (Conf. Publ. No. 487)*, Sante Fe, NM, USA, 2002, pp. 30-37.

[7] Y. Wang, W. Xie, X. Wang and D. Gerling, "A Precise Voltage Distortion Compensation Strategy for Voltage Source Inverters," in *IEEE Transactions on Industrial Electronics*, vol. 65, no. 1, pp. 59-66, Jan. 2018.

[8] Z. Shen and D. Jiang, "Dead-Time Effect Compensation Method Based on Current Ripple Prediction for Voltage-Source Inverters," in *IEEE Transactions on Power Electronics*, vol. 34, no. 1, pp. 971-983, Jan. 2019.

[9] D. E. Salt, D. Drury, D. Holliday, A. Griffo, P. Sangha and A. Dinu, "Compensation of Inverter Nonlinear Distortion Effects for Signal-Injection-Based Sensorless Control," in *IEEE Transactions on Industry Applications*, vol. 47, no. 5, pp. 2084-2092, Sept.-Oct. 2011.

[10] G. Shen, W. Yao, B. Chen, K. Wang, K. Lee and Z. Lu, "Automeasurement of the Inverter Output Voltage Delay Curve to Compensate for Inverter Nonlinearity in Sensorless Motor Drives," in *IEEE Transactions on Power Electronics*, vol. 29, no. 10, pp. 5542-5553, Oct. 2014.

[11] M. Seilmeier, C. Wolz and B. Piepenbreier, "Modelling and model based compensation of non-ideal characteristics of two-level voltage source inverters for drive control application," *2011 1st International Electric Drives Production Conference*, Nuremberg, 2011, pp. 17-22.

[12] M. El-daleel and A. Mahgoub, "Accurate and simple improved lookup table compensation for inverter dead time and nonlinearity compensation," *2017 Nineteenth International Middle East Power Systems Conference (MEPCON)*, Cairo, 2017, pp. 1358-1361.

[13] O. Lipcak and J. Bauer, "Optimization of Voltage Model for MRAS Based Sensorless Control of Induction Motor," presented at the 5th International Conference on Advance Engineering – Theory and Applications, Ostrava, Czech Republic, 2018.

[14] C. Schauder, "Adaptive speed identification for vector control of induction motors without rotational transducers," in *IEEE Transactions on Industry Applications*, vol. 28, no. 5, pp. 1054-1061, Sept.-Oct. 1992.

[15] Mitsubishi Electric. *IGBT Modules Application Note, The 5th Generation [CSTBT™] IGBT Chip Use, 12NF/24NF/24A series*. Mar. 2014. Available at: http://www.mitsubishielectric.com/semiconductors/files/manuals/igbt_note_e.pdf, accessed 10th December 2018.

3.2 Paper 2: Offline method for experimental identification of load-dependent saturation of induction motor taking into account variation of inverse rotor time constant

3.2.1 Motivation

The IM current model based on the traditional T-equivalent circuit requires the knowledge of the magnetizing inductance, rotor inductance, and rotor resistance. The model equation in the stationary $\alpha\beta$ system can be expressed as

$$\frac{\mathrm{d}\,\underline{\psi}_2^{\alpha\beta}}{\mathrm{d}t} = \frac{L_\mathrm{m}R_2}{L_2}\,\underline{i}_1^{\alpha\beta} - \frac{R_2}{L_2}\,\underline{\psi}_2^{\alpha\beta} + \mathrm{j}\omega\,\underline{\psi}_2^{\alpha\beta}. \tag{3.2-1}$$

The parameter combination at the first term on the right-hand side (RHS) of (3.2-1) can be rewritten as

$$\frac{L_\mathrm{m}R_2}{L_2} = \frac{L_\mathrm{m}}{L_\mathrm{m} + L_{2\sigma}}R_2. \tag{3.2-2}$$

Since the rotor leakage inductance is “small” compared to the magnetizing inductance (typically, the rotor leakage inductance represents only a few percent of the magnetizing inductance), one can assume that

$$\frac{L_\mathrm{m}}{L_\mathrm{m} + L_{2\sigma}} \approx 1. \tag{3.2-3}$$

Therefore, practically only the rotor resistance affects the first term on the RHS. The higher the machine load, the greater the significance of the accurate rotor resistance knowledge. Physically, this can be explained by looking at the well-known steady-state IM T-equivalent circuit. The higher the load, the higher the slip and the lower the impedance of the rotor branch, which permits the flow of a higher rotor current (i.e., the rotor branch becomes more significant)

The parameter combination at the second term on the RHS is the inverse of the so-called rotor time constant. At first glance, it is clear that this parameter makes the current model sensitive both to the rotor resistance and the magnetizing inductance. The sensitivity of the current model to the magnetizing inductance variation is the main idea behind the paper presented in this section

In section 2.2, a phenomenon of load-dependent saturation was described. In basic FOC strategies, the mismatch in the magnetizing inductance directly influences the accuracy of the transformation angle estimation and, therefore, the commanded d and q-axis current values. As mentioned earlier in the thesis, such a state when the position and amplitude of the rotor flux linkage vector do not correspond to the “real” value in the machine is called the FOC detuning. The conventional saturation can be compensated by offline or online measured dependency implemented as an analytical function or look-up table. However, if we accept the fact that the magnetizing inductance also depends on the load, then:

- The FOC detuning happens during the load conditions regardless of the no-load saturation characteristics compensation or the precise knowledge of other IM parameters.
- The dependency of the magnetizing inductance on the load cannot be experimentally identified by tests used for obtaining the no-load characteristics.

Of course, when the geometry and material composition of the IM is known, one can identify the load-dependent saturation characteristics using FEA. However, these data are nowadays considered a proprietary knowledge of the respective machine manufacturer, and obtaining them becomes a tough and challenging task.

Therefore, the paper presented in this section proposes a simple method capable of identifying the load-dependent saturation of inverter-fed IMs when certain conditions are met. The method compares the estimated torque calculated based on the rotor flux linkage vector components and measured IM torque. The difference between the two torque values is then used for adjusting the magnetizing inductance utilized by the current model. Due to the reasons mentioned above, the "actual" saturation characteristic of the utilized machine was unavailable. Therefore, the method verification is based on an indirect approach.

3.2.2 Main Contribution and Results

To sum up the contribution and main results of the paper:

- A novel experimental method that can be used for the IM load-dependent saturation identification has been proposed.
- The IM current model upon which the method is based is implemented using a robust Runge-Kutta 4th order (RK4) method for the current model evaluation. The algorithm is described in more detail in the paper from section 3.4.
- Since the method is sensitive to the rotor resistance variation, a parallel MRAS-based estimator for the inverse rotor time constant identification is implemented to work in parallel with the magnetizing inductance estimation.
- Detailed information on the method implementation is provided, along with a summary of the method's advantages, disadvantages, and suggestions.
- Implementation of the saturation characteristics as the function of the rotor flux linkage vector magnitude and q-axis stator current is proposed.
- The experimental results show a better IM dynamic response and lower current consumption in a steady-state.

3.2.3 Discussion and Suggestions for Future Work

The first thing to note is that the iterative algorithm could be replaced by a PI controller that would estimate the inductance by ensuring that the difference between the estimated and measured torque is zero. Such a scheme would practically result in a MRAS estimator. However, a rigorous stability proof using the Popov hyperstability criterion or Lyapunov second method would be difficult to perform since the torque equation itself does not represent a state-space model. The same goes for the small-signal analysis.

As acknowledged in the paper, mechanical losses are not considered since no fan is present on the shaft. The mechanical losses can be obtained as a byproduct when measuring iron losses at different supply frequencies. The simplest model that can be utilized for the mechanical losses analytical approximation is the so-called viscous plus Coulomb friction memoryless model given by [148]

$$T_{\mathrm{F}} = T_{\mathrm{C}}\mathrm{sgn}(\Omega) + B_{\mathrm{V}}\Omega, \tag{3.2-4}$$

where T_{F} is the resulting torque that corresponds to the mechanical losses, T_{C} is the Coulomb friction, B_{V} is the viscous friction constant, and Ω is the mechanical angular speed of the shaft.

Another issue that should be acknowledged is that the method does not consider the rotor leakage inductance variation since it can also be affected by the load-dependent saturation. The solution would be to implement another online identification method for the rotor leakage inductance based, for instance, on the signal injection technique [43], [149]. However, the accuracy of such methods heavily depends on the proper selection of the injected frequency [109]. At higher frequencies, the estimate is affected by the skin effect. At low frequencies, the estimated is affected by the transverse equivalent circuit branch with the magnetizing inductance.

A DC dynamometer measured the actual torque for the compensation algorithm. It is expected that the measurement could be improved using a more sophisticated system such as the

torque measuring shaft. However, at the time of the paper publication, no shaft equipped with a strain gauge for the torque measurement capable of handling the machine torque was available at the department.

The saturation characteristic was implemented using bilinear interpolation in a 3D look-up table. In [33] and [34], an analytical model for fitting the load-dependent saturation characteristics was proposed. However, the model is based on a Γ-equivalent circuit and utilizes the saturation value based on the rotor leakage flux. Therefore, the validity conditions and applicability of the model to the T-equivalent circuit and the saturation calculation with respect to more easily obtainable parameters could be elaborated.

IET Power Electronics

Research Article

IET Journals
The Institution of Engineering and Technology

Offline method for experimental identification of load-dependent saturation of induction motor taking into account variation of inverse rotor time constant

ISSN 1755-4535
Received on 11th November 2019
Revised 24th February 2020
Accepted on 9th March 2020
E-First on 3rd April 2020
doi: 10.1049/iet-pel.2019.1361
www.ietdl.org

Ondrej Lipcak[1] ✉, *Jan Bauer*[1]

[1]*Department of Electric Drives and Traction, Faculty of Electrical Engineering, CTU in Prague, Technicka 2, Prague, Czech Republic*

✉ *E-mail: lipcaond@fel.cvut.cz*

Abstract: Accurate knowledge of induction machine parameters has a direct impact on the overall performance of field-oriented control strategies. In the case of rotor flux oriented control, parameter mismatch causes a discrepancy in the estimated rotor flux position and amplitude. Magnetising inductance is one of the parameters whose detuning has a direct impact on the setpoints of the control loops and estimation of hardly or non-measurable quantities. Conventional iron saturation, which can be obtained by a standard no-load test, is not the only type of saturation occurring in the machine. Depending on the rotor design, the magnetising inductance and the rotor leakage inductance may also strongly saturate as a function of load and, thus, rotor current. Based on the authors' previous work, a new, improved experimental method for identifying the load-dependent saturation of induction motor, which takes into account variation of the inverse rotor time constant, is proposed. Experimental results conducted on 12 kW motor show improved static and dynamic behaviour of the drive compared to the constant parameter model.

1 Introduction

The induction motors (IMs) still belong to the most used electromechanical converters among high-performance electric drives. It is because of their reliability, overloadability, and relatively low-cost production and maintenance. One of the most common control strategies in demanding applications is the rotor flux oriented control (RFOC). To reach high performance and high efficiency of the drive, precise knowledge of the IM equivalent circuit parameters is needed. Those parameters are used within the RFOC to get correct setpoints for the controllers. Inaccurate knowledge of the IM equivalent circuit parameters leads to RFOC detuning, which causes misalignment of the estimated flux position and, thus, inaccuracy of the control [1–3]. Also, today's requirement for reliability and cost reduction lead to the deployment of sensorless control strategies. In the case of a sensorless drive, the negative influence of the incorrect parameters is more pronounced [4–6].

A common cause of the RFOC detuning is the inexact knowledge of the magnetising inductance. Due to the material savings, electrical machines are usually designed so that the rated point lies within the knee of the magnetisation curve. Due to the conventional iron saturation, the magnetising inductance of IM then may vary in a wide range [7, 8]. The saturation characteristics are mostly obtained indirectly out of measured power, voltage, and current during a no-load test [2, 9, 10].

However, as pointed out in [11–16], the IM magnetising inductance may also saturate as a function of torque or rotor current, respectively, especially if the rotor slots are skewed and closed. By the nature of this phenomenon, this dependency is not possible to experimentally determine by the standard no-load test. The majority of papers model the magnetising inductance only as a function of the magnetising current. Only a few works strive to include the influence of the load or torque, respectively [11, 16]. Those papers use mainly finite element methods (FEMs). However, FEM models require knowledge of IM geometry; therefore, they are suitable for prototyping or new machine design.

Some papers try to identify the inductance by observers or model reference adaptive system (MRAS) [17, 18]. However, these methods require precise knowledge of all the other IM parameters. Other authors try to identify the magnetising inductance by signal injection [9, 19–25].

This paper presents a new offline identification method based on a principle presented in [26]. It compares the values of the measured and estimated IM torque and tries to minimise the error between them by adjusting the value of the magnetising inductance. Unlike our previous method, it does not require knowledge of the stator resistance. It does, however, require the knowledge of the rotor resistance, which is naturally not constant and depends on the IM's temperature, but the problem of the rotor resistance temperature dependency is overcome by estimating the value of the rotor inverse time constant. Therefore, intensive cooling is not required as opposed to our previous method.

The paper is organised as follows: in Section 2, basic IM equations that are utilised throughout the paper are presented. A former and improved method of identification of the load-dependent saturation is presented in Section 3. Guidance for implementation of the improved method is outlined in Section 4. Finally, Section 5 is dedicated to the experimental results. These also include a comparison of our method with the previous one, which is focused mainly on showing the robustness of the improved method against changes of the rotor resistance. The experimental part is concluded by an indirect approach of verification of the obtained saturation characteristics in terms of comparison of measured and estimated quantities and dynamic and static behaviour of a 12-kW drive.

2 Field-oriented control and induction motor equations

In this paper, equations describing the so-called T-equivalent circuit depicted in Fig. 1 are utilised for the mathematical description of IM. In the figure, the symbols $\underline{\boldsymbol{\psi}}_1$ and $\underline{\boldsymbol{\psi}}_2$ represent the stator and rotor flux linkage space vectors, respectively, $\underline{\boldsymbol{u}}_1$ represents the stator voltage space vector, $\underline{\boldsymbol{i}}_1$ and $\underline{\boldsymbol{i}}_2$ represent the stator and rotor current space vectors, respectively, R_1 and R_2 denote the stator and rotor resistance, respectively, ω_k is the electrical angular speed of the general reference frame, ω is the rotor electrical angular speed, L_m is the magnetising inductance and

the symbol j represents an imaginary unit ($j^2 = -1$). A squirrel-cage rotor is considered; therefore, the rotor voltage equals zero. The stator inductance L_1 is defined as $L_1 = L_m + L_{1\sigma}$, where $L_{1\sigma}$ is the stator leakage inductance and the rotor inductance L_2 is defined as $L_2 = L_m + L_{2\sigma}$, where $L_{2\sigma}$ is the rotor leakage inductance.

2.1 Rotor flux estimation

In the case of RFOC (Fig. 2), the position of the rotor flux vector and its amplitude are of interest. For a direct RFOC, where the transformation angle between the stationary $\alpha\beta$ and synchronous dq reference frame is calculated from the components of the rotor flux vector, the models are expressed in a stator-fixed coordinate system, therefore $\omega_k = 0$. The commonly used model, called the current model, is given by the following vector equation

$$\frac{d\underline{\boldsymbol{\psi}}_2}{dt} = L_m \tau_r^{-1} \underline{\boldsymbol{i}}_1 - \tau_r^{-1} \underline{\boldsymbol{\psi}}_2 + j\omega \underline{\boldsymbol{\psi}}_2, \tag{1}$$

where

$$\tau_r^{-1} = \frac{R_2}{L_2} \tag{2}$$

is the inverse rotor time constant. The Park transformation angle ϑ is then calculated as $\tan^{-1}(\psi_{2\beta}/\psi_{2\alpha})$.

2.2 Torque estimation

The IM torque can be expressed by many equivalent formulas based on one's choice of state variables. In this paper, a combination of the rotor flux linkage and stator current vector is selected. In the case of Clarke's transformation coefficient equal to 2/3 we get

$$T_{IM} = \frac{3}{2} p_p \frac{L_m}{L_2} (\psi_{2\alpha} i_{1\beta} - \psi_{2\beta} i_{1\alpha}), \tag{3}$$

where p_p is the number of pole-pairs.

3 Load-dependent saturation of induction motor and proposed method for its determination

3.1 Saturation of the magnetising inductance as a function of the rotor current

It is well-known that the magnetising inductance saturates as a function of the magnetising current. This dependency is, for instance, obtainable from the standard no-load test. However, the magnetising inductance may also saturate as a function of the load and, thus, rotor current. Authors in [11, 14] summarise that this phenomenon is caused mainly by skewing of rotor slots. This effect can be further aggravated if the rotor slots are closed.

3.2 Previous method

In [26], a simple and intuitive method for offline identification of the load-dependent saturation of IM was proposed. The method in addition to the IM current model given by (1) also uses the so-called voltage model given by the following set of equations:

$$\begin{aligned} \underline{\boldsymbol{\psi}}_1 &= \int_0^t (\underline{\boldsymbol{u}}_1 - R_1 \underline{\boldsymbol{i}}_1) d\tau, \\ \underline{\boldsymbol{\psi}}_2 &= \frac{L_2}{L_m} (\underline{\boldsymbol{\psi}}_1 - \sigma L_1 \underline{\boldsymbol{i}}_1), \end{aligned} \tag{4}$$

where $\sigma = 1 - L_m^2/L_1 L_2$ is the leakage factor.

Let us suppose that the simplifying assumptions on which the vector equations of IM are derived are valid in practice. Then, in an ideal case, when all the motor parameters are known, there would be no difference between the magnitude of the estimated rotor flux vector from the current (1) and voltage model (4). If the results from the models differ, it means that there has to be some discrepancy in the motor parameters. Assuming that all motor parameters except the magnetising inductance are known, we can adjust the inductance to minimise the following error:

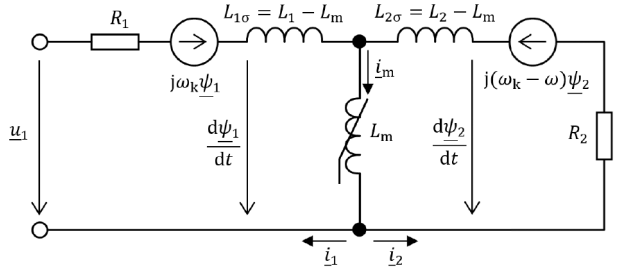

Fig. 1 *T-equivalent circuit of IM*

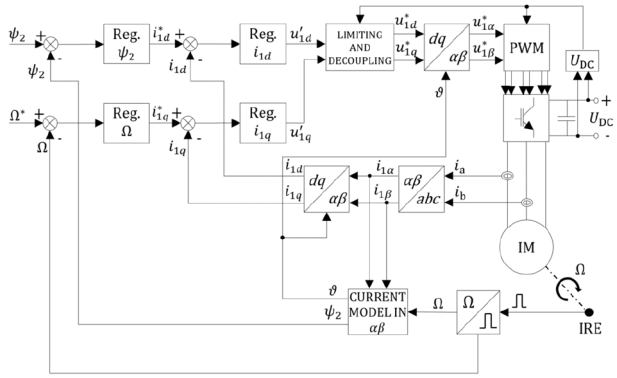

Fig. 2 *Block diagram of direct RFOC*

$$\varepsilon_\psi = \psi_{2VM} - \psi_{2CM}, \tag{5}$$

where ψ_{2VM} and ψ_{2CM} are the amplitudes of the rotor flux vector obtained from (4) and (1), respectively.

To suppress the change of the rotor resistance with temperature, the heavy-load measurements should be made as quickly as possible, and the motor should be cooled by forced convection.

3.3 Improved method

Consider that the IM runs within RFOC and that there is a difference between the measured T and estimated IM torque T_{IM}, i.e.

$$\varepsilon_T = T - T_{IM}. \tag{6}$$

As in the previous section, let us assume the validity of the simplifying assumption for the space-vector theory. Assuming that all parameters except the magnetising inductance are known, this means that the previous error (6) has to depend only on the magnetising inductance, i.e.

$$\varepsilon_T = f(L_m). \tag{7}$$

The following iterative algorithm based on (7) can then be used to obtain the magnetising inductance:

i. Set $k = 0$. Choose an initial value $L_m(k) = L_{m0}$. Choose an incremental inductance ΔL_m; $\Delta L_m \in \mathbb{R}^+$. Specify the minimal tolerance δ; $\delta \in \mathbb{R}^+$.
ii. Calculate $\varepsilon_T(k)$. If $|\varepsilon_T(k)| \leq \delta$ then $L_m = L_m(k)$ and the algorithm stops. Otherwise, go to step 3.
iii. If $\varepsilon_T(k) > (\delta/2)$ then calculate $L_m(k+1) = L_m(k) + \Delta L_m$, if $\varepsilon_T(k) < -(\delta/2)$ then calculate $L_m(k+1) = L_m(k) - \Delta L_m$. Increase k by one and go to step 4.

iv. If the convergence is too slow or if the output oscillates, adjust ΔL_{m} by multiplication with relaxation factor $\lambda \in \mathbb{R}^{+}$ and go back to step 2.

It is recommended to average the values of ε_T over multiple sampling periods. After calculating each new inductance, it is also necessary to wait for a few seconds for the drive to reach a new steady-state.

3.4 Reactive-power MRAS for estimation of rotor inverse time constant

To obtain the load-dependent saturation characteristics of IM, it is necessary to carry out measurements in the range of a few per cent of the machine's rated torque to the full machine's rated torque. Measurements at the high load will cause the rotor to heat up, leading to a deterioration in the accuracy of the proposed method.

To overcome the problem of the change of the rotor resistance with the temperature, we propose to implement the estimation of the rotor inverse time constant parallelly to the iteration algorithm. The adopted method is MRAS based on IM reactive power (Q-MRAS) [27–31]. The reference model is given by

$$Q = u_{1\beta} i_{1\alpha} - u_{1\alpha} i_{1\beta}. \tag{8}$$

The adaptive model is given by

$$\hat{Q} = \omega_{\mathrm{s}} L_{\mathrm{l}} \left(i_{1d}^{2} + \sigma i_{1q}^{2} \right). \tag{9}$$

Equation (8) is an expression for instantaneous reactive power, while (9) represents the steady-state reactive power. The synchronous speed can be calculated as

$$\omega_{\mathrm{s}} = \omega + \omega_{\mathrm{slip}}, \tag{10}$$

where ω_{slip} is the electrical slip speed which can be estimated as

$$\omega_{\mathrm{slip}} = \tau_{\mathrm{r0}}^{-1} \frac{i_{1q}}{i_{1d}}. \tag{11}$$

The error for the rotor time constant adaptation mechanism, which is a conventional PI controller, is calculated as

$$\varepsilon_{\tau} = Q - \hat{Q}. \tag{12}$$

The output of the PI controller is the deviation from the initial inverse rotor time constant τ_{r0}^{-1}, i.e.

$$\Delta \tau_{\mathrm{r}}^{-1}(t) = K_{\mathrm{p}} \varepsilon_{\tau}(t) + K_{\mathrm{i}} \int_{0}^{t} \varepsilon_{\tau}(\tau) \mathrm{d}\tau. \tag{13}$$

Finally, the estimated inverse time constant is given by

$$\hat{\tau}_{\mathrm{r}}^{-1} = \tau_{\mathrm{r0}}^{-1} + \Delta \tau_{\mathrm{r}}^{-1}. \tag{14}$$

The block diagram of the Q-MRAS is depicted in Fig. 3.

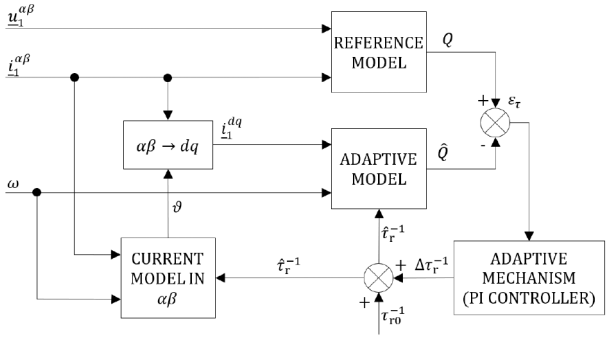

Fig. 3 *Q-MRAS for estimation of inverse rotor time constant*

3.4.1 Practical limitations of Q-MRAS: There are some practical limitations when considering the implementation of the Q-MRAS presented in the previous section. Those were summarised in [30, 31], respectively. The Q-MRAS should be active only if the motor speed and torque are higher than some threshold value. In this paper, the threshold values for the speed and torque were set to 10% of their nominal values.

3.5 Pros and cons of the proposed method

In this section, we shall briefly summarise the advantages and disadvantages of the proposed method. As this paper is intended to improve the method presented in [26] (which will be in the following text addressed as the 'previous method'), differences between those two shall also be emphasised.

3.5.1 Advantages:

i. The method uses the same hardware that is used during the drive regular operation or commissioning.
ii. The method can be automatised if a programmable load is available and if the information about load-torque can be fed into the control algorithm.
iii. The drive runs in the RFOC loop based on the current model (1) in $\alpha\beta$, which is a well-known FOC scheme.
iv. The current model (1) depends only on the magnetising inductance and inverse rotor time constant. Those parameters are calculated or estimated.
v. The current model (1), as opposed to the voltage model (4), is not impaired by the phenomenon of DC offset accumulation during pure integration. Therefore, modified integrators that deteriorate the accuracy of the model are not needed.
vi. The method does not depend on the stator resistance as opposed to the previous method.
vii. It does depend on the rotor resistance; however, the change in the rotor resistance with temperature is considered by estimating the inverse rotor time constant by Q-MRAS. The previous method does not try to compensate for the change of the rotor resistance.

3.5.2 Disadvantages:

i. The method does not work for load torques close to zero because of the Q-MRAS constraints. However, for the light-load measurements, the previous method can be used because the stator and rotor current will be relatively low, which means that the change in the stator and rotor resistance due to the rotor heating will not be significant.
ii. The need for the torque measurement makes the new method more hardware demanding than the previous one. A compromise between the new and previous method would be to implement the rotor time constant estimation into the previous method to eliminate the need for forced cooling. However, there is still the disadvantage of comparing two estimated quantities contrary to the new solution, where an estimated and measurable quantity is compared.
iii. There is still a problem with the uncertainty of the leakage inductances because these are used within the Q-MRAS. The method supposes that the leakage inductances are known accurately or that the effect of their inaccuracy on the output of the method is negligible. Since it is impossible in the case of a T-equivalent circuit to accurately determine the stator and rotor leakage inductance ratio, standardised approaches or rules of thumb have to be used. Also, there is another aspect, and that is the saturation of the rotor leakage inductance for some types of rotor design, as pointed out in [11, 14]. Experimental investigation of this phenomenon seems rather difficult.
iv. The effect of iron losses is neglected. However, it is possible to respect the iron losses in the IM model for the price of more complicated equations.
v. The method assumes that the space-vector theory simplifying assumptions are valid, which, of course, does not apply to a

real machine. It also neglects the effect of higher time and space harmonics. However, in most papers dealing with IM control and parameter estimation, these aspects are usually not taken into account.

vi. Mechanical losses are not taken into account, but in principle, they can be included in the torque equation.

4 Application of the proposed method

4.1 Requirements for initial induction motor parameters

The parameters required for the operation of the iteration algorithm and Q-MRAS are the initial value of the magnetising and leakage inductances and the initial value of the inverse rotor time constant, which is calculated from the initial rotor resistance and rotor inductance.

Any more or less sophisticated method can be used to obtain these parameters. However, since in the case of the current model and the iteration algorithm implementation, these parameters serve only as a starting value, the conventional no-load and locked-rotor test is the obvious choice.

4.2 Q-MRAS parameter update

As for the Q-MRAS, the adaptive model (9) uses the magnetising, stator, and rotor leakage inductances. The problem with the uncertainty of the leakage inductances was briefly acknowledged in Section 3.5.2. The stator inductance is updated using a new value of the magnetising inductance $L_{\mathrm{m}}(k+1)$ as

$$L_{1}(k+1) = L_{\mathrm{m}}(k+1) + L_{1\sigma}, \tag{15}$$

the rotor inductance as

$$L_{2}(k+1) = L_{\mathrm{m}}(k+1) + L_{2\sigma}, \tag{16}$$

and the leakage factor as

$$\sigma(k+1) = 1 - \frac{L_{\mathrm{m}}(k+1)\cdot L_{\mathrm{m}}(k+1)}{L_{1}(k+1)\cdot L_{2}(k+1)}. \tag{17}$$

The estimated inverse rotor time constant includes the rotor inductance, which mostly consists of the magnetising inductance. Therefore, the estimated inverse rotor time constant should vary not only with the rotor temperature but also with the load-independent and load-dependent saturation of IM.

On the one hand, the rotor inductance appears indirectly in the estimated inverse rotor time constant (2), on the other hand, it appears directly in the adaptive model (9) where it is updated according to (16). Strictly speaking, the rotor inductance should appear either as a standalone parameter or as a part of the inverse rotor time constant since the rotor leakage inductance may not be determined accurately, or it may also saturate as the function of the rotor current. In this paper, this discrepancy is neglected since the rotor inductance alone appears only in the leakage factor calculation, and therefore, the effect of the leakage inductance inaccuracy can be neglected [18].

4.3 Compensation of inverter non-linearity

The Q-MRAS reference model (8) uses components of the stator voltage vector in $\alpha\beta$. The inverter output voltage is very hard to measure directly due to its pulsating nature. A common approach to overcome this problem is to use a reference voltage vector within the control algorithm. However, due to the inverter non-linearities, among the most significant ones we can include dead-time and IGBT delayed switching, the fundamental wave of the inverter output voltage does not correspond to the reference voltage.

In this paper, we use a duty-cycle compensation for each leg of the three-phase two-level voltage-source inverter [32]. The relationship between the reference duty-cycle d_x^* and the corrected duty cycle d_x' is given as

$$d_x' = d_x^* + \frac{T_{\mathrm{eff}(x)}}{T_{\mathrm{PWM}}}\mathrm{sgn}(i_x) \quad x = a, b, c, \tag{18}$$

where T_{PWM} is the PWM period, i_x is the respective motor phase current and $T_{\mathrm{eff}(x)}$ is the so-called effective dead-time defined as

$$T_{\mathrm{eff}(x)} = T_{\mathrm{dt}} + T_{\mathrm{on}}(i_x) - T_{\mathrm{off}}(i_x) \quad x = a, b, c, \tag{19}$$

where T_{dt} is the actual dead-time inserted by the microcontroller or driver, $T_{\mathrm{on}}(i_x)$ is the current dependent turn-on time of the IGBT and $T_{\mathrm{off}}(i_x)$ is the current dependent turn-off time of the IGBT. The dependence of the effective dead-time on the collector current (19) was obtained by direct measurement on the inverter.

4.4 Measuring the load-dependent saturation characteristics

Considering the RFOC and steady-state, the d-axis rotor flux can be expressed as

$$\boldsymbol{\psi}_{2d} = \left|\underline{\boldsymbol{\psi}}_{2}\right| = \boldsymbol{\psi}_{2} = L_{\mathrm{m}} i_{1d}. \tag{20}$$

For a given flux, the IM torque can be written as

$$T_{\mathrm{IM}} = \frac{3}{2} p_{\mathrm{p}} \frac{L_{\mathrm{m}}}{L_{2}} \boldsymbol{\psi}_{2d} i_{1q}. \tag{21}$$

Therefore, in this paper, we consider the magnetising inductance as a function of the rotor flux magnitude and torque-producing (q-axis) current component, i.e.

$$L_{\mathrm{m}} = f\left(\left|\underline{\boldsymbol{\psi}}_{2}\right|, i_{1q}\right) = f\left(\boldsymbol{\psi}_{2d}, i_{1q}\right) = f\left(\boldsymbol{\psi}_{2}, i_{1q}\right) \tag{22}$$

The saturation due to the non-linear properties of the magnetic circuit is respected by the dependence $L_{\mathrm{m}} = f(\psi_2)$ and the load-dependent saturation by the dependence $L_{\mathrm{m}} = f(i_{1q})$.

The method can be divided into multiple steps:

i. Initial parameters of the IM are obtained, as discussed in Section 4.1.
ii. RFOC is implemented according to Fig. 2. along with Q-MRAS for the inverse rotor time constant estimation, which was described in Section 3.4.
iii. Inverter non-linearity compensation is implemented, as discussed in Section 4.3.
iv. The motor is running close to the rated speed.
v. The Q-MRAS is started with a set threshold torque.
vi. The dependence (22) should be measured for as many combinations of the rotor flux and torque-producing current as possible. This is done by adjusting the reference flux in the control algorithm along with the torque produced by the variable load.
vii. For the torques lower than the threshold torque set in Q-MRAS, our previous method should be used.

5 Experimental results

5.1 Experimental setup

The RFOC was implemented in C language into TMS320F28335 Delphino DSP. The clock frequency was set to 150 MHz, and the calculation loop of the FOC algorithm was selected to be 200 µs with a 10 kHz PWM. All the experimental data are sampled with 10 ms sampling period. As a drive, a machine set with 12 kW IM coupled with 8.8 kW separately excited DC motor (DCM) was used. The DCM serves as a dynamometer. The nameplate values of the IM and DCM, along with the IM initial model parameters measured by the conventional no-load (for the rated voltage) and locked-rotor test are given in Table 1. A picture of the experimental workplace is shown in Fig. 4.

Table 1 IM and DCM parameters

Induction motor				DC motor	
nominal power	12 kW	R_1	377 mΩ	nominal power	8.8 kW
nominal current	22 A	R_2	225 mΩ	nominal rotor current	38.3 A
nominal voltage	380 V	$L_{1\sigma}$	2.27 mH	nominal rotor voltage	230 V
nominal frequency	50 Hz	$L_{2\sigma}$	2.27 mH	nominal excit. current	2.8 A
nominal PF	0.8	R_{Fe}	202 Ω	nominal excit. voltage	110 V
nominal speed	1460 min^{-1}	L_m	82.5 mH	nominal speed	1460 min^{-1}

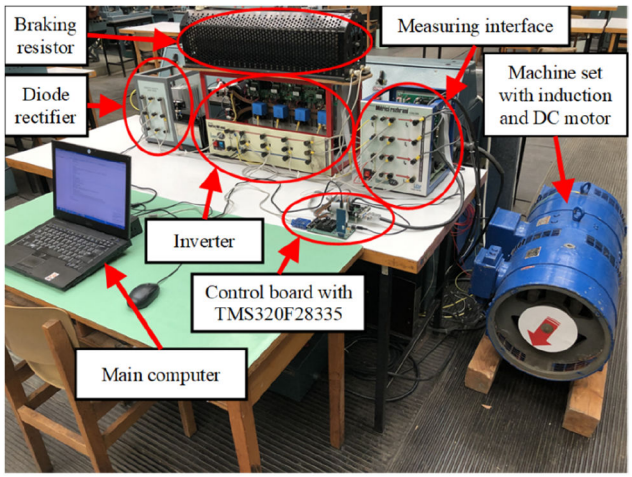

Fig. 4 *Experimental workplace*

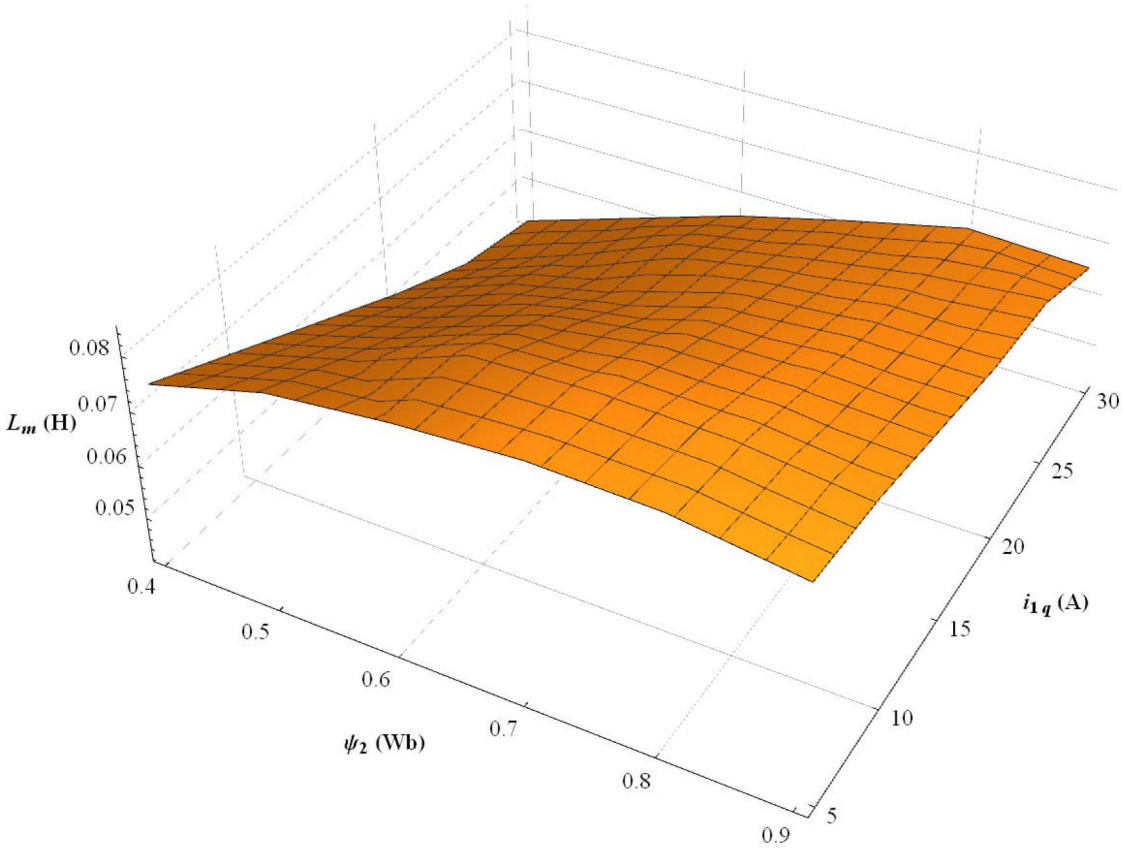

Fig. 5 *Measured dependence* $L_m = f(\psi_2, i_{1q})$

5.2 Measured saturation characteristics

The measured dependence $L_m = f(\psi_2, i_{1q})$ is depicted in the form of a 3D graph in Fig. 5. In the figure, the minimal flux is restricted to 0.4 Wb and the minimal torque-producing current to 5 A. According to the measured characteristics, the magnetising inductance heavily saturates with a load for lower flux levels where the rotor current or slip, respectively, must be high to maintain the torque. The characteristics were implemented as a look-up table.

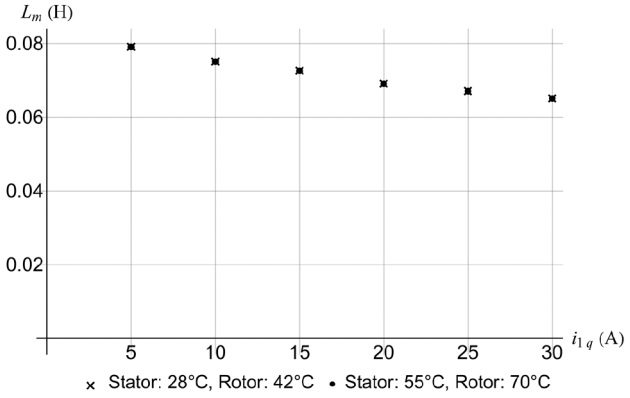

Fig. 6 *Improved method – measured values of $L_m = f(i_{1q})$ for reference rotor flux 0.8 Wb and two different stator and rotor temperatures*

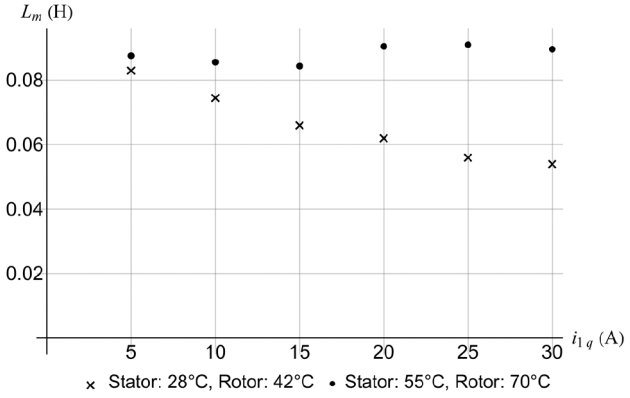

Fig. 7 *Previous method – measured values of $L_m = f(i_{1q})$ for reference rotor flux 0.8 Wb and two different stator and rotor temperatures*

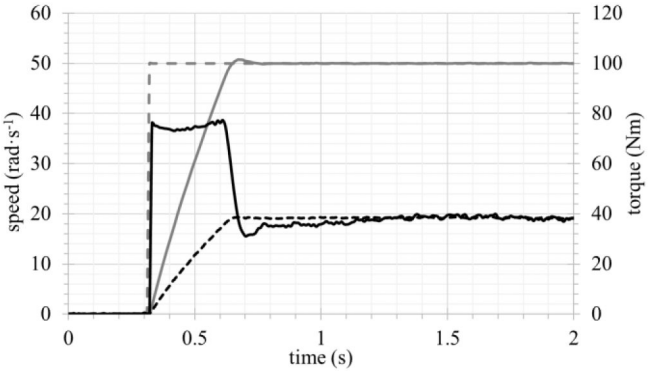

Fig. 8 *Start of the loaded drive from 0 to 50 rad s^{-1} – with L_m and τ_r^{-1} compensation; dashed grey: reference speed, solid grey: measured speed, dashed black: load torque developed by DC dynamometer, solid black: estimated IM torque; reference rotor flux: 0.85 Wb*

5.3 Robustness against thermal changes

To validate the robustness of the improved method against the changes in the rotor resistance, two sets of measurements of the magnetising inductance for two different stator and rotor temperatures were done. In both cases, the reference rotor flux was set to 0.8 Wb.

Fig. 6 shows the measured values for the improved method. The values for both the temperatures are in good accordance, which method robustness against changes in the motor resistance.

Fig. 7 shows the results for the previous method, where, contrary to Fig. 6, change in the stator and rotor winding temperature causes a significant deviation of the measured values.

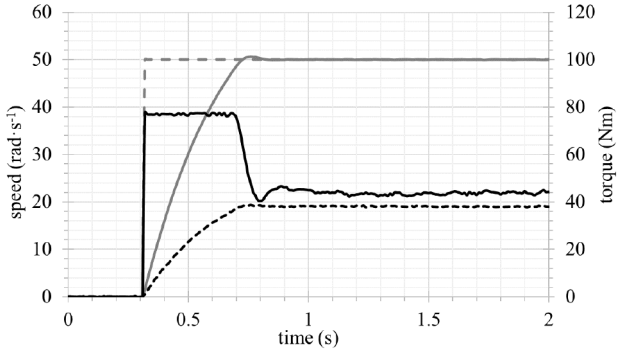

Fig. 9 *Start of the loaded drive from 0 to 50 rad s^{-1} – CPM; dashed grey: reference speed, solid grey: measured speed, dashed black: load torque developed by DC dynamometer, solid black: estimated IM torque; reference rotor flux: 0.85 Wb*

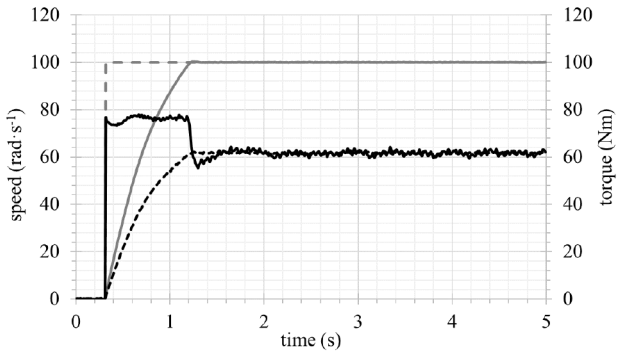

Fig. 10 *Start of the loaded drive from 0 to 100 rad s^{-1} – with L_m and τ_r^{-1} compensation; dashed grey: reference speed, solid grey: measured speed, dashed black: load torque developed by DC dynamometer, solid black: estimated IM torque; reference rotor flux: 0.85 Wb*

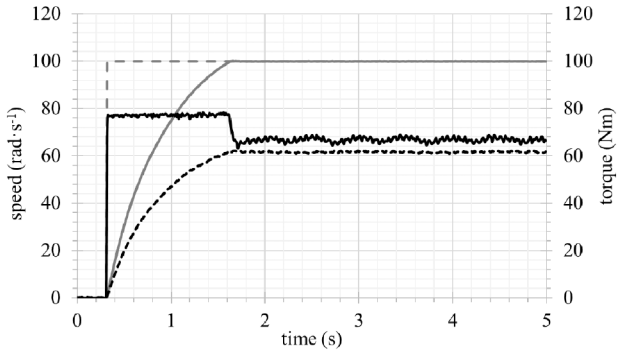

Fig. 11 *Start of the loaded drive from 0 to 100 rad s^{-1} – CPM; dashed grey: reference speed, solid grey: measured speed, dashed black: load torque developed by DC dynamometer, solid black: estimated IM torque; reference rotor flux: 0.85 Wb*

5.4 Comparison against constant parameter model

Figs. 8–13 show the start of the IM drive loaded by DCM for three different reference speed steps: Figs. 8 and 9 – from 0 to 50 rad s^{-1}, Figs. 10 and 11 – from 0 to 100 rad s^{-1} and Figs. 12 and 13 – from 0 to 150 rad s^{-1}. In all the cases, the reference rotor flux is set to 0.85 Wb (corresponding no-load magnetising inductance is 0.0867 H). In Figs. 8, 10, and 12 the magnetising inductance and inverse rotor time constant are compensated. In Figs. 9, 11, and 13, the model uses constant parameters. It can be seen that in the case of the parameter compensation, the start of the drive is always more or less faster. The higher the difference between the initial and final speed, the more significant the difference between the constant parameter model (CPM) and the compensated model. Furthermore, the steady-state measured and estimated torque are in very good accordance in the case of the compensated model as opposed to the

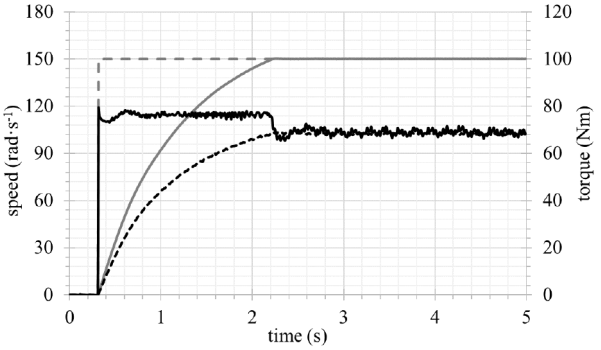

Fig. 12 *Start of the loaded drive from 0 to 150 rad s^{-1} – with L_m and τ_r^{-1} compensation; dashed grey: reference speed, solid grey: measured speed, dashed black: load torque developed by DC dynamometer, solid black: estimated IM torque; reference rotor flux: 0.85 Wb*

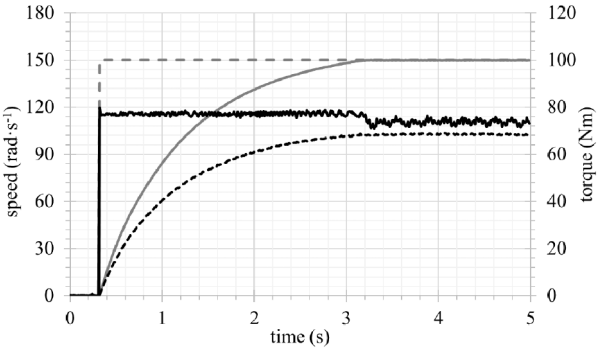

Fig. 13 *Start of the loaded drive from 0 to 150 rad s^{-1} – CPM; dashed grey: reference speed, solid grey: measured speed, dashed black: load torque developed by DC dynamometer, solid black: estimated IM torque; reference rotor flux: 0.85 Wb*

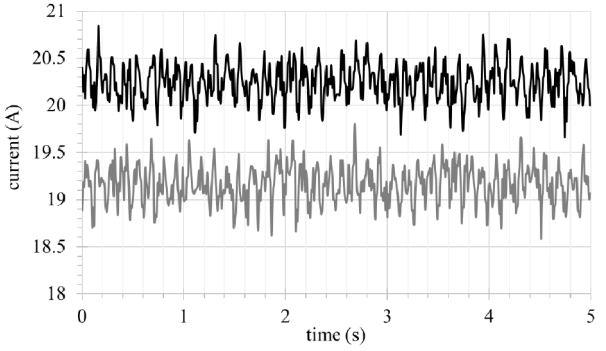

Fig. 14 *Measured current vector amplitude in steady-state – speed: 50 rad s^{-1}, load torque developed by DC dynamometer: 38 Nm; black: CPM, grey: L_m and τ_r^{-1} compensation; reference rotor flux: 0.85 Wb*

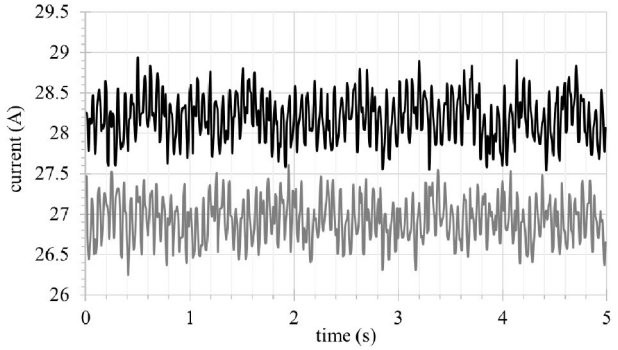

Fig. 15 *Measured current vector amplitude in steady-state – speed: 100 rad s^{-1}, load torque developed by DC dynamometer: 60 Nm; black: CPM, grey: L_m and τ_r^{-1} compensation; reference rotor flux: 0.85 Wb*

CPM, where an error between the estimated and measured torque exists. In the case of the compensated model, a slight ripple in the

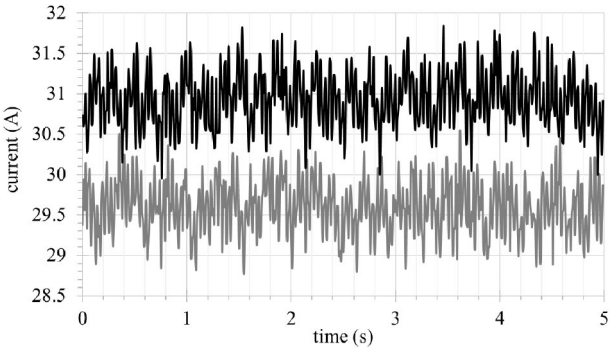

Fig. 16 *Measured current vector amplitude in steady-state – speed: 150 rad s^{-1}, load torque developed by DC dynamometer: 68 Nm; black: CPM, grey: L_m and τ_r^{-1} compensation; reference rotor flux: 0.85 Wb*

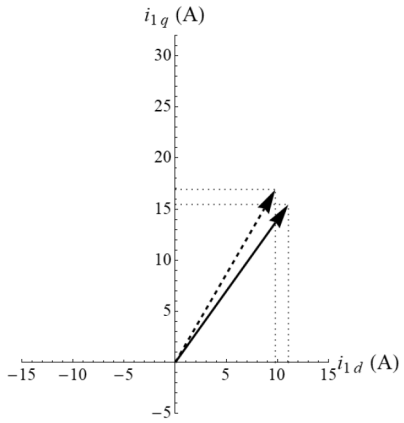

Fig. 17 *Current vector diagram in dq – speed: 50 rad s^{-1}, load torque developed by DC dynamometer: 38 Nm; dashed: CPM, solid: L_m and τ_r^{-1} compensation; reference rotor flux: 0.85 Wb*

calculated torque exists due to the continuous recalculation of the magnetising inductance based on the bilinear interpolation.

Another important consequence of the parameter detuning is shown in Figs. 14–16, where the measured amplitudes of the stator current vector are shown for the corresponding steady-speed cases in Figs. 8–13. In the case of the CPM, the amplitude of the current is higher in all the cases with the average difference around 1 A. Therefore, proper parameter identification and compensation can lead to energy savings because for the same reference flux and speed the drive controlled by the compensated model draws lower current.

Figs. 17–19 shows the current vector diagram for the cases corresponding to Figs. 14–16. The single-value current components are obtained by averaging per 5 s window. In the case of CPM, the flux controller demands lower flux-producing current component which, because of the saturation, produces lower flux than the reference one and, therefore, the speed controller has to demand higher torque-producing current component to maintain the same

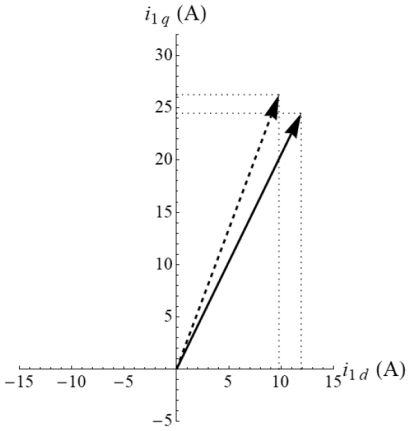

Fig. 18 *Current vector diagram in dq – speed: 100 rad s^{-1}, load torque developed by DC dynamometer: 60 Nm; dashed: CPM, solid: L_m and τ_r^{-1} compensation; reference rotor flux: 0.85 Wb*

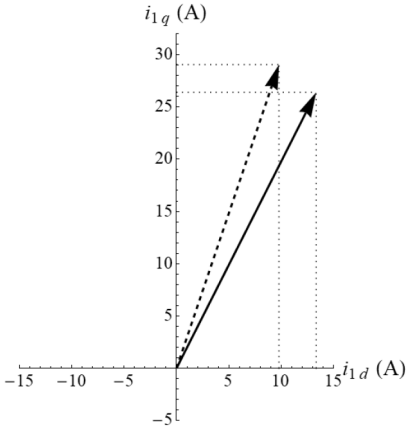

Fig. 19 *Current vector diagram in dq – speed: 150 rad s^{-1}, load torque developed by DC dynamometer: 68 Nm; dashed: CPM, solid: L_m and τ_r^{-1} compensation; reference rotor flux: 0.85 Wb*

torque, which is the cause of the higher current drawn from the source.

6 Conclusion

Load-dependent saturation of an IM is a phenomenon that is often neglected but which, if not considered, can deteriorate the behaviour of the IM drive controlled by the modern control strategies.

In this paper, a novel experimental method for identification of the load-dependent saturation of IM, which respects the variation of the inverse rotor time constant, was presented. The proposed method is intended to be an improved version of our previous method. The main advantages are that the new method does not require knowledge of the stator resistance. Secondly, it respects the variation of the rotor resistance by estimating the inverse rotor time constant and, thirdly, compares the IM estimated quantity (estimated torque) to a measurable quantity (load torque).

According to the experimental results, compared to the constant-parameter model, the compensation of the load-dependent saturation based on the measured values by our proposed method along with the compensation of the inverse rotor time constant by Q-MRAS show improvement of the drive static and dynamic behaviour.

7 Acknowledgments

The research described in this paper was supported by the Student Grant Competition of the Czech Technical University in Prague under grant no. SGS20/062/OHK3/1T/13.

8 References

[1] Levi, E., Lamine, A., Cavagnino, A.: 'Impact of stray load losses on vector control accuracy in current-fed induction motor drives', *IEEE Trans. Energy Convers.*, 2006, **21**, (2), pp. 442–450

[2] Chatterjee, D.: 'A simple leakage inductance identification technique for three-phase induction machines under variable flux condition', *IEEE Trans. Ind. Electron.*, 2012, **59**, (11), pp. 4041–4048

[3] Sokola, M., Levi, E.: 'Combined impact of iron loss and main flux saturation on operation of vector controlled induction machines'. 1996 Sixth Int. Conf. on Power Electronics and Variable Speed Drives, Nottingham, UK, 1996, pp. 36–41

[4] Zaky, M.S., Khater, M.M., Shokralla, S.S., *et al.*: 'Wide speed range estimation with online parameter identification schemes of sensorless induction motor drives', *IEEE Trans. Ind. Electron.*, 2009, **56**, (5), pp. 1699–1707

[5] Levi, E., Wang, M.: 'A speed estimator for high performance sensorless control of induction motors in the field-weakening region', *IEEE Trans. Power Electron.*, 2002, **17**, (3), pp. 365–378

[6] Shen, G., Yao, W., Chen, B., *et al.*: 'Auto measurement of the inverter output voltage delay curve to compensate for inverter nonlinearity in sensorless motor drives', *IEEE Trans. Power Electron.*, 2014, **29**, (10), pp. 5542–5553

[7] Levi, E.: 'Main flux saturation modeling in double-cage and deep-bar induction machines', *IEEE Trans. Energy Convers.*, 1996, **11**, (2), pp. 305–311

[8] Tataru, L.L.: 'A flux-based expression of induction machine magnetizing inductance', *IEEE Trans. Energy Convers.*, 2010, **25**, (1), pp. 268–270

[9] Rasmussen, H., Knudsen, M., Tonnes, M.: 'Parameter estimation of inverter and motor model at standstill using measured currents only'. Proc. IEEE Int. Symp. Ind. Electron., Warsaw, Poland, 1996, pp. 331–336

[10] Levi, E., Kola, M., Vukosavic, S.N.: 'A method for magnetizing curve identification in rotor flux oriented induction machines', *IEEE Trans. Energy Convers.*, 2000, **15**, (2), pp. 157–162

[11] Tuovinen, T., Hinkkanen, M., Luomi, J.: 'Modeling of saturation due to main and leakage flux interaction in induction machines', *IEEE Trans. Ind. Appl.*, 2010, **46**, (3), pp. 937–945

[12] Gerada, C., Bradley, K., Sumner, M., *et al.*: 'Evaluation and modelling of cross saturation due to leakage flux in vector controlled induction machines'. IEEE Int. Electric Machines and Drives Conf., Madison, WI, USA, 2003, pp. 1983–1989

[13] Klaes, N.R.: 'Parameter identification of an induction machine with regard to dependencies on saturation', *IEEE Trans. Ind. Appl.*, 2003, **29**, (6), pp. 1135–1140

[14] Hinkkanen, M., Repo, A., Luomi, J.: 'Influence of magnetic saturation on induction motor model selection'. Proc. ICEM'06, Chania, Greece, September 2006

[15] Immonen, P., Ruuskanen, V., Nerg, J., *et al.*: 'Inductance saturation of the induction machine as a function of stator voltage and load with steady state AC magnetic finite element solver'. Int. Review of Modeling and Simulation (IREMOS), 2004, 7, (3)

[16] Nerg, J., Pyrhonen, J., Partanen, J.: 'Finite element modeling of the magnetizing inductance of an induction motor as a function of torque', *IEEE Trans. Magn.*, 2004, **40**, (4), pp. 2047–2049

[17] Ranta, M., Hinkkanen, M.: 'Online identification of parameters defining the saturation characteristics of induction machines', *IEEE Trans. Ind. Appl.*, 2013, **49**, (5), pp. 2136–2145

[18] Liu, L., Guo, Y., Wang, J.: 'Online identification of mutual inductance of induction motor without magnetizing curve'. 2018 Annual American Control Conf. (ACC), Milwaukee, WI, USA, 2018, pp. 3293–3297

[19] Bertoluzzo, M., Buja, G.S., Menis, R.: 'Self-commissioning of RFO IM drives: one-test identification of the magnetization characteristic of the motor', *IEEE Trans. Ind. Appl.*, 2001, **37**, (6), pp. 1801–1806

[20] Zigliotto, M., Carraro, M.: 'Automatic parameter identification of inverter-fed induction motors at standstill', *IEEE Trans. Ind. Electron.*, 2014, **61**, (9), pp. 4605–4613

[21] Bellini, A., Bifaretti, S.: 'A method for magnetizing curve identification in vector controlled induction motor drives'. Proc. Int. SPEEDAM, Taormina, Italy, May 2006, pp. 955–959

[22] He, Y., Wang, Y., Feng, Y., *et al.*: 'Parameter identification of an induction machine at standstill using the vector constructing method', *IEEE Trans. Power Electron.*, 2012, **27**, (2), pp. 905–915

[23] Wang, K., Yao, W., Chen, B., *et al.*: 'Magnetizing curve identification for induction motors at standstill without assumption of analytical curve functions', *IEEE Trans. Ind. Electron.*, 2015, **62**, (4), pp. 2144–2155

[24] Jiayang, R., Shanming, W.: 'Estimation of saturation characteristic of induction motors by injecting sinusoidal currents with customized low frequency'. 17th Int. Conf. on Electrical Machines and Systems (ICEMS), Hangzhou, China, 2014, pp. 3166–3174

[25] Kalamen, L., Rafajdus, P., Sekerak, P., *et al.*: 'A novel method of magnetizing inductance investigation of self-excited induction generators', *IEEE Trans. Magn.*, 2012, **48**, (4), pp. 1657–1660

[26] Lipcak, O., Bauer, J., Kobrle, P.: 'Offline method for determination of non-linear dependence of machine magnetising inductance utilising parallel operation of current and voltage model', *IET Power Electron.*, 2019, **12**, (11), pp. 2843–2850

[27] Maiti, S., Chakraborty, C., Hori, Y., *et al.*: 'Model reference adaptive controller-based rotor resistance and speed estimation techniques for vector controlled induction motor drive utilizing reactive power', *IEEE Trans. Ind. Electron.*, 2008, **55**, (2), pp. 594–601

[28] Cao, P., Zhang, X., Yang, S.: 'A unified-model-based analysis of MRAS for online rotor time constant estimation in an induction motor drive', *IEEE Trans. Ind. Electron.*, 2017, **64**, (6), pp. 4361–4371
[29] Cao, P., Zhang, X, Yang, S., *et al.*: 'Reactive-power-based MRAS for online rotor time constant estimation in induction motor drives', *IEEE Trans. Power Electron.*, 2017, **33**, (12), pp. 10835–10845
[30] Mapelli, F.L., Bezzolato, A., Tarsitano, D.: 'A rotor resistance MRAS estimator for induction motor traction drive for electrical vehicles'. XXth Int. Conf. on Electrical Machines, Marseille, France, 2012, pp. 823–829
[31] Mapelli, F.L., Tarsitano, D., Cheli, F.: 'A rotor resistance MRAS estimator for EV induction motor traction drive based on torque and reactive stator power: simulation and experimental results'. Int. Conf. on Electrical Machines (ICEM), Berlin, Germany, 2014, pp. 31–37
[32] Lipcak, O., Bauer, J.: 'Analysis of voltage distortion and comparison of two simple voltage compensation methods for sensorless control of induction motor'. IEEE Int. Symp. on Sensorless Control for Electrical Drives, Torino, Italy, September 2019

3.3 Paper 3: MRAS-Based Induction Machine Magnetizing Inductance Estimator with Included Effect of Iron Losses and Load

3.3.1 Motivation

The method presented in the previous section cannot accurately determine the no-load magnetizing characteristic. This fact and its other disadvantages, such as the necessity of external torque measurement, omission of iron losses, no rigorous proof of stability, and no sensitivity analysis, lead the author to develop a new method subject to an article presented in this section.

The article deals with identifying the magnetizing inductance based on the MRAS approach. The majority of papers dealing with IM parameter identification based on MRAS do not consider the effect of iron losses. Therefore, the paper presented in this section proposes MRAS based on improved IM current and voltage models that enables the identification of the no-load and load-dependent saturation while considering the effect of iron losses. Furthermore, the adaptation mechanism and the error variable are rigorously derived based on Lyapunov's second method. Small-signal analysis and the derivation of the sensitivity function are also presented.

With regard to prerequisites, this article uses:

- inverter model from paper in section 3.1 for the compensation of the most significant nonlinearities,
- modified integrator for the IM voltage model evaluation described in section 2.6.1,
- robust RK4 order method for the current model evaluation, which is described in more detail in paper from section 3.4,
- parallel estimation of the rotor resistance by Q-MRAS used in section 3.2.,
- iron losses measurement and implementation described in section 2.4.3.

3.3.2 Main Contribution and Results

To sum up the contribution and main results of the paper:

- The paper presents both simulation and experimental results.
- For the simulation results, a complex model of the IM drive with the possibility of iron losses inclusion was built in MATLAB/Simulink.
- Improved IM current and voltage models with the included effect of iron losses are presented.
- A novel magnetizing inductance MRAS estimator able to identify both the no-load and load-dependent saturation is derived using Lyapunov's second method.
- For the compensation of the variation of the rotor resistance, modified Q-MRAS with the included effect of iron losses is presented to improve the method's accuracy.
- Comparison with the magnetizing characteristics obtained from the standard no-load test shows an excellent match and validates the proposed approach.

3.3.3 Discussion and Suggestions for Future Work

As the vast majority of methods presented in the literature, even the method proposed in the following paper is sensitive to the other machine parameter such as the leakage inductances and the stator resistance. The influence of stator resistance (and the voltage distortion) on the voltage model accuracy can be mitigated by identifying the magnetizing inductance at higher motor speeds. Furthermore, the stator resistance temperature variation can be compensated using a thermal sensor in the machine's stator winding. The situation with the leakage inductances is more complicated than with the stator resistance. The inductances can be identified, for instance, by the signal injection as mentioned in section 3.2.3. However, this approach also brings some problems and challenges (that were also tackled in section 3.2.3).

The performance of the proposed method also depends on the utilized modified integrator. The paper uses the scheme presented in section 2.6.1. The algorithm belongs to the group of adaptive integrators, which should exhibit the best performance among the modified integrators [150].

As discussed at the end of the paper, the reference model is not free of the magnetizing inductance. However, the fact that was not explicitly mentioned in the paper is that also the voltage model utilizes the estimated magnetizing inductance value needed for recalculation of the stator flux linkage vector to the rotor flux linkage vector. Thus, it can be said that the model self-improves its behavior through the estimated parameter.

It shall also be acknowledged that the improved Q-MRAS for the rotor resistance estimation with the included effect of iron losses was derived using the known reference model formula and the adaptive by directly substituting for the d and q-axis stator voltage vector components from the IM state-space model with included iron losses. Therefore, no rigorous proof of stability is presented. Such an analysis would be quite involved since the IM state-space model with the iron losses is of a higher order.

Again, an indirect comparison was presented to demonstrate the benefits of cooperation of the magnetizing inductance and rotor resistance estimators at load conditions. Unfortunately, the problem of insufficient detailed machine documentation for FEA, as discussed in section 3.2, still persisted at the time of the paper's publication.

The iron loss model was simplified by only considering the no-load iron loss characteristics. An analysis of the contribution of the slip-dependent additional losses would be interesting also from a general point of view, not only from the point of view of the accuracy of the proposed method.

Lastly, it is worth mentioning that the IGBT modules CM100DY-24NF from Mitsubishi Electric used in the papers from sections 3.1 and 3.2 were replaced due to fault by modules SKM100GB12T4 from SEMIKRON. Of course, the inverter model necessary for the voltage compensation was reidentified using the approach from section 2.1.3 again.

IEEE Access
Multidisciplinary | Rapid Review | Open Access Journal

Received October 18, 2021, accepted December 13, 2021, date of publication December 14, 2021,
date of current version December 24, 2021.

Digital Object Identifier 10.1109/ACCESS.2021.3135763

MRAS-Based Induction Machine Magnetizing Inductance Estimator With Included Effect of Iron Losses and Load

ONDREJ LIPCAK, (Graduate Student Member, IEEE), AND JAN BAUER, (Member, IEEE)
Department of Electric Drives and Traction, Faculty of Electrical Engineering, Czech Technical University in Prague, 16627 Prague, Czech Republic

Corresponding author: Ondrej Lipcak (lipcaond@fel.cvut.cz)

This work was supported by the Student Grant Competition of the Czech Technical University in Prague under Grant SGS21/116/OHK3/2T/13.

ABSTRACT Although still widely used due to its robustness, reliability, and low cost, induction motor (IM) has a disadvantage of more complicated mathematical description than permanent magnet AC machines. In high-demanding applications, the decoupled control of the machine's flux and torque along with the proper function of selected efficiency-improving and flux-weakening algorithms can be achieved only if the IM parameters are known with sufficient accuracy. For parameter estimation, many algorithms have been proposed in the literature so far. Due to its simple and straightforward implementation, one of the popular estimation strategies is the model reference adaptive system (MRAS). However, MRAS-based algorithms for a specific parameter estimation tend to be sensitive to other machine parameters. For instance, most of the proposed MRAS algorithms do not consider the influence of the phenomena such as iron losses and load-dependent saturation. Since one of the most performance-decisive parameters of the popular rotor flux-oriented control (RFOC) are the magnetizing inductance and the rotor resistance, this paper aims to present a novel MRAS-based magnetizing inductance estimator (Lm-MRAS) with the included effect of iron losses. Furthermore, to enable the identification of the load-dependent saturation, another MRAS with included iron losses based on reactive power is proposed to work parallelly with Lm-MRAS, since under load conditions, the rotor resistance mismatch causes RFOC detuning. The adaptation law of the Lm-MRAS is obtained using the Lyapunov function approach and further examined using small-signal analysis. The proposed algorithms are verified on a 3.6 kW IM drive both in simulations and experiments.

INDEX TERMS Induction motor drives, iron losses, magnetizing flux saturation, model reference adaptive systems, parameter estimation, stability analysis.

I. INTRODUCTION

Real-time identification of induction machine (IM) parameters in the rotor flux-oriented control (RFOC) is still an ongoing topic amongst researchers in the field of electric drives and power electronics. For example, in the European Union, due to the emerging legislation and the growing societal demands, the requirements for the efficiency of electrical equipment are constantly increasing. Following this trend, the task of software engineers dealing with the control of electric drives is to design the most efficient software. Within the scope of the machine control, this essentially includes the compensation of various IM drive nonlinearities and deployment of control algorithms such as maximum torque per ampere (MTPA). However, many of the proposed efficiency-improving strategies are parameter-dependent [1], [2].

The traditional and widely used circuit is the so-called T-equivalent circuit which can be obtained using the space-vector theory of electrical machines. Furthermore, the equivalent circuit can be augmented to include the specific nonlinear phenomena such as magnetizing flux or rotor leakage flux saturation [4]–[7], iron losses [7], [8], or stray-load losses [9] that are difficult to capture at the stage of the mathematical derivation of machine's fundamental flux and voltage equations.

To ensure an effective operation of IM drives in high-demanding applications such as electric traction vehicles,

The associate editor coordinating the review of this manuscript and approving it for publication was Alfeu J. Sguarezi Filho.

precise decoupled control of the machine's flux and torque is needed. This demand goes hand in hand with the accurate knowledge of the IM parameters [10]. Also, an appropriate equivalent circuit that captures the most performance-decisive phenomena must be selected to obtain relevant results through the estimation algorithms.

For instance, although omitted in many papers, iron losses undoubtedly affect the IM RFOC [8], [10]. One way to respect the influence of iron losses is to add a fictitious resistance either in parallel or in series with the magnetizing branch [8]. Another phenomenon that is overlooked in many papers is load-dependent saturation. Due to the complicated distribution of the electromagnetic field inside the machine, the magnetizing flux can also saturate as a consequence of the load [11], especially if the rotor slots are skewed or closed [4]–[6]. Since the accurate knowledge of the magnetizing inductance has a decisive influence on the performance of the RFOC strategies, this nonlinear phenomenon should be respected in high-efficiency drives.

So far, many methods for the online identification of IM parameters have been proposed. These include recursive least-square algorithms (RLS) [12]–[14], model reference adaptive systems (MRAS) [15]–[21], signal injection (SI) techniques [22]–[24], state observers (SO) [25]–[27], and artificial intelligence (ANN) [28]–[30]. Typically, the greater the estimation accuracy and independence from other machine parameters, the greater the algorithm complexity, which demands sufficient computational power of the used hardware and the knowledge and experience of the implementation engineer. For example, methods based on MRAS that are quite popular within electric drives offer the comfort of ease of implementation but at the price of dependency on other machine parameters.

This paper aims to present a novel MRAS-type estimator for identifying both the no-load and load-dependent saturation of IM that can respect the effect of the machine's iron losses. The main disadvantage of the MRAS schemes, i.e., the dependence on other machine's parameters, can manifest itself during the load operation because, at load conditions, the rotor flux estimation depends on the rotor resistance [30]. This disadvantage is solved by utilizing a second, parallelly operating MRAS estimator based on the machine's reactive power that is also augmented to respect the iron losses.

The adaptation law of the magnetizing inductance MRAS estimator is designed using the Lyapunov function approach. Furthermore, a small-signal analysis is also presented to assess the stability of the estimator with respect to the controller gain selection. Simulations and experiments conducted on a 3.6 kW IM drive are presented to verify the proposed concept of magnetizing inductance identification.

II. INDUCTION MACHINE EQUIVALENT CIRCUIT

In this paper, the so-called T-equivalent circuit with included magnetizing flux saturation and equivalent iron loss resistance placed in parallel with the magnetizing inductance [31] depicted in Fig. 1 is utilized for the mathematical description of IM. In the figure, the symbols $\underline{\psi}_1$, $\underline{\psi}_2$ and $\underline{\psi}_\mathrm{m}$ represent the stator, rotor, and magnetizing flux linkage space vectors, respectively, $\underline{u}_1$ represents the stator voltage space vector, $\underline{i}_1$, $\underline{i}_2$, $\underline{i}_\mathrm{m}$ and $\underline{i}_\mathrm{Fe}$ represent the stator, rotor, magnetizing, and equivalent iron loss current space vectors, respectively, R_1, R_2, and R_Fe denote the stator, rotor, and equivalent iron loss resistance, respectively, ω_k is the electrical angular speed of the general reference frame, ω is the rotor electrical angular speed, L_m is the magnetizing inductance and the symbol j represents an imaginary unit ($\mathrm{j}^2 = -1$). A short-circuited rotor is considered; therefore, the rotor voltage equals zero. The stator inductance L_1 is defined as $L_1 = L_\mathrm{m} + L_{1\sigma}$, where $L_{1\sigma}$ is the stator leakage inductance and the rotor inductance L_2 is defined as $L_2 = L_\mathrm{m} + L_{2\sigma}$, where $L_{2\sigma}$ is the rotor leakage inductance.

The superscript k denotes that the space vectors are expressed in an arbitrary reference frame. The two specific reference frames used in this paper are the stator-fixed (real and imaginary axis denoted as α and β, respectively) and rotor flux vector-attached (real and imaginary axis denoted as d and q, respectively) reference frames.

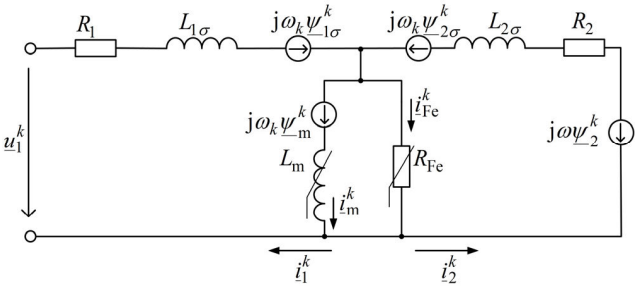

FIGURE 1. Induction machine T-equivalent circuit with included magnetizing inductance variation and iron losses.

A. STATE-SPACE MODEL WITH INCLUDED IRON LOSSES AND MAIN FLUX SATURATION

The full-order state space-model in the stationary $\alpha\beta$ reference frame with the current space vector, magnetizing space vector, and rotor space vector components as state variables is given by [10], [31]

$$\dot{\xi} = \mathbf{A}'\boldsymbol{\xi} + \mathbf{B}'\boldsymbol{v}, \tag{1}$$

where

$$\mathbf{A}' = \begin{pmatrix} a'_1 & 0 & a'_2 & 0 & a'_3 & 0 \\ 0 & a'_1 & 0 & a'_2 & 0 & a'_3 \\ R_\mathrm{Fe} & 0 & a'_4 & 0 & \tau^{-1}_{\mathrm{Fe}\sigma} & 0 \\ 0 & R_\mathrm{Fe} & 0 & a'_4 & 0 & \tau^{-1}_{\mathrm{Fe}\sigma} \\ 0 & 0 & \tau^{-1}_{\mathrm{r}\sigma} & 0 & -\tau^{-1}_{\mathrm{r}\sigma} & -\omega \\ 0 & 0 & 0 & \tau^{-1}_{\mathrm{r}\sigma} & \omega & -\tau^{-1}_{\mathrm{r}\sigma} \end{pmatrix}, \tag{2}$$

$$\mathbf{B}' = \begin{pmatrix} \frac{1}{L_{1\sigma}} & 0 & 0 & 0 & -\frac{1}{L_{1\sigma}} & 0 \\ 0 & \frac{1}{L_{1\sigma}} & 0 & 0 & 0 & -\frac{1}{L_{1\sigma}} \\ 0 & 0 & 0 & 0 & 1 & 0 \\ 0 & 0 & 0 & 0 & 0 & 1 \\ 0 & 0 & 1 & 0 & 0 & 0 \\ 0 & 0 & 0 & 1 & 0 & 0 \end{pmatrix}^{\mathrm{T}}, \tag{3}$$

$$\boldsymbol{\xi} = \begin{pmatrix} i_{1\alpha} & i_{1\beta} & \psi_{\mathrm{m}\alpha} & \psi_{\mathrm{m}\beta} & \psi_{2\alpha} & \psi_{2\beta} \end{pmatrix}^{\mathrm{T}}, \tag{4}$$

$$\boldsymbol{v} = \begin{pmatrix} u_{1\alpha} & u_{1\beta} & 0 & 0 & 0 & 0 \end{pmatrix}^{\mathrm{T}}, \tag{5}$$

and where $\tau_{\mathrm{r}\sigma} = L_{2\sigma}/R_2$, $\tau_{\mathrm{Fe}\sigma} = L_{2\sigma}/R_{\mathrm{Fe}}$, $a'_1 = -(R_1 + R_{\mathrm{Fe}})/L_{1\sigma}$, $a'_2 = L_2/(L_{1\sigma}L_{\mathrm{m}}\tau_{\mathrm{Fe}\sigma})$, $a'_3 = -1/(L_{1\sigma}\tau_{\mathrm{Fe}\sigma})$, $a_4 = -L_{1\sigma}a'_2$.

Considering Clarke's transformation constant equal to 2/3, the electromechanical torque can be expressed as

$$T_{\mathrm{e}} = \frac{3}{2}p_{\mathrm{p}}\frac{L_{\mathrm{m}}}{L_2}\left|\underline{\psi}_2^k \times \left(\underline{i}_1^k - \underline{i}_{\mathrm{Fe}}^k\right)\right|, \tag{6}$$

where p_{p} is the number of pole-pairs, and the operator $\times$ denotes cross product.

B. ROTOR FLUX ESTIMATION

The two standard IM reduced-order models used within the RFOC are the so-called current and voltage models. However, conventionally, these two models are derived out of the equivalent circuit with neglected iron losses. Therefore, in the following subsections, improved models with included iron losses will be presented.

1) CURRENT MODEL WITH INCLUDED IRON LOSSES

The model will be derived in an arbitrary reference frame. According to Fig. 1, the rotor voltage equation and the rotor flux linkage vector equation, respectively, can be expressed as

$$0 = R_2\underline{i}_2^k + \frac{\mathrm{d}\underline{\psi}_2^k}{\mathrm{d}t} + \mathrm{j}(\omega_k - \omega)\underline{\psi}_2^k, \tag{7}$$

$$\underline{\psi}_2^k = L_{2\sigma}\underline{i}_2^k + L_{\mathrm{m}}\underline{i}_{\mathrm{m}}^k = L_2\underline{i}_2^k + L_{\mathrm{m}}\left(\underline{i}_1^k - \underline{i}_{\mathrm{Fe}}^k\right). \tag{8}$$

Substituting for the rotor current vector in (7) from (8) yields after a few arrangements

$$\frac{\mathrm{d}\underline{\psi}_2^k}{\mathrm{d}t} = \frac{L_{\mathrm{m}}R_2}{L_2}\underline{i}_1'^k - \frac{R_2}{L_2}\underline{\psi}_2^k - \mathrm{j}(\omega_k - \omega)\underline{\psi}_2^k, \tag{9}$$

where $\underline{i}_1'^k = \underline{i}_1^k - \underline{i}_{\mathrm{Fe}}^k$. Considering the stator-fixed reference frame ($\omega_k = 0$), the model can be rewritten as

$$\frac{\mathrm{d}\underline{\psi}_2^{\alpha\beta}}{\mathrm{d}t} = \frac{L_{\mathrm{m}}R_2}{L_2}\underline{i}_1'^{\alpha\beta} - \frac{R_2}{L_2}\underline{\psi}_2^{\alpha\beta} + \mathrm{j}\omega\underline{\psi}_2^{\alpha\beta}. \tag{10}$$

Furthermore, choosing the rotor flux linkage vector-attached reference frame, one can obtain the steady-state expression for the rotor flux magnitude and slip frequency in the form

$$\psi_2 = L_{\mathrm{m}}i'_{1d}, \tag{11}$$

$$\omega_{\mathrm{sl}} = \frac{L_{\mathrm{m}}R_2}{L_2}\frac{i'_{1q}}{\psi_{2d}}, \tag{12}$$

where $\psi_2 = \psi_{2d} = \left|\underline{\psi}_2\right|$, $i'_{1d} = i_{1d} - i_{\mathrm{Fe}d}$, and $i'_{1q} = i_{1q} - i_{\mathrm{Fe}q}$.

2) VOLTAGE MODEL WITH INCLUDED IRON LOSSES

The model is almost exclusively used in the $\alpha\beta$ reference frame. According to Fig. 1, the stator flux linkage vector can be expressed as

$$\underline{\psi}_1^k = L_{1\sigma}\underline{i}_1^k + L_{\mathrm{m}}\underline{i}_{\mathrm{m}}^k = L_1\underline{i}_1^k + L_{\mathrm{m}}\left(\underline{i}_2^k - \underline{i}_{\mathrm{Fe}}^k\right). \tag{13}$$

Substituting for the rotor current vector in (8) from (13) and considering the stator-fixed reference frame yields

$$\underline{\psi}_2^{\alpha\beta} = \frac{L_2}{L_{\mathrm{m}}}\left(\underline{\psi}_1^{\alpha\beta} - L_{1\sigma}\underline{i}_1^{\alpha\beta}\right) + L_{2\sigma}\underline{i}_{\mathrm{Fe}}^{\alpha\beta}, \tag{14}$$

where $\sigma = 1 - L_{\mathrm{m}}^2/L_1L_2$ is the leakage factor. The stator flux linkage vector is obtained as

$$\underline{\psi}_1^{\alpha\beta} = \int_0^t \left(\underline{u}_1^{\alpha\beta} - R_1\underline{i}_1^{\alpha\beta}\right)\mathrm{d}\tau. \tag{15}$$

C. SENSITIVITY OF VOLTAGE MODEL TO MAGNETIZING INDUCTANCE VARIATION

The evaluation of the stator flux linkage vector using (15) is free of the magnetizing inductance. However, the magnetizing inductance appears in (14) when the stator flux linkage vector is recalculated to the rotor flux linkage vector. For convenience, new parameters containing the magnetizing inductance-dependent terms are introduced as

$$c_1 = \frac{L_2}{L_{\mathrm{m}}} = 1 + \frac{L_{2\sigma}}{L_{\mathrm{m}}}, \tag{16}$$

$$c_2 = L_1\sigma = L_{1\sigma} + \frac{L_{2\sigma}L_{\mathrm{m}}}{L_{\mathrm{m}} + L_{2\sigma}}. \tag{17}$$

The percentage change of these parameters with respect to the percentage deviation of the magnetization inductance ΔL_{m} from its nominal value can be written as

$$\Delta c_1 = \frac{L_{2\sigma}\,\Delta L_{\mathrm{m}}}{L_2\,(100 + \Delta L_{\mathrm{m}})} \cdot 100, \tag{18}$$

$$\Delta c_2 = -\frac{L_{2\sigma}^2 L_{\mathrm{m}}\Delta L_{\mathrm{m}}}{(L_{2\sigma}L_{\mathrm{m}} + L_{1\sigma}L_2)\,(100L_2 + L_{\mathrm{m}}\Delta L_{\mathrm{m}})} \cdot 100. \tag{19}$$

The dependencies $\Delta c_1 = f(\Delta L_{\mathrm{m}})$ and $\Delta c_2 = f(\Delta L_{\mathrm{m}})$ calculated using the nominal tested motor parameters (Table 1) are shown in Fig. 2. The variation of ΔL_{m} in the range of tens of percent causes the variation of the parameter only in the range of units of percent. Contrary to that, equation (11) states that if a steady-state is considered, then the variation of the magnetizing inductance directly proportional affects the output of the flux controller, i.e., d-axis current command.

III. PROPOSED MRAS-BASED MAGNETIZING INDUCTANCE ESTIMATOR WITH INCLUDED IRON LOSSES

The basic MRAS principle is that two mathematical models, the reference and adaptive, are evaluated parallelly. The reference model does not depend on the estimated quantity. On the contrary, the adaptive model utilizes directly or indirectly the estimated quantity. An adaptation mechanism

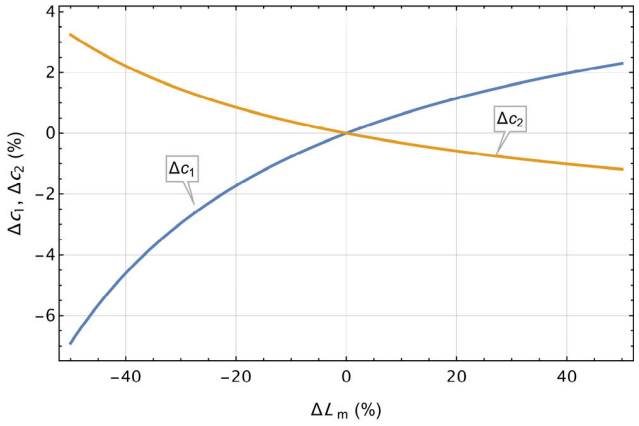

FIGURE 2. Percentage variation of the voltage model magnetizing inductance-dependent parameters due to percentage deviation of the magnetizing inductance from its nominal value.

(usually a simple PI controller) estimates the desired variable by forcing the difference between the reference and adaptive model to be zero. For the MRAS design, the Lyapunov theory or hyperstability theory can be utilized [19]. In this paper, the Lyapunov approach is adopted for the derivation of the adaptation mechanism

A. ADAPTATION MECHANISM DERIVATION USING LYAPUNOV THEORY

Let us consider a current model in the stationary reference frame, which utilizes the estimated magnetizing inductance $\hat{L}_\mathrm{m}$, i.e.,

$$\frac{\mathrm{d}\hat{\underline{\psi}}_2^{\alpha\beta}}{\mathrm{d}t} = \frac{\hat{L}_\mathrm{m}R_2}{\hat{L}_2}\underline{i}_1^{\alpha\beta} - \frac{R_2}{\hat{L}_2}\hat{\underline{\psi}}_2^{\alpha\beta} + \mathrm{j}\omega\hat{\underline{\psi}}_2^{\alpha\beta}, \tag{20}$$

where $\hat{L}_2 = \hat{L}_\mathrm{m} + L_{2\sigma}$. It is supposed that all the other parameters are known.

The error vector, i.e., the difference between the estimated and actual flux linkage space vector components, can be defined as

$$\boldsymbol{\varepsilon} = \begin{pmatrix} \varepsilon_\alpha \\ \varepsilon_\beta \end{pmatrix} = \begin{pmatrix} \psi_{2\alpha} - \hat{\psi}_{2\alpha} \\ \psi_{2\beta} - \hat{\psi}_{2\beta} \end{pmatrix}, \tag{21}$$

and its time derivative as

$$\dot{\boldsymbol{\varepsilon}} = \frac{\mathrm{d}}{\mathrm{d}t}\begin{pmatrix} \varepsilon_\alpha \\ \varepsilon_\beta \end{pmatrix} = \frac{\mathrm{d}}{\mathrm{d}t}\begin{pmatrix} \psi_{2\alpha} - \hat{\psi}_{2\alpha} \\ \psi_{2\beta} - \hat{\psi}_{2\beta} \end{pmatrix}. \tag{22}$$

By resolving (20) and (10) into their real and imaginary parts, respectively, and substituting the result into (22), one can obtain the error dynamics in the form

$$\dot{\boldsymbol{\varepsilon}} = \mathbf{H}\boldsymbol{\varepsilon} - \mathbf{W}, \tag{23}$$

where

$$\mathbf{H} = \begin{pmatrix} -\frac{R_2}{L_2} & -\omega \\ \omega & -\frac{R_2}{L_2} \end{pmatrix}, \tag{24}$$

$$\mathbf{W} = \begin{pmatrix} \frac{\Delta L_\mathrm{m}R_2}{\hat{L}_2L_2} & 0 & \frac{\Delta L_\mathrm{m}R_2L_{2\sigma}}{\hat{L}_2L_2} & 0 \\ 0 & \frac{\Delta L_\mathrm{m}R_2}{\hat{L}_2L_2} & 0 & \frac{\Delta L_\mathrm{m}L_{2\sigma}R_2}{\hat{L}_2L_2} \end{pmatrix} \times \begin{pmatrix} \hat{\psi}_{2\alpha} \\ \hat{\psi}_{2\beta} \\ i'_{1\alpha} \\ i'_{1\beta} \end{pmatrix}, \tag{25}$$

and where $\Delta L_\mathrm{m} = L_\mathrm{m} - \hat{L}_\mathrm{m}$.

Now, let us consider the Lyapunov function candidate [16], [32]

$$V = \boldsymbol{\varepsilon}^\mathrm{T}\boldsymbol{\varepsilon} + \frac{\Delta L_\mathrm{m}^2}{\delta}, \tag{26}$$

and its time derivative

$$\dot{V} = \boldsymbol{\varepsilon}^\mathrm{T}\left(\mathbf{H}^\mathrm{T}+\mathbf{H}\right)\boldsymbol{\varepsilon} - \boldsymbol{\varepsilon}^\mathrm{T}\mathbf{W} - \mathbf{W}^\mathrm{T}\boldsymbol{\varepsilon} - \frac{2\Delta L_\mathrm{m}}{\delta}\frac{\mathrm{d}\hat{L}_\mathrm{m}}{\mathrm{d}t}, \tag{27}$$

where δ is a positive parameter.

By expanding the term containing the matrix $\mathbf{H}$, it can be verified that it is non-positive, i.e.,

$$\boldsymbol{\varepsilon}^\mathrm{T}\left(\mathbf{H}^\mathrm{T}+\mathbf{H}\right)\boldsymbol{\varepsilon} = -\frac{2R_2}{L_2}\left(\varepsilon_\alpha^2 + \varepsilon_\beta^2\right) \leq 0. \tag{28}$$

The sufficient condition for the stability is that the remaining term at least satisfy the condition [16], [32]

$$-\boldsymbol{\varepsilon}^\mathrm{T}\mathbf{W} - \mathbf{W}^\mathrm{T}\boldsymbol{\varepsilon} - \frac{2\Delta L_\mathrm{m}}{\delta}\frac{\mathrm{d}\hat{L}_\mathrm{m}}{\mathrm{d}t} = 0. \tag{29}$$

Substituting (24) and (25) into (29), the inductance estimate time derivative can be expressed as

$$\frac{\mathrm{d}\hat{L}_\mathrm{m}}{\mathrm{d}t} = \frac{\delta R_2}{\hat{L}_2L_2}\left[\varepsilon_\alpha\left(\hat{\psi}_{2\alpha}+L_{2\sigma}i'_{1\alpha}\right) + \varepsilon_\beta\left(\hat{\psi}_{2\beta}+L_{2\sigma}i'_{1\beta}\right)\right]. \tag{30}$$

Out of (30), the adaptation law in the form of an I controller directly follows. In practice, a PI controller is used for better dynamic performance [19], [32]. The resulting magnetizing inductance MRAS-type estimator can be written as

$$\hat{L}_\mathrm{m} = K_{\mathrm{P}\psi}\varepsilon_\psi^{\alpha\beta} + K_{\mathrm{I}\psi}\int_0^t \varepsilon_\psi^{\alpha\beta}\mathrm{d}\tau + L_{\mathrm{m(init)}}, \tag{31}$$

where $L_{\mathrm{m(init)}}$ is the initial magnetizing inductance value and

$$\varepsilon_\psi^{\alpha\beta} = \varepsilon_\alpha\left(\hat{\psi}_{2\alpha}+L_{2\sigma}i'_{1\alpha}\right) + \varepsilon_\beta\left(\hat{\psi}_{2\beta}+L_{2\sigma}i'_{1\beta}\right). \tag{32}$$

Due to the low sensitivity to magnetizing inductance variation, the voltage model (equations (14) and (15)) is selected as the reference model, and the current model (equation (20)) is selected as the adaptive model. The block diagram of the proposed estimator is depicted in Fig. 3.

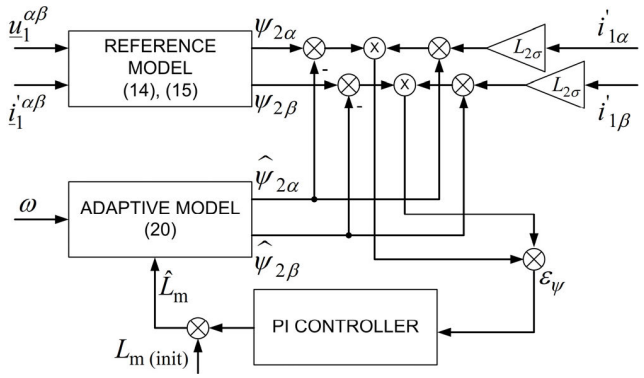

FIGURE 3. MRAS for magnetizing inductance estimation with the included effect of iron losses.

B. SMALL SIGNAL ANALYSIS

The stability with respect to the adaptive controller gain constants can be investigated using the linearization approach, which permits the system analysis via transfer functions [33]. For this purpose, a state-space model with the rotor flux linkage space vector and stator current space vector components is utilized. However, to obtain mathematically reasonable expressions, several simplifications and modifications must be adopted, namely:

- For the small-signal analysis, the equations must be transformed to a rotor flux-attached dq reference frame [33].
- Initially, the perfect flux orientation (zero q axis component) is considered for both the reference and adaptive model.
- The rotor flux linkage vector components from the adaptive model are considered ideal and constant.
- The analysis neglects iron losses since the state-space models with iron losses are mathematically more complicated.
- The influence of the dynamic inductances in the state-space model is neglected.

The full-order IM state-space model is considered in the form [18]

$$\dot{\mathbf{x}} = \mathbf{A}\mathbf{x} + \mathbf{B}\mathbf{u}, \tag{33}$$

$$\mathbf{y} = \mathbf{C}\mathbf{x}, \tag{34}$$

where

$$\mathbf{A} = \begin{pmatrix} a_1 & \omega_\mathrm{s} & a_2 & a_3\omega \\ -\omega_\mathrm{sl} & a_1 & -a_3\omega & a_2 \\ a_4 & 0 & a_5 & \omega_\mathrm{sl} \\ 0 & a_4 & -\omega_\mathrm{sl} & a_5 \end{pmatrix}, \tag{35}$$

$$\mathbf{B} = \begin{pmatrix} 0 & \frac{1}{L_1\sigma} & 0 & 0 \\ \frac{1}{L_1\sigma} & 0 & 0 & 0 \end{pmatrix}^\mathrm{T}, \tag{36}$$

$$\mathbf{C} = \begin{pmatrix} 1 & 0 & 0 & 0 \\ 0 & 1 & 0 & 0 \end{pmatrix}, \tag{37}$$

$$\mathbf{x} = \begin{pmatrix} i_{1d} & i_{1q} & \psi_{2d} & \psi_{2q} \end{pmatrix}^\mathrm{T}, \tag{38}$$

$$\mathbf{u} = \begin{pmatrix} u_{1d} & u_{1q} \end{pmatrix}^\mathrm{T}, \tag{39}$$

$$\mathbf{y} = \begin{pmatrix} i_{1d} & i_{1q} \end{pmatrix}^\mathrm{T}, \tag{40}$$

and where $a_1 = -\left(R_1L_2^2 + L_\mathrm{m}^2R_2\right)/(\sigma L_1L_2^2)$, $a_2 = (L_\mathrm{m}R_2)/(\sigma L_1L_2^2)$, $a_3 = L_\mathrm{m}/(\sigma L_1L_2)$, $a_4 = (L_\mathrm{m}R_2)/L_2$, $a_5 = -R_2/L_2$, and ω_s is the synchronous speed.

Linearizing (33) and (34) around the operating point $\mathbf{x}_0 = \begin{pmatrix} i_{1d0} & i_{1q0} & \psi_{2d0} & \psi_{2q0} \end{pmatrix}^\mathrm{T}$ and L_m0 yields

$$\Delta\dot{\mathbf{x}} = \Delta\mathbf{A}_\mathrm{L}\mathbf{x}_0 + \mathbf{A}\Delta\mathbf{x} + \Delta\mathbf{B}_\mathrm{L}\mathbf{u}, \tag{41}$$

$$\Delta\mathbf{y} = \mathbf{C}\Delta\mathbf{x}, \tag{42}$$

where $\Delta\mathbf{x} = x - \mathbf{x}_0$ and

$$\Delta\mathbf{A}_\mathrm{L} = \left(\frac{\partial}{\partial L_\mathrm{m}}\mathbf{A}\right)\Delta L_\mathrm{m}, \tag{43}$$

$$\Delta\mathbf{B}_\mathrm{L} = \left(\frac{\partial}{\partial L_\mathrm{m}}\mathbf{B}\right)\Delta L_\mathrm{m}, \tag{44}$$

where $\Delta L_\mathrm{m} = L_\mathrm{m} - L_\mathrm{m0}$. After performing Laplace transform, (42) can be rewritten with the help of (41) as

$$\Delta\mathbf{y} = \begin{pmatrix} \Delta i_{1d} \\ \Delta i_{1q} \end{pmatrix} = \mathbf{C}\left(s\mathbf{I} - \mathbf{A}\right)^{-1}\left(\Delta\mathbf{A}_\mathrm{L}\mathbf{x}_0 + \Delta\mathbf{B}_\mathrm{L}\mathbf{u}\right), \tag{45}$$

where s is the Laplace operator, $\Delta i_{1d} = i_{1d} - i_{1d0}$, $\Delta i_{1q} = i_{1q} - i_{1q0}$, and $\mathbf{I}$ is the identity matrix. Equation (45) can be utilized to obtain the expressions for Δi_{1d} and Δi_{1q} (used further in the section).

The error equation (32) with neglected iron losses transformed into dq reference frame takes the form

$$\varepsilon_\psi^{dq} = \varepsilon_d\left(\hat{\psi}_{2d} + L_{2\sigma}i_{1d}\right) + \varepsilon_q\left(\hat{\psi}_{2q} + L_{2\sigma}i_{1q}\right). \tag{46}$$

Now, (46) must be linearized around an operating point $\hat{\psi}_{2d0}$, $\hat{\psi}_{2q0}$, ψ_{2d0}, ψ_{2q0}, i_{1d0}, i_{1q0}. Under the above assumptions it follows that $\hat{\psi}_{2d0} = \psi_{2d0} = \psi_{2d}$, $\hat{\psi}_{2q0} = \psi_{2q0} = \psi_{2q} = 0$. The linearized error equation can be then expressed as

$$\Delta\varepsilon_\psi^{dq} = -\left(L_{2\sigma}i_{1d0} + \hat{\psi}_{2d0}\right)\Delta\hat{\psi}_{2d}, \tag{47}$$

where $\Delta\hat{\psi}_{2d} = \hat{\psi}_{2d} - \hat{\psi}_{2d0}$.

Transforming the current model (9) into the dq reference frame, neglecting the iron losses, and using the slip speed equation (12), the model now becomes

$$\frac{\mathrm{d}\underline{\psi}_2^{dq}}{\mathrm{d}t} = \frac{L_\mathrm{m}R_2}{L_2}\underline{i}_1^{dq} - \frac{R_2}{L_2}\underline{\psi}_2^{dq} - \mathrm{j}\frac{L_\mathrm{m}R_2}{L_2}\frac{i_{1q}}{\psi_{2d}}\underline{\psi}_2^{dq}. \tag{48}$$

Linearizing (48) around the operating point $\hat{\psi}_{2d0}$, $\hat{\psi}_{2q0}$, i_{1d0}, i_{1q0}, and L_m0, separating the result into the real and imaginary part, respectively, and performing the Laplace transform, (48) can be rewritten as

$$\Delta\hat{\psi}_{2d}s = \frac{R_2L_\mathrm{m0}}{L_{20}}\Delta i_{1d} - \frac{R_2}{L_{20}}\Delta\hat{\psi}_{2d} + \frac{L_\mathrm{m0}R_2i_{1q0}}{L_{20}\psi_{2d0}}\Delta\hat{\psi}_{2q} + \frac{R_2\left(L_{2\sigma}i_{1d0} + \hat{\psi}_{2d0}\right)}{L_{20}^2}\Delta L_\mathrm{m}, \tag{49}$$

$$\Delta\hat{\psi}_{2q}s = -\frac{R_2}{L_{20}}\Delta\hat{\psi}_{2q}, \tag{50}$$

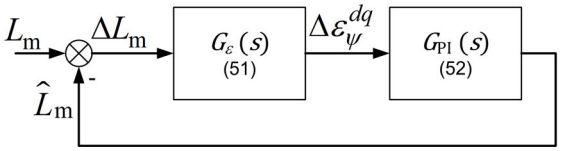

FIGURE 4. A block diagram of the linearized Lm-MRAS.

where $L_{20} = L_{m0} + L_{2\sigma}$. The error transfer function can be written as

$$G_\varepsilon(s) = -\frac{\Delta\varepsilon_\psi^{dq}}{\Delta L_m} = \left(L_{2\sigma} i_{1d0} + \hat{\psi}_{2d0}\right) \frac{\Delta\hat{\psi}_{2d}}{\Delta L_m}. \quad (51)$$

Resolving $\Delta\hat{\psi}_{2d}$ out of (49) and (50), substituting the result into (51) and also using (45) to substitute for the newly formed expression $\Delta i_{1d}/\Delta L_m$, the final error transfer function can be obtained. Due to its complexity, this equation is not explicitly stated in the paper.

The adaptive PI controller transfer function is considered in the form

$$G_{PI}(s) = K_{P\psi} + \frac{K_{I\psi}}{s}. \quad (52)$$

Therefore, the closed-loop transfer function of the whole estimator can be written as

$$G_C(s) = \frac{G_{PI}(s)\, G_\varepsilon(s)}{1 + G_{PI}(s)\, G_\varepsilon(s)}. \quad (53)$$

The block diagram of the linearized estimator is depicted in Fig. 4. Fig. 5 and Fig. 6 show the root locus of (53) for nominal parameters, nominal excitation, and a nominal load of the IM utilized in the simulations and experiments (nameplate values and model parameters given in Table 1). Fig. 5 for the case when $K_{P\psi} = 1$ and $K_{I\psi}$ changes within $\langle 0, 300\rangle$, and Fig. 6 for the case when $K_P = 0$ and K_I changes again within $\langle 0, 300\rangle$. In all these cases, the estimator remains stable.

Furthermore, (53) can also be used for the design of the adaptive controller gain constants. However, given the number of adopted simplifications and the fact that linearization is valid only around a specific operating point, the obtained results should be considered only as starting values that must be carefully adjusted.

C. SENSITIVITY TO ROTOR RESISTANCE VARIATION

Unfortunately, the proposed Lm-MRAS is sensitive to the rotor resistance variation. The sensitivity function can be obtained using a similar procedure to the one described in the previous section.

According to Fig. 4, the expression for ΔL_m can be obtained as

$$\Delta L_m = -\left(K_{P\psi} + \frac{K_{I\psi}}{s}\right) \Delta\varepsilon_\psi^{dq}. \quad (54)$$

The sensitivity function can be then expressed as

$$\frac{\Delta L_m}{\Delta R_2} = \left(K_{P\psi} + \frac{K_{I\psi}}{s}\right) \left(L_{2\sigma} i_{1d0} + \hat{\psi}_{2d0}\right) \frac{\Delta\hat{\psi}_{2d}}{\Delta R_2}. \quad (55)$$

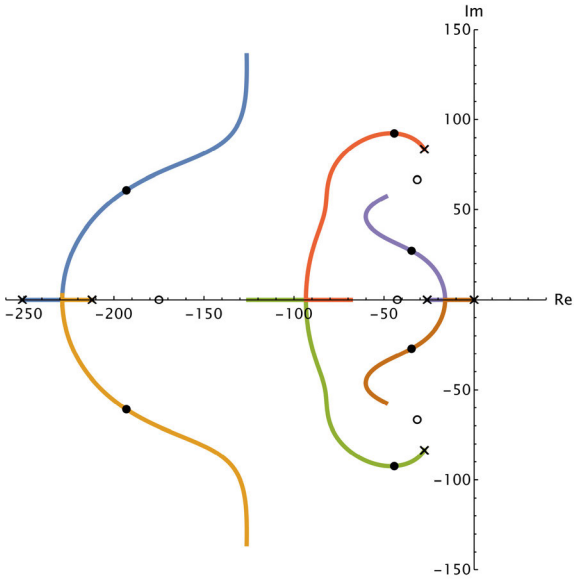

FIGURE 5. Root locus of the linearized L_m MRAS-type estimator, $K_{P\psi} = 1$ and $K_{I\psi}$ changes from 0 to 300; nominal excitation and speed, half of the nominal load torque. Crosses, dots, and circles represent the roots for the starting value, value in the middle of the interval, and value in infinity, respectively.

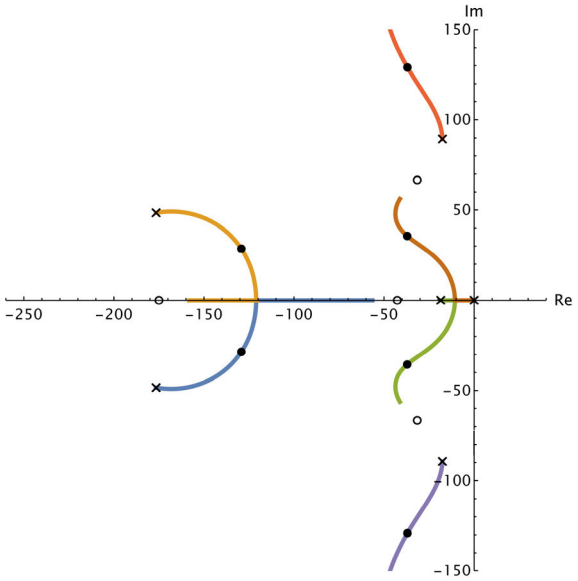

FIGURE 6. Root locus of the linearized L_m MRAS-type estimator, $K_{P\psi} = 0$ and $K_{I\psi}$ changes from 0 to 300; nominal excitation and speed, half of the nominal load torque. Crosses, dots, and circles represent the roots for the starting value, value in the middle of the interval, and value in infinity, respectively.

Using (48), the expressions for $\Delta\hat{\psi}_{2d}$ can be obtained similarly as in the previous section. However, this time the linearization is performed around the operating point $\hat{\psi}_{2d0}$, $\hat{\psi}_{2q0}$, i_{1d0}, i_{1q0}, L_{m0}, and R_{20}. To substitute for the newly formed expression $\Delta i_{1d}/\Delta R_2$, state-space model (33) and (34) is linearized around the operating point $\mathbf{x}_0 = \left(i_{1d0}\ i_{1q0}\ \psi_{2d0}\ \psi_{2q0}\right)^T$ and R_{20}. The resulting expression for

the output vector is

$$\Delta \mathbf{y} = \begin{pmatrix} \Delta i_{1d} \\ \Delta i_{1q} \end{pmatrix} = \mathbf{C}\left(s\mathbf{I} - \mathbf{A}\right)^{-1} \mathbf{\Delta A}_{\mathrm{R}} \mathbf{x}_0, \tag{56}$$

where

$$\mathbf{\Delta A}_{\mathrm{R}} = \left(\frac{\partial}{\partial R_2}\mathbf{A}\right) \Delta R_2. \tag{57}$$

After these operations, the resulting sensitivity function can be obtained. Fig. 7 shows the step response of the sensitivity function to the 10 % decrease in the rotor resistance. The PI controller parameters are selected as $K_{\mathrm{P}\psi} = 0.01$ and $K_{\mathrm{I}\psi} = 1$. Nominal excitation, speed, and load torque are considered.

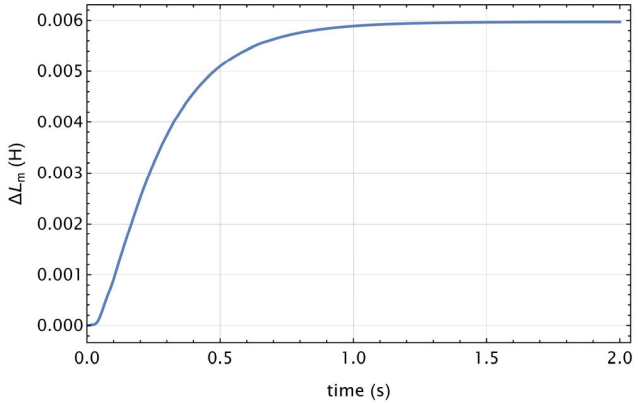

FIGURE 7. Step response of the rotor resistance sensitivity function to 10% decrease in the rotor resistance, $K_{P\psi} = 0.01$ and $K_{I\psi} = 1$. Nominal excitation, speed, and load torque.

IV. MEASUREMENT, MODELLING, AND COMPENSATION OF IRON LOSSES

Considering arbitrary reference frame, the equivalent iron loss current can be expressed according to Fig. 1 as

$$\underline{i}^{k}_{\mathrm{Fe}} = \frac{\underline{u}^{k}_{\mathrm{m}}}{R_{\mathrm{Fe}}}, \tag{58}$$

where $\underline{u}^{k}_{\mathrm{m}}$ is the voltage across the magnetizing (parallel) branch.

Considering Clarke's transformation constant equal to 2/3, the power dissipated in the iron core is given by

$$P_{\mathrm{Fe}} = \frac{3}{2}\Re\left\{\underline{u}^{k}_{\mathrm{m}}\bar{\underline{i}}^{k}_{\mathrm{Fe}}\right\}, \tag{59}$$

where $\bar{\underline{i}}^{k}_{\mathrm{Fe}}$ denotes the complex conjugate of the equivalent iron loss current. Substituting (58) into (59), the iron loss resistance can be expressed as

$$R_{\mathrm{Fe}} = \frac{3}{2}\frac{u^2_{\mathrm{m}}}{P_{\mathrm{Fe}}}. \tag{60}$$

Substituting (60) into (58) and considering the stationary reference, the iron loss current is obtained as

$$\underline{i}^{\alpha\beta}_{\mathrm{Fe}} = \frac{2}{3}P_{\mathrm{Fe}}\frac{\underline{u}^{\alpha\beta}_{\mathrm{m}}}{u^2_{\mathrm{m}}}. \tag{61}$$

The voltage across the magnetizing branch can be expressed in case of a steady-state operation and sinusoidal supply as

$$\underline{u}^{\alpha\beta}_{\mathrm{m}} = \underline{u}^{\alpha\beta}_{1} - R_1\underline{i}^{\alpha\beta}_{1} - \mathrm{j}\omega_{\mathrm{s}}L_{1\sigma}\underline{i}^{\alpha\beta}_{1}. \tag{62}$$

The measurement of iron losses and their implementation into the control algorithm will be discussed in the next section.

A. MEASUREMENT AND MODEL FITTING

The iron losses can be obtained by a series of no-load tests at various fundamental supply frequencies. The separation procedure based on the IEC standard can then be used for the loss calculation [34]. For the measurement, the inverter is programmed to generate a fundamental voltage at a given frequency and magnitude that corresponds to the reference stator flux linkage vector magnitude (obtained from the voltage model).

Out of the measured input power P_{in}, the iron losses are calculated as

$$P_{\mathrm{Fe}} = P_{\mathrm{c}} - P_{\mathrm{fw}}, \tag{63}$$

where P_{c} are the constant losses defined as

$$P_{\mathrm{c}} = P_0 - P_{\mathrm{s},0}, \tag{64}$$

where P_0 is the fundamental component of the input no-load power, $P_{\mathrm{s},0}$ are the stator copper losses calculated from the known value of the stator resistance and measured RMS current, and P_{fw} are the friction and windage losses, i.e., the mechanical losses.

The mechanical losses are calculated from four or more constant loss points between 30 % and 60 % of the rated motor stator flux by developing a curve against no-load voltage squared and then performing linear extrapolation to zero voltage [34]. The intersection of the extrapolation line with the vertical axis then corresponds to the mechanical losses.

For the iron loss modeling, the following analytical function is adopted [7]

$$P_{\mathrm{Fe}} = \frac{f_{\mathrm{s}}^2\psi_1^2 + \kappa f_{\mathrm{s}}\psi_1^n}{R_{\mathrm{Fe0}}}, \tag{65}$$

where f_{s} is the fundamental supply frequency and κ, n and R_{Fe0} are the model parameters. The measured iron losses are then fitted to the model using Wolfram Mathematica's command *NMinimize* with the *RandomSearch* option. The minimization is performed on a sum of squares of the error. The fitted dependence of the iron losses on the stator flux linkage vector magnitude and fundamental supply frequency is depicted in Fig. 8. The found model parameters are presented in the figure caption.

The iron losses are also a function of the slip [9]. If more precise results are required, an appropriate model considering the slip dependence can be used.

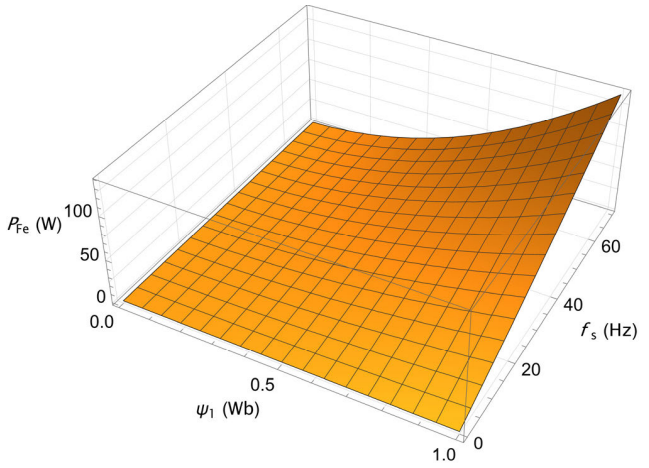

FIGURE 8. Iron losses as a function of fundamental supply frequency and stator flux linkage vector amplitude. The fitted model parameters are $R_{Fe0} = 277$, $\kappa = 460$, $n = 1.77$.

B. REAL-TIME COMPENSATION

In the control algorithm, the iron losses are calculated based on the estimated synchronous frequency and stator flux linkage vector amplitude. The synchronous frequency is obtained using the measured rotor speed and estimated slip speed (equation (12)), and the stator flux amplitude is calculated using the voltage model (equation (15)).

The resulting block diagram of the proposed FOC is depicted in Fig. 9.

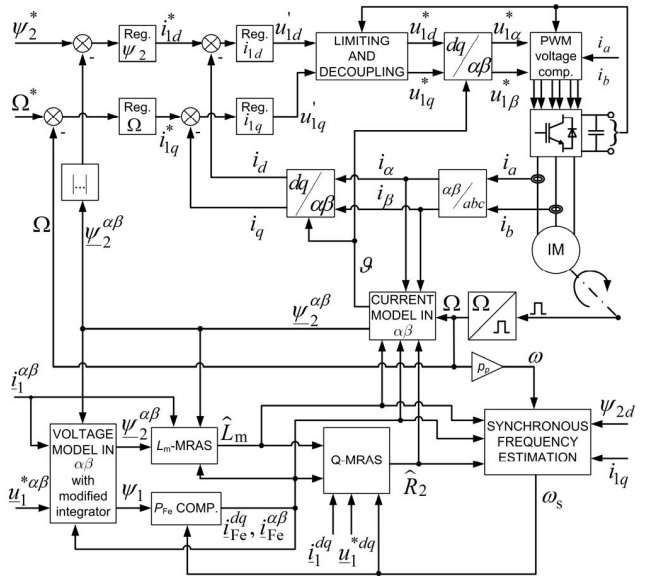

FIGURE 9. Block diagram of the proposed field-oriented control with the iron losses, magnetizing inductance, and rotor resistance compensation.

V. SELECTED IMPLEMENTATION ISSUES

A few problems arise during the practical implementation of the FOC along with the presented estimation algorithms. The two most important ones – DC offset accumulation problem during pure integration and inverter voltage distortion will be discussed in the following sections.

A. VOLTAGE MODEL – DC OFFSET ACCUMULATION IN CASE OF PURE INTEGRATION

First, it is not possible to use a pure integrator for the voltage model (eq. (15)) evaluation because of the unknown initial conditions and DC offset accumulation problem [35]. However, an advanced modified integrator based on the current model depicted in Fig. 10 can be used since the current model is also implemented in the control algorithm. The main drawback of this type of integrator is that it utilizes another PI controller, for which no satisfactory gain design method has been proposed yet. Therefore, before drive commissioning, the controller should be tuned adequately in the simulation model.

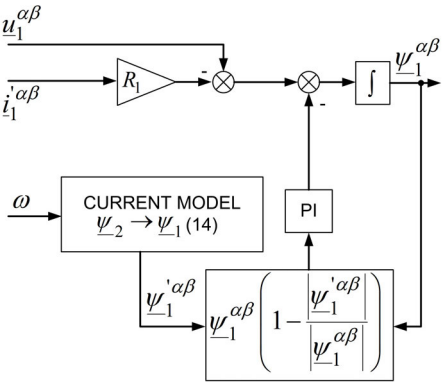

FIGURE 10. Current model-based modified integrator with the DC offset elimination.

B. INVERTER OUTPUT VOLTAGE DISTORTION

Another major issue that impairs the performance of all the advanced AC drive control strategies, if not accounted for, is the distortion of the inverter output voltage [36]. The primary sources of the voltage distortion are the inserted dead-time and the delayed load current-dependent transistor switching. It is assumed that the most common space-vector modulation (SVM) with a constant switching period T_{PWM} is used. The resulting effective dead-time that needs to be compensated is defined as [37]

$$T_{eff}(i_x) = T_{dt} + T_{on}(i_x) - T_{off}(i_x) \quad x = a, b, c, \quad (66)$$

where T_{dt} is the dead-time inserted by the microcontroller or driver, $T_{on}(i_x)$ is the current-dependent turn-on delay, $T_{off}(i_x)$ is the current-dependent turn-off delay and symbols a, b, c denote the respective inverter leg.

The compensation characteristics in the form of the dependence of the so-called effective dead-time on the load current can be easily determined by direct measurement [37]. In the control algorithm, a look-up table can be used for the effective

dead-time compensation, or it is possible to fit the measured data using the function

$$T_{\text{eff}}(i_x) = \frac{m}{k_1 |i_x| + k_2} + n, \tag{67}$$

where k_1, k_2, m, n are parameters to be determined.

The most convenient way is to compensate the output duty-cycle from the modulator [37]. Within SVM, the duty-cycle d_x for each VSI leg is defined in such a way that the average value of the corresponding inverter line-to-neutral voltage u_{x0} per modulation period with respect to given DC-link voltage U_{DC} equals to $-U_{\text{DC}}/2$ if $d_x = 0$ and $+U_{\text{DC}}/2$ if $d_x = 1$. The relation between the reference d_x^* and the compensated duty cycle d_x' then takes the following form [37]

$$d_x' = d_x^* + \frac{T_{\text{eff}(x)}}{T_{\text{PWM}}} \text{sgn}(i_x) \quad x = a, b, c. \tag{68}$$

VI. Q-MRAS FOR ROTOR RESISTANCE ESTIMATION, LOAD-DEPENDENT SATURATION

As mentioned in the Introduction, the IM magnetizing inductance may also depend on the load. Theoretically, the proposed Lm-MRAS with included iron losses should be capable of estimating this type of saturation. However, as shown in section III. C., another parameter that affects the accuracy of the current model and, consequently, the performance of the RFOC during the load conditions is the rotor resistance. Therefore, rotor resistance adaptation could improve the identification process. For this purpose, the traditional and widely used reactive power MRAS (Q-MRAS) can be utilized. In this paper, this type of estimator will be augmented to include the iron loss effect to improve the estimation accuracy further.

The reference model is given by [19]

$$Q = \Im \left\{ \underline{u}_1^{dq} \underline{\bar{i}}_1^{dq} \right\} = u_{1q} i_{1d} - u_{1d} i_{1q}, \tag{69}$$

where $\underline{\bar{i}}_1^{dq}$ denotes the conjugated current space vector. Using (14) transformed into dq reference frame, the stator flux linkage vector can be obtained as

$$\underline{\psi}_1^{dq} = \frac{L_{\text{m}}}{L_2} \underline{\psi}_2^{dq} + L_1 \sigma \underline{i}_1^{dq} - \frac{L_{2\sigma} L_{\text{m}}}{L_2} \underline{i}_{\text{Fe}}^{dq}. \tag{70}$$

The stator voltage equation in the dq reference frame can be written as

$$\underline{u}_1^{dq} = R_1 \underline{i}_1^{dq} + \frac{\text{d}\underline{\psi}_1^{dq}}{\text{d}t} + \text{j}\omega_{\text{s}} \underline{\psi}_1^{dq}. \tag{71}$$

By substituting (70) into (71) and considering the steady-state operation, we obtain

$$\underline{u}_1^{dq} = R_1 \underline{i}_1^{dq} + \text{j}\omega_s \left(\frac{L_{\text{m}}}{L_2} \underline{\psi}_2^{dq} + L_1 \sigma \underline{i}_1^{dq} - \frac{L_{2\sigma} L_{\text{m}}}{L_2} \underline{i}_{\text{Fe}}^{dq} \right). \tag{72}$$

Separating (72) into the real and imaginary parts, respectively, while considering that $\psi_{2d} = L_{\text{m}}(i_{1d} - i_{\text{Fe}d})$ and $\psi_{2q} = 0$, the adaptive model is finally obtained as

$$\hat{Q} = \omega_{\text{s}} \Big[L_1 \sigma \left(i_{1d}^2 + i_{1q}^2 \right) + \frac{L_{\text{m}}}{L_2} \left(L_{\text{m}} i_{1d}^2 - L_2 i_{\text{Fe}d} i_{1d} - L_{2\sigma} i_{\text{Fe}q} i_{1q} \right) \Big]. \tag{73}$$

The synchronous speed is obtained as the sum of the measured speed and estimated slip speed.

The error for the rotor resistance adaptation mechanism is calculated as

$$\varepsilon_Q = Q - \hat{Q}. \tag{74}$$

The estimated rotor resistance is then the output of the PI controller, i.e.,

$$\hat{R}_2 = K_{\text{p}Q} \varepsilon_Q + K_{\text{i}Q} \int_0^t \varepsilon_Q \text{d}\tau + R_{2(\text{init})}, \tag{75}$$

where $R_{2(\text{init})}$ is the initial rotor resistance. The block diagram of the Q-MRAS estimator with included iron loss effect is presented in Fig. 11.

The stability analysis of the parallel operation of the Lm-MRAS and Q-MRAS represents a complex task. Generally, no satisfactory approach to investigating multiple simultaneous MRAS-type estimators' stability within FOC has been proposed yet. The analysis is usually omitted or greatly simplified [17].

VII. SIMULATION RESULTS

The simulation model was built in MATLAB/Simulink version 2021a. The simulated machine nameplate values and nominal model parameters are given in Table 1. The block diagram of the control algorithm agrees with Fig. 9. The selected model solver is *ode4* with a fixed-step size equal to 5 μs. The machine is modeled using the full-order state-space model with the iron loss effect presented in section II. A. The iron losses are calculated using (65) fitted to the measured data.

To eliminate the effect of numerical errors and the effect of the pulse voltage (i.e., the effect of the inverter) on the estimator accuracy, the model of FOC is implemented using the same solver and fixed-step size as in the case of the IM model. The stator flux linkage vector magnitude and the slip speed for the iron loss compensation (utilizing (65) again) are calculated using the voltage model (15) and the slip speed equation (12), respectively.

To assess the functionality of the proposed estimator, the following sequence is simulated:

- The magnetizing inductance in the FOC model is set to 110 % of the nominal value. All other parameters are exact.
- The reference flux is set to the nominal value.
- The machine is started at 0.1 s to half of the nominal speed. The reference speed is increased to the nominal value at 4 s.

- Magnetizing inductance compensation is turned on at 1 s.
- Initially, the machine is unloaded. The load is increased to half of the nominal torque and nominal torque at 2 s and 3 s, respectively. Furthermore, the load is decreased to half of the nominal torque and zero torque at 5 s and 6 s, respectively.

The time sequence of the step changes of the reference speed and torque is depicted in Fig. 12. The Lm-MRAS PI controller proportional and integral gains are set to 0.01 and 1, respectively. The resulting magnetizing inductance estimates are depicted in Fig. 13 and Fig. 14. In Fig. 13, the iron losses are compensated, and in Fig. 14, the compensation is inactive.

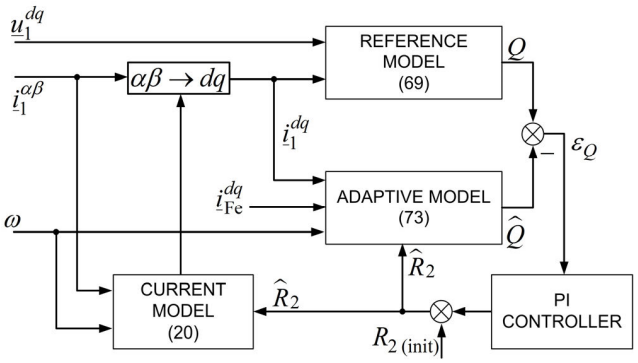

FIGURE 11. Modified reactive power MRAS for rotor resistance estimation.

TABLE 1. Induction machine nameplate data and nominal model parameters.

Nameplate Data		Model Parameters	
Nominal power	3.6 kW	Stator resistance	1.688 Ω
Nominal voltage	380 V	Rotor Resistance	3.685 Ω
Nominal current	11.5 A	Stator leakage inductance	0.0139 H
Nominal speed	935 min^{-1}	Rotor leakage inductance	0.0139 H
Number of poles	6	Magnetizing inductance	0.175 H
Winding connection	Y	Iron core resistance	520 Ω

In the iron loss compensation case, the estimated inductance converges to the actual value and is almost unaffected by the speed and torque change. However, if the iron losses are not compensated, the estimated inductance differs from the actual value. The difference is the lowest during the no-load conditions and further increases with the load. This confirms the results of earlier works where it was found that the error in rotor flux can have an increasing tendency with respect to the load then reach a maximum value to start further descending with increasing load [10].

Another simulation sequence was designed to test the ability of the estimator to track the change of the magnetizing inductance with the load:

- The magnetizing inductance in the FOC model is set to 110 % of the nominal value to simulate the parameter detuning. All other parameters are exact.
- The reference flux is set to the nominal value.
- The machine is started at 0.1 s to the nominal speed.
- Magnetizing inductance compensation is turned on at 1 s.
- At 2 s, the load torque starts to increase from zero to half of the nominal value linearly.
- The magnetizing inductance inside the IM model is modeled to decrease with the torque (also linearly).

The integral gain of the estimator is increased five times for better tracking performance which causes an overshoot at the beginning of the estimation process. The results are depicted in Fig. 14 and Fig. 16. In Fig. 15, the iron losses are compensated, and in Fig. 16, the compensation is inactive. In the case of the compensated iron losses, the estimator can track the change of the magnetizing inductance with the load almost perfectly. However, if the iron losses are not compensated, the estimator is able to monitor the monotonically decreasing trend, but the estimated value differs from the actual one. The difference is then increasing as the function of the increased torque.

The third simulation sequence tested the performance of the parallel operation of Q-MRAS and Lm-MRAS.

- The FOC model's magnetizing inductance and rotor resistance are set to 110 % and 120 %, respectively, of their nominal values to simulate the parameter detuning. All other parameters are exact.
- The reference flux is set to the nominal value.
- The machine is started at 0.1 s to the nominal speed.
- Half of the nominal load torque is applied at 1 s.
- Magnetizing inductance compensation is turned on at 2 s.
- Rotor resistance compensation is turned on at 4 s.

The Q-MRAS PI controller proportional and integral gains are set to 0.0001 and 0.03, respectively. The resulting magnetizing inductance and rotor resistance estimates are presented in Fig. 17 and Fig. 18. In Fig. 17, the iron losses are compensated, and in Fig. 18, the compensation is inactive. The results show that the rotor resistance detuning significantly influences the Lm-MRAS under load conditions. However, parallel operation with the Q-MRAS ensures that both the magnetizing inductance and rotor resistance are compensated correctly if the improved version with the iron losses is used. Again, the estimates are incorrect if the iron loss compensation is inactive, although both estimators successfully converge.

The last simulation sequence tested Lm-MRAS performance in a regenerative mode and during speed reversal.

- The magnetizing inductance in the FOC model is set to 110 % of the nominal value. All other parameters are exact.
- The reference flux is set to the nominal value.

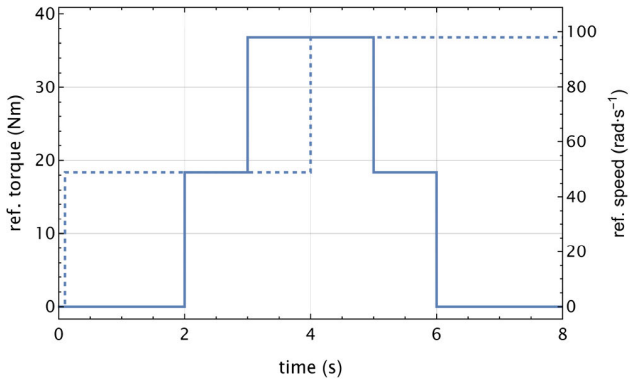

FIGURE 12. The simulated sequence of reference torque (solid) and speed (dashed).

- The machine is started at 0.1 s to the nominal speed. The sign of the reference speed is inverted, i.e., the drive is reversed at 4 s.
- Magnetizing inductance compensation is turned on at 1 s.
- Initially, the machine is unloaded. The load is increased to half of the nominal torque in a regenerative mode at 2 s. The machine is then unloaded at 3 s. At 5 s, the load increases to half of the nominal torque in a regenerative mode and decreases to zero at 5 s. Then, the machine is unloaded, and the load torque is increased to half of the nominal torque in a motoring mode at 7 s.

The time sequence of the step changes of the reference speed and torque is depicted in Fig. 19. The resulting magnetizing inductance estimates are depicted in Fig. 20 and Fig. 21. In Fig. 20, the iron losses are compensated, and in Fig. 21, the compensation is inactive. Overall, the simulation sequence confirms the ability of Lm-MRAS to estimate the magnetizing inductance in a four-quadrant operation of the drive. When the iron losses are compensated, slight variations in the estimated inductance value appear during the speed reversal. The variations during the change of the load are negligible. However, if the iron losses are not accounted for, the variation of the inductance increases, and the estimator operates with an error that depends on the loading of the machine.

VIII. EXPERIMENTAL RESULTS

The proposed Lm-MRAS estimator was also tested experimentally. The whole control algorithm was programmed in C language into Texas Instruments TMS320F28335 digital signal processor with the CPU clock set to 150 MHz. The calculation loop of the FOC is tied to the PWM frequency, which is selected to be 8 kHz. The data were sampled with a 400 μs period. The IM drive was loaded by an 8 kW DC motor supplied from a Siemens SINAMICS DCM converter. The experimental machine setup is depicted in Fig. 22.

For the motor current and DC-link voltage measurements, LEM LF 205-S with four conductor turns and LEM LV25-P,

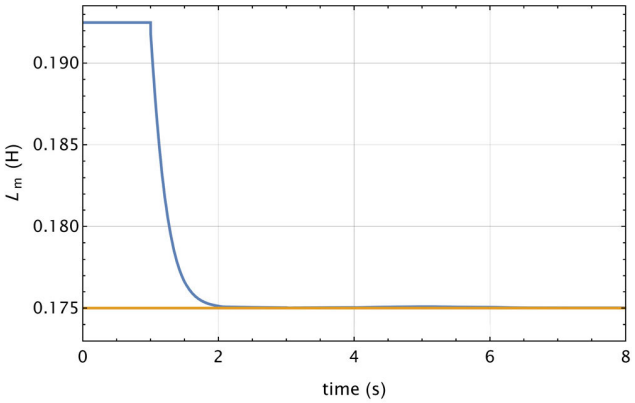

FIGURE 13. Estimated (blue) and actual (orange) magnetizing inductance during the step changes of speed and load; iron losses compensated.

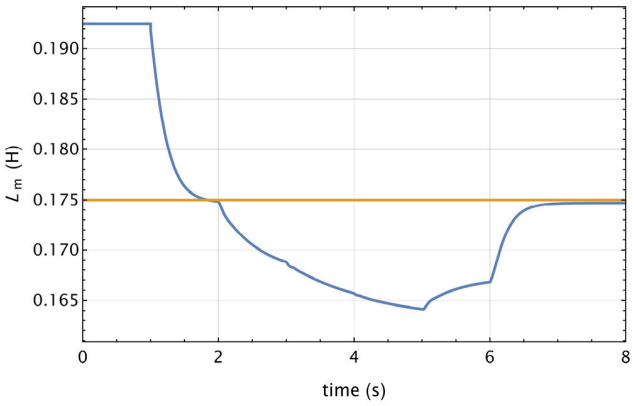

FIGURE 14. Estimated (blue) and actual (orange) magnetizing inductance during the step changes of speed and load; iron losses not compensated.

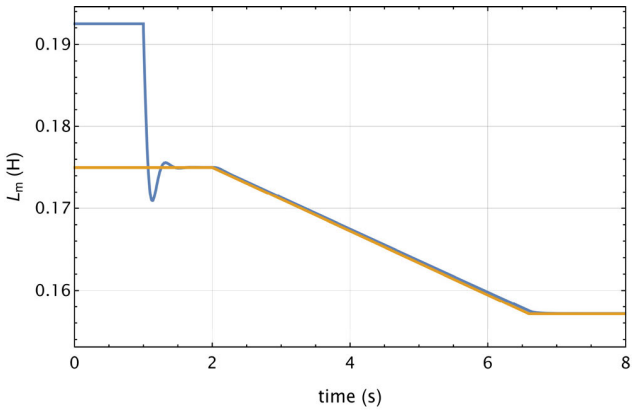

FIGURE 15. Estimated (blue) and actual (orange) magnetizing inductance. The magnetizing inductance in the motor model decreases as a function of torque; iron losses compensated.

respectively, were used along with our custom signal adjustment board. The board performs LEM output scaling via op-amp circuitry. All ADC conversions are synchronized with PWM and regularly triggered with a modulation period of 125 μs. As the machine supply converter, a standard three-phase two-level voltage-source inverter was utilized. The inverter is supplied from a diode rectifier that is connected

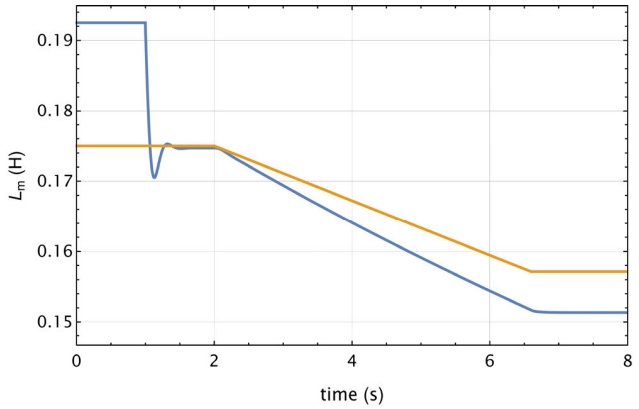

FIGURE 16. Estimated (blue) and actual (orange) magnetizing inductance. The magnetizing inductance in the motor model decreases as a function of torque; iron losses not compensated.

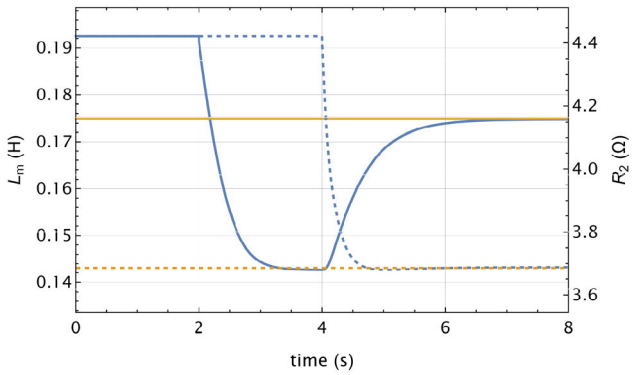

FIGURE 17. Parallel operation of Q-MRAS and Lm-MRAS. Estimated values (blue) and actual values (orange) of the magnetizing inductance (solid) and rotor resistance (dashed). Iron losses compensated. The load is applied at 1 s, Lm-MRAS is started at 2 s, and Q-MRAS is started at 4 s.

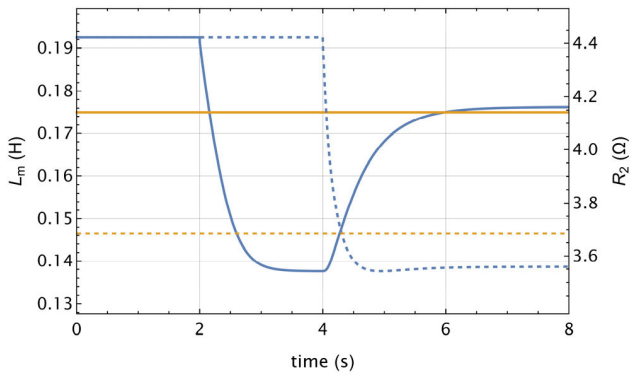

FIGURE 18. Parallel operation of Q-MRAS and Lm-MRAS. Estimated values (blue) and actual values (orange) of the magnetizing inductance (solid) and rotor resistance (dashed). Iron losses are not compensated. The load is applied at 1 s, Lm-MRAS is started at 2 s, and Q-MRAS is started at 4 s.

to a 400 V, 50 Hz AC grid. The rotor speed was measured using a LARM incremental encoder with 2500 pulses per revolution. The encoder output is scaled using the same signal

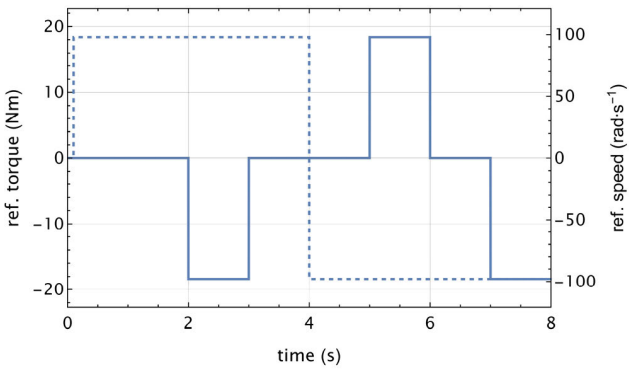

FIGURE 19. The simulated sequence of reference torque (solid) and speed (dashed) for a regenerative mode and speed reversal.

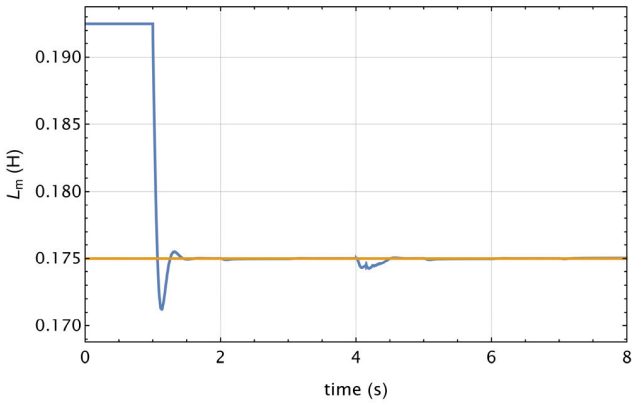

FIGURE 20. Estimated (blue) and actual (orange) magnetizing inductance for a regenerative mode and speed reversal; iron losses compensated.

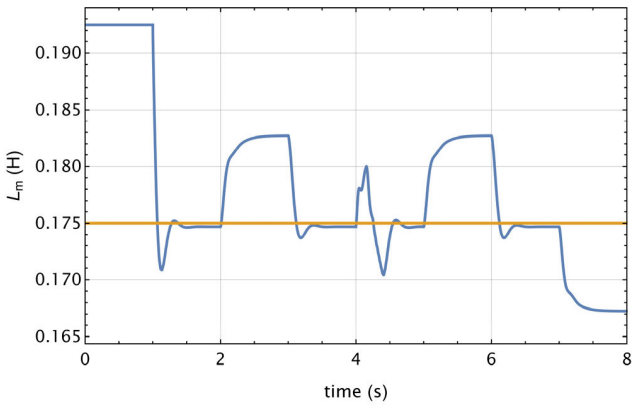

FIGURE 21. Estimated (blue) and actual (orange) magnetizing inductance for a regenerative mode and speed reversal; iron losses not compensated.

adjustment board and processed by the eQEP module of the TMS320F28335 DSP.

First, the no-load magnetizing characteristics in the form of the dependence of the magnetizing flux on the magnetizing current (i.e., $\psi_m = f\ (i_m)$) was measured during a no-load test from a 50 Hz supply with variable voltage amplitude. Because the utilized IM is a slip-ring type, the rotor winding was left open to rule out the influence of the rotor branch entirely.

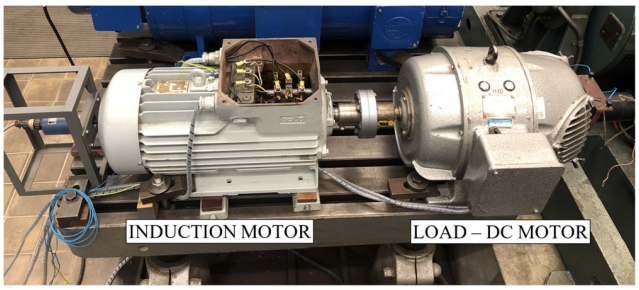

FIGURE 22. The tested induction motor and loading DC motor.

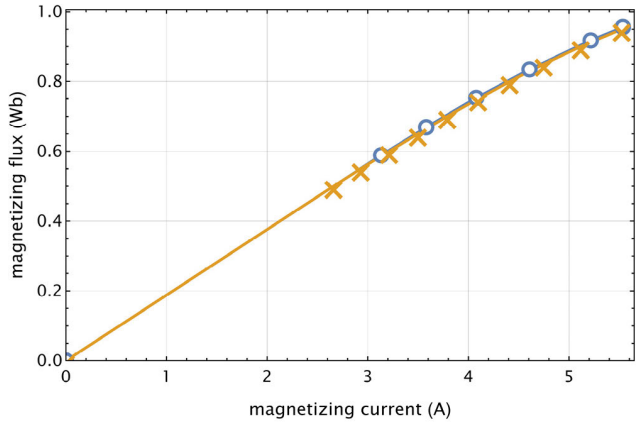

FIGURE 23. No-load magnetizing characteristics in the form $\psi_m = f\,(i_m)$ obtained from the modified no-load test (blue) and Lm-MRAS (orange).

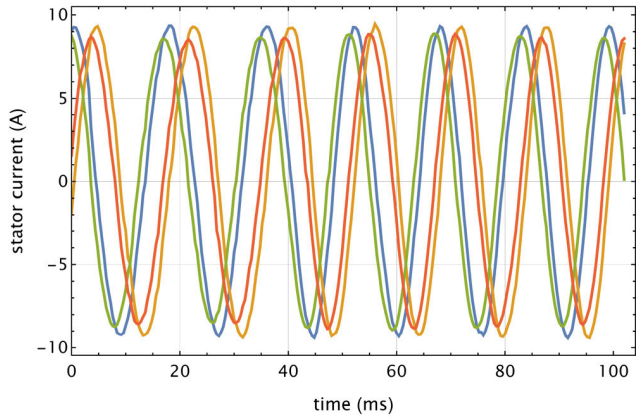

FIGURE 24. Measured α (blue) and β (orange) components of the stator current and estimated α (green) and β (red) components of the stator current. Nominal speed and rotor flux, half of the nominal load torque, iron loss compensation only.

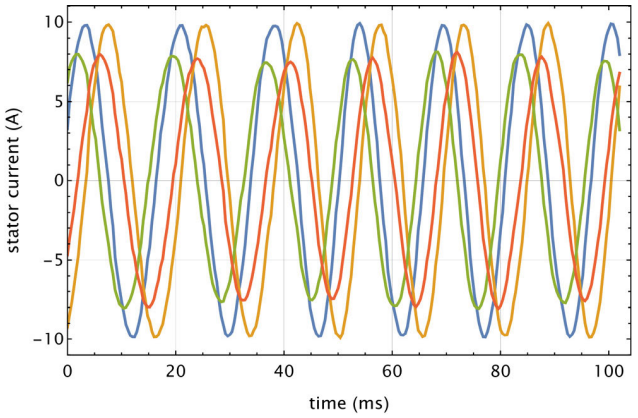

FIGURE 25. Measured α (blue) and β (orange) components of the stator current and estimated α (green) and β (red) components of the stator current. Nominal speed and rotor flux, half of the nominal load torque, iron loss and rotor resistance compensation.

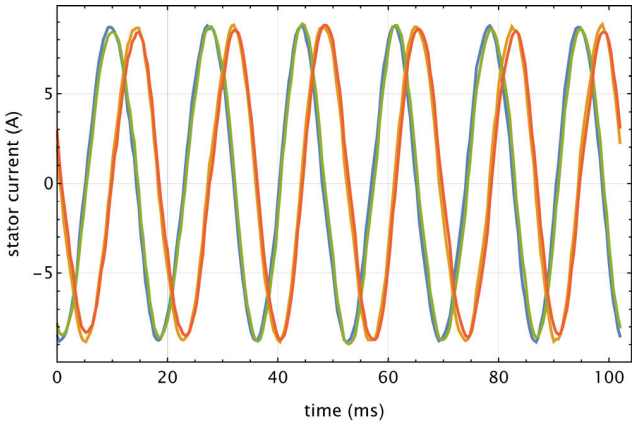

FIGURE 26. Measured α (blue) and β (orange) components of the stator current and estimated α (green) and β (red) components of the stator current. Nominal speed and rotor flux, half of the nominal load torque, iron loss, rotor resistance, and magnetizing inductance compensation.

To compare the no-load test results with the proposed Lm-MRAS, the unloaded drive was then connected to the inverter. To ensure a similar fundamental voltage frequency as during the no-load test, the reference speed was set to 104 rad·s^{-1}. Under the no-load conditions, the rotor current is close to zero, i.e., $i_2 \approx 0$ which, according to (8), means that the magnetizing flux is almost identical with the rotor flux, i.e., $\psi_\mathrm{m} \approx \psi_2$. Under these assumptions it is easy to obtain the magnetizing characteristics in the form $\psi_\mathrm{m} = f\,(i_\mathrm{m})$. The resulting comparison is depicted in Fig. 23. Out of the figure, it is evident that both the magnetizing characteristics are in excellent agreement.

To validate the performance of the parallel estimation of the magnetizing inductance and rotor resistance, the reference flux and speed were set to their nominal values and the load torque to half of the nominal value. Then, the actual and estimated $\alpha\beta$ current components were measured and calculated, respectively. The estimated currents were obtained using the current equation of the state-space model (33) transformed into $\alpha\beta$. The rotor flux vector components for the current estimator were obtained using (10).

The data were recorded for multiple cases. In all of them, the iron loss compensation was active. Also, between the measurements, the machine was stopped to cool back to ambient temperature. Fig. 24 shows the case when the Lm-MRAS was turned on at the beginning during the no-load operation to obtain the no-load value of the magnetizing inductance. Then the Lm-MRAS was deactivated,

and the drive was loaded with half of the nominal torque. Fig. 25 shows a similar case with the difference that only the rotor resistance compensation was active. Finally, Fig. 26 shows the case when both the magnetizing inductance and rotor resistance estimation were active.

Interestingly, the worst case is obtained when only the rotor resistance compensation is active. The incorrect value of the magnetizing inductance influences the Q-MRAS performance, leading to incorrectly estimated rotor resistance. If neither the magnetizing inductance nor the rotor resistance compensation is active, the results are better. However, it is expected that the resulting estimates would be worse after a long-time loading when the rotor temperature would be increased. The best match between the current components is obtained if all the compensations are active, indicating the correct estimation of the parameters.

IX. CONCLUSION

This paper presented a novel MRAS-type estimator with the included effect of iron losses and load. Despite the drawback that the reference model is not entirely free of the magnetizing inductance, the simulation and experimental results proved its ability to estimate the conventional and load-dependent magnetizing inductance saturation correctly. Furthermore, the estimator operation during load conditions was improved by introducing a simultaneously working reactive power MRAS with the included iron losses for the rotor resistance adaptation. It was found out that the influence of the iron losses on the accuracy of both parameters estimation becomes significant at higher loads.

Still, a few issues connected with the proposed estimation schemes should be acknowledged. First, it is assumed that the stator resistance and stator and rotor leakage inductance are known accurately. The stator resistance can be easily measured and corrected during the drive operation, but the leakage inductances cannot be measured directly. Furthermore, the rotor leakage inductance can also saturate as the function of the rotor current. One possibility of overcoming these problems would be adding a leakage inductance estimation through signal injection or recursive least-square methods.

Secondly, the iron losses were measured during the no-load operation. However, the iron losses are also dependent on the slip due to the different mutual speeds of the rotating magnetic field (fundamental component) and rotor. Furthermore, additional losses are present in the machine during load conditions. Therefore, the models and the estimates could be improved using a more sophisticated induction motor equivalent circuit.

Lastly, as mentioned in the beginning, the reference model is not free of magnetizing inductance. At this time, the authors are working on an improved estimator that eliminates this problem.

REFERENCES

[1] A. M. Bazzi and P. T. Krein, "Review of methods for real-time loss minimization in induction machines," *IEEE Trans. Ind. Appl.*, vol. 46, no. 6, pp. 2319–2328, Nov./Dec. 2010.

[2] Z. Peng, "Analysis and implementation of constrained MTPA criterion for induction machine drives," *IEEE Access*, vol. 8, pp. 176445–176453, 2020.

[3] Z. Qu, M. Ranta, M. Hinkkanen, and J. Luomi, "Loss-minimizing flux level control of induction motor drives," *IEEE Trans. Ind. Appl.*, vol. 48, no. 3, pp. 952–961, May/Jun. 2012.

[4] T. Tuovinen, M. Hinkkanen, and J. Luomi, "Modeling of saturation due to main and leakage flux interaction in induction machines," *IEEE Trans. Ind. Appl.*, vol. 46, no. 3, pp. 937–945, Jun. 2010.

[5] M. Hinkkanen, A.-K. Repo, M. Ranta, and J. Luomi, "Small-signal modeling of mutual saturation in induction machines," *IEEE Trans. Ind. Appl.*, vol. 46, no. 3, pp. 965–973, Jun. 2010.

[6] E. Molsa, S. E. Saarakkala, and M. Hinkkanen, "Influence of magnetic saturation on modeling of an induction motor," in *Proc. 13th Int. Conf. Electr. Mach. (ICEM)*, Sep. 2018, pp. 1572–1578.

[7] M. Ranta, M. Hinkkanen, E. Dlala, A.-K. Repo, and J. Luomi, "Inclusion of hysteresis and eddy current losses in dynamic induction machine models," in *Proc. IEEE Int. Electric Mach. Drives Conf.*, May 2009, pp. 1387–1392.

[8] K. Wang, R. Huai, Z. Yu, X. Zhang, F. Li, and L. Zhang, "Comparison study of induction motor models considering iron loss for electric drives," *Energies*, vol. 12, no. 3, p. 503, Feb. 2019.

[9] C. Mastorocostas, I. Kioskeridis, and N. Margaris, "Thermal and slip effects on rotor time constant in vector controlled induction motor drives," *IEEE Trans. Power Electron.*, vol. 21, no. 2, pp. 495–504, Mar. 2006.

[10] M. Sokola, "Vector control of induction machines using improved machine models," Ph.D. dissertation, School Eng., Liverpool John Moores Univ., Liverpool, U.K., 1998.

[11] J. Nerg, J. Pyrhonen, and J. Partanen, "Finite element modeling of the magnetizing inductance of an induction motor as a function of torque," *IEEE Trans. Magn.*, vol. 40, no. 4, pp. 2047–2049, Jul. 2004.

[12] D. C. Huynh, M. W. Dunnigan, and S. J. Finney, "On-line parameter estimation of an induction machine using a recursive least-squares algorithm with multiple time-varying forgetting factors," in *Proc. IEEE Int. Conf. Power Energy*, Nov. 2010, pp. 444–449.

[13] R. P. R. Siddavatam and U. Loganathan, "Identification of induction machine parameters including core loss resistance using recursive least mean square algorithm," in *Proc. 45th Annu. Conf. IEEE Ind. Electron. Soc. (IECON)*, Oct. 2019, pp. 1095–1100.

[14] H. Zhao, H. H. Eldeeb, J. Wang, J. Kang, Y. Zhan, G. Xu, and O. A. Mohammed, "Parameter identification based online noninvasive estimation of rotor temperature in induction motors," *IEEE Trans. Ind. Appl.*, vol. 57, no. 1, pp. 417–426, Jan. 2021.

[15] S. A. Bednarz and M. Dybkowski, "Estimation of the induction motor stator and rotor resistance using active and reactive power based model reference adaptive system estimator," *Appl. Sci.*, vol. 9, no. 23, p. 5145, Nov. 2019.

[16] P. Cao, X. Zhang, and S. Yang, "A unified-model-based analysis of MRAS for online rotor time constant estimation in an induction motor drive," *IEEE Trans. Ind. Electron.*, vol. 64, no. 6, pp. 4361–4371, Jun. 2017.

[17] M. Dybkowski, "Universal speed and flux estimator for induction motor," *Power Electron. Drives*, vol. 3, no. 1, pp. 157–169, Dec. 2018.

[18] S. Maiti, C. Chakraborty, Y. Hori, and M. C. Ta, "Model reference adaptive controller-based rotor resistance and speed estimation techniques for vector controlled induction motor drive utilizing reactive power," *IEEE Trans. Ind. Electron.*, vol. 55, no. 2, pp. 594–601, Feb. 2008.

[19] P. Cao, X. Zhang, S. Yang, Z. Xie, and Y. Zhang, "Reactive-power-based MRAS for online rotor time constant estimation in induction motor drives," *IEEE Trans. Power Electron.*, vol. 33, no. 12, pp. 10835–10845, Dec. 2018.

[20] L. Liu, Y. Guo, and J. Wang, "Online identification of mutual inductance of induction motor without magnetizing curve," in *Proc. Annu. Amer. Control Conf. (ACC)*, Jun. 2018, pp. 3293–3297.

[21] F. L. Mapelli, D. Tarsitano, and F. Cheli, "A rotor resistance MRAS estimator for EV induction motor traction drive based on torque and reactive stator power: Simulation and experimental results," in *Proc. Int. Conf. El. Mach. (ICEM)*, Berlin, Germany, 2014, pp. 31–37.

[22] K. R. Cho and J. K. Seok, "Induction motor rotor temperature estimation based on a high-frequency model of a rotor bar," *IEEE Trans. Ind. Appl.*, vol. 45, no. 4, pp. 1267–1275, Jul. 2009.

[23] F. Baneira, A. G. Yepes, O. López, and J. Doval-Gandoy, "Estimation method of stator winding temperature for dual three-phase machines based on DC-signal injection," *IEEE Trans. Power Electron.*, vol. 31, no. 7, pp. 5141–5148, Jul. 2016.

[24] F. Briz, M. W. Degner, J. M. Guerrero, and A. B. Diez, "Temperature estimation in inverter fed machines using high frequency carrier signal injection," in *Proc. IEEE Ind. Appl. Annu. Meeting*, Sep. 2007, pp. 2030–2037.
[25] S. M. N. Hasan and I. Husain, "A Luenberger–sliding mode observer for online parameter estimation and adaptation in high-performance induction motor drives," *IEEE Trans. Ind. Appl.*, vol. 45, no. 2, pp. 772–781, Apr. 2009.
[26] S. Yang, D. Ding, X. Li, Z. Xie, X. Zhang, and L. Chang, "A novel online parameter estimation method for indirect field oriented induction motor drives," *IEEE Trans. Energy Convers.*, vol. 32, no. 4, pp. 1562–1573, Dec. 2017.
[27] E. Zerdali, "A comparative study on adaptive EKF observers for state and parameter estimation of induction motor," *IEEE Trans. Energy Convers.*, vol. 35, no. 3, pp. 1443–1452, Sep. 2020.
[28] O. Çetin, A. Dalcalı, and F. Temurtaş, "A comparative study on parameters estimation of squirrel cage induction motors using neural networks with unmemorized training," *Eng. Sci. Technol., Int. J.*, vol. 23, no. 5, pp. 1126–1133, Oct. 2020.
[29] M. Wlas, Z. Krzeminski, and H. A. Toliyat, "Neural-network-based parameter estimations of induction motors," *IEEE Trans. Ind. Electron.*, vol. 55, no. 4, pp. 1783–1794, Apr. 2008.
[30] T. P. Van, D. V. Tien, Z. Leonowicz, M. Jasinski, T. Sikorski, and P. Chakrabarti, "Online rotor and stator resistance estimation based on artificial neural network applied in sensorless induction motor drive," *Energies*, vol. 13, no. 18, p. 4946, Sep. 2020.
[31] M. Sokola and E. Levi, "A novel induction machine model and its application in the development of an advanced vector control scheme," *Int. J. Elect. Eng. Educ.*, vol. 37, no. 3, pp. 48–233, Jul. 2000.
[32] M. Korzonek, G. Tarchala, and T. Orlowska-Kowalska, "A review on MRAS-type speed estimators for reliable and efficient induction motor drives," *ISA Trans.*, vol. 93, pp. 1–13, Oct. 2019.
[33] A. Pal, S. Das, and A. K. Chattopadhyay, "An improved rotor flux space vector based MRAS for field-oriented control of induction motor drives," *IEEE Trans. Power Electron.*, vol. 33, no. 6, pp. 5131–5141, Jun. 2018.
[34] H. Karkkainen, L. Aarniovuori, M. Niemela, and J. Pyrhonen, "Converter-fed induction motor efficiency: Practical applicability of IEC methods," *IEEE Ind. Electron. Mag.*, vol. 11, no. 2, pp. 45–57, Jun. 2017.
[35] M. Koteich, "Flux estimation algorithms for electric drives: A comparative study," in *Proc. 3rd Int. Conf. Renew. Energies Developing Countries (REDEC)*, Jul. 2016, pp. 1–6.
[36] Y. Wang, W. Xie, X. Wang, and D. Gerling, "A precise voltage distortion compensation strategy for voltage source inverters," *IEEE Trans. Ind. Electron.*, vol. 65, no. 1, pp. 59–66, Jan. 2018.
[37] O. Lipcak and J. Bauer, "Analysis of voltage distortion and comparison of two simple voltage compensation methods for sensorless control of induction motor," in *Proc. IEEE 10th Int. Symp. Sensorless Control Electr. Drives (SLED)*, Sep. 2019, pp. 1–6.

ONDREJ LIPCAK (Graduate Student Member, IEEE) was born in Prague, Czech Republic, in 1993. He received the M.S. degree in electrical machines, apparatus and drives from Czech Technical University in Prague (CTU), in 2018, where he is currently pursuing the Ph.D. degree in electrical machines and drives with the Department of Electric Drives and Traction, Faculty of Electrical Engineering.

Since 2018, he has been involved in research and teaching activities with the Department of Electric Drives. His research interests include mathematical modeling, parameter estimation, and efficient control of AC machines.

JAN BAUER (Member, IEEE) was born in Prague, Czech Republic, in 1983. He received the M.S. and Ph.D. degrees in electrical engineering from Czech Technical University in Prague (CTU), in 2007 and 2015, respectively.

He is currently an Assistant Professor with the Department of Electric Drives and Traction, Faculty of Electrical Engineering, CTU. His research interests include the control of electric drives and power converters with the aim of efficiency increase.

3.4 Paper 4: Influence of Selected Non-Ideal Aspects on Active and Reactive Power MRAS for Stator and Rotor Resistance Estimation

3.4.1 Motivation

The paper presented in this section can be viewed as an accompanying article to the other author's publications. The problem with the MRAS based estimators presented in the literature is that many non-ideal aspects are neglected during the estimator derivation, calculation, or implementation stage.

First, as already mentioned several times, the papers in the literature usually do not consider the effect of the machine's iron losses or additional (stray-load) losses. Secondly, many of the presented algorithms require stator voltage vector knowledge. However, the influence of a proper voltage compensation on the resulting estimated quantity is also usually not examined. Lastly, the algorithms are derived and presented in the continuous-time domain. However, in reality, the algorithms have to be implemented on a microcontroller, meaning that the accuracy of the MRAS estimators and the whole FOC algorithm will depend on the sampling time and used discretization or numerical method.

The paper presents only simulation results based on the MATLAB/Simulink environment. The reason is that on a real drive, the individual negative phenomena mentioned above cannot be easily decoupled from each other and also from the additional imperfections present on the actual drive. Furthermore, the paper was intended for publication in a special issue, "*Modeling and Simulation of Power Systems and Power Electronics*."

3.4.2 Main Contribution and Results

To sum up the contribution and main results of the paper:

- For the simulation results, a complex model of the IM drive with the possibility of modeling the iron losses, inverter nonlinearity, and effect discretization was built in MATLAB/Simulink.
- The paper gives clear and comprehensive guidelines to various IM nonlinearities measurement, modeling, and implementation.
- Improved IM current and voltage models with the included effect of iron losses are presented.
- Improved P-MRAS and Q-MRAS estimators for the stator and rotor resistance identification, respectively, are presented.
- The effect of sampling time, discretization, and numerical method selection is examined.

3.4.3 Discussion and Suggestions for Future Work

The state-space model of the machine with the included effect of iron losses for simulation of the actual machine is based on the T-equivalent circuit with the iron loss resistance placed in parallel with the magnetizing branch. This equivalent circuit cannot model the rotor iron losses and additional (stray-load) losses due to the slip. Therefore, a suitable topic for future research would be to augment the simulation model with the possibility of modeling also these types of losses.

Also, in some situations, a voltage drop may also play a not negligible role in the voltage distortion, as discussed in section 3.1. Therefore, the nonlinear inverter model could also be brought closer to reality by implementing the possibility of simulating the voltage distortion caused by the voltage drop across the semiconductor devices.

Another interesting topic for future research based on simulations would be a more thorough examination of multiple different methods for the solution of the differential equations of the IM. The analysis would be interesting from the point of view of the resulting approximation and the point of view of the computational burden. The topic of numerical mathematics is vast and

complex, and since the motor control algorithms are implemented on the DSP or field-programmable gate array (FPGA), the utilized numerical algorithms definitely influence the overall drive performance.

Lastly, it is worth mentioning for completeness that the inverter model was also based on the new IGBT modules, as in the case of the previous paper.

energies

MDPI

Article

Influence of Selected Non-Ideal Aspects on Active and Reactive Power MRAS for Stator and Rotor Resistance Estimation

Ondrej Lipcak *, Filip Baum and Jan Bauer

Department of Electric Drives and Traction, Czech Technical University in Prague, 160 00 Prague, Czech Republic; baumfili@fel.cvut.cz (F.B.); bauerja2@fel.cvut.cz (J.B.)

* Correspondence: lipcaond@fel.cvut.cz

Abstract: Mathematical models of induction motor (IM) used in direct field-oriented control (DFOC) strategies are characterized by parametrization resulting from the IM equivalent circuit and model-type selection. The parameter inaccuracy causes DFOC detuning, which deteriorates the drive performance. Therefore, many methods for parameter adaptation were developed in the literature. One class of algorithms, popular due to their simplicity, includes estimators based on the model reference adaptive system (MRAS). Their main disadvantage is the dependence on other machines' parameters. However, although typically not considered in the respective literature, there are other aspects that impair the performance of the MRAS estimators. These include, but are not limited to, the nonlinear phenomenon of iron losses, the effect of necessary discretization of the algorithms and selection of the sampling time, and the influence of the supply inverter nonlinear behavior. Therefore, this paper aims to study the effect of the above-mentioned negative aspects on the performance of selected MRAS estimators: active and reactive power MRAS for the stator and rotor resistance estimation. Furthermore, improved reduced-order models and MRAS estimators that consider the iron loss phenomenon are also presented to examine the iron loss influence. Another merit of this paper is that it shows clearly and in one place how DFOC, with the included effect of iron losses and inverter nonlinearities, can be modeled using simulation tools. The modeling of the IM and DFOC takes place in MATLAB/Simulink environment.

Keywords: induction motor modeling; iron losses; MRAS; numerical methods; inverter nonlinearity

Citation: Lipcak, O.; Baum, F.; Bauer, J. Influence of Selected Non-Ideal Aspects on Active and Reactive Power MRAS for Stator and Rotor Resistance Estimation. *Energies* **2021**, *14*, 6826. https://doi.org/10.3390/en14206826

Academic Editors: James Cale and Reinaldo Tonkoski

Received: 23 September 2021
Accepted: 16 October 2021
Published: 19 October 2021

1. Introduction

Mathematical models of the induction motor (IM) are needed for two purposes: the modeling of the machine itself and for the real-time high-performance control strategies, among which we can include field-oriented control (FOC), direct torque control (DTC), and model predictive control (MPC) [1]. The set of the parameters utilized by the mathematical models is defined by the IM equivalent circuit selection and model type [2–4]. The key parameters in the traditional T-equivalent circuit are the stator and rotor resistances, leakage inductances, and magnetizing inductance. Unfortunately, these parameters are not constant during the drive operation since they are affected mainly by the temperature rise and magnetic flux saturation [5]. For instance, the nonlinear magnetizing characteristics can be respected within the control algorithm using offline-measured data. However, the compensation of the resistances must be handled online since it depends on the machine's loading.

So far, numerous online identification methods of IM parameters have been proposed in the literature. These include model-based methods [6], recursive least-square algorithms (RLS) [7–9], model reference adaptive systems (MRAS) [10–16], signal injection (SI) techniques [17–19], state observers (SO) [20–22], and artificial intelligence (ANN) [23–25] methods. Typically, the greater the estimation accuracy and insensitivity to other machine parameters, the greater the algorithm complexity, which puts demands on hardware computational power and the experience of the implementation engineer. Therefore, due to

the ease of implementation, MRAS-based estimators are quite popular for IM speed or parameter estimation.

The basic MRAS principle is that two mathematical models are evaluated parallelly: the so-called reference and adaptive. The reference model does not depend on the estimated quantity. On the contrary, the adaptive model utilizes the estimated quantity directly or indirectly. An adaptation mechanism (usually a simple PI controller) estimates the desired variable by driving the difference between the reference and adaptive model to zero. For the MRAS design, the Lyapunov theory or hyperstability theory can be utilized [11].

Numerous MRAS estimators based on various quantities have been proposed in the literature so far. These include MRAS based on: reactive power [10–14], rotor flux [26–28], active power [29,30], PY fictitious quantity [31], X fictitious quantity [32], q-axis rotor flux [33], d-axis air-gaip flux [34], d-axis stator voltage [35], or electromagnetic torque [14]. The major drawback of the MRAS schemes is that they inherently suppose that the error between the reference and adaptive model is caused by the estimated parameter only. The papers that focus on MRAS techniques usually strive to analyze the estimation process in terms of the stability [11–13] and sensitivity to the machine parameters [36,37] or speed [30,38,39]. However, other issues affecting the parameter estimation that are usually not acknowledged or examined in the respective papers include:

- **Effect of solver and sampling time selection.** MRAS design is, in most cases, carried out in the continuous-time domain. However, the actual control algorithms are implemented on a discrete system: either a digital signal processor (DSP) or field-programmable gate array (FPGA). Only a few papers consider the effect of discretization [40,41]. However, they are focused on a specific MRAS for speed estimation.
- **Effect of voltage-source inverter (VSI) nonlinearity.** Most of the MRAS algorithms utilize directly or indirectly the stator voltage vector. As the real-time voltage measurement is hardware demanding and requires properly designed filters, the reference voltage (i.e., the input to the modulator) is usually utilized instead of the direct measurement. However, the fundamental output voltage of the commonly used IGBT inverters is distorted, mainly due to the inserted deadtime and finite semiconductor switching.
- **Effect of iron losses.** Iron losses are a phenomenon that undoubtedly affects the IM flux, torque, speed, and parameter estimation [42–44]. However, most of the proposed MRAS estimators are based on IM equivalent circuits that do not consider iron losses.

This paper aims to examine and quantify the influence of the issues mentioned above on the performance of MRAS-type IM parameter estimators. The most popular reactive power MRAS (Q-MRAS) for the rotor resistance estimation and active power MRAS (P-MRAS) for the stator resistance estimation are selected as the candidates for the investigation. The presented results are based on simulations of the direct FOC (DFOC) of a 3.6 kW IM drive in the MATLAB/Simulink because, in a real drive, it is not possible to efficiently study the decoupled effects of various phenomena acting on the system. For machine modeling, the traditional T-equivalent circuit is utilized. The circuit is augmented with the fictitious iron loss resistance placed in parallel with the magnetizing branch to study the effect of iron losses.

This paper is organized as follows: Section 2 shows full-order state-space models of IM with and without the included effect of iron losses that are used to model the machine itself. Section 3 then presents improved reduced-order models with the included effect of iron losses used in the DFOC model to assess the influence of iron losses on the parameter estimation. Furthermore, this section also introduces the numerical methods whose influence on the estimation accuracy is further examined in the simulations. In Section 4, the mathematical model of the VSI with the possibility of simulating the nonlinear behavior of the actual inverter is presented. Section 5 gives an overview of iron losses measurement, modeling, and implementation into the FOC and IM models. Section 6 demonstrates the derivation of the improved P-MRAS and Q-MRAS estimators that consider the influence

of iron losses. Finally, the paper is concluded with Sections 7 and 8 dedicated to the results and discussion of the simulations.

2. Induction Machine Equivalent Circuit

The IM traditional T-equivalent circuit can be augmented to include the effect of the iron losses (Figure 1). In this case, the losses are considered load-independent. In Figure 1, the symbols $\underline{\psi}_1$, $\underline{\psi}_2$, and $\underline{\psi}_\mathrm{m}$ represent the stator, rotor, and magnetizing flux linkage space vectors, respectively; $\underline{u}_1$ represents the stator voltage space vector; $\underline{i}_1$, $\underline{i}_2$, $\underline{i}_\mathrm{m}$, and $\underline{i}_\mathrm{Fe}$ represent the stator, rotor, magnetizing, and equivalent iron loss current space vectors, respectively; R_1, R_2, and R_Fe denote the stator, rotor, and equivalent iron loss resistance, respectively; ω_k is the electrical angular speed of the general reference frame; ω is the rotor electrical angular speed; L_m is the magnetizing inductance; and the symbol j represents an imaginary unit ($\mathrm{j}^2 = -1$). A short-circuited rotor is considered; therefore, the rotor voltage equals zero. The stator inductance L_1 is defined as $L_1 = L_\mathrm{m} + L_{1\sigma}$, where $L_{1\sigma}$ is the stator leakage inductance and the rotor inductance L_2 is defined as $L_2 = L_\mathrm{m} + L_{2\sigma}$, where $L_{2\sigma}$ is the rotor leakage inductance.

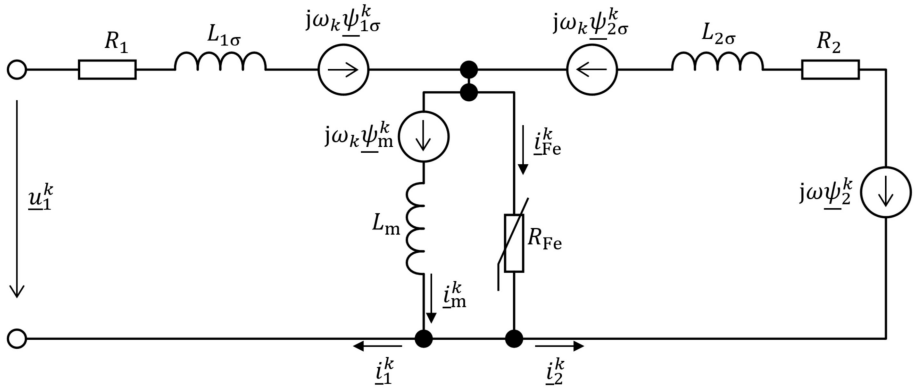

Figure 1. Induction machine T-equivalent circuit with the included effect of iron losses.

The superscript k denotes that the space vectors are expressed in an arbitrary reference frame. The two specific reference frames used in this paper are the stator-fixed (real and imaginary axis denoted as α and β, respectively) and rotor flux vector-attached (real and imaginary axis denoted as d and q, respectively) reference frames.

2.1. Full-Order State-Space Model with Included Effect of Iron Losses

For modeling IM with the included effect of iron losses, the full-order state-space model in the stationary $\alpha\beta$ reference frame with the current space vector, magnetizing flux space vector, and rotor flux space vector components as state variables can be used [45]. The model is deductible from Figure 1 and can be expressed mathematically as

$$\dot{\mathbf{x}} = \mathbf{A}\mathbf{x} + \mathbf{B}\mathbf{u}, \tag{1}$$

where

$$\mathbf{A} = \begin{pmatrix} a_1 & 0 & a_2 & 0 & a_3 & 0 \\ 0 & a_1 & 0 & a_2 & 0 & a_3 \\ R_\mathrm{Fe} & 0 & a_4 & 0 & \tau_{\mathrm{Fe}\sigma}^{-1} & 0 \\ 0 & R_\mathrm{Fe} & 0 & a_4 & 0 & \tau_{\mathrm{Fe}\sigma}^{-1} \\ 0 & 0 & \tau_{\mathrm{r}\sigma}^{-1} & 0 & -\tau_{\mathrm{r}\sigma}^{-1} & -\omega \\ 0 & 0 & 0 & \tau_{\mathrm{r}\sigma}^{-1} & \omega & -\tau_{\mathrm{r}\sigma}^{-1} \end{pmatrix}, \tag{2}$$

$$\mathbf{B} = \begin{pmatrix} \frac{1}{L_{1\sigma}} & 0 & 0 & 0 & -\frac{1}{L_{1\sigma}} & 0 \\ 0 & \frac{1}{L_{1\sigma}} & 0 & 0 & 0 & -\frac{1}{L_{1\sigma}} \\ 0 & 0 & 0 & 0 & 1 & 0 \\ 0 & 0 & 0 & 0 & 0 & 1 \\ 0 & 0 & 1 & 0 & 0 & 0 \\ 0 & 0 & 0 & 1 & 0 & 0 \end{pmatrix}^{\mathrm{T}}, \tag{3}$$

$$\mathbf{x} = \begin{pmatrix} i_{1\alpha} & i_{1\beta} & \psi_{\mathrm{m}\alpha} & \psi_{\mathrm{m}\beta} & \psi_{2\alpha} & \psi_{2\beta} \end{pmatrix}^{\mathrm{T}}, \tag{4}$$

$$\mathbf{u} = \begin{pmatrix} u_{1\alpha} & u_{1\beta} & 0 & 0 & 0 & 0 \end{pmatrix}^{\mathrm{T}}, \tag{5}$$

and where $\tau_{\mathrm{r}\sigma} = L_{2\sigma}/R_2$, $\tau_{\mathrm{Fe}\sigma} = L_{2\sigma}/R_{\mathrm{Fe}}$, $a_1 = -(R_1 + R_{\mathrm{Fe}})/L_{1\sigma}$, $a_2 = L_2/(L_{1\sigma}L_{\mathrm{m}}\tau_{\mathrm{Fe}\sigma})$, $a_3 = -1/(L_{1\sigma}\tau_{\mathrm{Fe}\sigma})$, $a_4 = -L_{1\sigma}a_2'$.

The electromechanical torque and the motion equation, respectively, are considered in the form

$$T = \frac{3}{2}p_{\mathrm{p}}\frac{1}{L_{2\sigma}}\left(\underline{\psi}_2^k \times \underline{\psi}_{\mathrm{m}}^k\right), \tag{6}$$

$$T - T_{\mathrm{L}} = \frac{J}{p_{\mathrm{p}}}\frac{\mathrm{d}\omega}{\mathrm{d}t}, \tag{7}$$

where p_{p} is the number of pole-pairs, T is the electromagnetic torque, T_{L} is the load torque, J is the moment of inertia, and the operator $\times$ denotes cross product.

2.2. Full-Order State-Space Model without Iron Losses

For the modeling of the machine without the effect of iron losses, it is convenient to use a model with the stator and rotor flux linkage vector components as state variables. The model in its state-space form can be written as [46]

$$\dot{\boldsymbol{\xi}} = \mathbf{A}'\boldsymbol{\xi} + \boldsymbol{\upsilon}, \tag{8}$$

where

$$\mathbf{A}' = \begin{pmatrix} -\frac{R_1L_2}{D} & 0 & \frac{R_1L_{\mathrm{m}}}{D} & 0 \\ 0 & -\frac{R_1L_2}{D} & 0 & \frac{R_1L_{\mathrm{m}}}{D} \\ \frac{R_2L_{\mathrm{m}}}{D} & 0 & -\frac{R_2L_1}{D} & -\omega \\ 0 & \frac{R_2L_{\mathrm{m}}}{D} & \omega & -\frac{R_2L_1}{D} \end{pmatrix}, \tag{9}$$

$$\boldsymbol{\xi} = \begin{pmatrix} \psi_{1\alpha} & \psi_{1\beta} & \psi_{2\alpha} & \psi_{2\beta} \end{pmatrix}^{\mathrm{T}}, \tag{10}$$

$$\boldsymbol{\upsilon} = \begin{pmatrix} u_{1\alpha} & u_{1\beta} & 0 & 0 \end{pmatrix}^{\mathrm{T}}, \tag{11}$$

and where $D = L_1L_2 - L_{\mathrm{m}}^2$.

The electromechanical torque is given by

$$T = \frac{3}{2}p_{\mathrm{p}}\frac{L_{\mathrm{m}}}{D}\left(\underline{\psi}_2^k \times \underline{\psi}_1^k\right). \tag{12}$$

The equation of motion is the same as (7).

3. Reduced-Order Models for Rotor Flux Estimation Considering Iron Loss Effect

In the FOC strategies, the decoupled regulation of flux-producing and torque-producing current components is done in the synchronously rotating dq system where the electromagnetic quantities become DC values. This paper implements a DFOC where the transformation angle, i.e., the angle between the stationary $\alpha\beta$ and rotation dq system, is calculated from the rotor flux linkage vector components. For this purpose, two IM reduced-order models can be used: the so-called IM current and voltage models. Conventionally, these models do not consider the effect of iron losses, contrary to the multiple known full-order models that are based on the respective modification (i.e., placement of the iron loss re-

sistance) of the IM equivalent circuit. Since the reduced-order models that consider the iron losses are not often mentioned in the literature, their derivation is, for convenience, presented in the following subsections.

3.1. Current Model with Included Iron Losses

The model will be derived in an arbitrary reference frame and then concretized to $\alpha\beta$ and dq reference frames. Using Figure 1, the rotor voltage equation and the rotor flux linkage vector equation, respectively, can be expressed as

$$0 = R_2 \underline{i}_2^k + \frac{\mathrm{d}\,\underline{\psi}_2^k}{\mathrm{d}t} + \mathrm{j}(\omega_k - \omega)\,\underline{\psi}_2^k, \tag{13}$$

$$\underline{\psi}_2^k = L_{2\sigma}\underline{i}_2^k + L_\mathrm{m}\underline{i}_\mathrm{m}^k = L_2\underline{i}_2^k + L_\mathrm{m}\left(\underline{i}_1^k - \underline{i}_\mathrm{Fe}^k\right). \tag{14}$$

Substituting for the rotor current vector in (13) from (14) yields

$$\frac{\mathrm{d}\,\underline{\psi}_2^k}{\mathrm{d}t} = \frac{L_\mathrm{m}R_2}{L_2}\underline{i}_1'^{\,k} - \frac{R_2}{L_2}\underline{\psi}_2^k - \mathrm{j}(\omega_k - \omega)\,\underline{\psi}_2^k, \tag{15}$$

where $\underline{i}_1'^{\,k} = \underline{i}_1^k - \underline{i}_\mathrm{Fe}^k$. If the stator-fixed reference frame is considered ($\omega_k = 0$), the model becomes

$$\frac{\mathrm{d}\,\underline{\psi}_2^{\alpha\beta}}{\mathrm{d}t} = \frac{L_\mathrm{m}R_2}{L_2}\underline{i}_1'^{\,\alpha\beta} - \frac{R_2}{L_2}\underline{\psi}_2^{\alpha\beta} + \mathrm{j}\omega\,\underline{\psi}_2^{\alpha\beta}. \tag{16}$$

On the other hand, choosing the rotor flux linkage vector-attached dq reference frame, the steady-state expression for the rotor flux magnitude and slip frequency, respectively, can be expressed as

$$\psi_2 = L_\mathrm{m} i_{1d}', \tag{17}$$

$$\omega_\mathrm{sl} = \frac{L_\mathrm{m}R_2}{L_2}\frac{i_{1q}'}{\psi_{2d}}, \tag{18}$$

where $\psi_2 = \psi_{2d} = \left|\underline{\psi}_2\right|$, $i_{1d}' = i_{1d} - i_{\mathrm{Fe}d}$, and $i_{1q}' = i_{1q} - i_{\mathrm{Fe}q}$.

3.2. Voltage Model with Included Iron Losses

The model will be derived in the $\alpha\beta$ reference frame. According to Figure 1, the stator flux linkage vector can be expressed as

$$\underline{\psi}_1^k = L_{1\sigma}\underline{i}_1^k + L_\mathrm{m}\underline{i}_\mathrm{m}^k = L_1\underline{i}_1^k + L_\mathrm{m}\left(\underline{i}_2^k - \underline{i}_\mathrm{Fe}^k\right). \tag{19}$$

Substituting for the rotor current vector in (14) from (19) and considering the stator-fixed reference frame yields

$$\underline{\psi}_2^{\alpha\beta} = \frac{L_2}{L_\mathrm{m}}\left(\underline{\psi}_1^{\alpha\beta} - L_1\sigma\underline{i}_1^{\alpha\beta}\right) + L_{2\sigma}\underline{i}_\mathrm{Fe}^{\alpha\beta}, \tag{20}$$

where $\sigma = 1 - L_\mathrm{m}^2/L_1L_2$ is the leakage factor. The stator flux linkage vector is obtained as

$$\underline{\psi}_1^{\alpha\beta} = \int_0^t \left(\underline{u}_1^{\alpha\beta} - R_1\underline{i}_1^{\alpha\beta}\right)\mathrm{d}\tau. \tag{21}$$

3.3. Implementation of Current and Voltage Model into Discrete System

The real-time motor control algorithm is implemented either on DSP or FPGA. Therefore, the continuous mathematical models must be solved numerically. The current model (16) represents a complicated set of coupled differential equations when resolved into the real and imaginary parts. Therefore, as mentioned in the introduction, one of the

aims of this paper is to compare the influence of the solver and sampling time selection on the accuracy of the DFOC and MRAS algorithms. The following numerical methods are considered: the forward Euler method (FWEM), the trapezoidal rule (TR), and the fourth-order Runge–Kutta method (RK4). These approaches are well-known algorithms for the solution of ordinary differential equations (ODE); therefore, they will be described here only briefly.

Let us consider a first-order ODE in the form

$$\dot{y}(t) = f\ (t, y(t)),\ \ y(t_0) = y_0. \tag{22}$$

The most straightforward approach for numerically solving (22) is the forward Euler method given by the rule (a fixed step Δt is assumed) [47]

$$y_i = y_{i-1} + \Delta t \cdot f(t_{i-1}, y_{i-1}). \tag{23}$$

The method is first order, making it computationally undemanding but with limited accuracy and stability. An improvement can be achieved by using the trapezoidal rule: at the cost of one extra function evaluation, we improve the order of the method by one. The rule is given by the following formula [47]

$$y_i = y_{i-1} + \frac{\Delta t}{2}[f(t_{i-1}, y_{i-1}) + f(t_i, y_i)]. \tag{24}$$

The last numerical approach considered in this paper is the popular fourth-order Runge–Kutta method, which can be summarized as [47]

$$y_i = y_{i-1} + \frac{1}{6}\Delta t(k_1 + 2k_2 + 2k_3 + k_4), \tag{25}$$

$$k_1 = f(t_{i-1}, y_{i-1}), \tag{26}$$

$$k_2 = f\left(t_{i-1} + \frac{1}{2}\Delta t, y_{i-1} + \frac{1}{2}\Delta t \cdot k_1\right), \tag{27}$$

$$k_3 = f\left(t_{i-1} + \frac{1}{2}\Delta t, y_{i-1} + \frac{1}{2}\Delta t \cdot k_2\right), \tag{28}$$

$$k_4 = f(t_i,\ y_{i-1} + \Delta t \cdot k_3). \tag{29}$$

4. Modelling of Inverter Nonlinearities

A proper inverter model is needed to assess the effect of the IGBT inverter nonlinearities on the DFOC and MRAS algorithms. By a nonlinear inverter behavior, we mean the semiconductor's finite turn-on and turn-off times, the voltage drop across the devices, and necessary protective time, i.e., dead-time inserted by the microcontroller or the transistor driver [48]. Since a 400 V IM drive is considered, the voltage drop across the devices will be neglected.

Let us consider the most common space-vector modulation (SVM) with a fixed switching period T_{PWM}. By a simple graphical analysis, it can be concluded that the turn-on time T_{on} increases and the turn-off time T_{off} decreases the distortion given by the dead-time T_{dt} [48]. Therefore, it is convenient to define the so-called effective dead-time as

$$T_{\mathrm{eff}}(i_x) = T_{\mathrm{dt}} + T_{\mathrm{on}}(i_x) - T_{\mathrm{off}}(i_x) \quad x = a,\ b,\ c, \tag{30}$$

where it is assumed that the turn-on and turn-off times are only the function of the load current, and the symbols a, b, c denote the respective inverter leg. A direct inverter measurement can be performed to easily determine the dependence of the effective deadtime

on the load current. The resulting characteristics can then be implemented as a look-up table or analytically approximated using the expression

$$T_{\text{eff}}(i_x) = \frac{m}{c_1|i_x| + c_2} + n, \tag{31}$$

where c_1, c_2, m, and n are parameters. The measured and approximated dependence of the effective deadtime on the collector/load current of an IGBT module SKM100GB12T4 from SEMIKRON that is used later in the simulation model is depicted in Figure 2 The actual deadtime is selected as 2 µs.

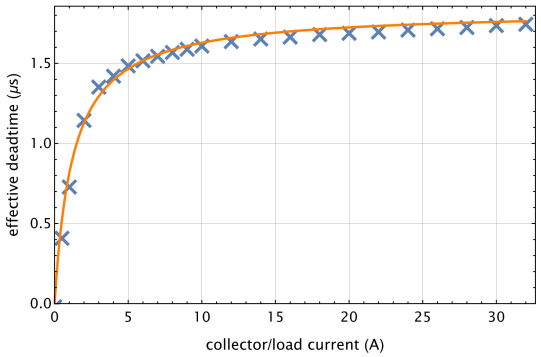

Figure 2. Measured (blue) and approximated (orange) dependence of the effective deadtime on the collector current; SEMIKRON SKM100GB12T4 IGBT module; actual deadtime 2 µs.

Let us assume that, within SVM, the standard up-down counters are utilized with the top value normalized to one and the period of the signal equal to T_{PWM}. Moreover, suppose that the comparator, which compares the counter with the reference compare value, outputs a logical one when a match during up-count occurs and logical zero when a match during a down-count occurs. Then, to model the voltage distortion of an ideal inverter, the reference compare value d_x^* for the respective VSI leg (i.e., the SVM output) must be adjusted as

$$d'_x = d_x^* + d_{\text{dist}(x)} \quad x = a, b, c, \tag{32}$$

where

$$d_{\text{dist}(x)} = \frac{T_{\text{eff}(x)}}{T_{\text{PWM}}} \text{sgn}(i_x) \quad x = a, b, c. \tag{33}$$

The following well-known expression can be utilized for the reconstruction of the actual phase voltage of a wye-connected machine:

$$\begin{bmatrix} u_{\text{a}} \\ u_{\text{b}} \\ u_{\text{c}} \end{bmatrix} = \frac{1}{3} U_{\text{DC}} \begin{bmatrix} 2 & -1 & -1 \\ -1 & 2 & -1 \\ -1 & -1 & 2 \end{bmatrix} \begin{bmatrix} S_{\text{a}} \\ S_{\text{b}} \\ S_{\text{c}} \end{bmatrix}, \tag{34}$$

where u_{a}, u_{b}, and u_{c} are the respective motor phase voltages and S_{a}, S_{b}, and S_{c} are the logical switching variables (1—high-side switch in the respective inverter leg is on, 0—low-side switch in the respective inverter leg is on) from the comparator. Knowing the effective deadtime of each VSI leg, the nonideal inverter can be modeled using (32)–(34).

5. Measuring, Modelling, and Compensation of Iron Losses

The last phenomenon examined in this paper is the influence of iron losses on the DFOC and MRAS performance. This section describes the integration of the iron losses measured on a real machine either into a machine or DFOC model. According to Figure 1, the equivalent iron loss current in an arbitrary reference frame can be expressed as

$$i_{\text{Fe}}^k = \frac{u_{\text{m}}^k}{R_{\text{Fe}}}, \tag{35}$$

where $\underline{u}_{\mathrm{m}}^{k}$ is the voltage across the magnetizing (parallel) branch. The power dissipated in the fictitious iron loss resistance can be expressed as

$$P_{\mathrm{Fe}} = \frac{3}{2}\Re\left\{\underline{u}_{\mathrm{m}}^{k}\,\overline{\underline{i}}_{\mathrm{Fe}}^{k}\right\}, \tag{36}$$

where $\overline{\underline{i}}_{\mathrm{Fe}}^{k}$ denotes the complex conjugate of the equivalent iron loss current. Substituting (35) into (36), the iron loss resistance is obtained as

$$R_{\mathrm{Fe}} = \frac{3}{2}\frac{u_{\mathrm{m}}^{2}}{P_{\mathrm{Fe}}}. \tag{37}$$

The iron loss current in the stationary system is obtained using (37) to substitute for the equivalent iron loss resistance in (35):

$$\underline{i}_{\mathrm{Fe}}^{\alpha\beta} = \frac{2}{3}P_{\mathrm{Fe}}\frac{\underline{u}_{\mathrm{m}}^{\alpha\beta}}{u_{\mathrm{m}}^{2}}. \tag{38}$$

Within the model of the machine, the voltage across the magnetizing branch can be obtained directly using the magnetizing flux vector time derivative. In the control algorithm, the voltage can be approximately calculated as

$$\underline{u}_{\mathrm{m}}^{\alpha\beta} = \underline{u}_{1}^{\alpha\beta} - R_1\underline{i}_{1}^{\alpha\beta} - \mathrm{j}\omega_{\mathrm{s}}L_{1\sigma}\,\underline{i}_{1}^{\alpha\beta}. \tag{39}$$

Equation (39) supposes a steady-state operation and considers the fundamental wave only.

Iron Losses Measurement and Model Fitting

The iron losses can be obtained by a series of no-load tests at various fundamental supply frequencies. The separation procedure based on the IEC standard (IEC 60034-2-1: 2014 [49]) can then be used for the loss calculation [50]. For the measurement, the inverter is programmed to generate a fundamental voltage at a given frequency and magnitude that corresponds to the reference stator flux linkage vector magnitude (obtained from the voltage model). For the iron loss modeling, the following analytical function can be used [4]

$$P_{\mathrm{Fe}} = \frac{f_{\mathrm{s}}^{2}\psi_{1}^{2} + \kappa f_{\mathrm{s}}\psi_{1}^{n}}{R_{\mathrm{Fe0}}}, \tag{40}$$

where f_{s} is the fundamental supply frequency, ψ_1 is the stator flux linkage amplitude, and κ, n, and R_{Fe0} are the model parameters. Figure 3 shows (40) fitted to the measured losses of a 3.6 kW IM drive (nameplate data and nominal model parameters are given in Table A1).

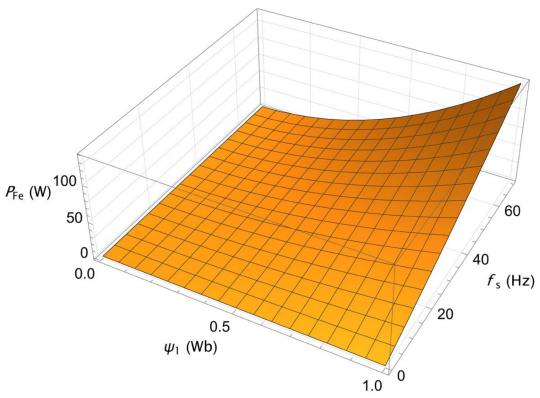

Figure 3. Iron losses as a function of fundamental supply frequency and stator flux linkage vector amplitude. The fitted model parameters are R_{Fe0} = 277, κ = 460, n = 1.77.

6. Improved MRAS Estimators with Included Effect of Iron Losses

The philosophy behind MRAS estimators is that the estimated parameter should somehow influence the adaptive model. In the case of the active power MRAS, the adaptive model directly depends on the stator resistance, making it suitable for the stator resistance estimation. Contrary to that, the adaptive model of the reactive power MRAS used for the rotor resistance estimation depends on the rotor resistance indirectly. By indirect dependence, we mean that the model utilizes quantities affected by the rotor resistance, i.e., the calculated slip speed and d and q-axis current components.

Since most of the MRAS algorithms for the parameter estimation proposed in the literature do not include the effect of iron losses, this section presents improved stator and rotor resistance estimators based on the active (P-MRAS) reactive (Q-MRAS) power.

6.1. Improved Reactive Power MRAS with Included Effect of Iron Losses

The reference model of the popular and widely used Q-MRAS for the rotor resistance (or inverse rotor time constant) estimation is given by [10–14]

$$Q = \Im\left\{\underline{u}_1^{dq}\bar{\underline{i}}_1^{dq}\right\} = u_{1q}i_{1d} - u_{1d}i_{1q}, \tag{41}$$

where $\bar{\underline{i}}_1^{dq}$ denotes the conjugated current space vector. Using (20) transformed into the dq reference frame, the stator flux linkage vector can be obtained as

$$\underline{\psi}_1^{dq} = \frac{L_\mathrm{m}}{L_2}\underline{\psi}_2^{dq} + L_1\sigma\underline{i}_1^{dq} - \frac{L_{2\sigma}L_\mathrm{m}}{L_2}\underline{i}_\mathrm{Fe}^{dq}. \tag{42}$$

The stator voltage equation in the dq reference frame can be written as

$$\underline{u}_1^{dq} = R_1\underline{i}_1^{dq} + \frac{\mathrm{d}\underline{\psi}_1^{dq}}{\mathrm{d}t} + \mathrm{j}\omega_\mathrm{s}\underline{\psi}_1^{dq}. \tag{43}$$

By substituting (41) into (43) and considering the steady-state operation, we obtain

$$\underline{u}_1^{dq} = R_1\underline{i}_1^{dq} + \mathrm{j}\omega_s\left(\frac{L_\mathrm{m}}{L_2}\underline{\psi}_2^{dq} + L_1\sigma\underline{i}_1^{dq} - \frac{L_{2\sigma}L_\mathrm{m}}{L_2}\underline{i}_\mathrm{Fe}^{dq}\right). \tag{44}$$

Separating (44) into the real and imaginary parts, respectively, while considering that $\psi_{2d} = L_\mathrm{m}(i_{1d} - i_{\mathrm{Fe}d})$ and $\psi_{2q} = 0$, the adaptive model is finally obtained as

$$\hat{Q} = \omega_\mathrm{s}\left[L_1\sigma\left(i_{1d}^2 + i_{1q}^2\right) + \frac{L_\mathrm{m}}{L_2}\left(L_\mathrm{m}i_{1d}^2 - L_2i_{\mathrm{Fe}d}i_{1d} - L_{2\sigma}i_{\mathrm{Fe}q}i_{1q}\right)\right]. \tag{45}$$

The synchronous speed is calculated as the sum of the measured speed and estimated slip speed (Equation (18)). The error for the rotor resistance adaptation mechanism is given by

$$\varepsilon_Q = Q - \hat{Q}. \tag{46}$$

The estimated rotor resistance is then the output of the PI controller, i.e.,

$$\hat{R}_2 = K_{\mathrm{p}Q}\varepsilon_Q + K_{\mathrm{i}Q}\int_0^t \varepsilon_Q\mathrm{d}\tau + R_{2(\mathrm{init})}, \tag{47}$$

where $R_{2(\mathrm{init})}$ is the initial rotor resistance. The block diagram of the Q-MRAS estimator with the included iron loss effect is presented in Figure 4. Due to its dependency on the rotor resistance, the current model is used for the transformation angle calculation.

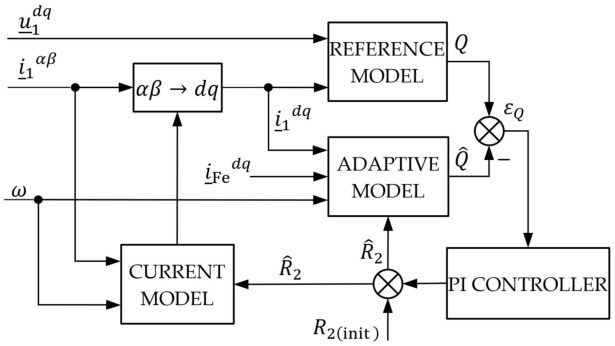

Figure 4. Modified reactive power MRAS for rotor resistance estimation.

6.2. Improved Active Power MRAS with Included Effect of Iron Losses

The reference model of the P-MRAS is given by [10,29,30]

$$P = \Re\left\{\underline{u}_1^{k}\underline{i}_1^{-k}\right\} = u_{1d}i_{1d} + u_{1q}i_{1q}. \tag{48}$$

Separating (44) into the real and imaginary parts, respectively, and substituting the resulting expression into (48) while considering that $\psi_{2d} = L_{\mathrm{m}}(i_{1d} - i_{\mathrm{Fe}d})$ and $\psi_{2q} = 0$, the adaptive model is obtained as

$$\hat{P} = R_1\left(i_{1d}^2 + i_{1q}^2\right) + \omega_{\mathrm{s}}L_{\mathrm{m}}\left(\frac{L_{\mathrm{m}}}{L_2}i_{1d}i_{1q} + \frac{L_{2\sigma}}{L_2}i_{\mathrm{Fe}q}i_{1d} - i_{\mathrm{Fe}d}i_{1q}\right). \tag{49}$$

The error for the rotor resistance adaptation mechanism is calculated as

$$\varepsilon_P = P - \hat{P}. \tag{50}$$

The estimated stator resistance is then the output of the PI controller, i.e.,

$$\hat{R}_1 = K_{\mathrm{p}P}\varepsilon_P + K_{\mathrm{i}P}\int_0^t \varepsilon_P \mathrm{d}\tau + R_{1(\mathrm{init})}, \tag{51}$$

where $R_{1(\mathrm{init})}$ is the initial stator resistance. The block diagram of the modified P-MRAS estimator is presented in Figure 5. Here, the voltage model is selected for the transformation angle calculation due to its dependency on the stator resistance.

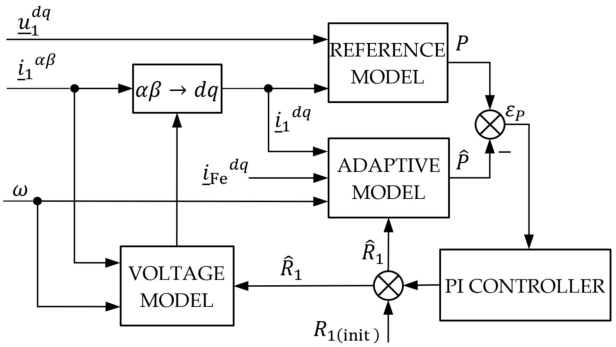

Figure 5. Modified active power MRAS for stator resistance estimation.

7. Simulation Results

As mentioned in the introduction, this paper aims to examine selected phenomena that impair the performance of motor control algorithms. These include inverter nonlinearity, iron losses, ODE solver type, and sampling time. The presented results are based on simulations in MATLAB/Simulink because:

- It is not possible to fully separate the influence of the aforementioned adverse effects in an actual application.
- Many additional nonlinearities and imperfections are present in a real system.
- The exact system parameters are usually not known.

7.1. Simulation Setup Description

The principal block diagram of the Simulink model is depicted in Figure 6. The model permits to switch between the machine model with the iron losses (1)–(6) and without the iron losses (8)–(12). The simulated machine is a 3.6 kW IM whose nameplate data and nominal model parameters are given in Table A1. The iron losses are measured and implemented in accordance with Section 5. Both machine models are simulated using the *ode4* solver with a fixed-step size equal to 1 µs.

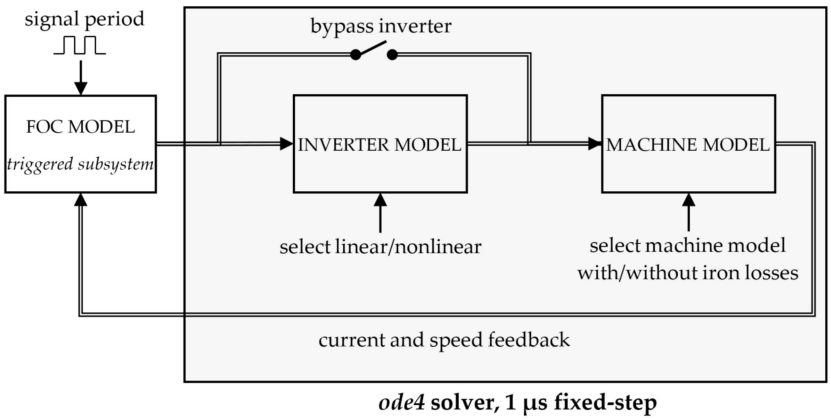

Figure 6. Principal block diagram of simulation setup.

The inverter model is implemented using SVM in a linear mode with the possibility to simulate the inverter nonlinearity using the approach described in Section 4. The switching frequency is selected as 10 kHz. Again, the inverter is simulated using the *ode4* solver with a fixed-step size 1 µs.

The block diagram of the considered DFOC scheme is depicted in Figure 7. The advantage of the presented DFOC scheme is the ability to estimate the stator and rotor resistance variation in the presence of iron losses using improved estimators. The disadvantage is that machine iron losses and nonlinear inverter characteristics need to be measured and implemented for proper functionality, and additional PI controllers have to be tuned. Moreover, in an actual application, the DFOC performance can be further improved by respecting the saturation of the main flux paths.

The FOC model is simulated as a triggered subsystem to mimic the fact that motor control algorithms are implemented on a discrete system. The type of the ODE solver (FWEM or TR) is selected by setting the appropriate integration method in the Discrete-Time Integrator blocks. The RK4 method is implemented using the MATLAB Function Block. Within FOC, it is also possible to switch between the voltage model and the current model, both either with or without the iron losses. Concerning the MRAS testing, the Q-MRAS is tested with the current model, and the P-MRAS is tested with the voltage model active.

The initial gains of the PI controllers within the FOC were calculated using the optimum modulus method. The obtained values were further adjusted to improve the controllers' performance. The gains of the adaptive PI controllers inside the MRAS estimators were tuned experimentally (the values are given in Table A2).

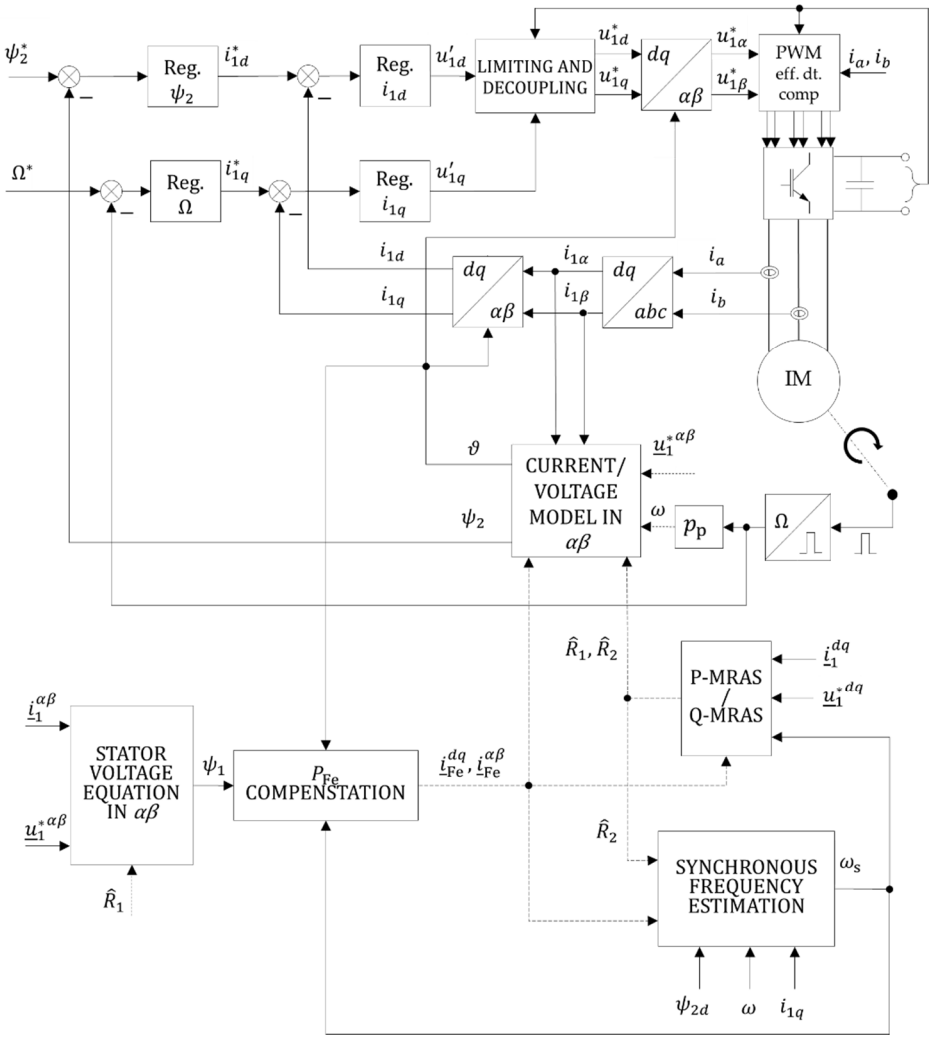

Figure 7. Block diagram of the utilized direct field-oriented control.

7.2. Influence of VSI Nonlinearities on P-MRAS and Q-MRAS Estimators

This simulation series aims to examine the influence of the inverter nonlinearity on the accuracy of the MRAS estimators. The simulation setup is as follows:

- The IM model is implemented without iron losses using (8)–(12).
- The sample time of the FOC model (triggered subsystem) is selected as 100 µs (synchronized with PWM).
- The rotor flux is set to a nominal value.

Within FOC control strategies, it is common that a reference voltage (i.e., the input to the modulator) is utilized instead of a measured voltage. However, when this approach is used, inverter nonlinearities should be compensated appropriately. The influence of the nonideal inverter on the estimation of the stator flux linkage vector α component using (21) is depicted in Figure 8. As expected, the nonlinearities become more significant at small speeds and light loads (Figure 8a). At higher speeds and loads (Figure 8b), the relative influence of the distorting voltage vector decreases.

Figure 9 shows the influence of the nonlinear inverter behavior on the stator resistance (Figure 9a) and rotor resistance (Figure 9b) estimation. The resistances are presented in a per-unit system (indicated by lower-case letters), with the base impedance selected as the ratio of the machine nominal phase voltage and current.

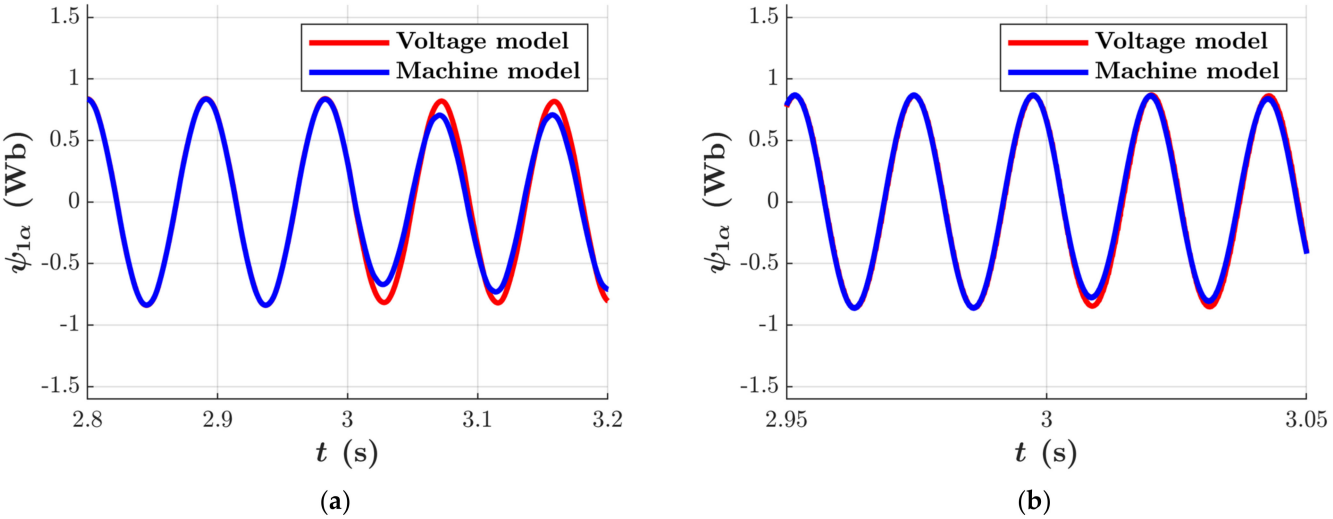

Figure 8. The effect of inverter nonlinearities on the accuracy of stator flux linkage estimation at different operating points. (**a**) 20% of the nominal speed and torque; (**b**) 80% of the nominal speed and torque. Inverter nonlinearity turned on at 3 s.

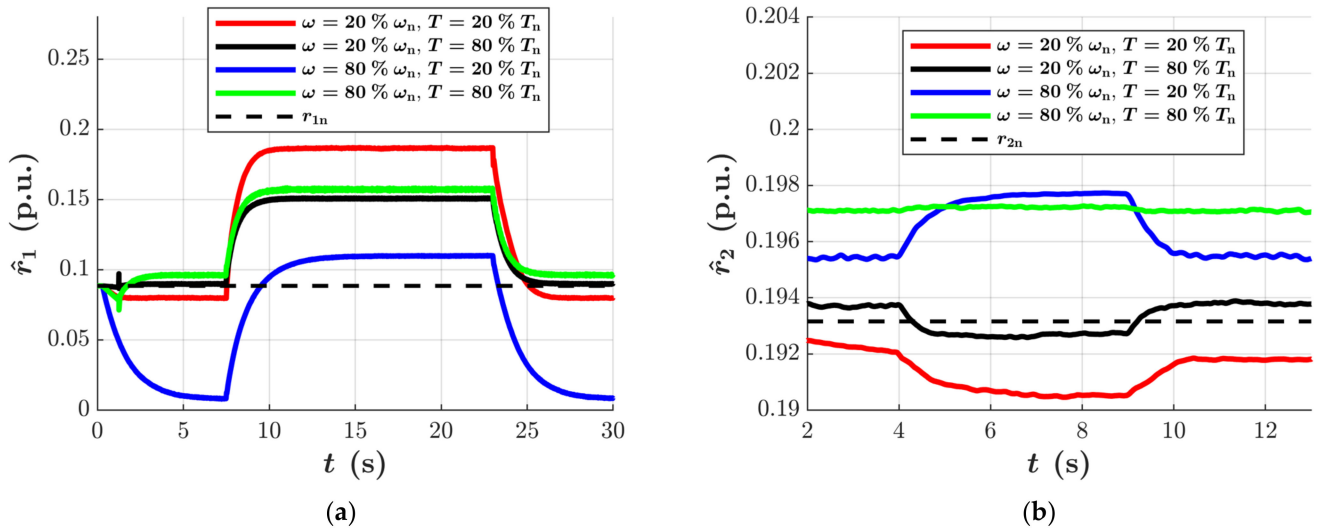

Figure 9. The effect of inverter nonlinearities on the performance of MRAS-type estimators (ω_n denotes the nominal electrical rotor angular speed, T_n denotes the nominal torque, and r_{1n} and r_{2n} are the nominal stator and rotor resistance, respectively). (**a**) P-MRAS for stator resistance estimation; (**b**) Q-MRAS for the rotor resistance estimation. In the case of the P-MRAS, the inverter nonlinearity is activated at 7.5 s and deactivated at 23 s, and, in the case of the Q-MRAS, the inverter nonlinearity is activated at 4 s and deactivated at 9 s.

In the case of the stator resistance, the voltage nonlinearity significantly impacts the estimation accuracy because the distorted voltage is utilized not only by the voltage model but also by the P-MRAS reference and adaptive models. The wrong estimate during the low-speed and light-load operation is given mainly by the relatively low ratio of the fundamental and distorting voltage vector. At higher speeds, the relative influence of the stator resistance on the FOC performance decreases, which also impairs the estimator's performance.

The rotor resistance estimation depicted in Figure 9b is, overall, much less sensitive to the voltage distortion because the stator voltage influences the estimator only through the Q-MRAS reference and adaptive models. Like the P-MRAS, the resulting estimates are influenced by the voltage nonlinearity mainly during low-speed and high-speed low-load operations.

7.3. Influence of Iron Losses on P-MRAS and Q-MRAS Estimators

The simulation setup is as follows:

- The IM model is implemented with iron losses using (1)–(6).
- The inverter is bypassed, i.e., the machine is supplied by a sinusoidal voltage.
- The FOC model makes it possible to switch between voltage, current, and synchronous speed estimation with and without iron losses.
- The sample time of the FOC model (triggered subsystem) is selected as 10 µs.
- The rotor flux is set to a nominal value.

Figure 10 shows the influence of the iron losses on the stator resistance (Figure 10a) and rotor resistance (Figure 10b) estimation. The iron losses are a non-linear phenomenon whose influence on the flux estimation at different speeds and applied load torques is described by complicated functions [42]. Combining the FOC with MRAS creates a complex system where it is complicated to express the influence of the iron losses on the whole system performance by explicit analytical expression. Overall, it can be stated that the iron losses definitely and not negligibly affect the parameter estimation process and that the influences of the speed and load are interconnected. However, in the case of the P-MRAS, the impact of the iron losses on the estimation accuracy is relatively lower compared to the inverter nonlinearity.

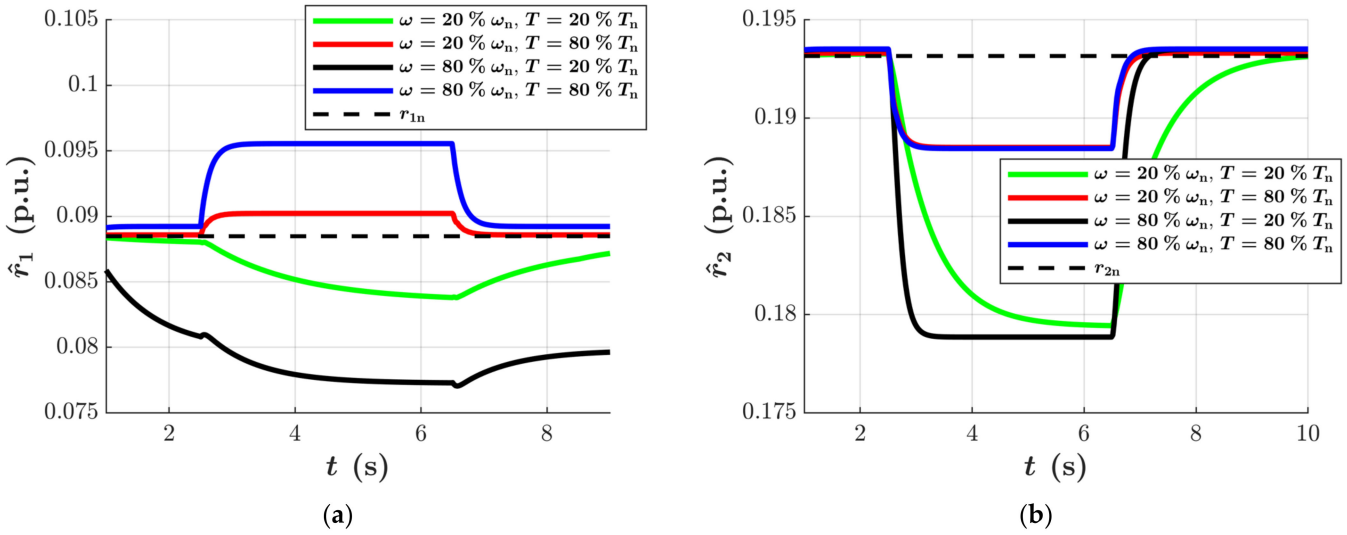

Figure 10. The effect of iron losses on the performance of MRAS-type estimators (ω_n denotes the nominal electrical rotor angular speed, T_n denotes the nominal torque, and r_{1n} and r_{2n} are the nominal stator and rotor resistance, respectively). (**a**) P-MRAS for the stator resistance estimation; (**b**) Q-MRAS for the rotor resistance estimation. Compensation of iron losses in the FOC model deactivated at 2.5 s and activated again at 6.5 s.

7.4. Influence of Discretization and Sampling Time on P-MRAS and Q-MRAS Estimators

The last examined phenomenon is the effect of the discretization and sampling time on the relative error of the estimate. The simulation setup is as follows:

- The IM model is implemented without iron losses using (8)–(12).
- The inverter is bypassed, i.e., the machine is supplied by a sinusoidal voltage.
- The sample time of the FOC model (triggered subsystem) is varied from 10 µs to 300 µs.
- The FWEM and TR are selected by specifying an integration method in the Discrete-Time Integrator blocks used in the DFOC model. The RK4 method is implemented manually using the MATLAB Function block.
- The rotor flux is set to a nominal value.

Figure 11 shows the influence of the discretization method and sampling time on the resulting relative error of the stator resistance estimation. As expected, the influence of the discretization method grows with the increasing sampling time. Furthermore, the relative error is much more significant at higher speeds because of the higher fundamental and sampling frequency ratio. Since the order of the trapezoidal method is only one order higher than the Euler method, it should be a preferred choice.

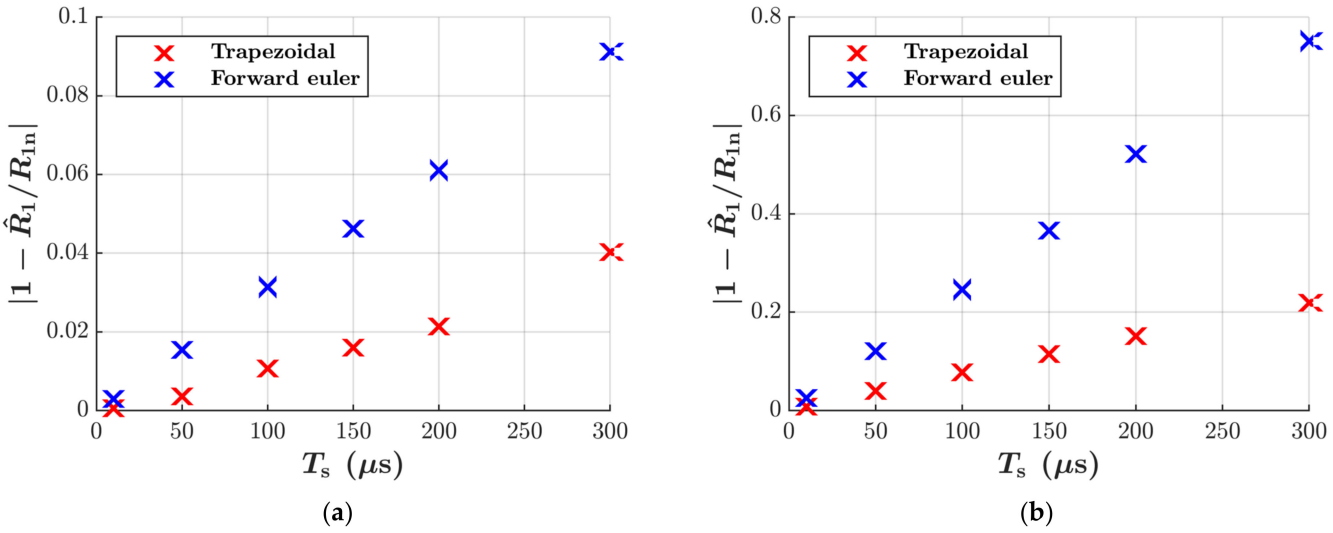

Figure 11. The effect of discretization and sampling time T_s on P-MRAS accuracy at different operating points. (**a**) 20% of the nominal speed and 50% of the nominal torque; (**b**) 80% of the nominal speed and 50% of the nominal torque.

Figure 12 shows the results for the Q-MRAS estimator. Here, because of the current model, the RK4 solver is also tested. The results and conclusions for the TR and FWEM are the same as in the case of Figure 11. The RK4 method can increase the estimation accuracy, especially at higher sampling times. Moreover, it is supposed to maintain higher numerical stability during fast transients.

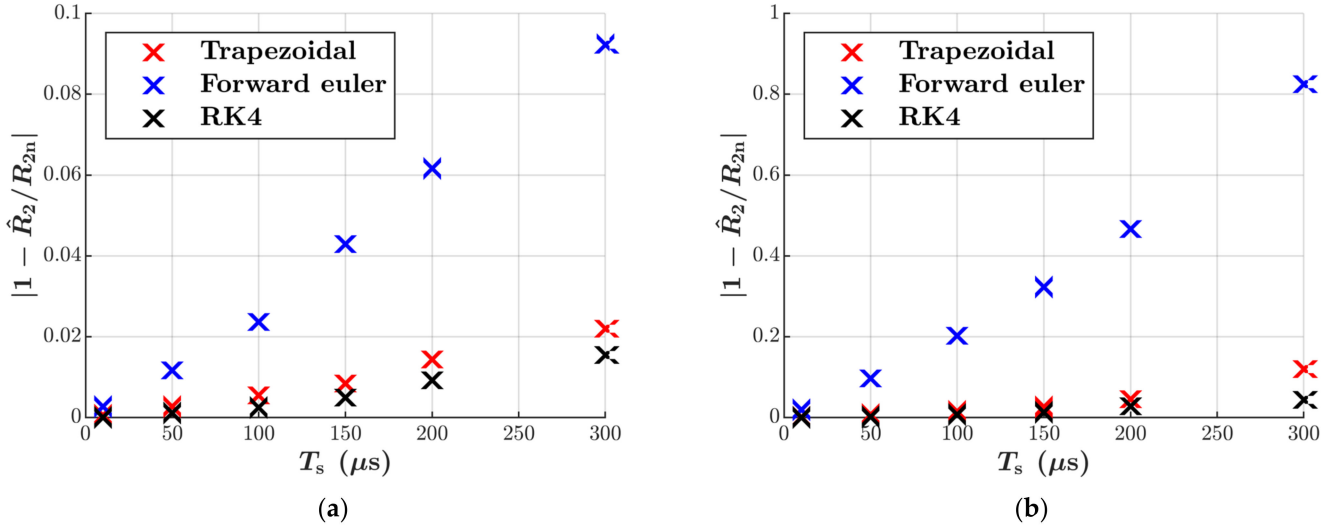

Figure 12. The effect of discretization and sampling time T_s on Q-MRAS accuracy at different operating points. (**a**) 20% of the nominal speed and 50% of the nominal torque; (**b**) 80% of the nominal speed and 50% of the nominal torque.

If hardware with sufficient computational power, such as FPGA or DSP with FPGA, is used in real applications, the FOC performance can be increased by oversampling. However, this might not always be the most cost-effective solution. The sampling time is often tied to the PWM period in medium-power drives operating with the switching

frequencies around 10 kHz, which, according to Figures 11 and 12, can deteriorate the accuracy of the MRAS-type estimators.

8. Discussion

This paper investigated three actual application phenomena on the accuracy of the popular Q-MRAS and P-MRAS rotor and stator resistance estimators. The studied adverse effects include inverter nonlinearity, iron losses, ODE solver type, and sampling time selection. The main results and contributions of the paper can be summarized as follows:

- If not adequately accounted for, the inverter nonlinearity has a key influence on the parameter estimation in the case of the P-MRAS and voltage model. The Q-MRAS is also affected by the inaccurate voltage evaluation, but relatively much less.
- The influence of iron losses on the stator and rotor resistance estimation accuracy is investigated using improved reduced-order IM models and improved Q-MRAS and P-MRAS estimators with the included iron losses. The simulation results show that, if not adequately compensated, the nonlinear phenomenon of iron losses impairs the estimation process and leads to inaccurately identified parameters. The error can become quite significant and is comparable for both the stator and rotor resistance estimation.
- Numerical method and sampling time selection can also affect the MRAS-based parameter estimation. When oversampling is impossible, and the drive control system operates with the sampling time around 100 µs, it is recommended to use at least the trapezoidal rule because the improvement compared to Euler's method is significant. The difference between the Runge–Kutta fourth-order method and the trapezoidal rule is not so pronounced. However, the RK4 method is expected to exhibit better numerical stability.

In the case of the inverter nonlinearity and iron losses, the operating conditions, i.e., the applied load and the rotor speed, represent a complicated mixed influence on the stator and rotor estimation accuracy. The analytical description of the observed would represent a highly complex task due to the nonlinearity of the whole system.

Author Contributions: Conceptualization, O.L., F.B. and J.B.; methodology, O.L. and F.B.; software, O.L. and F.B.; validation, O.L. and F.B.; formal analysis, O.L. and F.B.; investigation, O.L.; resources, O.L.; data curation, F.B.; writing—original draft preparation, O.L.; writing—review and editing, O.L.; visualization, O.L. and F.B.; supervision, J.B. and O.L.; project administration, J.B. and O.L.; funding acquisition, J.B. and O.L. All authors have read and agreed to the published version of the manuscript.

Funding: This research was funded by the Student Grant Agency of the Czech Technical University in Prague under grant No. SGS21/116/OHK3/2T/13.

Institutional Review Board Statement: Not applicable.

Informed Consent Statement: Not applicable.

Conflicts of Interest: The authors declare no conflict of interest.

List of Symbols

The following symbols are used in the paper:

$\underline{i}_1$, $\underline{i}_2$, $\underline{i}_m$, $\underline{i}_{Fe}$	stator, rotor, magnetizing, and iron loss current space vector (A)
$\underline{u}_1$, $\underline{u}_m$	stator and magnetizing voltage space vector (V)
$\underline{\psi}_1$, $\underline{\psi}_2$, $\underline{\psi}_m$	stator, rotor, and magnetizing flux linkage space vector (Wb)
L_1, L_2, L_m	stator, rotor, and magnetizing inductance (H)
$L_{1\sigma}$, $L_{2\sigma}$	stator and rotor leakage inductance (H)
R_1, R_2, R_{Fe}	stator resistance, rotor resistance, equivalent iron loss resistance
S_a, S_b, S_c	logical switching variables (-)
T_{on}, T_{off}, T_{dt}, T_{eff}	turn-on time, turn-off time, dead-time, and effective dead-time (s)
T_{PWM}, T_s	PWM period, sampling time (s)

U_{DC}	DC-link voltage (V)
d_x^*, d_x', $d_{dist(x)}$	reference, adjusted, and distorting compare value (-)
p_p	number of pole-pairs (-)
Ω	mechanical rotor speed (rad·s^{-1})
J	moment of inertia (kg·m^2)
P, P_{Fe}	active power, iron losses (W)
Q	reactive power (VAr)
T, T_L, T_n	motor electromechanical torque, load torque, nominal torque (Nm)
σ	leakage factor (-); $\sigma = 1 - L_m^2/(L_1 L_2)$
ω, ω_s, ω_{sl}, ω_n	electrical rotor speed, synchronous speed, slip speed, nominal speed (rad·s^{-1})
$*$	reference value
a, b, c	notation of stator phases
d, q	real and imaginary axis of the synchronous reference frame
k	notation of a general reference frame
α, β	real and imaginary axis of the stator-fixed reference frame

Appendix A

Table A1. Induction motor nameplate data and mathematical model parameters.

Nameplate Data		Mathematical Model Parameters	
Nominal power	3.6 kW	Stat. resistance	1.688 Ω
Nominal voltage	380 V	Rot. resistance	3.685 Ω
Nominal current	11.5 A	Stat. leak inductance	0.012 H
Nominal speed	935 min^{-1}	Rot. leak. inductance	0.013 H
Number of poles	6	Mag. inductance	0.175 H
Winding connection	Y	Iron core resistance	520 Ω

Table A2. P-MRAS and Q-MRAS adaptive PI controller gain values.

P-MRAS		Q-MRAS	
Proportional gain	10^{-4}	Proportional gain	10^{-6}
Integral gain	0.25	Integral gain	0.05

References

1. Wang, F.; Zhang, Z.; Mei, X.; Rodríguez, J.; Kennel, R. Advanced Control Strategies of Induction Machine: Field Oriented Control, Direct Torque Control and Model Predictive Control. *Energies* **2018**, *11*, 120. [CrossRef]
2. Wang, K.; Huai, R.; Yu, Z.; Zhang, X.; Li, F.; Zhang, L. Comparison Study of Induction Motor Models Considering Iron Loss for Electric Drives. *Energies* **2019**, *12*, 503. [CrossRef]
3. Hinkkanen, M.; Repo, A.; Luomi, J. Influence of magnetic saturation on induction motor model selection. In Proceedings of the 17th International Conference on Electrical Machines (ICEM), Chania, Greece, 2–5 September 2006.
4. Ranta, M.; Hinkkanen, M.; Dlala, E.; Repo, A.; Luomi, J. Inclusion of hysteresis and eddy current losses in dynamic induction machine models. In Proceedings of the 2009 IEEE International Electric Machines and Drives Conference, Miami, FL, USA, 3–6 May 2009; pp. 1387–1392.
5. Tang, J.; Yang, Y.; Blaabjerg, F.; Chen, J.; Diao, L.; Liu, Z. Parameter Identification of Inverter-Fed Induction Motors: A Review. *Energies* **2018**, *11*, 2194. [CrossRef]
6. Kostal, T.; Kobrle, P. Induction Machine On-Line Parameter Identification for Resource-Constrained Microcontrollers Based on Steady-State Voltage Model. *Electronics* **2021**, *10*, 1981. [CrossRef]
7. Huynh, D.C.; Dunnigan, M.W.; Finney, S.J. On-line parameter estimation of an induction machine using a recursive least-squares algorithm with multiple time-varying forgetting factors. In Proceedings of the 2010 IEEE International Conference on Power and Energy, Kuala Lumpur, Malaysia, 29 November–1 December 2010; pp. 444–449.
8. Reddy Siddavatam, R.P.; Loganathan, U. Identification of Induction Machine parameters including Core Loss Resistance using Recursive Least Mean Square Algorithm. In Proceedings of the 45th Annual Conference of the IEEE Industrial Electronics Society, Lisbon, Portugal, 14–17 October 2019; pp. 1095–1100.
9. Zhao, H.; Eldeeb, H.H.; Wang, J.; Kang, J.; Zhan, Y.; Xu, G.; Mohammed, O.A. Parameter Identification Based Online Noninvasive Estimation of Rotor Temperature in Induction Motors. *IEEE Trans. Ind. Appl.* **2021**, *57*, 417–426. [CrossRef]

10. Bednarz, S.A.; Dybkowski, M. Estimation of the Induction Motor Stator and Rotor Resistance Using Active and Reactive Power Based Model Reference Adaptive System Estimator. *Appl. Sci.* **2019**, *9*, 5145. [CrossRef]
11. Cao, P.; Zhang, X.; Yang, S. A Unified-Model-Based Analysis of MRAS for Online Rotor Time Constant Estimation in an Induction Motor Drive. *IEEE Trans. Ind. Electron.* **2017**, *64*, 4361–4371. [CrossRef]
12. Maiti, S.; Chakraborty, C.; Hori, Y.; Ta, M.C. Model Reference Adaptive Controller-Based Rotor Resistance and Speed Estimation Techniques for Vector Controlled Induction Motor Drive Utilizing Reactive Power. *IEEE Trans. Ind. Electron.* **2008**, *55*, 594–601. [CrossRef]
13. Cao, P.; Zhang, X.; Yang, S.; Xie, Z.; Zhang, Y. Reactive-Power-Based MRAS for Online Rotor Time Constant Estimation in Induction Motor Drives. *IEEE Trans. Power Electron.* **2018**, *33*, 10835–10845. [CrossRef]
14. Mapelli, F.L.; Tarsitano, D.; Cheli, F. A rotor resistance MRAS estimator for EV induction motor traction drive based on torque and reactive stator power: Simulation and experimental results. In Proceedings of the 2014 International Conference on Electric Machines (ICEM), Berlin, Germany, 2–5 September 2014; pp. 31–37.
15. Dybkowski, M. Universal Speed and Flux Estimator for Induction Motor. *Power Electron. Drives.* **2018**, *3*, 157–169. [CrossRef]
16. Liu, L.; Guo, Y.; Wang, J. Online identification of mutual inductance of induction motor without magnetizing curve. In Proceedings of the 2018 Annual American Control Conference (ACC), Milwaukee, WI, USA, 27–29 June 2018; pp. 3293–3297.
17. Cho, K.; Seok, J. Induction Motor Rotor Temperature Estimation Based on a High-Frequency Model of a Rotor Bar. *IEEE Trans. Ind. Appl.* **2009**, *45*, 1267–1275.
18. Baneira, F.; Yepes, A.G.; Lópezm, Ó.; Doval-Gandoy, J. Estimation Method of Stator Winding Temperature for Dual Three-Phase Machines Based on DC-Signal Injection. *IEEE Trans. Power Electron.* **2016**, *31*, 5141–5148. [CrossRef]
19. Briz, F.; Degner, M.W.; Guerrerom, J.M.; Diez, A.B. Temperature estimation in inverter fed machines using high frequency carrier signal injection. In Proceedings of the 2007 IEEE Industry Applications Annual Meeting, New Orleans, LA, USA, 23–27 September 2007; pp. 2030–2037.
20. Hasan, S.M.N.; Husain, I. A Luenberger–Sliding Mode Observer for Online Parameter Estimation and Adaptation in High-Performance Induction Motor Drives. *IEEE Trans. Ind. Appl.* **2009**, *45*, 772–781. [CrossRef]
21. Yang, S.; Ding, D.; Li, X.; Xie, Z.; Zhang, X.; Chang, L. A Novel Online Parameter Estimation Method for Indirect Field Oriented Induction Motor Drives. *IEEE Trans. Energy Convers.* **2017**, *32*, 1562–1573. [CrossRef]
22. Zerdali, E. A Comparative Study on Adaptive EKF Observers for State and Parameter Estimation of Induction Motor. *IEEE Trans. Energy Convers.* **2020**, *35*, 1443–1452. [CrossRef]
23. Cetin, O.; Dalcalı, A.; Temurtas, F. A comparative study on parameters estimation of squirrel cage induction motors using neural networks with unmemorized training. *Eng. Sci. Technol. Int. J.* **2020**, *23*, 1126–1133.
24. Wlas, M.; Krzeminski, Z.; Toliyat, H.A. Neural-Network-Based Parameter Estimations of Induction Motors. *IEEE Trans. Ind. Electron.* **2008**, *55*, 1783–1794. [CrossRef]
25. Pham Van, T.; Vo Tien, D.; Leonowicz, Z.; Jasinski, M.; Sikorski, T.; Chakrabarti, P. Online Rotor and Stator Resistance Estimation Based on Artificial Neural Network Applied in Sensorless Induction Motor Drive. *Energies* **2020**, *13*, 4946. [CrossRef]
26. Vasic, V.; Vukosavic, S.N.; Levi, E. A stator resistance estimation scheme for speed sensorless rotor flux oriented induction motor drives. *IEEE Trans. Energy Convers.* **2003**, *18*, 476–483. [CrossRef]
27. Agrebi, Y.; Yassine, K.; Boussak, M. Sensorless Speed Control with MRAS for Induction Motor Drive. In Proceedings of the 20th International Conference on Electrical Machines (ICEM), Marseille, France, 2–5 September 2012; pp. 2259–2265.
28. Jo, G.-J.; Choi, J.-W. A Novel Method for the Identification of the Rotor Resistance and Mutual Inductance of Induction Motors Based on MRAC and RLS Estimation. *J. Power Electron.* **2018**, *18*, 492–501.
29. Perng, S.-S.; Lai, Y.-S.; Liu, C.-H. Sensorless vector controller for induction motor drives with parameter identification. In Proceedings of the 24th Annual Conference of the IEEE Industrial Electronics Society, Aachen, Germany, 31 August–4 September 1998; pp. 1008–1013.
30. Mapelli, F.L.; Bezzolato, A.; Tarsitano, D. A rotor resistance MRAS estimator for induction motor traction drive for electrical vehicles. In Proceedings of the 2012 20th International Conference on Electrical Machines, Marseille, France, 2–5 September 2012; pp. 823–829.
31. Basak, S.; Ravi Teja, A.V.; Chakraborty, C.; Hori, Y. A new model reference adaptive formulation to estimate stator resistance in field oriented induction motor drive. In Proceedings of the 39th Annual Conference of the IEEE Industrial Electronics Society, Vienna, Austria, 10–13 November 2013; pp. 8470–8475.
32. Ravi Teja, A.V.; Chakraborty, C.; Maiti, S.; Hori, Y. A New Model Reference Adaptive Controller for Four Quadrant Vector Controlled Induction Motor Drives. *IEEE Trans. Ind. Electron.* **2012**, *59*, 3757–3767. [CrossRef]
33. Yang, S.; Cao, P.; Zhang, X. Stability analysis of q-axis rotor flux based model reference adaptive system updating rotor time constant in induction motor drives. *CES Trans. Electr. Mach. Syst.* **2017**, *1*, 109–116. [CrossRef]
34. Moreira, J.C.; Lipo, T.A. A new method for rotor time constant tuning in indirect field oriented control. In Proceedings of the 21st Annual IEEE Conference on Power Electronics Specialists, San Antonio, TX, USA, 11–14 June 1990; pp. 573–580.
35. Yu, X.; Dunnigan, M.W.; Williams, B.W. A novel rotor resistance identification method for an indirect rotor flux-orientated controlled induction machine system. *IEEE Trans. Power Electron.* **2002**, *17*, 353–364.
36. Mapelli, F.L.; Tarsitano, D.; Cheli, F. MRAS rotor resistance estimators for EV vector controlled induction motor traction drive: Analysis and experimental results. *Elect. Power Syst. Res.* **2017**, *146*, 298–307. [CrossRef]

37. Das, S.; Kumar, R.; Pal, A. MRAS-Based Speed Estimation of Induction Motor Drive Utilizing Machines' d- and q-Circuit Impedances. *IEEE Trans. Ind. Electron.* **2019**, *66*, 4286–4295. [CrossRef]
38. Kumar, R.; Das, S.; Chattopadhyay, A.K. Comparative assessment of two different model reference adaptive system schemes for speed-sensorless control of induction motor drives. *IET Elect. Power Appl.* **2016**, *10*, 141–154. [CrossRef]
39. Pal, A.; Das, S.; Chattopadhyay, A.K. An Improved Rotor Flux Space Vector Based MRAS for Field-Oriented Control of Induction Motor Drives. *IEEE Trans. Power Electron.* **2018**, *33*, 5131–5141. [CrossRef]
40. Korzonek, M.; Orlowska-Kowalska, T. Discrete Implementation of Sensorless IM Drive with MRAS-type Speed Estimator. In Proceedings of the 2019 International Conference on Electrical Drives & Power Electronics (EDPE), The High Tatras, Slovakia, 24–26 September 2019; pp. 242–247.
41. Korzonek, M.; Orlowska-Kowalska, T. Application of Different Numerical Integration Methods for Discrete Mras^{CC} Estimator of Induction Motor Speed—Comparative Study. In Proceedings of the 2018 IEEE 18th International Power Electronics and Motion Control Conference (PEMC), Budapest, Hungary, 26–30 August 2018; pp. 806–811.
42. Sokola, M. Vector Control of Induction Machines Using Improved Models. Ph.D. Thesis, Liverpool John Moores University, Liverpool, UK, 1998.
43. Chatterjee, D. Impact of core losses on parameter identification of three-phase induction machines. *IET Power Electron.* **2014**, *7*, 3126–3136. [CrossRef]
44. Chen, W.; Cheng, K.; Chen, K. Derivation and verification of a vector controller for induction machines with consideration of stator and rotor core losses. *IET Elect. Power Appl.* **2018**, *12*, 1–11. [CrossRef]
45. Sokola, M.; Levi, E. A Novel Induction Machine Model and Its Application in the Development of an Advanced Vector Control Scheme. *Int. J. Electr. Eng. Educ.* **2000**, *37*, 233–248. [CrossRef]
46. Popescu, M. *Induction Motor Modelling for Vector Control Purposes*; Helsinki University of Technology: Espoo, Finland, 2000; p. 144.
47. Butcher, J.C. *Numerical Methods for Ordinary Differential Equations*, 3rd ed.; John Wiley & Sons Inc.: New York, NY, USA, 2016.
48. Lipcak, O.; Bauer, J. Analysis of Voltage Distortion and Comparison of Two Simple Voltage Compensation Methods for Sensorless Control of Induction Motor. In Proceedings of the 2019 IEEE 10th International Symposium on Sensorless Control for Electric Drives (SLED), Torino, Italy, 9–10 September 2019; pp. 1–6.
49. *Rotating Electrical Machines—Part 2-1: Standard Methods for Determining Losses and Efficiency from Tests (Excluding Machines for Traction Vehicles)*, 2nd ed.; IEC 60034-2-1; IEEE: New York, NY, USA, 2014.
50. Karkkainen, H.; Aarniovuori, L.; Niemela, M.; Pyrhonen, J. Converter-Fed Induction Motor Efficiency: Practical Applicability of IEC Methods. *IEEE Ind. Electron. Mag.* **2017**, *11*, 45–57. [CrossRef]

CONCLUSION

This doctoral thesis is submitted as a set of three impact factor articles and one conference article with accompanying text. The additional sections beyond the articles were mainly devoted to the theoretical background that supports or supplements the presented papers. Furthermore, more detailed information regarding the respective topics was moved into appendices to keep the theoretical part concise and clear.

Based on a survey of the methods and approaches in the available literature, the author of this dissertation has identified several problems that occur in IM drives that have not yet been adequately addressed and fully resolved. The main prerequisite for the author's further research was the determination and compensation of the inverter nonlinearities, which was the subject of interest of the paper presented in section 3.1. The paper clearly describes the most significant sources of the inverter voltage distortion, including a simple method for their measurement. The paper's novelty lies mainly in assessing and comparing two compensation strategies and two compensation characteristics with respect to computational requirements, distorting voltage vector elimination, and overall influence on the MRAS-based sensorless vector control. The paper can be of use to researchers that need to select a practical and non-demanding approach to voltage distortion measurement and compensation.

One of the critical IM parameters that strongly affects the FOC quality is the magnetizing inductance, which appears in the transverse branch of the IM equivalent circuits. The magnetizing inductance is usually used in vector control as a constant parameter or better, as a magnetizing curve determined mainly from the standard no-load test. In most cases, both solutions lead to satisfactory results but do not fully respect reality because they neglect the saturation due to the load. The phenomenon of load-dependent saturation was mentioned several times in papers published before the year 2000 and in recent years tackled in a series of papers from Aalto University. However, it still needs further in-depth investigation and, therefore, the attention of the researchers. Therefore, the thesis author has developed a novel, simple experimental method to determine the IM saturation characteristics with respect to the load. The proposed method is described in the paper presented in section 3.2. The experimental results show that lower current consumption and better drive dynamics can be achieved when the proposed 3D magnetizing characteristic is implemented. The energy savings resulting from reduced current consumption of about 0.5 to 1 A may seem small but imagine extrapolating the savings to a megawatt locomotive drive, which will probably be in operation for at least 20 years. Therefore, it would be quite exciting and purposeful to see whether the proposed method also applies to high-power traction motors, usually designed differently than small and medium power low-voltage motors.

The main contribution to the field can be considered the paper presented in section 3.3, which is the author's latest publication and incorporates ideas, approaches, and methods from previous papers. The paper gives guidance on how the iron losses can be included in MRAS-based IM magnetizing inductance estimator and rigorously derives the adaptation mechanism together with the error variable based on the Lyapunov function. Thus, the paper can be a stepping stone for deriving further improved estimators, including, for example, additional losses, which are even more often neglected in the IM parameter estimation process than the classically understood (i.e., load-independent) iron losses. Another contribution of the paper is that it also mentions and strives to identify the often neglected phenomena of load-dependent saturation.

Neglecting the influence of the iron losses does not necessarily mean a significant deterioration of the control quality as such. However, it may reduce the accuracy of algorithms such as MRAS or observers trying to identify IM parameters or speed. Furthermore, the literature also lacks quantitative analysis of other non-ideal aspects, such as the influence of discretization and voltage distortion, on the parameter estimation process. For this task, a simulation analysis is very useful since we can define the “real” value in the system model (i.e., in the model of IM) and

compare it with the estimated value in the control model. It is also possible to study the decoupled influence of the individual negative phenomena acting on the system. Such an analysis was a subject of research presented in the paper in section 3.4. The paper is based on a complex simulation model in the MATLAB/Simulink environment, which permits to study the effects of iron losses, voltage distortion, and discretization on the performance of MRAS-based stator and rotor resistance estimation. The paper also derives improved voltage and current models and extends the MRAS estimators to include the effect of iron losses. A significant contribution of the paper is that it gives the reader a clear and one-stop guide on how to model and simulate certain nonlinearities and imperfections occurring in IM drive.

To sum up the work done within the author's doctoral study and thesis, it can be concluded that, among others:

- Novel magnetizing inductance estimation methods were developed. The first method permits the identification of the load-dependent saturation, while the other can also identify the no-load magnetizing inductance in the presence of iron losses.
- FOC and the additional algorithms were programmed in C into a Texas Instruments TMS320F28335 DSP and verified on 12 kW (papers in sections 3.1 and 3.2) and 3.6 kW (papers in sections 3.3 and 3.4) IM laboratory drives.
- Complex simulation models of IM drive with included selected nonlinearities were created in MATLAB/Simulink environment.
- A nonlinear model of the voltage-source inverter was identified, and the voltage compensation was incorporated into the FOC algorithms.
- Iron losses were measured, fitted, and incorporated into the control algorithms.
- Reduced-order IM models (current and voltage model) with the effect of iron losses were derived.
- Advanced modified integrator with the DC offset elimination was proposed and implemented.
- The IM current model was implemented using a robust Runge-Kutta 4^{th} order method.
- MRAS stator and rotor resistance estimators with the included effect of iron losses were derived.

The motivation behind the presented papers, along with the summary of the main contribution, discussion about the presented results, and suggestions about the possible improvement and future work, were stated in more detail in the respective sections.

The thesis author would like to dedicate his future research to the advanced modeling of AC machines for FOC purposes. Still, after many years and countless papers that were devoted to modeling and control algorithms of AC electrical machines, there are many phenomena such as the load-dependent saturation, stray-load losses, influence of higher spatial and time harmonics that need further investigation with respect to the overall accuracy and robustness of the sensorless and sensored control algorithms and parameter estimation techniques.

REFERENCES

[1] Y. Wang, W. Xie, X. Wang and D. Gerling, "A Precise Voltage Distortion Compensation Strategy for Voltage Source Inverters," in *IEEE Transactions on Industrial Electronics*, vol. 65, no. 1, pp. 59-66, Jan. 2018.

[2] N.P. Quang and J. Dittrich, *Vector Control of Three-Phase AC Machines: System Development in the Practice*. 1. Aufl. ed. Berlin, Heidelberg: Springer-Verlag; 2008.

[3] S. Bolognani and M. Zigliotto, "Self-commissioning compensation of inverter non-idealities for sensorless AC drives applications," *2002 International Conference on Power Electronics, Machines and Drives (Conf. Publ. No. 487)*, Santa Fe, NM, USA, 2002, pp. 30-37.

[4] Z. Shen and D. Jiang, "Dead-Time Effect Compensation Method Based on Current Ripple Prediction for Voltage-Source Inverters," in *IEEE Transactions on Power Electronics*, vol. 34, no. 1, pp. 971-983, Jan. 2019.

[5] D. E. Salt, D. Drury, D. Holliday, A. Griffo, P. Sangha and A. Dinu, "Compensation of Inverter Nonlinear Distortion Effects for Signal-Injection-Based Sensorless Control," in *IEEE Transactions on Industry Applications*, vol. 47, no. 5, pp. 2084-2092, Sept.-Oct. 2011.

[6] G. Shen, W. Yao, B. Chen, K. Wang, K. Lee and Z. Lu, "Automeasurement of the Inverter Output Voltage Delay Curve to Compensate for Inverter Nonlinearity in Sensorless Motor Drives," in *IEEE Transactions on Power Electronics*, vol. 29, no. 10, pp. 5542-5553, Oct. 2014.

[7] M. Seilmeier, C. Wolz and B. Piepenbreier, "Modelling and model based compensation of non-ideal characteristics of two-level voltage source inverters for drive control application," *2011 1st International Electric Drives Production Conference*, Nuremberg, 2011, pp. 17-22.

[8] M. El-daleel and A. Mahgoub, "Accurate and simple improved look-up table compensation for inverter dead time and nonlinearity compensation," *2017 Nineteenth International Middle East Power Systems Conference (MEPCON)*, Cairo, 2017, pp. 1358-1361.

[9] A. Wintrich, U. Nicolai, W. Tursky and T. Reimann, *Application manual power semiconductors*. SEMIKRON International GmbH, Ilmenau: ISLE Verlag, 2015.

[10] Mitsubishi Electric. *IGBT Modules Application Note, The 5th Generation [CSTBT™] IGBT Chip Use, 12NF/24NF/24A series.* Mar. 2014.

[11] ABB. *Applying IGBTs.* Application Note 5SYA-2053-04. Sep. 2013.

[12] STM. *IGBT datasheet tutorial*. Application Note AN4544. Sep. 2014.

[13] R. McArthur, "Making use of gate charge information in MOSFET and IGBT data sheets," *Application Note APT0103*, Rev – Oct. 31, 2001.

[14] J. Pyrhönen, T. Jokinen, V. Hrabovcova, *Design of rotating electrical machines*, 2nd ed. Chichester: Wiley; 2014.

[15] B. Heller and V. Hamata, *Přídavná pole, síly a ztráty v asynchronním stroji*, (in Czech), Praha: Nakladatelství Čsl. akademie věd, 1961.

[16] J. Štěpina, *Souměrné složky v teorii točivých elektrických strojů*, (in Czech), Vyd. 1 ed. Praha: Academia; 1969.

[17] J. Stepina, "Matrix Calculation of Inductances for the General Theory of Electrical Machines," in *Electric Machines & Power Systems*, 1986, 11:1, 53-63.

[18] M. Srndovic, R. Fišer, and G. Grandi, "Analysis of Equivalent Inductance of Three-phase Induction Motors in the Switching Frequency Range," in *Electronics*, vol. 8, no. 2, p. 120, Jan. 2019.

[19] A. Boglietti, A. Cavagnino, L. Ferraris and M. Lazzari, "Skin effect experimental validations of induction motor squirrel cage parameters," *2008 18th International Conference on Electrical Machines*, 2008, pp. 1-4.

[20] B. Mirafzal, G. L. Skibinski, R. M. Tallam, D. W. Schlegel and R. A. Lukaszewski, "Universal Induction Motor Model With Low-to-High Frequency-Response Characteristics," in *IEEE Transactions on Industry Applications*, vol. 43, no. 5, pp. 1233-1246, Sept.-oct. 2007.

[21] M. S. Toulabi, L. Wang, L. Bieber, S. Filizadeh and J. Jatskevich, "A Universal High-Frequency Induction Machine Model and Characterization Method for Arbitrary Stator Winding Connections," in IEEE Transactions on Energy Conversion, vol. 34, no. 3, pp. 1164-1177, Sept. 2019.

[22] M. Sokola, "Vector Control of Induction Machines Using Improved Models," *PhD thesis*, Liverpool John Moores University, Liverpool, U.K., 1998.

[23] E. Levi, "Main flux saturation modelling in double-cage and deep-bar induction machines," in *IEEE Transactions on Energy Conversion*, vol. 11, no. 2, pp. 305-311, June 1996.

[24] L. Lupsa-Tataru, "A Flux-Based Expression of Induction Machine Magnetizing Inductance," in *IEEE Transactions on Energy Conversion*, vol. 25, no. 1, pp. 268-270, March 2010.

[25] D. Chatterjee, "A Simple Leakage Inductance Identification Technique for Three-Phase Induction Machines Under Variable Flux Condition," in *IEEE Transactions on Industrial Electronics*, vol. 59, no. 11, pp. 4041-4048, Nov. 2012

[26] H. Rasmussen, M. Knudsen and M. Tonnes, "Parameter estimation of inverter and motor model at standstill using measured currents only," *Proceedings of IEEE International Symposium on Industrial Electronics*, Warsaw, Poland, 1996, pp. 331-336 vol.1.

[27] E. Levi, M. Sokola and S. N. Vukosavic, "A method for magnetizing curve identification in rotor flux oriented induction machines," in *IEEE Transactions on Energy Conversion*, vol. 15, no. 2, pp. 157-162, June 2000.

[28] P. Vas, "*Parameter Estimation, Condition Monitoring, and Diagnosis of Electrical Machines*," Oxford, U.K.: Clarendon, 1993.

[29] C. R. Sullivan and S. R. Sanders, "Models for induction machines with magnetic saturation of the main flux path," *Conference Record of the 1992 IEEE Industry Applications Society Annual Meeting*, Houston, TX, USA, 1992, pp. 123-131 vol.1.

[30] G. R. Slemon, "Modelling of induction machines for electric drives," in *IEEE Transactions on Industry Applications*, vol. 25, no. 6, pp. 1126-1131, Nov.-Dec. 1989.

[31] S. Moulahoum, O. Touhami, R. Ibtiouen and M. Fadel, "Induction Machine Modeling With Saturation and Series Iron Losses Resistance," *2007 IEEE International Electric Machines & Drives Conference*, Antalya, 2007, pp. 1067-1072.

[32] O. Kiselychnyk, M. Bodson and J. Wang, "Comparison of Two Magnetic Saturation Models of Induction Machines and Experimental Validation," in *IEEE Transactions on Industrial Electronics*, vol. 64, no. 1, pp. 81-90, Jan. 2017

[33] T. Tuovinen, M. Hinkkanen and J. Luomi, "Modeling of Saturation Due to Main and Leakage Flux Interaction in Induction Machines," in *IEEE Transactions on Industry Applications*, vol. 46, no. 3, pp. 937-945, May-june 2010.

[34] E. Molsa, S. E. Saarakkala and M. Hinkkanen, "Influence of Magnetic Saturation on Modeling of an Induction Motor," 2018 XIII International Conference on Electrical Machines (ICEM), 2018, pp. 1572-1578.a

[35] C. Gerada, K. Bradley, M. Sumner and P. Sewell, "Evaluation and modelling of cross saturation due to leakage flux in vector controlled induction machines," *IEEE International Electric Machines and Drives Conference, 2003. IEMDC'03.*, Madison, WI, USA, 2003, pp. 1983-1989 vol.3.

[36] O. I. Butler and T. S. Birch, "Comparison of alternative skew-effect parameters of cage induction motors," in *Proceedings of the Institution of Electrical Engineers*, vol. 118, no. 7, pp. 879-883, July 1971.

[37] N. R. Klaes, "Parameters identification of an induction machine with regard to dependencies on saturation," *Conference Record of the 1991 IEEE Industry Applications Society Annual Meeting*, Dearborn, MI, 1991, pp. 21-27 vol.1.

[38] M. Hinkkanen, A. Repo, J. Luomi, J, "Influence of magnetic saturation on induction motor model selection, "*Proc. ICEM'06,* Chania, Greece, September 2006.

[39] P. Immonen, V. Ruuskanen, J. Nerg, et al., "Inductance saturation of the induction machine as a function of stator voltage and load with steady state AC magnetic finite element solver, "*International Review of Modeling and Simulation (IREMOS),* 2004.

[40] J. Nerg, J. Pyrhonen and J. Partanen, "Finite element modeling of the magnetizing inductance of an induction motor as a function of torque," in *IEEE Transactions on Magnetics*, vol. 40, no. 4, pp. 2047-2049, July 2004.

[41] J. Nerg, J. Pyrhönen, J. Partanen, M. Niemelä, A.E. Ritchie, "Induction Motor Magnetizing Inductance Modeling as a Function of Torque," in *Proceedings ICEM 2004, XVI International Conference On Electrical Machines*, Krakow, Poland, 2004, vol. 2, pp. 309.

[42] M. Hinkkanen, A. Repo, M. Cederholm and J. Luomi, "Small-Signal Modelling of Saturated Induction Machines With Closed or Skewed Rotor Slots," *2007 IEEE Industry Applications Annual Meeting*, New Orleans, LA, 2007, pp. 1200-1206.

[43] M. Ranta, M. Hinkkanen and J. Luomi, "Inductance identification of an induction machine taking load-dependent saturation into account," *2008 18th International Conference on Electrical Machines*, 2008, pp. 1-6.

[44] S. Bozhko, S. Dymko, S. Kovbasa and S. M. Peresada, "Maximum Torque-per-Amp Control for Traction IM Drives: Theory and Experimental Results," in *IEEE Transactions on Industry Applications*, vol. 53, no. 1, pp. 181-193, Jan.-Feb. 2017.

[45] R. Tarvirdilu-Asl and J. Bauman, "Efficiency Analysis of Induction Motor Control Strategies Using a System-Level EV Model," *2019 IEEE Transportation Electrification Conference and Expo (ITEC)*, Detroit, MI, USA, 2019.

[46] R. Krishnan, "Review of flux-weakening in high performance vector controlled induction motor drives," *Proceedings of IEEE International Symposium on Industrial Electronics*, Warsaw, Poland, 1996, pp. 917-922 vol.2.

[47] P. Xie, G. Li, F. Xie, C. Hu and X. Qi, "Research on field-weakening control of induction motor based on torque current component of the voltage closed-loop," *2015 IEEE 10th Conference on Industrial Electronics and Applications (ICIEA)*, Auckland, 2015, pp. 1618-1621.

[48] C. I. McClay and S. Williamson, "Influence of rotor skew on cage motor losses," in *IEE Proceedings - Electric Power Applications*, 1998, 145, (5), p. 414-422.

[49] K. J. Binns, R. Hindmarsh and B. P. Short, "Effect of skewing slots on flux distribution in induction machines," in *Proceedings of the Institution of Electrical Engineers*, vol. 118, no. 3.4, pp. 543-549, March-April 1971.

[50] T. S. Birch and O. I. Butler, "Permeance of closed-slot bridges and its effect on induction-motor-current computation," in *Proceedings of the Institution of Electrical Engineers*, vol. 118, no. 1, pp. 169-172, January 1971.

[51] S. Williamson and M. C. Begg, "Calculation of the bar resistance and leakage reactance of cage rotors with closed slots," in *IEE Proceedings B - Electric Power Applications*, vol. 132, no. 3, pp. 125-132, May 1985.

[52] H. Karkkainen, L. Aarniovuori, M. Niemela and J. Pyrhonen, "Converter-Fed Induction Motor Efficiency: Practical Applicability of IEC Methods," in *IEEE Industrial Electronics Magazine*, vol. 11, no. 2, pp. 45-57, June 2017.

[53] *Rotating Electrical Machines – Part 30-1: Efficiency Classes of Line Operated AC Motors (IE code),* Ed. 1, IEC 60034-30-1, 2014.

[54] *COMMISSION REGULATION (EU) 2019/1781 of 1 October 2019 laying down ecodesign requirements for electric motors and variable speed drives pursuant to Directive 2009/125/EC of the European Parliament and of the Council, amending Regulation (EC) No 641/2009 with regard to ecodesign requirements for glandless standalone circulators and glandless circulators integrated in products and repealing Commission Regulation (EC) No 640/2009*, [2019], OJ L272/74.

[55] *Rotating electrical machines - Part 30-2: Efficiency classes of variable speed AC motors (IE-code),* Ed. 1, IEC TS 60034-30-2, 2016.

[56] *Rotating Electrical Machines – Part 2-1: Standard Methods for Determining Losses and Efficiency from Tests (Excluding Machines for Traction Vehicles)*, Ed. 2, IEC 60034-2-1, 2014.

[57] L. Aarniovuori, P. Rasilo, M. Niemelä and J. J. Pyrhönen, "Analysis of 37-kW Converter-Fed Induction Motor Losses," in *IEEE Transactions on Industrial Electronics*, vol. 63, no. 9, pp. 5357-5365, Sept. 2016.

[58] J. Wang et al., "Stray Load Loss Calculation for Induction Motor by Combination of General Airgap Field Modulation Theory and 2D FEA," in *IEEE Transactions on Energy Conversion*, vol. 36, no. 3, pp. 2524-2533, Sept. 2021.

[59] *Rotating electrical machines - Part 2-3: Specific test methods for determining losses and efficiency of converter-fed AC motors,* Ed. 1, IEC 60034-2-3, 2020.

[60] M. Pablo, G.R. Bossio, J.A. Solsona and G.O. García, G.O., "Online iron loss resistance identification by a state observer for rotor-flux-oriented control of induction motor," *Energy Conversion and Management,* vol. 49, no. 10, 2008, pp. 2742-2747.

[61] D. Chatterjee, "Impact of core losses on parameter identification of three-phase induction machines," in *IET Power Electronics*, vol. 7, no. 12, pp. 3126-3136, Dec. 2014.

[62] W. Chen, K. Cheng and K. Chen, "Derivation and verification of a vector controller for induction machines with consideration of stator and rotor core losses," in *IET Electric Power Applications*, vol. 12, no. 1, pp. 1-11, Jan. 2018.

[63] S. Yamamoto, H. Hirahara, A. Tanaka, T. Ara and K. Matsuse, "Universal Sensorless Vector Control of Induction and Permanent-Magnet Synchronous Motors Considering Equivalent Iron Loss Resistance," in *IEEE Transactions on Industry Applications*, vol. 51, no. 2, pp. 1259-1267, March-April 2015.

[64] Z. Wang, H. Lv, X. Zhou, Z. Chen and Y. Yang, "Design and Modeling of a Test Bench for Dual-Motor Electric Drive Tracked Vehicles Based on a Dynamic Load Emulation Method," in *Sensors* (Basel, Switzerland), 18, 2008.

[65] M. Torrent, J.I. Perat and J.A. Jiménez, "Permanent Magnet Synchronous Motor with Different Rotor Structures for Traction Motor in High Speed Trains," in *Energies, 11*, 1549, 2008.

[66] A. Krings, S. Nategh, A. Stening, H. Grop, O. Wallmark, and J. Soulard, "*Measurement and modeling of iron losses in electrical machines*," inProc. 5th Int. Conf. WMM, Gent, Belgium, Jun. 2012, pp. 101–119.

[67] G. Bertotti, "General properties of power losses in soft ferromagnetic materials," in *IEEE Transactions on Magnetics*, vol. 24, no. 1, pp. 621-630, Jan. 1988.

[68] G. Bertotti, *Hysteresis in Magnetism*. San Diego, CA: Academic, 1998.

[69] A. Boglietti, A. Cavagnino, M. Lazzari and M. Pastorelli, "Predicting iron losses in soft magnetic materials with arbitrary voltage supply: an engineering approach," in *IEEE Transactions on Magnetics*, vol. 39, no. 2, pp. 981-989, March 2003.

[70] L. Petrescu, V. Ionita, E. Cazacu and C. Petrescu, "Steinmetz' parameters fitting procedure for the power losses estimation in soft magnetic materials," *2017 International Conference on Optimization*

of Electrical and Electronic Equipment (OPTIM) & 2017 Intl Aegean Conference on Electrical Machines and Power Electronics (ACEMP), Brasov, 2017.

[71] M. Popescu and D. M. Ionel, "A Best-Fit Model of Power Losses in Cold Rolled-Motor Lamination Steel Operating in a Wide Range of Frequency and Magnetization," in *IEEE Transactions on Magnetics*, vol. 43, no. 4, pp. 1753-1756, April 2007.

[72] A. Boglietti, A. Cavagnino, M. Lazzari and M. Pastorelli, "Two simplified methods for the iron losses prediction in soft magnetic materials supplied by PWM inverter," *IEMDC 2001. IEEE International Electric Machines and Drives Conference (Cat. No.01EX485)*, Cambridge, MA, USA, 2001

[73] S. Xue *et al*., "Iron Loss Model for Electrical Machine Fed by Low Switching Frequency Inverter," in *IEEE Transactions on Magnetics*, vol. 53, no. 11, pp. 1-4, Nov. 2017.

[74] A. Boglietti, A. Cavagnino, D. M. Ionel, M. Popescu, D. A. Staton and S. Vaschetto, "A General Model to Predict the Iron Losses in PWM Inverter-Fed Induction Motors," in *IEEE Transactions on Industry Applications*, vol. 46, no. 5, pp. 1882-1890, Sept.-Oct. 2010.

[75] D. M. Ionel, M. Popescu, M. I. McGilp, T. J. E. Miller, S. J. Dellinger and R. J. Heideman, "Computation of Core Losses in Electrical Machines Using Improved Models for Laminated Steel," in *IEEE Transactions on Industry Applications*, vol. 43, no. 6, pp. 1554-1564, Nov.-dec. 2007.

[76] M. Popescu, D. M. Ionel, A. Boglietti, A. Cavagnino, C. Cossar and M. I. McGilp, "A General Model for Estimating the Laminated Steel Losses Under PWM Voltage Supply," in *IEEE Transactions on Industry Applications*, vol. 46, no. 4, pp. 1389-1396, July-Aug. 2010.

[77] R. Roy, K. K. Prabhakar, and P. Kumar, "Core-loss calculation in different parts of induction motor," *IET Elect. Power Appl.*, vol. 11, no. 9, pp. 1664–1674, Nov. 2017.

[78] E. Dlala, O. Bottauscio, M. Chiampi, M. Zucca, A. Belahcen and A. Arkkio, "Numerical Investigation of the Effects of Loading and Slot Harmonics on the Core Losses of Induction Machines," in *IEEE Transactions on Magnetics*, vol. 48, no. 2, pp. 1063-1066, Feb. 2012.

[79] R. Kumar, P. Kumar, T. Kanekawa and K. Oishi, "Stray Loss Model for Induction Motors With Using Equivalent Circuit Parameters," in *IEEE Transactions on Energy Conversion*, vol. 35, no. 2, pp. 1036-1045, June 2020.

[80] K. Yamazaki and N. Fukushima, "Iron-Loss Modeling for Rotating Machines: Comparison Between Bertotti's Three-Term Expression and 3-D Eddy-Current Analysis," in *IEEE Transactions on Magnetics*, vol. 46, no. 8, pp. 3121-3124, Aug. 2010.

[81] J. Reinert, A. Brockmeyer and R. W. A. A. De Doncker, "Calculation of losses in ferro- and ferrimagnetic materials based on the modified Steinmetz equation," in *IEEE Transactions on Industry Applications*, vol. 37, no. 4, pp. 1055-1061, July-Aug. 2001.

[82] J. Muhlethaler, J. Biela, J. W. Kolar and A. Ecklebe, "Improved Core-Loss Calculation for Magnetic Components Employed in Power Electronic Systems," in *IEEE Transactions on Power Electronics*, vol. 27, no. 2, pp. 964-973, Feb. 2012.

[83] B.A. Nasir, "An Accurate Iron Core Loss Model in Equivalent Circuit of Induction Machines," in *Journal of Energy*, vol. 2020, pp. 1-10, 2020.

[84] M. Fasil, N. Mijatovic, B. B. Jensen and J. Holboll, "Nonlinear Dynamic Model of PMBLDC Motor Considering Core Losses," in *IEEE Transactions on Industrial Electronics*, vol. 64, no. 12, pp. 9282-9290, Dec. 2017.

[85] A. Kosonen, L. Aarniovuori, J. Ahola, J. Backman, J. Pyrhönen and M. Niemelä, "Loss Definition of Electric Drives by a Calorimetric System With Data Processing," in *IEEE Transactions on Industrial Electronics*, vol. 61, no. 8, pp. 4432-4442, Aug. 2014.

[86] V. Ruuskanen, J. Nerg, M. Rilla and J. Pyrhönen, "Iron Loss Analysis of the Permanent-Magnet Synchronous Machine Based on Finite-Element Analysis Over the Electrical Vehicle Drive Cycle," in *IEEE Transactions on Industrial Electronics*, vol. 63, no. 7, pp. 4129-4136, July 2016.

[87] D. Zhang, R. An and T. Wu, "Effect of voltage unbalance and distortion on the loss characteristics of three-phase cage induction motor," in *IET Electric Power Applications*, vol. 12, no. 2, pp. 264-270, 2 2018.

[88] A. Boglietti, P. Ferraris, M. Lazzari and M. Pastorelli, "Change of the iron losses with the switching supply frequency in soft magnetic materials supplied by PWM inverter," in *IEEE Transactions on Magnetics*, vol. 31, no. 6, pp. 4250-4252, Nov. 1995.

[89] D. Zhang, H. Dai, H. Zhao and T. Wu, "A Fast Identification Method for Rotor Flux Density Harmonics and Resulting Rotor Iron Losses of Inverter-Fed Induction Motors," in *IEEE Transactions on Industrial Electronics*, vol. 65, no. 7, pp. 5384-5394, July 2018.

[90] D. Zhang, T. Liu, H. Zhao and T. Wu, "An Analytical Iron Loss Calculation Model of Inverter-Fed Induction Motors Considering Supply and Slot Harmonics," in *IEEE Transactions on Industrial Electronics*, vol. 66, no. 12, pp. 9194-9204, Dec. 2019.

[91] S. Xue *et al*., "Iron Loss Model for Electrical Machine Fed by Low Switching Frequency Inverter," in *IEEE Transactions on Magnetics*, vol. 53, no. 11, pp. 1-4, Nov. 2017.

[92] A. Boglietti, P. Ferraris, M. Lazzari and M. Pastorelli, "Influence of the inverter characteristics on the iron losses in PWM inverter-fed induction motors," in *IEEE Transactions on Industry Applications*, vol. 32, no. 5, pp. 1190-1194, Sept.-Oct. 1996.

[93] A. Boglietti, P. Ferraris, M. Lazzari and F. Profumo, "Iron losses in magnetic materials with six-step and PWM inverter supply (induction motors)," in *IEEE Transactions on Magnetics*, vol. 27, no. 6, pp. 5334-5336, Nov. 1991.

[94] E. Levi, "Impact of iron loss on behavior of vector controlled induction machines," in *IEEE Transactions on Industry Applications*, vol. 31, no. 6, pp. 1287-1296, Nov.-Dec. 1995.

[95] M. Farasat, A. M. Trzynadlowski and M. S. Fadali, "Efficiency improved sensorless control scheme for electric vehicle induction motors," in *IET Electrical Systems in Transportation*, vol. 4, no. 4, pp. 122-131, Dec. 2014.

[96] Sung-Don Wee, Myoung-Ho Shin and Dong-Seok Hyun, "Stator-flux-oriented control of induction motor considering iron loss," in *IEEE Transactions on Industrial Electronics*, vol. 48, no. 3, pp. 602-608, June 2001.

[97] M. Sokola, and E. Levi, "A Novel Induction Machine Model and Its Application in the Development of an Advanced Vector Control Scheme." *The Int. Journal of El. Eng. & Education*, vol. 37, no. 3, pp. 233–48, July 2000.

[98] K. Aissa, K.D. Eddine, "Vector control using series iron loss model of induction motors and power loss minimization, " in *World Acad. Sci. Eng. Technol*, 52, 142–148, 2009.

[99] Jinhwan Jung and Kwanghee Nam, "A vector control scheme for EV induction motors with a series iron loss model," in *IEEE Transactions on Industrial Electronics*, vol. 45, no. 4, pp. 617-624, Aug. 1998.

[100] M. Hasegawa, S. Doki and S. Okuma, "Compensation method of stator iron loss of vector controlled induction motor using robust flux observer," *6th International Workshop on Advanced Motion Control. Proceedings (Cat. No.00TH8494)*, Nagoya, Japan, 2000, pp. 287-292.

[101] K. Wang. R. Huai, Z. Yu, X. Zhang, F. Li and L. Zhang, "Comparison Study of Induction Motor Models Considering Iron Loss for Electric Drives," in *Energies,* 2019, *12*, 503.

[102] Z. Qu, M. Ranta, M. Hinkkanen and J. Luomi, "Loss-Minimizing Flux Level Control of Induction Motor Drives," in *IEEE Transactions on Industry Applications*, vol. 48, no. 3, pp. 952-961, May-June 2012.

[103] M. Ranta, M. Hinkkanen, E. Dlala, A. Repo and J. Luomi, "Inclusion of hysteresis and eddy current losses in dynamic induction machine models," *2009 IEEE International Electric Machines and Drives Conference*, Miami, FL, 2009.

[104] M. N. Uddin and S. W. Nam, "New Online Loss-Minimization-Based Control of an Induction Motor Drive," in *IEEE Transactions on Power Electronics*, vol. 23, no. 2, pp. 926-933, March 2008.

[105] D. M. Reed, H. F. Hofmann and J. Sun, "Offline Identification of Induction Machine Parameters With Core Loss Estimation Using the Stator Current Locus," in *IEEE Transactions on Energy Conversion*, vol. 31, no. 4, pp. 1549-1558, Dec. 2016.

[106] E. Levi, A. Lamine and A. Cavagnino, "Impact of stray load losses on vector control accuracy in current-fed induction motor drives," in *IEEE Transactions on Energy Conversion*, vol. 21, no. 2, pp. 442-450, June 2006.

[107] E. Levi, M. Sokola, A. Boglietti and M. Pastorelli, "Iron loss in rotor-flux-oriented induction machines: identification, assessment of detuning, and compensation," in *IEEE Transactions on Power Electronics*, vol. 11, no. 5, pp. 698-709, Sept. 1996.

[108] E. Levi, "Impact of iron loss on behavior of vector controlled induction machines," in *IEEE Transactions on Industry Applications*, vol. 31, no. 6, pp. 1287-1296, Nov.-Dec. 1995.

[109] J. Tang et. al., "Parameter Identification of Inverter-Fed Induction Motors: A Review," in *Energies*, 11, 2194, 2018.

[110] H. A. Toliyat, E. Levi and M. Raina, "A review of RFO induction motor parameter estimation techniques," in IEEE Transactions on Energy Conversion, vol. 18, no. 2, pp. 271-283, June 2003.

[111] S. Tamai, H. Sugimoto and M. Yano, "Speed sensorless vector control of induction motor with model reference adaptive system," *in Proceedings of the IEEE 1987 industry applications society annual meeting*, 1987, pp. 189–95.

[112] C. Schauder, "Adaptive speed identification for vector control of induction motors without rotational transducers," in *IEEE Transactions on Industry Applications*, vol. 28, no. 5, pp. 1054-1061, Sept.-Oct. 1992.

[113] Y. D. Landau*, Adaptive Control–The Model Reference Approach*. New York Marcel Dekker, 1979.

[114] P. Cao, X. Zhang and S. Yang, "A Unified-Model-Based Analysis of MRAS for Online Rotor Time Constant Estimation in an Induction Motor Drive," in *IEEE Transactions on Industrial Electronics*, vol. 64, no. 6, pp. 4361-4371, June 2017.

[115] Z. Kandoussi, B. Zakaria, A. Elbacha, and T. Abdelouahed, "Sensorless control of induction motor drives using an improved MRAS observer," in *J. Elect. Eng. Technol.*, vol. 12, no. 4, pp. 1456–1470, 2017.

[116] M. Dybkowski, "Universal Speed and Flux Estimator for Induction Motor," in *Power Electronics and Drives*, vol. 3 (38), 2018, pp. 157-169.

[117] V. M. Popov, *Hyperstability of Control Systems*. Springer-Verlag, Berlin, Heidelberg, 1973.

[118] M. Korzonek, G. Tarchala and T. Orlowska-Kowalska, "A review on MRAS-type speed estimators for reliable and efficient induction motor drives," in *ISA Transactions,* Volume 93, pp. 1-13. 2019.

[119] V. Vasic, S. N. Vukosavic and E. Levi, "A stator resistance estimation scheme for speed sensorless rotor flux oriented induction motor drives," in *IEEE Transactions on Energy Conversion*, vol. 18, no. 4, pp. 476-483, Dec. 2003

[120] Y. Agrebi, K. Yassine and M. Boussak, "Sensorless Speed Control With MRAS for Induction Motor Drive," in *Proceedings of the 20th International Conference on Electrical Machines*, ICEM 2012.

[121] G.-J. Jo and J.-W. Choi, "A Novel Method for the Identification of the Rotor Resistance and Mutual Inductance of Induction Motors Based on MRAC and RLS Estimation," in *Journal of Power Electronics*, vol. 18, no. 2, pp. 492–501, Mar. 2018.

[122] M. Koteich, "Flux estimation algorithms for electric drives: A comparative study," 2016 3rd International Conference on Renewable Energies for Developing Countries (REDEC), 2016, pp. 1-6.

[123] L. J. Garces, "Parameter Adaption for the Speed-Controlled Static AC Drive with a Squirrel-Cage Induction Motor," in *IEEE Transactions on Industry Applications*, vol. IA-16, no. 2, pp. 173-178, March 1980.

[124] P. Cao, X. Zhang, S. Yang, Z. Xie and Y. Zhang, "Reactive-Power-Based MRAS for Online Rotor Time Constant Estimation in Induction Motor Drives," in *IEEE Transactions on Power Electronics*, vol. 33, no. 12, pp. 10835-10845, Dec. 2018.

[125] O. Lipcak, J. Bauer and M. Chomat, "Reactive Power MRAS for Rotor Resistance Estimation Taking Into Account Load-Dependent Saturation of Induction Motor," *2019 International Conference on Electrical Drives & Power Electronics (EDPE)*, The High Tatras, Slovakia, 2019, pp. 255-260.

[126] F. L. Mapelli, D. Tarsitano and F. Cheli, "A rotor resistance MRAS estimator for EV induction motor traction drive based on torque and reactive stator power: Simulation and experimental results," *2014 International Conference on Electrical Machines (ICEM)*, Berlin, 2014, pp. 31-37.

[127] F. L. Mapelli, A. Bezzolato and D. Tarsitano, "A rotor resistance MRAS estimator for induction motor traction drive for electrical vehicles," *2012 XXth International Conference on Electrical Machines*, Marseille, 2012.

[128] S. Maiti, C. Chakraborty, Y. Hori and M. C. Ta, "Model Reference Adaptive Controller-Based Rotor Resistance and Speed Estimation Techniques for Vector Controlled Induction Motor Drive Utilizing Reactive Power," in *IEEE Transactions on Industrial Electronics*, vol. 55, no. 2, pp. 594-601, Feb. 2008.

[129] S.A. Bednarz and M. Dybkowski, "Estimation of the Induction Motor Stator and Rotor Resistance Using Active and Reactive Power Based Model Reference Adaptive System Estimator, " in *Appl. Sci.*, *9*, 5145, 2009.

[130] M. S. Nait Said and M. E. H. Benbouzid, "Induction motors direct field oriented control with robust on-line tuning of rotor resistance," in *IEEE Transactions on Energy Conversion*, vol. 14, no. 4, pp. 1038-1042, Dec. 1999.

[131] Shyh-Shing Perng, Yen-Shin Lai and Chang-Huan Liu, "Sensorless vector controller for induction motor drives with parameter identification," *IECON '98. Proceedings of the 24th Annual Conference of the IEEE Industrial Electronics Society (Cat. No.98CH36200)*, 1998, pp. 1008-1013, vol.2.

[132] A. V. Ravi Teja, C. Chakraborty, S. Maiti and Y. Hori, "A New Model Reference Adaptive Controller for Four Quadrant Vector Controlled Induction Motor Drives," in *IEEE Transactions on Industrial Electronics*, vol. 59, no. 10, pp. 3757-3767, Oct. 2012.

[133] S. Basak, A. V. Ravi Teja, C. Chakraborty and Y. Hori, "A new model reference adaptive formulation to estimate stator resistance in field oriented induction motor drive," *IECON 2013 - 39th Annual Conference of the IEEE Industrial Electronics Society*, 2013, pp. 8470-8475.

[134] S. Yang, P. Cao and X. Zhang, "Stability analysis of q-axis rotor flux based model reference adaptive system updating rotor time constant in induction motor drives," in *CES Transactions on Electrical Machines and Systems*, vol. 1, no. 2, pp. 109-116, 2017.

[135] J. C. Moreira and T. A. Lipo, "A new method for rotor time constant tuning in indirect field oriented control," *21st Annual IEEE Conference on Power Electronics Specialists*, San Antonio, TX, USA, 1990, pp. 573-580.

[136] T. M. Rowan, R. J. Kerkman and D. Leggate, "A simple on-line adaptation for indirect field orientation of an induction machine," Conference Record of the IEEE Industry Applications Society Annual Meeting, 1989, pp. 579-587 vol.1.

[137] Xing Yu, M. W. Dunnigan and B. W. Williams, "A novel rotor resistance identification method for an indirect rotor flux-orientated controlled induction machine system," in *IEEE Transactions on Power Electronics*, vol. 17, no. 3, pp. 353-364, May 2002.

[138] S. N. Vukosavic and M. R. Stojic, "Online tuning of the rotor time constant for vector-controlled induction motor in position control applications," in *IEEE Transactions on Industrial Electronics*, vol. 40, no. 1, pp. 130-138, Feb. 1993.

[139] X. Zhang, Y. Zhang, S. Yang, Z. Xie and P. Cao, "An Improved MRAS for Rotor Time Constant Updating in Induction Motor Drives Utilizing Dot Product of Stator Current and Rotor Flux," in *IEEE Transactions on Power Electronics*, vol. 34, no. 9, pp. 8905-8915, Sept. 2019.

[140] Fang-Zheng Peng and T. Fukao, "Robust speed identification for speed-sensorless vector control of induction motors," in *IEEE Transactions on Industry Applications*, vol. 30, no. 5, pp. 1234-1240, Sept.-Oct. 1994.

[141] L. Zhen and L. Xu, "Sensorless field orientation control of induction machines based on a mutual MRAS scheme," in *IEEE Transactions on Industrial Electronics*, vol. 45, no. 5, pp. 824-831, Oct. 1998.

[142] K. Tungpimolrut, Fang-Zheng Peng and T. Fukao, "Robust vector control of induction motor without using stator and rotor circuit time constants," in IEEE Transactions on Industry Applications, vol. 30, no. 5, pp. 1241-1246, Sept.-Oct. 1994.

[143] L. Umanand and S. R. Bhat, "Adaptation of the rotor time constant for variations in the rotor resistance of an induction motor," *Proceedings of 1994 Power Electronics Specialist Conference - PESC'94*, 1994, pp. 738-743 vol.1.

[144] V. Verma and C. Chakraborty, "New series of MRAS for speed estimation of vector controlled induction motor drive," *IECON 2014 - 40th Annual Conference of the IEEE Industrial Electronics Society*, 2014, pp. 755-761.

[145] C. Mastorocostas, I. Kioskeridis and N. Margaris, "Thermal and slip effects on rotor time constant in vector controlled induction motor drives," in *IEEE Transactions on Power Electronics*, vol. 21, no. 2, pp. 495-504, March 2006.

[146] J. Holtz and Juntao Quan, "Drift- and parameter-compensated flux estimator for persistent zero-stator-frequency operation of sensorless-controlled induction motors," in *IEEE Transactions on Industry Application*s, vol. 39, no. 4, pp. 1052-1060, July-Aug. 2003.

[147] C. Lascu and G. -. Andreescu, "Sliding-mode observer and improved integrator with DC-offset compensation for flux estimation in sensorless-controlled induction motors," in IEEE Transactions on Industrial Electronics, vol. 53, no. 3, pp. 785-794, June 2006.

[148] R. Kelly, J. Llamas and R. Campa, "A measurement procedure for viscous and coulomb friction," in *IEEE Transactions on Instrumentation and Measurement*, vol. 49, no. 4, pp. 857-861, Aug. 2000.

[149] M. Ranta, M. Hinkkanen and J. Luomi, "Rotor parameter identification of saturated induction machines," *2009 IEEE Energy Conversion Congress and Exposition*, 2009, pp. 1524-1531.

[150] F. Baum, "Comparison of DC Offset Elimination Integrators Used for Evaluation of Induction Motor Voltage Model," (in Czech), B.S. thesis, FEE Dept. of Elect. Drives and Traction, CTU in Prague, Prague, 2020.

[151] P. Vas, *Sensorless vector and direct torque control*. New York: Oxford University Press; 1998.

[152] A. Boglietti, A. Cavagnino and M. Lazzari, "*Computational Algorithms for Induction-Motor Equivalent Circuit Parameter Determination—Part I: Resistances and Leakage Reactances*," in IEEE Transactions on Industrial Electronics, vol. 58, no. 9, pp. 3723-3733, Sept. 2011.

[153] M. Comanescu and L. Xu, "An improved flux observer based on PLL frequency estimator for sensorless vector control of induction motors," in *IEEE Transactions on Industrial Electronics*, vol. 53, no. 1, pp. 50-56, Feb. 2006.

[154] D. Stojić, M. Milinković, S. Veinović and I. Klasnić, "Improved Stator Flux Estimator for Speed Sensorless Induction Motor Drives," in *IEEE Transactions on Power Electronics*, vol. 30, no. 4, pp. 2363-2371, April 2015.

[155] Myoung-Ho Shin, Dong-Seok Hyun, Soon-Bong Cho and Song-Yul Choe, "An improved stator flux estimation for speed sensorless stator flux orientation control of induction motors," in *IEEE Transactions on Power Electronics*, vol. 15, no. 2, pp. 312-318, March 2000.

[156] N. R. N. Idris and A. H. M. Yatim, "An improved stator flux estimation in steady-state operation for direct torque control of induction machines," in *IEEE Transactions on Industry Applications*, vol. 38, no. 1, pp. 110-116, Jan.-Feb. 2002.

[157] Hinkkanen and J. Luomi, "Modified integrator for voltage model flux estimation of induction motors," in *IEEE Transactions on Industrial Electronics*, vol. 50, no. 4, pp. 818–820, 2003.

[158] Jun Hu and Bin Wu, "New integration algorithms for estimating motor flux over a wide speed range," in *IEEE Transactions on Power Electronics*, vol. 13, no. 5, pp. 969-977, Sept. 1998.

[159] C. Lascu, I. Boldea and F. Blaabjerg, "A modified direct torque control (DTC) for induction motor sensorless drive," *Conference Record of 1998 IEEE Industry Applications Conference. Thirty-Third IAS Annual Meeting (Cat. No.98CH36242)*, 1998, pp. 415-422 vol.1.

[160] P. L. Jansen and R. D. Lorenz, "A physically insightful approach to the design and accuracy assessment of flux observers for field oriented induction machine drives," in *IEEE Transactions on Industry Applications*, vol. 30, no. 1, pp. 101-110, Jan.-Feb. 1994.

[161] H.K. Khalil, *Nonlinear systems*, 3rd ed., Upper Saddle River, NJ: Prentice Hall, 2002.

APPENDIX A LIST OF AUTHOR'S PUBLICATIONS

A.1 Publications Related to Thesis

A.1.1 Publications in Journals with Impact Factor

- O. Lipcak and J. Bauer, "MRAS-Based Induction Machine Magnetizing Inductance Estimator With Included Effect of Iron Losses and Load," in *IEEE Access*, vol. 9, pp. 166234-166248, 2021. Contribution **50 %**.
- O. Lipcak, F. Baum, and J. Bauer, "Influence of Selected Non-Ideal Aspects on Active and Reactive Power MRAS for Stator and Rotor Resistance Estimation," in *Energies*, vol. 14, no. 20, p. 6826, Oct. 2021. Contribution **33 %**.
- O. Lipcak and J. Bauer, "Offline method for experimental identification of load-dependent saturation of induction motor taking into account variation of inverse rotor time constant," in *IET Power Electronics*, vol. 13, no. 9, pp. 1828-1836, 2020. Contribution **50 %**.
- O. Lipcak, J. Bauer and P. Kobrle, "Offline method for determination of non-linear dependence of machine magnetising inductance utilising parallel operation of current and voltage model," in *IET Power Electronics*, vol. 12, no. 11, pp. 2843-2850, 2019. Contribution **33 %**.

A.1.2 Publications Excerpted in Web of Science

- O. Lipcak, J. Bauer and M. Chomat, "Reactive Power MRAS for Rotor Resistance Estimation Taking Into Account Load-Dependent Saturation of Induction Motor," *2019 International Conference on Electrical Drives & Power Electronics (EDPE)*, 2019, pp. 255-260. Contribution **33 %**.
- O. Lipcak and J. Bauer, "Analysis of Voltage Distortion and Comparison of Two Simple Voltage Compensation Methods for Sensorless Control of Induction Motor," *2019 IEEE 10th International Symposium on Sensorless Control for Electrical Drives (SLED)*, 2019, pp. 1-6. Contribution **50 %**.
- J. Bauer, O. Lipcak and J. Kyncl, "Different Approaches in Numerical Solution of Continuous Mathematical Models of Induction Machine," *2018 IEEE 18th International Power Electronics and Motion Control Conference (PEMC)*, 2018, pp. 669-674. Contribution **33 %**.

A.1.3 Other publications

- O. Lipcak and J. Bauer, Optimization of Voltage Model for MRAS Based Sensorless Control of Induction Motorm, *Lecture Notes in Electrical Engineering*. Recent Advances in Electrical Engineering and Related Sciences: Theory and Application, Ostrava, 2018-09-11/2018-09-13. Cham: Springer, 2020. p. 758-768. vol. 554. Contribution **50 %**.
- O. Lipcak and J. Bauer, "Identifikace a kompenzace zkreslení výstupního napětí střídače pro bezsenzorově řízený asynchronní motor," *XXXVI. CELOSTÁTNÍ KONFERENCE O ELEKTRICKÝCH POHONECH*, Plzeň, Praha: Česká elektrotechnická společnost, 2019. Contribution **50 %**.

A.2 Publications Related to Topics Different from Thesis

A.2.1 Publications in Journals with Impact Factor

- O. Lipcak, P. Karlovsky, P. Kobrle and J. Bauer, "Current Ripple Reduction of Predictive Torque-Controlled Induction Motor Drive Using Delta-Star Switchover," in *Applied Sciences*, vol. 11, no. 6, p. 2863, Mar. 2021. Contribution **25 %**.
- P. Skarolek, F. Frolov, O. Lipcak, and J. Lettl, "Reverse Conduction Loss Minimization in GaN-Based PMSM Drive," *Electronics*, vol. 9, no. 11, p. 1973, Nov. 2020. Contribution **25 %**.

- P. Karlovsky, O. Lipcak, J. Bauer and J. Lettl, "Predictive torque control of induction motor with integrated DC-link voltage optimisation," in *IET Power Electronics*, vol. 13, no. 15, pp. 3396-3406, 2020. Contribution **25 %**.
- P. Karlovsky, O. Lipcak and J. Bauer, "Iron Loss Minimization Strategy for Predictive Torque Control of Induction Motor," in *Electronics*, vol. 9, no. 4, p. 566, Mar. 2020. Contribution **33 %**.

A.2.2 Publications Excerpted in Web of Science

A.2.3 Other publications

- P. Karlovsky, O. Lipcak and J. Lettl, "Estimation of Stator Voltage of Inverter-Supplied Induction Motor Using Kalman Filter," *AETA 2019 - Recent Advances in Electrical Engineering and Related Sciences: Theory and Application*. The 6th International Conference on Advanced Engineering – Theory and Applications 2019, Bogotá, 2019-11-06/2019-11-08. Cham: Springer, 2021. p. 64-73. Contribution **33 %**.

APPENDIX B NOMENCLATURE

General Symbols

$\overline{x}$	the complex conjugate of space vector
$\hat{x}$	estimated value
$\underline{x}$	space vector
x^*	reference value
$\mathbf{X}$	matrix
$\mathbf{x}$	vector
x	instantaneous scalar quantity

Operators

$\frac{\mathrm{d}}{\mathrm{d}x}$	derivative
$\dot{x}$	time derivative
$\frac{\partial}{\partial x}$	partial derivative
$\Im\{\dots\}$	imaginary part of complex number
$\Re\{\dots\}$	real part of complex number

Subscripts

1	stator and general enumeration
2	rotor and general enumeration
a, b, c	notation of machine phases
c	constant
CE	collector-emitter
CG	collector-gate
dt	dead time
eff	effective
Fe	related to the machine core
G	gate
GE	gate-emitter
i	inner, integral
m	magnetizing
mech	mechanical
min, max	minimum, maximum
on, off	denotes relation to turning on and turning off process
p	poles, proportional
r	rotor, rise
f, d	fall, delay
rr	reverse-recovery
s	stator, synchronous
d	direct-axis (real) value in the synchronous reference frame
q	quadrature-axis (imaginary) value in the synchronous reference frame
α	direct-axis (real) value in the stator-fixed reference frame
β	quadrature-axis (imaginary) value in the stator-fixed reference frame
σ	leakage

Superscripts

dq	quantity expressed in a synchronous reference frame
k	quantity expressed in a general reference frame
$\alpha\beta$	quantity expressed in a stator-fixed reference frame
*	reference value

Symbols and Variables

T_e	electromechanical torque (Nm)
f_s	synchronous frequency (Hz)
p_p	number of machine pole-pairs (-)
ω_c	cutoff angular frequency (rad·s^{-1})
j	imaginary unit (-)
Ω	mechanical angular rotor speed (rad·s^{-1})
B	flux density (T)
L	inductance (H)
P	active power (W)
Q	reactive power (VAr)
R	resistance (Ω)
T	period, time (s)
i, I	current (A)
s	slip (-)
t	time (s)
u, U	voltage (V)
θ	Park's transformation angle (rad)
σ	leakage factor (-)
ψ	flux linkage (Wb)
$\omega, \omega_s, \omega_{slip}$	electrical angular rotor speed, synchronous speed, slip speed (rad·s^{-1})
ϑ	temperature (°C)

Abbreviations

DFOC	direct FOC
DOL	direct-online
DSP	digital signal processor
FEA	finite-element analysis
FOC	field-oriented control
FPGA	field-programmable gate array
IEC	International Electrotechnical Commission
IFOC	indirect FOC
IM	induction machine
MMF	magnetomotive force
MRAS	model reference adaptive system
PMSM	permanent magnet synchronous machine
PWM	pulse-width modulation
RFOC	rotor flux linkage vector-oriented FOC
RHS	right-hand side
RK4	Runge-Kutta 4th order method
RLS	recursive least-square
RMS	root mean square
SVM	space-vector modulation
SVT	space-vector theory
VSI	voltage-source inverter

APPENDIX C INDUCTION MACHINE EQUIVALENT CIRCUITS

C.1 Traditional T-Equivalent Circuit

The fundamental IM flux and voltage equations can be derived using the space-vector theory [151]. The theory assumes that both the stator and rotor winding resulting inductances can be split into two parts – the so-called magnetizing inductance, which quantifies the amount of useful flux passing throughout the air-gap and the so-called leakage inductance, which quantifies the other flux components. The leakage flux is mainly composed of [14], [79], [152]

- stator and rotor slot leakage flux,
- tooth-tip leakage flux,
- over-hang / end turn leakage flux,
- harmonic / air-gap leakage flux,
- skew leakage flux.

The detailed physical analysis of these fluxes components is beyond the scope of this thesis. However, the important consequence is that the separation of the inductances into their magnetizing and leakage part permits the fundamental flux and voltage IM equations to be graphically visualized as the so-called T-equivalent circuit. Typically, the rotor variables are recalculated onto the stator side, which causes the stator and rotor magnetizing inductances to be equal. The stator and rotor branches can then be drawn as galvanically connected. The resulting T-equivalent circuit is depicted in Fig. C-1. The equivalent circuit is mathematically described as

$$\underline{u}_1^k = R_1 \underline{i}_1^k + \frac{\mathrm{d}\,\underline{\psi}_1^k}{\mathrm{d}t} + \mathrm{j}\omega_k\,\underline{\psi}_1^k, \tag{C-1}$$

$$\underline{u}_2^k = 0 = R_2 \underline{i}_2^k + \frac{\mathrm{d}\,\underline{\psi}_2^k}{\mathrm{d}t} + \mathrm{j}(\omega_k - \omega)\,\underline{\psi}_2^k, \tag{C-2}$$

$$\underline{\psi}_1^k = L_{1\sigma}\underline{i}_1^k + L_\mathrm{m}\underline{i}_\mathrm{m}^k, \tag{C-3}$$

$$\underline{\psi}_2^k = L_{2\sigma}\underline{i}_2^k + L_\mathrm{m}\underline{i}_\mathrm{m}^k, \tag{C-4}$$

$$\underline{\psi}_{1\sigma}^k = L_{1\sigma}\underline{i}_1^k, \tag{C-5}$$

$$\underline{\psi}_{2\sigma}^k = L_{2\sigma}\underline{i}_2^k, \tag{C-6}$$

$$\underline{u}_\mathrm{m}^k = \frac{\mathrm{d}\,\underline{\psi}_\mathrm{m}^k}{\mathrm{d}t}, \tag{C-7}$$

$$\underline{i}_1^k + \underline{i}_2^k = \underline{i}_\mathrm{m}^k, \tag{C-8}$$

$$\underline{\psi}_\mathrm{m}^k = L_\mathrm{m}\underline{i}_\mathrm{m}^k. \tag{C-9}$$

where $\underline{\psi}_1^k$, $\underline{\psi}_2^k$ and $\underline{\psi}_\mathrm{m}^k$ are the stator, rotor, and magnetizing flux linkage space vectors, respectively, $\underline{u}_1^k$, $\underline{u}_2^k$ and $\underline{u}_\mathrm{m}^k$ are the stator, rotor, and magnetizing voltage space vectors, respectively, $\underline{i}_1^k$, $\underline{i}_2^k$ and $\underline{i}_\mathrm{m}^k$ are the stator, rotor, and magnetizing current space vectors, respectively, R_1 and R_2 denote the stator and rotor resistance, respectively, ω_k is the electrical angular speed of the general reference frame, ω is the rotor electrical angular speed, L_m is the magnetizing inductance, p_p denotes the number of pole-pairs and the symbol j represents an imaginary unit ($\mathrm{j}^2 = -1$). A shorted rotor is considered; therefore, the rotor voltage equals zero.

The stator inductance L_1 is defined as $L_1 = L_\mathrm{m} + L_{1\sigma}$, where $L_{1\sigma}$ is the stator leakage inductance and the rotor inductance L_2 is defined as $L_2 = L_\mathrm{m} + L_{2\sigma}$, where $L_{2\sigma}$ is the rotor leakage inductance. Furthermore, $\underline{\psi}_{1\sigma}^k$ and $\underline{\psi}_{2\sigma}^k$ denote the stator and rotor leakage flux linkage vectors, respectively. The superscript k indicates that the quantities are expressed in a general reference frame. The two specific reference frames used in the thesis are the stator-fixed (real axis denoted as α and imaginary axis as β) and rotor flux linkage vector-attached synchronous frame (real axis denoted as d and imaginary axis as q).

Also, other quantities calculated from the above parameters are used in the thesis:

$$\tau_\mathrm{r} = \frac{L_2}{R_2}, \tag{C-10}$$

$$\sigma = 1 - \frac{L_\mathrm{m}^2}{L_1 L_2}, \tag{C-11}$$

where τ_r is the rotor time constant, and σ is the leakage factor.

Furthermore, if the saturation of the main flux path is considered, then the magnetizing inductance is considered as a variable parameter, i.e., $L_\mathrm{m} = f(i_\mathrm{m})$ or $L_\mathrm{m} = f(\psi_\mathrm{m})$. If the stator or rotor resistance variation is considered, these are then also treated as variable parameters but without any predefined analytical dependence.

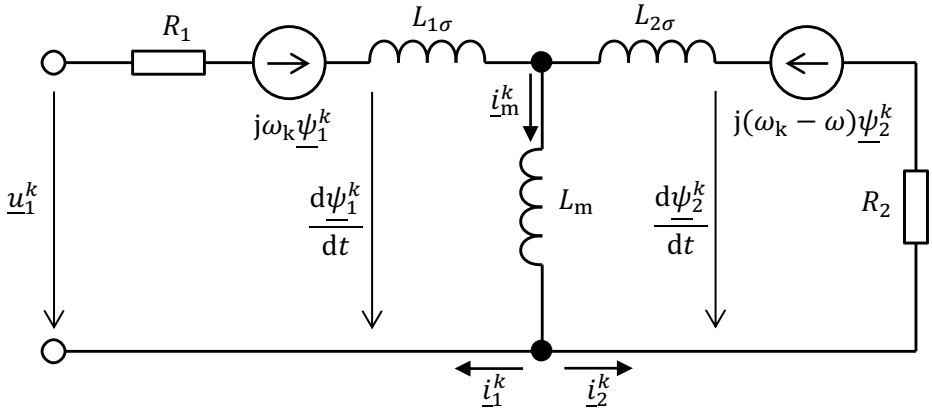

Fig. C-1 Induction machine linear T-equivalent circuit.

The electromagnetic torque can be expressed in many equivalent ways as

$$\begin{aligned} T_\mathrm{e} &= \frac{2}{3K^2} p_\mathrm{p} \gamma \Im\left\{\underline{\mu}\overline{\underline{\nu}}\right\} = \frac{2}{3K^2} p_\mathrm{p} \gamma (\nu_\mathrm{Re}\mu_\mathrm{Im} - \nu_\mathrm{Im}\mu_\mathrm{Re}) = \frac{2}{3K^2} p_\mathrm{p} \gamma \left|\underline{\nu} \times \underline{\mu}\right| \\ &= \frac{2}{3K^2} p_\mathrm{p} \gamma \left|\underline{\mu}\right| \left|\underline{\nu}\right| \sin\delta, \end{aligned} \tag{C-12}$$

where K is Clarke's transformation constant, p_p is the number of pole-pairs and δ is the angle measured from the vector $\underline{\nu}$ to the vector $\underline{\mu}$ in a positive sense of rotation. The different combinations for the torque expression are listed in Tab. C-1.

Tab. C-1 Different combinations of the torque expression.

Variant	1	2	3	4	5	6	7	8
μ	$\underline{i}_1^k$	$\underline{i}_1^k$	$\underline{i}_1^k$	$\underline{i}_1^k$	$\underline{i}_2^k$	$\underline{i}_2^k$	$\underline{i}_2^k$	$\underline{\psi}_1^k$
ν	$\underline{i}_2^k$	$\underline{\psi}_1^k$	$\underline{\psi}_\mathrm{m}^k$	$\underline{\psi}_2^k$	$\underline{\psi}_1^k$	$\underline{\psi}_\mathrm{m}^k$	$\underline{\psi}_2^k$	$\underline{\psi}_2^k$
γ	L_m	1	1	$\frac{L_\mathrm{m}}{L_2}$	$\frac{L_\mathrm{m}}{L_1}$	1	1	$\frac{L_\mathrm{m}}{\sigma L_1 L_2}$

C.2 T-Equivalent Circuit with Included Effect of Iron Losses, Main Flux Saturation and Rotor Resistance Variation

Papers in sections 3.3 and 3.4 are based on the IM T-equivalent circuit with the iron loss resistance placed in parallel with the magnetizing branch depicted in Fig. C-2 [22], [97]. The set of equations describing the equivalent circuit can be summarized as

$$\underline{u}_1^k = R_1 \underline{i}_1^k + \frac{\mathrm{d}\,\underline{\psi}_1^k}{\mathrm{d}t} + \mathrm{j}\omega_k\,\underline{\psi}_1^k, \tag{C-13}$$

$$\underline{u}_2^k = 0 = R_2 \underline{i}_2^k + \frac{\mathrm{d}\,\underline{\psi}_2^k}{\mathrm{d}t} + \mathrm{j}(\omega_k - \omega)\,\underline{\psi}_2^k, \tag{C-14}$$

$$\underline{\psi}_1^k = L_{1\sigma}\underline{i}_1^k + L_\mathrm{m}\underline{i}_\mathrm{m}^k, \tag{C-15}$$

$$\underline{\psi}_2^k = L_{2\sigma}\underline{i}_2^k + L_\mathrm{m}\underline{i}_\mathrm{m}^k, \tag{C-16}$$

$$\underline{\psi}_{1\sigma}^k = L_{1\sigma}\underline{i}_1^k, \tag{C-17}$$

$$\underline{\psi}_{2\sigma}^k = L_{2\sigma}\underline{i}_2^k, \tag{C-18}$$

$$\underline{u}_\mathrm{m}^k = \frac{\mathrm{d}\,\underline{\psi}_\mathrm{m}^k}{\mathrm{d}t} = R_\mathrm{Fe}\underline{i}_\mathrm{Fe}^k + \mathrm{j}\omega_k\,\underline{\psi}_\mathrm{m}^k, \tag{C-19}$$

$$\underline{i}_1^k + \underline{i}_2^k = \underline{i}_\mathrm{m}^k + \underline{i}_\mathrm{Fe}^k, \tag{C-20}$$

$$\underline{\psi}_\mathrm{m}^k = L_\mathrm{m}\underline{i}_\mathrm{m}^k, \tag{C-21}$$

$$L_\mathrm{m} = f(\text{flux level, load}), \tag{C-22}$$

$$R_\mathrm{Fe} = f(\text{flux level, frequency}), \tag{C-23}$$

$$T_\mathrm{e} = \frac{3}{2} p_\mathrm{p} \frac{L_\mathrm{m}}{L_{2\sigma}} \left(\underline{\psi}_2^k \times \underline{i}_\mathrm{m}^k\right), \tag{C-24}$$

where $\underline{i}_\mathrm{Fe}^k$ is the current space vector of the equivalent iron loss resistance path, R_Fe is the equivalent iron loss resistance, and $\underline{u}_\mathrm{m}^k$ is the voltage across the magnetizing branch.

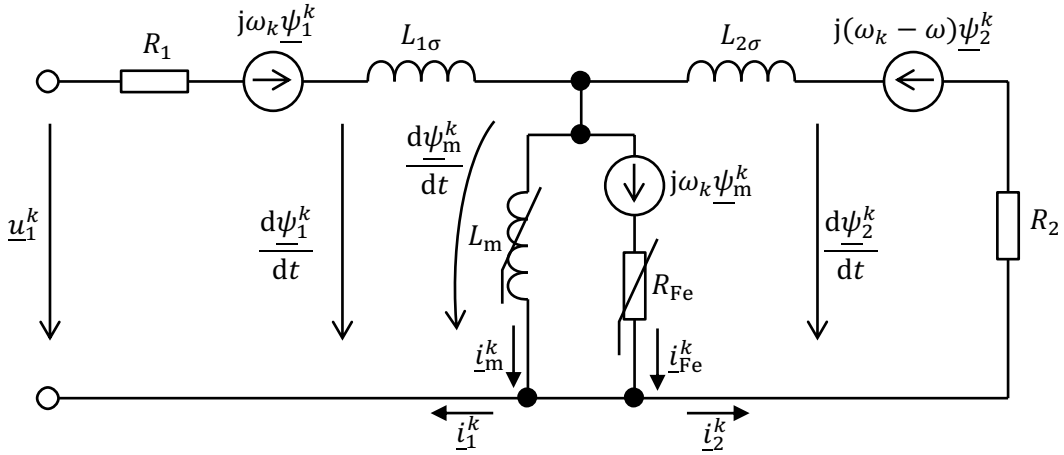

Fig. C-2 T-equivalent circuit of a saturated induction machine with included fictitious iron loss resistance.

In the papers from sections 3.2 (iron losses are neglected here) and 3.3, the magnetizing inductance is considered a variable parameter that is a function of the machine's magnetic flux and load. Therefore, (C-22) applies. Furthermore, the rotor resistance is also considered a variable parameter that changes with the winding temperature. On the contrary, the paper from section 3.4 considers the magnetizing inductance constant and studies the influence of the iron loss resistance and rotor resistance variation only. The state-space models suitable for modeling the machine in simulation tools are also given in the respective papers.

APPENDIX D CONSIDERATIONS ABOUT MODELING OF SATURATED MACHINE (IRON LOSSES EXCLUDED)

If the stator and rotor leakage inductances are constant, then during the derivation of some type of the IM state-space equations, the following term needs to be differentiated

$$\frac{\mathrm{d}\underline{\psi}_\mathrm{m}}{\mathrm{d}t} = \frac{\mathrm{d}\left(L_\mathrm{m}\underline{i}_\mathrm{m}\right)}{\mathrm{d}t}. \tag{D-1}$$

Of course, if $L_\mathrm{m} = \text{const.}$, then

$$\frac{\mathrm{d}\underline{\psi}_\mathrm{m}}{\mathrm{d}t} = L_\mathrm{m}\frac{\mathrm{d}\underline{i}_\mathrm{m}}{\mathrm{d}t}, \tag{D-2}$$

otherwise

$$\frac{\mathrm{d}\underline{\psi}_\mathrm{m}}{\mathrm{d}t} = \dot{L}_\mathrm{m}\underline{i}_\mathrm{m} + L_\mathrm{m}\frac{\mathrm{d}\underline{i}_\mathrm{m}}{\mathrm{d}t}. \tag{D-3}$$

where $\dot{L}_\mathrm{m} = \mathrm{d}L_\mathrm{m}/\mathrm{d}t$. The inductance derivative term can be expanded as

$$\dot{L}_\mathrm{m} = \frac{\mathrm{d}L_\mathrm{m}}{\mathrm{d}i_\mathrm{m}}\frac{\mathrm{d}i_\mathrm{m}}{\mathrm{d}t} = \frac{\mathrm{d}(\psi_\mathrm{m}/i_\mathrm{m})}{\mathrm{d}i_\mathrm{m}}\frac{\mathrm{d}i_\mathrm{m}}{\mathrm{d}t} = \frac{1}{i_\mathrm{m}}\left(\frac{\mathrm{d}\psi_\mathrm{m}}{\mathrm{d}i_\mathrm{m}} + \frac{\psi_\mathrm{m}}{i_\mathrm{m}}\right)\frac{\mathrm{d}i_\mathrm{m}}{\mathrm{d}t} = \frac{L_\mathrm{dyn} - L_\mathrm{m}}{i_\mathrm{m}}\frac{\mathrm{d}i_\mathrm{m}}{\mathrm{d}t}, \tag{D-4}$$

where $i_\mathrm{m} = \left|\underline{i}_\mathrm{m}^k\right|$, $\psi_\mathrm{m} = \left|\underline{\psi}_\mathrm{m}^k\right|$ and $L_\mathrm{dyn} = \mathrm{d}\psi_\mathrm{m}/\mathrm{d}i_\mathrm{m}$ is the so-called dynamic inductance determined by the slope of the magnetizing characteristic. An example of an IM real magnetizing characteristic is given in Fig. D-1.

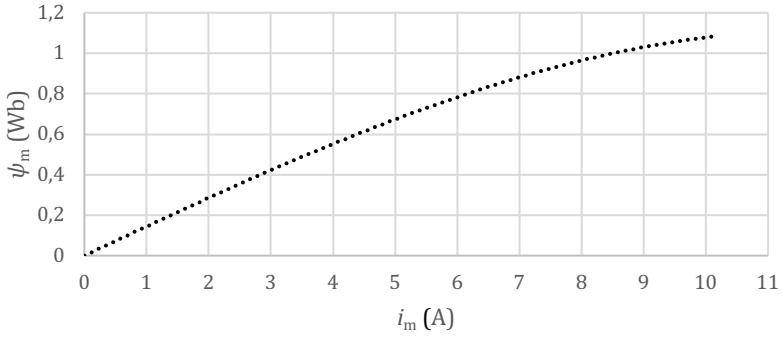

Fig. D-1 An example of induction machine no-load magnetizing characteristic.

To get a better insight into the so-called cross-saturation phenomena, we start by expressing the components of the magnetizing flux linkage space vector in a general coordinate system xy, i.e.,

$$\psi_{\mathrm{m}x} = L_\mathrm{m}i_{\mathrm{m}x} = L_\mathrm{m}(i_{1x} + i_{2x}), \tag{D-5}$$

$$\psi_{\mathrm{m}y} = L_\mathrm{m}i_{\mathrm{m}y} = L_\mathrm{m}\left(i_{1y} + i_{2y}\right). \tag{D-6}$$

Time differentiation of (D-5) and (D-6), respectively, yields

$$u_{\mathrm{m}x} = \frac{\mathrm{d}\psi_{\mathrm{m}x}}{\mathrm{d}t} = \frac{\partial\psi_{\mathrm{m}x}}{\partial i_{\mathrm{m}x}}\frac{\mathrm{d}i_{\mathrm{m}x}}{\mathrm{d}t} + \frac{\partial\psi_{\mathrm{m}x}}{\partial i_{\mathrm{m}y}}\frac{\mathrm{d}i_{\mathrm{m}y}}{\mathrm{d}t} = L_{\mathrm{m}x}\frac{\mathrm{d}i_{\mathrm{m}x}}{\mathrm{d}t} + L_{xy}\frac{\mathrm{d}i_{\mathrm{m}y}}{\mathrm{d}t}, \tag{D-7}$$

$$u_{\mathrm{m}y} = \frac{\mathrm{d}\psi_{\mathrm{m}y}}{\mathrm{d}t} = \frac{\partial\psi_{\mathrm{m}y}}{\partial i_{\mathrm{m}y}}\frac{\mathrm{d}i_{\mathrm{m}y}}{\mathrm{d}t} + \frac{\partial\psi_{\mathrm{m}y}}{\partial i_{\mathrm{m}x}}\frac{\mathrm{d}i_{\mathrm{m}x}}{\mathrm{d}t} = L_{\mathrm{m}y}\frac{\mathrm{d}i_{\mathrm{m}y}}{\mathrm{d}t} + L_{xy}\frac{\mathrm{d}i_{\mathrm{m}x}}{\mathrm{d}t}. \tag{D-8}$$

Due to the saturation, $L_{\mathrm{m}x} \neq L_{\mathrm{m}y}$ and $L_{xy} \neq 0$. The inductances in (D-7) and (D-8) can be expressed as [13]

$$L_{\mathrm{m}x} = L_{\mathrm{m}} + \left(L_{\mathrm{dyn}} - L_{\mathrm{m}}\right)\cos^2(\rho_{\mathrm{m}} - \theta_k), \tag{D-9}$$

$$L_{\mathrm{m}y} = L_{\mathrm{m}} + \left(L_{\mathrm{dyn}} - L_{\mathrm{m}}\right)\sin^2(\rho_{\mathrm{m}} - \theta_k), \tag{D-10}$$

$$L_{xy} = \frac{\left(L_{\mathrm{dyn}} - L_{\mathrm{m}}\right)\sin[2(\rho_{\mathrm{m}} - \theta_k)]}{2}. \tag{D-11}$$

Furthermore, in the magnetizing current vector-fixed coordinate system, it follows that

$$u_{\mathrm{m}} = \frac{\mathrm{d}\psi_{\mathrm{m}}}{\mathrm{d}t} = \frac{\mathrm{d}\psi_{\mathrm{m}}}{\mathrm{d}i_{\mathrm{m}}}\frac{\mathrm{d}i_{\mathrm{m}}}{\mathrm{d}t} = L_{\mathrm{dyn}}\frac{\mathrm{d}i_{\mathrm{m}}}{\mathrm{d}t}. \tag{D-12}$$

The angles are defined according to Fig. D-2. Equations (D-7) to (D-11) describe the so-called cross-saturation by which we mean that under the saturated conditions, the rate of change of the real axis current induces a voltage in the imaginary axis and vice versa. However, mathematically the cross saturation diminishes in the magnetizing current-fixed coordinate system.

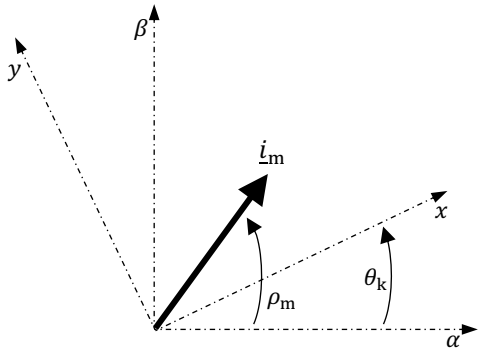

Fig. D-2 A magnetizing current vector in the stationary and general reference frame.

The effect of saturation is particularly apparent in the IM matrix impedance equation ($p = \mathrm{d}/\mathrm{d}t$), i.e.,

$$\mathbf{U} = \mathbf{Z}\mathbf{I}, \tag{D-13}$$

$$\mathbf{U} = \begin{bmatrix} u_{1x} \\ u_{1y} \\ u_{2x} \\ u_{2y} \end{bmatrix}, \quad \mathbf{I} = \begin{bmatrix} i_{1x} \\ i_{1y} \\ i_{2x} \\ i_{2y} \end{bmatrix}, \tag{D-14}$$

$$\mathbf{Z} = \begin{bmatrix} R_1 + L_{1x}p & L_{xy}p - \omega_{\mathrm{k}}L_1 & L_{\mathrm{m}x}p & L_{xy}p - \omega_{\mathrm{k}}L_{\mathrm{m}} \\ L_{xy}p + \omega_{\mathrm{k}}L_1 & R_1 + L_{1y}p & L_{xy}p + \omega_{\mathrm{k}}L_{\mathrm{m}} & L_{\mathrm{m}y}p \\ L_{\mathrm{m}x}p & -(\omega_{\mathrm{k}} - \omega)L_{\mathrm{m}} + L_{xy}p & R_2 + L_{2x}p & -(\omega_{\mathrm{k}} - \omega)L_2 + L_x \\ (\omega_{\mathrm{k}} - \omega)L_{\mathrm{m}} + L_{xy}p & L_{\mathrm{m}y}p & (\omega_{\mathrm{k}} - \omega)L_2 + L_{xy}p & R_2 + L_{2y}p \end{bmatrix} \tag{D-15}$$

$$\begin{aligned} L_{1x} &= L_{1\sigma} + L_{\mathrm{m}x}, \quad & L_{1y} &= L_{1\sigma} + L_{\mathrm{m}y}, \\ L_{2x} &= L_{2\sigma} + L_{\mathrm{m}x}, \quad & L_{2y} &= L_{2\sigma} + L_{\mathrm{m}y}. \end{aligned} \tag{D-16}$$

The impedance equation is suitable for the derivation of the IM state-space model with stator and rotor current space vectors as the state variables. However, this model is quite complicated when considering the saturation effects. Therefore, it is more convenient for the IM state-space models to use a combination of flux linkage space vectors.

APPENDIX E POSSIBLE PROOFS OF MODEL REFERENCE ADAPTIVE SYSTEM STABILITY

E.1 Stability Proof and Adaptation Mechanism Derivation Using Popov Hyperstability Concept

The hyperstability concept was introduced by Popov [117] as a generalization of the absolute stability problem. The criterion was then utilized for the MRAS stability proof by Landau [113]. The hyperstability concept mainly concerns the class of multivariable nonlinear time-varying feedback systems depicted in Fig. E-1. The global stability of such a system is ensured by fulfilling the following two conditions [113]:

1. The forward path transfer matrix of the feedforward linear time-invariant (LTI) system is strictly positive real.
2. The nonlinear time-varying feedback (which includes the adaptation mechanism) satisfies the Popov hyperstability criterion expressed as an integral inequality

$$\eta(t_0, t_1) = \int_{t_0}^{t_1} \mathbf{w}^{\mathrm{T}}\mathbf{v}\,\mathrm{d}t \geq -\gamma_0^2, \tag{E-1}$$

where $\mathbf{v}$ is the input vector, $\mathbf{w}$ is the output vector of the feedback block and γ_0^2 is a positive constant.

The validity of (E-1) is usually proved using the following integral inequality.

$$\int_{t_0}^{t_1} \frac{\mathrm{d}f(t)}{\mathrm{d}t} k_1 f(t)\,\mathrm{d}t \geq -\frac{1}{2} k_1 f(t_0)^2. \tag{E-2}$$

The candidate adaptation law, which is usually used for ensuring stability, is mostly conventional PI controller, or more generally, the adaptation mechanism in the form

$$\hat{\xi} = \Phi_2(\boldsymbol{\varepsilon}) + \int_0^t \Phi_1(\boldsymbol{\varepsilon})\,\mathrm{d}\tau. \tag{E-3}$$

where $\hat{\xi}$ is the estimated quantity and $\boldsymbol{\varepsilon}$ is the adaptation mechanism input and Φ_1, Φ_2 are scalar functions. The specific applications of the presented theorems to different MRAS estimators in electric drives and the formation of the equivalent circuits similar to Fig. E-1 can be found in the respective literatures.

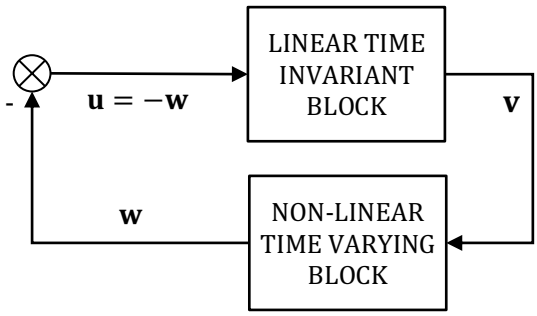

Fig. E-1 Multivariable nonlinear time-varying feedback system.

E.2 Stability Proof and Adaptation Mechanism Derivation Using Lyapunov Function

The respective MRAS scheme's stability or the adaptation mechanism's derivation can also be done using the Lyapunov theorem, which utilizes the so-called Lyapunov function [114]. A scalar function $V(x)$ is said to be a Lyapunov function if [161]

- $V(x)$ has a continuous first partial derivative and is positive definite, meaning that

$$V(x) > 0. \tag{E-4}$$

- $\dot{V}(x)$ is at least negative semi-definite, meaning that

$$\dot{V}(x) \leq 0. \tag{E-5}$$

Let us consider the IM reference model in the form

$$\dot{\mathbf{x}} = \mathbf{A}(\xi)\mathbf{x} + \mathbf{B}\mathbf{u}, \tag{E-6}$$

$$\mathbf{y} = \mathbf{C}\boldsymbol{x}, \tag{E-7}$$

and the adaptive model in the form

$$\dot{\hat{\mathbf{x}}} = \widehat{\mathbf{A}}\left(\hat{\xi}\right)\hat{\mathbf{x}} + \widehat{\mathbf{B}}\mathbf{u}, \tag{E-8}$$

$$\hat{\mathbf{y}} = \mathbf{C}\hat{\boldsymbol{x}}. \tag{E-9}$$

The error between the reference and adaptive model is defined as $\mathbf{e} = \boldsymbol{x} - \hat{\mathbf{x}}$. Its dynamics is given by

$$\dot{\mathbf{e}} = \dot{\mathbf{x}} - \dot{\hat{\mathbf{x}}} = \mathbf{A}(\xi)\mathbf{e} + \Delta\mathbf{A}(\Delta\xi)\hat{\mathbf{x}} + \Delta\mathbf{B}\mathbf{u}, \tag{E-10}$$

where

$$\Delta\mathbf{A}(\Delta\xi) = \mathbf{A}(\xi) - \widehat{\mathbf{A}}\left(\hat{\xi}\right), \tag{E-11}$$

$$\Delta\mathbf{B} = \mathbf{B} - \widehat{\mathbf{B}}, \tag{E-12}$$

$$\Delta\xi = \xi - \hat{\xi}. \tag{E-13}$$

The Lyapunov function candidate for IM MRAS estimators is usually selected as [114], [118]

$$V = \mathbf{e}^{\mathrm{T}}\mathbf{e} + \frac{\Delta\xi^2}{\lambda}, \tag{E-14}$$

where λ is a positive constant.

The time derivative of the Lyapunov function can be expressed as

$$\begin{aligned}\dot{V} &= \dot{\mathbf{e}}^{\mathrm{T}}\mathbf{e} + \mathbf{e}^{\mathrm{T}}\dot{\mathbf{e}} - 2\Delta\xi\frac{\dot{\hat{\xi}}}{\lambda} \\ &= \left(\mathbf{A}(\xi)\mathbf{e} + \Delta\mathbf{A}(\Delta\xi)\hat{\mathbf{x}} + \Delta\mathbf{B}\mathbf{u}\right)^{\mathrm{T}}\mathbf{e} + \mathbf{e}^{\mathrm{T}}\left(\mathbf{A}(\xi)\mathbf{e} + \Delta\mathbf{A}(\Delta\xi)\hat{\mathbf{x}} + \Delta\mathbf{B}\mathbf{u}\right) - 2\Delta\xi\frac{\dot{\hat{\xi}}}{\lambda}.\end{aligned} \tag{E-15}$$

Equation (E-15) can be manipulated into the form

$$\dot{V} = \mathbf{e}^{\mathrm{T}}\left(\mathbf{A}(\xi)^{\mathrm{T}} + \mathbf{A}(\xi)\right)\mathbf{e} + \left(\mathbf{u}^{\mathrm{T}}\Delta\mathbf{B}^{\mathrm{T}}\mathbf{e} + \mathbf{e}^{\mathrm{T}}\Delta\mathbf{B}\mathbf{u}\right) + \left(\hat{\mathbf{x}}^{\mathrm{T}}\Delta\mathbf{A}(\Delta\xi)^{\mathrm{T}}\mathbf{e} + \mathbf{e}^{\mathrm{T}}\Delta\mathbf{A}(\Delta\xi)\hat{\mathbf{x}}\right) - 2\Delta\xi\frac{\dot{\hat{\xi}}}{\lambda}. \tag{E-16}$$

Under the assumption that $\Delta\mathbf{B} = \mathbf{0}$, (E-16) can be rewritten as

$$\dot{V} = \mathbf{e}^{\mathrm{T}}\left(\mathbf{A}(\xi)^{\mathrm{T}} + \mathbf{A}(\xi)\right)\mathbf{e} + \hat{\mathbf{x}}^{\mathrm{T}}\Delta\mathbf{A}(\Delta\xi)^{\mathrm{T}}\mathbf{e} + \mathbf{e}^{\mathrm{T}}\Delta\mathbf{A}(\Delta\xi)\hat{\mathbf{x}} - 2\Delta\xi\frac{\dot{\hat{\xi}}}{\lambda}. \tag{E-17}$$

The conditions for the negative-semidefiniteness of the Lyapunov function time derivative is usually written in the form [118]

$$\mathbf{e}^{\mathrm{T}}\left(\mathbf{A}(\xi)^{\mathrm{T}} + \mathbf{A}(\xi)\right)\mathbf{e} < 0, \tag{E-18}$$

$$\hat{\mathbf{x}}^{\mathrm{T}}\Delta\mathbf{A}(\Delta\xi)^{\mathrm{T}}\mathbf{e} + \mathbf{e}^{\mathrm{T}}\Delta\mathbf{A}(\Delta\xi)\hat{\mathbf{x}} - 2\Delta\xi\frac{\dot{\hat{\xi}}}{\lambda} = 0. \tag{E-19}$$

The estimated variable can be obtained by manipulating (E-19) and performing an integration which yields

$$\hat{\xi} = \lambda\int_0^t \varepsilon\,\mathrm{d}\tau + \hat{\xi}_0, \tag{E-20}$$

where $\hat{\xi}_0$ is the initial value and

$$\varepsilon = \frac{1}{2\Delta\xi}\left(\hat{\mathbf{x}}^{\mathrm{T}}\Delta\mathbf{A}(\Delta\xi)^{\mathrm{T}}\mathbf{e} + \mathbf{e}^{\mathrm{T}}\Delta\mathbf{A}(\Delta\xi)\hat{\mathbf{x}}\right), \tag{E-21}$$

Equation (E-20) is the expression for an I controller. However, for better dynamics of the estimate, the PI controller is mostly utilized [118]. Therefore, the final equation of the adaptation mechanism which ensures the asymptotic stability of the system takes the form

$$\hat{\xi} = K_{\mathrm{I(MRAS)}}\int_0^t \varepsilon\,\mathrm{d}\tau + K_{\mathrm{P(MRAS)}}\varepsilon, \tag{E-22}$$

where $K_{\mathrm{P(MRAS)}}$ and $K_{\mathrm{I(MRAS)}}$ are proportional and integral gains, respectively.

APPENDIX F OVERVIEW OF MODIFIED INTEGRATORS FOR VOLTAGE MODEL CALCULATION

Generally, the modified integrators can be mathematically described as [122]

$$\frac{\mathrm{d}\,\underline{\hat{\psi}}_1^{\alpha\beta}}{\mathrm{d}t} = \underline{e}_1^{\alpha\beta} + \omega_\mathrm{c}(t)\left(\underline{\psi}_{1(\mathrm{cor})}^{\alpha\beta} - \underline{\hat{\psi}}_1^{\alpha\beta}\right), \tag{F-1}$$

where $\underline{\psi}_{1(\mathrm{cor})}^{\alpha\beta}$ is the correction flux used for the comparison with the estimated flux $\underline{\hat{\psi}}_1^{\alpha\beta}$, $\omega_\mathrm{c}(t)$ is the cutoff frequency that can be variable or fixed, and

$$\underline{e}_1^{\alpha\beta} = \underline{u}_1^{\alpha\beta} - R_1\underline{i}_1^{\alpha\beta}. \tag{F-2}$$

Taking the Laplace transform of (F-1) and assuming that $\omega_\mathrm{c} = \text{const.}$ yields

$$\underline{\hat{\boldsymbol{\psi}}}_1^{\alpha\beta}(s) = \frac{\underline{\mathbf{e}}_1^{\alpha\beta}(s) + \omega_\mathrm{c}\,\underline{\boldsymbol{\psi}}_{1(\mathrm{cor})}^{\alpha\beta}}{s + \omega_\mathrm{c}}. \tag{F-3}$$

By a specific selection of $\underline{\psi}_{1(\mathrm{cor})}^{\alpha\beta}$ we can obtain the various modified integrator algorithms. The block diagram of the generalized modified integrator is shown in Fig. F-1.

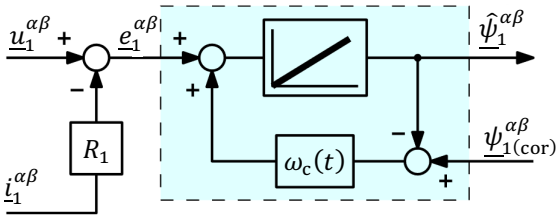

Fig. F-1 General modified integrator structure [122] (edited).

F.1 Integrator Approximation by Low-Pass Filter

Implementing a high-pass filter (HPF) in series with the pure integrator and considering that $\underline{\psi}_{1(\mathrm{cor})}^{\alpha\beta} = 0$ results in the approximation of the integrator by a low-pass filter (LPF) which can be described in the Laplace domain as

$$\frac{\underline{\hat{\boldsymbol{\psi}}}_1^{\alpha\beta}(s)}{\underline{\mathbf{e}}_1^{\alpha\beta}(s)} = \frac{1}{s + \omega_\mathrm{c}}. \tag{F-4}$$

The block diagram of the integrator is depicted in Fig. F-2. The integration scheme is able to remove the DC offset, but the resulting stator flux linkage vector is shifted both in amplitude and in phase. The amplitude and frequency response of the integrator can be written as

$$|G(\mathrm{j}\omega)| = \frac{1}{\sqrt{\omega_\mathrm{s}^2 + \omega_\mathrm{c}^2}}, \tag{F-5}$$

$$\arg\big(G(\mathrm{j}\omega)\big) = -\tan^{-1}\left(\frac{\omega_\mathrm{s}}{\omega_\mathrm{c}}\right). \tag{F-6}$$

Looking at (F-5) and (F-6), it follows that the lower the cutoff frequency, the closer the low-pass filter to the pure integrator but at the same time, the worse the ability to compensate the DC offset accumulation. For proper functionality, it should always be ensured that $\omega_\mathrm{c} < \omega_\mathrm{s}$.

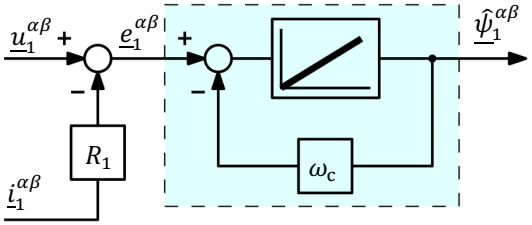

Fig. F-2 Simple low-pass filter-approximated integrator [122] (edited).

F.2 Compensated Filters

The evaluated stator flux linkage vector signal attenuation and lag can be mitigated by implementing compensated filters [153]-[157]. The approaches can be divided into methods with a fixed cutoff frequency and a variable synchronous frequency-dependent cutoff frequency.

F.2.1 Fixed Cutoff Frequency Filters

The fixed-frequency filters are suitable mainly if the drive operates in a narrow band of frequencies since it is not generally possible to find an optimal cutoff frequency ideal for the whole speed range. The amplitude attenuation and phase lag are generally compensated by the inverse transfer function of a high-pass filter in the form

$$\frac{s+\omega_c}{s}. \tag{F-7}$$

Fig. F-3 and Fig. F-4 show the modified integrator scheme with output and input compensation, respectively. The algorithms work well, especially at a steady state and higher speeds. The disadvantage of the schemes lies in the necessity of division by the synchronous frequency, which impairs the integrators' performance around the zero-speed area [154].

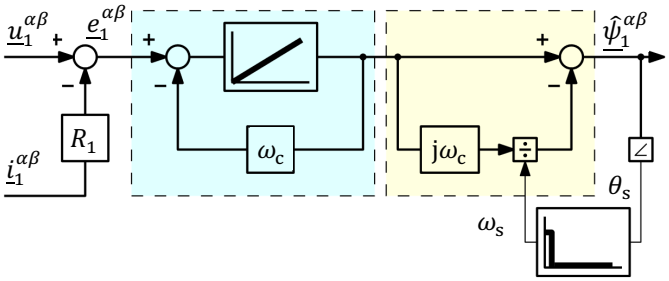

Fig. F-3 Compensated low-pass filter with output compensation [122] (edited).

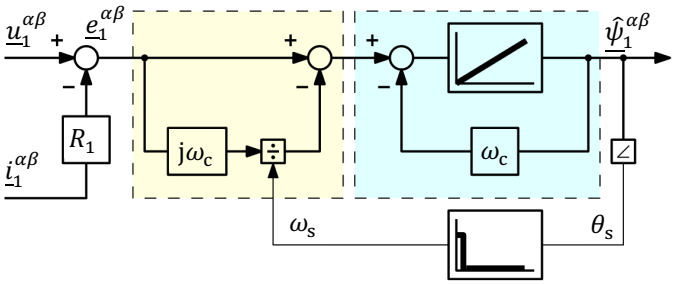

Fig. F-4 Compensated low-pass filter with input compensation [122] (edited).

F.2.2 Variable Cutoff Frequency Filters

Better results are achieved if the cutoff frequency of the filters is variable and somehow dependent on the synchronous frequency, i.e., when $\omega_c = f(\omega_s)$. According to [122], the most common choice is the linear dependence in the form

$$\omega_c = \lambda|\omega_s|, \tag{F-8}$$

where $\lambda \in \langle 0, 1\rangle$. As a rule of thumb, at lower speeds, the parameter λ can be selected "low" (e.g., 0.1), and at higher speeds, higher values closer to 1 are preferred.

Similarly, as in the case of the constant cutoff frequency filters, the proposed schemes can be divided into input and output-compensated filters [153]-[157]. An example of an output-compensated filter based on [156] is depicted in Fig. F-5. The LPF output is multiplied by a term with gain and phase lag, respectively, given by

$$|G_{cor}(j\omega)| = \sqrt{1+\lambda^2}, \tag{F-9}$$

$$\arg G_{cor}(j\omega) = -\operatorname{sign}(\omega_s)\tan^{-1}(\lambda). \tag{F-10}$$

An example of an input-compensated LPF based on [157] is depicted in Fig. F-6. The scheme represents an integration in the form

$$\underline{\hat{\psi}}_1^{\alpha\beta} = \int \left[-\lambda|\omega_s| + (1 - j\lambda \operatorname{sign}\omega_s)\underline{e}_1^{\alpha\beta}\right] dt. \tag{F-11}$$

According to [122], the algorithms presented in Fig. F-5 are Fig. F-6 comparable in terms of the initial error response, but the input-compensated LPF shows better behavior during the speed reversals. Reference [122] also reports that higher values of the parameter λ yield faster rejection of the DC offset and the lower values on the other hand offer better transient response of the integrators.

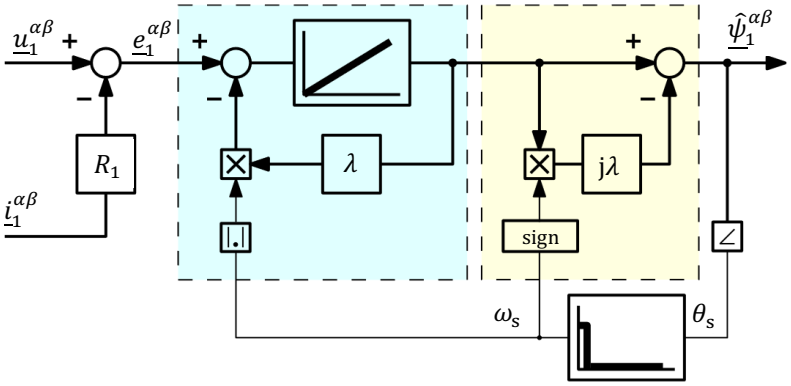

Fig. F-5 Compensated low-pass filter with output compensation [122] (edited).

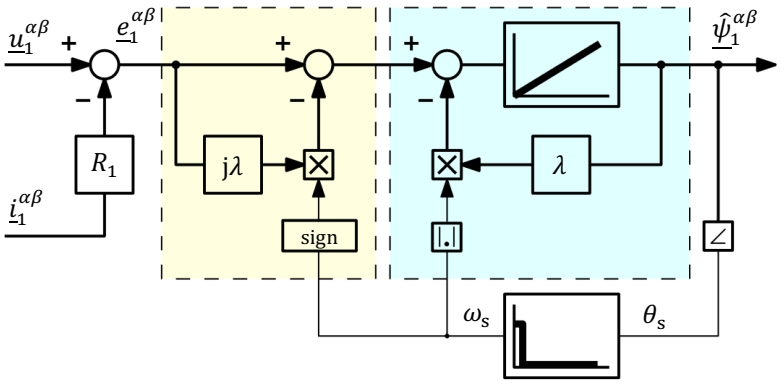

Fig. F-6 Compensated low-pass filter with input compensation [122] (edited).

F.3 Amplitude Saturation Integrators

These algorithms can be viewed as "closed-loop" since in (F-1), the term $\underline{\psi}_{1(\mathrm{cor})}^{\alpha\beta} \neq 0$. This class of integrators chooses the correction flux vector, which has the same phase as the integrator output. Its magnitude then serves as the limiter for the integrator output.

Three integration schemes are presented in [158], which can be described in a general form as

$$\hat{\underline{\boldsymbol{\psi}}}_1^{\alpha\beta}(s) = \frac{\underline{\mathbf{e}}_1^{\alpha\beta}(s)}{s+\omega_\mathrm{c}} + \frac{\omega_\mathrm{c}}{s+\omega_\mathrm{c}} z(s), \tag{F-12}$$

where $z(s)$ is the compensation term. Choosing $z(s) = 0$ yields the equation of an uncompensated LPF. Contrary to that, choosing $z(s)$ based on some modification of $\hat{\underline{\boldsymbol{\psi}}}_1^{\alpha\beta}$ yields the amplitude saturable integrator.

The first and straightforward scheme of the amplitude saturation integrator is presented in Fig. F-7. The correction term $z(s) = \hat{\underline{\boldsymbol{\psi}}}_1^{\alpha\beta}$ until the saturation occurs. Then the output becomes

$$\hat{\underline{\boldsymbol{\psi}}}_1^{\alpha\beta}(s) = \frac{\underline{\mathbf{e}}_1^{\alpha\beta}(s)}{s+\omega_\mathrm{c}} + \frac{\omega_\mathrm{c}}{s+\omega_\mathrm{c}} Z(L), \tag{F-13}$$

where $Z(L)$ is the saturation block output, which is limited to value L. The limiting value should be ideally equal to the actual amplitude of the integrator output. Larger values will superimpose a DC component on the evaluated stator flux linkage vector. The lower values will then distort the integrator output.

Fig. F-8 presents an improved version where only the amplitude of the estimated flux linkage vector is saturated. Such an algorithm mitigates the negative effect of the distortion of the output flux waveform. Fig. F-9 then shows a scheme where the limiting value L is determined by an adaptive controller. The integrator error variable is represented by a dot product of the signals $\hat{\underline{\psi}}_1^{\alpha\beta}$ and $\hat{\underline{e}}_1^{\alpha\beta}$ divided by the magnitude of $\hat{\underline{\psi}}_1^{\alpha\beta}$. Such an error becomes zero when the dot product is zero, meaning that the signals $\hat{\underline{\psi}}_1^{\alpha\beta}$ and $\hat{\underline{e}}_1^{\alpha\beta}$ are orthogonal (i.e., no offset present). The disadvantage is the necessity of tuning an additional PI controller.

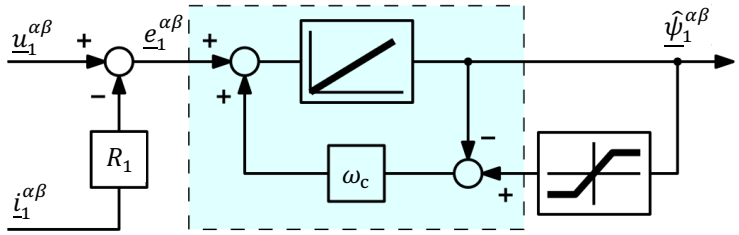

Fig. F-7 Saturable feedback integrator [122] (edited).

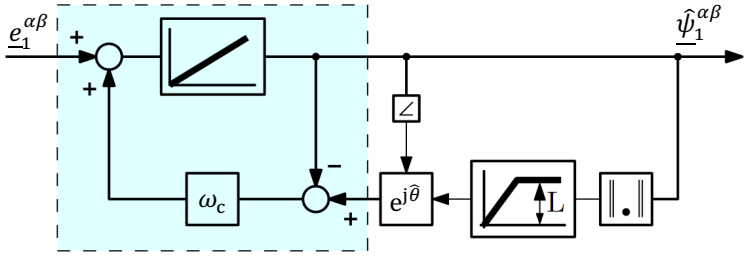

Fig. F-8 Amplitude limiter [122] (edited).

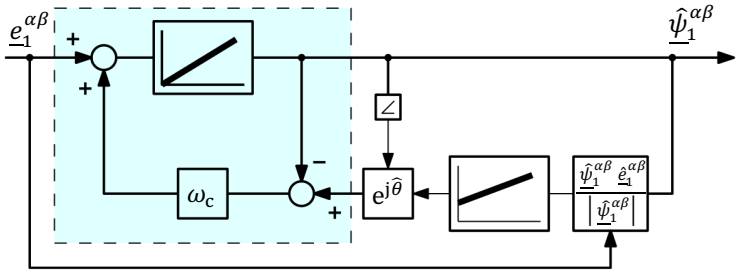

Fig. F-9 Adaptive compensation using quadrature detector [122] (edited).

F.4 Adaptive Stator Flux Observers

The last group of algorithms mentioned in more detail are the so-called adaptive flux observers [159]-[160]. These relatively complex schemes are based on the parallel operation of the IM voltage and current model. The current model is not impaired by the DC offset accumulation problem since cross-terms are present when the vector equation is resolved into the real and imaginary parts. These cross-terms ensure the suppression of the DC offset accumulation. It is generally accepted that the current model yields better performance in the low-speed area than the voltage model and vice versa in the high-speed area.

A general structure of such an integrator is depicted in Fig. F-10. The rotor flux linkage vector obtained from the current model is recalculated into the stator flux linkage vector that is used during the correction process. The correction is mainly based on an adaptive PI controller. The PI controller's output is the estimated offset which is then summed with / subtracted from the pure integrator input. The general integrator equation can be written as

$$\hat{\underline{\psi}}_1^{\alpha\beta} = \int \left(\underline{u}_1^{\alpha\beta} - R_1 \underline{i}_1^{\alpha\beta} \pm \hat{\underline{u}}_{\text{off}}^{\alpha\beta} \right) \mathrm{d}t, \tag{F-14}$$

where $\hat{\underline{u}}_{\text{off}}^{\alpha\beta}$ is the estimated offset from the adaptive PI controller that processes an error variable based on the current and voltage model stator flux linkage vector components.

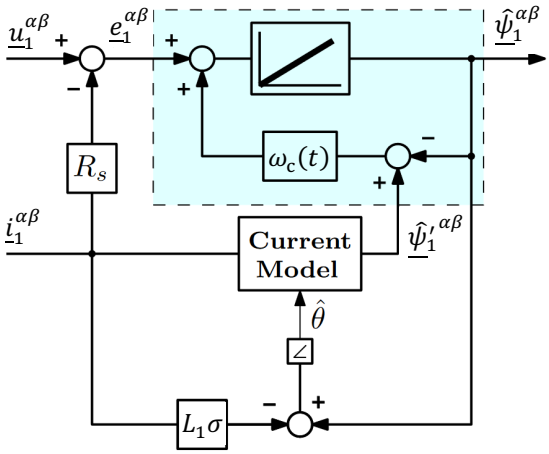

Fig. F-10 General scheme of an adaptive flux observer [122] (edited).

A few other schemes were proposed in the literature that resemble the current model-based adaptive integrator. In [146], the author used a parallel integrator with a saturation based on the reference stator flux linkage vector and an algebraic equation for the offset calculation that is then filtered by a first-order low-pass filter. The scheme also utilizes an additional compensator for high-frequency noise rejection. In [147], the authors presented an integrator with an adaptive PI controller that utilizes the error variable based on the reference and calculated stator flux. This scheme was an inspiration for the algorithm proposed by the thesis author.